

Iowa Research Online

Synthesis of carbon nitrides and composite photocatalyst materials

Montoya, Anthony Tristan

https://iro.uiowa.edu/discovery/delivery/01IOWA_INST:ResearchRepository/12730529290002771?#13730784900002771

Montoya. (2018). Synthesis of carbon nitrides and composite photocatalyst materials [University of Iowa].
<https://doi.org/10.17077/etd.kd68t7cb>

<https://iro.uiowa.edu>
Free to read and download
Copyright © 2018 Anthony Tristan Montoya
Downloaded on 2022/10/11 22:20:05 -0500

SYNTHESIS OF CARBON NITRIDES AND COMPOSITE PHOTOCATALYST
MATERIALS

by

Anthony Tristan Montoya

A thesis submitted in partial fulfillment
of the requirements for the Doctor of Philosophy
degree in Chemistry in the
Graduate College of
The University of Iowa

August 2018

Thesis Supervisor: Associate Professor Edward G. Gillan

Graduate College
The University of Iowa
Iowa City, Iowa

CERTIFICATE OF APPROVAL

PH.D. THESIS

This is to certify that the Ph.D. thesis of

Anthony Tristan Montoya

has been approved by the Examining Committee for
the thesis requirement for the Doctor of Philosophy degree
in Chemistry at the August 2018 graduation.

Thesis Committee:

Edward G. Gillan, Thesis Supervisor

Ned B. Bowden

Tori Z. Forbes

Johna Leddy

Lou Messerle

To you, the reader

“Chemistry is the study of matter, but I prefer to see it as the study of change.”

-Walter White

ACKNOWLEDGEMENTS

I feel that I need to start at the beginning and thank Tom Chung and Frank Sticha, for without these two, I would never have taken such an interest in chemistry in the first place. Then John Bender, who gave me my start in chemical research, giving me the drive to set off on the long journey towards this PhD.

I would like to thank my advisor, Dr. Edward Gillan, for guiding me over these last years. Your patience, understanding, and willingness to work through each of the many problems I came across were *instrumental* to making it through this process. To the Nates (Coleman and Black), you were great people to share an office with for the bulk of these years. Nate C, you were very helpful at setting an example of how to get things done, and otherwise survive without going crazy. Nate B, from the time I taught you as an undergrad to when you officially joined the group as a grad student, I hope I was a suitable mentor. Matt, Ashley and Janaka, I wish you luck with the rest of your careers. To my undergrads Dan Waterhouse and Tony Downs, thank you for your contributions to the work within this thesis.

Thank you to all the Chemistry department staff that helped out with so much of the graduate student paperwork, teaching, billing issues, and room reservations over the years. Sharon Robertson, Lindsay Elliot, Earlene Erbe, Brian Morrison, Janet Kugley, Zoe Peterson, Nick Fransisco, all of your assistance has been greatly appreciated. Thank you to Dr. Sarah Larsen and the GAANN fellowship program for funding and travel support, which provided me opportunities to share my research at ACS and Gordon Conferences. I would also like to thank Santhana Vellupilai, Fu Chen, and George Crull in the NMR facility. Thank you to Dale Swenson in the X-ray diffraction facility for

being available whenever the D8 needed troubleshooting. Thank you to the staff in the Central Microscopy Research Facility, particularly Sylvia Lee for the time and assistance with collecting XPS measurement data. Thank you to Majid Nada for help with running the BET and ICP.

To the rest of the Isotopes, thank you for providing me with some athletic diversion and fresh air from the confines of the Chemistry Building or my apartment. Thanks for getting the team together Michael, and for keeping it going Reid. Bring home that tournament championship. To my fellow TAs, particularly Jake Duncan, Justine Olson, Nick Schnicker, Adam Brummett for making lab prep fun and taking part in cookie breaks.

And finally, my family. My mother and father who raised me and instilled enough discipline and work ethic to get me through everything these years of my life. My sister Beth, whose examples growing up taught me what to do and what not to do, and also gave me a somewhat competitive edge. I finally have more degrees than you. You are all responsible for what I have accomplished.

ABSTRACT

This thesis describes the synthesis, characterization and photocatalytic applications of carbon nitride (C_3N_4) and titanium dioxide (TiO_2) materials. C_3N_4 was prepared from the thermal decomposition of a trichloromelamine (TCM) precursor. Several different reactor designs and decomposition temperatures were used to produce chemically and thermally stable orange powders. These methods included a low temperature glass Schlenk reactor, a high mass scale stainless steel reactor, and decomposition at higher temperatures by the immersion of a Schlenk tube into a furnace. These products share many of the same structural and chemical properties when produced by these different methods compared to products from more common alternate precursors in the literature, determined by infrared spectroscopy (IR), nuclear magnetic resonance spectroscopy (NMR), powder X-ray diffraction (XRD), X-ray photoelectron spectroscopy (XPS), and elemental analysis. C_3N_4 is capable of utilizing light for photocatalysis due to its moderate band gap (E_g), measured to be between 2.2 and 2.5 eV. This enables C_3N_4 to be used in the photocatalytic degradation of organic dyes and the production of hydrogen via the water-splitting reaction. C_3N_4 degraded methylene blue dye to less than 10% of its initial concentration in less than an hour of UV light illumination and 60% under filtered visible light in 150 minutes. It also degraded methyl orange dye to below 20% in 70 minutes under UV light and below 60% in 150 minutes under visible light. Using precious metal co-catalysts (Pt, Pd, and Ag) photo-reduced onto the surface of C_3N_4 , hydrogen was produced from a 10% aqueous solution of triethanolamine at rates as high as $260 \mu\text{mol h}^{-1} \text{g}^{-1}$.

C_3N_4 was also modified by mixing the precursor with different salts (NaCl, KBr, KI, KSCN, and NH_4SCN) as hard templates. Many of these salts reacted with TCM by exchanging the anion with the chlorine in TCM. The products were mostly prepared using the high temperature Schlenk tube reactor, and resulted in yellow, orange, or tan-brown products with E_g values between 2.2 and 2.7 eV. Each of these products had subtle differences in the IR spectra and elemental composition. The morphology of these C_3N_4 products appeared to be more porous than unmodified C_3N_4 , and the surface area for some increased by a factor of 4. These products demonstrated increased activity for photocatalytic hydrogen evolution, with the product from TCM-KI reaching a peak rate as high as $1,300 \mu\text{mol h}^{-1} \text{g}^{-1}$. C_3N_4 was coated onto metal oxide supports (SiO_2 , Al_2O_3 , TiO_2 , and WO_3) with the goal of utilizing enhanced surface area of the support or synergy between two different semiconductors. These products typically required higher temperature synthesis conditions in order to fully form. The compositions of the SiO_2 and Al_2O_3 products were richer in nitrogen and hydrogen compared to unmodified C_3N_4 . The higher temperature reactions with C_3N_4 and WO_3 resulted in the formation of the H_xWO_3 phase, and an alternate approach of coating WO_3 on C_3N_4 was used. The degradation of methyl orange showed a significant increase in adsorption of dye for the composites with SiO_2 and Al_2O_3 , which was not seen with any of the individual components. The composite between C_3N_4 and TiO_2 showed improved activity for hydrogen evolution compared to unmodified C_3N_4 .

The surface of TiO_2 was modified by the reductive photodeposition of several first row transition metals (Mn, Fe, Co, Ni, and Cu). This process resulted in the slight color change of the white powder to shades of light yellow, blue or grey. Bulk elemental

analysis showed that these products contained between 0.04-0.6 at% of the added metal, which was lower than the targeted deposit amount. The Cu modified TiO₂ had the largest enhancement of photocatalytic hydrogen evolution activity with a rate of 8,500 μmol h⁻¹ g⁻¹, a factor of 17 higher than unmodified TiO₂.

PUBLIC ABSTRACT

Carbon nitride and titanium dioxide are semiconductors capable of harnessing energy from light and using it to facilitate different chemical reactions in a process called photocatalysis. This thesis describes the preparation and modification of these materials with the intent of testing and improving their photocatalytic activity. Carbon nitride is formed via the decomposition of trichloromelamine at temperatures above 180 °C. This produces an orange powder that is largely inert to common solvents and thermally stable. Carbon nitrides have been modified by incorporating different salts or metal oxide supports to increase available surface area, an important property when studying catalytic applications. The surface of titanium dioxide was modified using different earth abundant metals as an alternative to a more expensive platinum co-catalyst.

The photocatalytic reactions studied were the degradation of dyes in water and the production of hydrogen gas from water. The degradation of dyes serves as an analog to the removal of pollutants from environmental water systems. Using the described catalysts, up to 90% of the dye can be degraded in the presence of UV light or up to 60% in the presence of visible light. Hydrogen has applications as a clean renewable fuel, though challenges lie in its storage and transportation. By using these catalysts and light energy, hydrogen can be produced from water.

TABLE OF CONTENTS

LIST OF TABLES	xiv
LIST OF FIGURES	xvi
CHAPTER 1 INTRODUCTION AND BACKGROUND	1
1.1 Introduction.....	1
1.2 Carbon Nitrides.....	1
1.3 Titanium Dioxide	4
1.4 Principles of Photocatalysis	6
1.5 Thesis Overview	9
CHAPTER 2 SYNTHESIS AND ACTIVATION OF CARBON NITRIDE FROM TRICHLOROMELAMINE DECOMPOSITION	11
2.1 Introduction.....	11
2.2 Experimental.....	13
Reagents.....	13
Thermal decomposition of TCM	14
Characterization	16
Photocatalytic reactions	17
2.3 Results and Discussion	19
Formation of carbon nitride from the decomposition of TCM.....	19
Solid state characterization of carbon nitride from TCM decomposition.....	22
Compositional analysis of carbon nitride	26
Microstructure and morphology	31
Optical properties.....	33
Photocatalytic studies.....	36
2.4 Conclusions.....	51
CHAPTER 3 POROUS ENGINEERING BY SALT MODIFICATIONS TO CARBON NITRIDE SYNTHESIS	53
3.1 Introduction.....	53
3.2 Experimental.....	55
Reagents.....	55
C ₃ N ₄ synthesis from alkali halide mixtures with TCM	55

C ₃ N ₄ synthesis from thiocyanate mixtures with TCM.....	57
Solid state mixtures with salts.....	58
Water wash of C ₃ N ₄ -salt composites	59
Characterization	59
Photocatalytic reactions	60
3.3 Results and Discussion	62
Initial reactions between TCM and salt additives.....	62
Carbon nitride formation from decomposition of TCM-salt mixtures	67
Chemical and structural characterization of carbon nitride salt composites.....	72
Morphology and surface area.....	77
Optical properties.....	80
Photocatalytic studies.....	83
3.4 Conclusions.....	90
CHAPTER 4 DEPOSITION OF CARBON NITRIDE ONTO METAL OXIDE	
SUPPORTS.....	91
4.1 Introduction.....	91
4.2 Experimental.....	92
Reagents	92
Coating of C ₃ N ₄ onto SiO ₂ , TiO ₂ and Al ₂ O ₃ oxide supports	93
Preparation of C ₃ N ₄ -WO ₃ composite materials	94
Annealing of C ₃ N ₄ -metal oxide composites	96
Reaction of a physical mixture of C ₃ N ₄ and metal oxide support	96
Characterization	97
Photocatalytic reactions	97
4.3 Results and Discussion	99
Decomposition reaction and thermal stability of C ₃ N ₄ in oxide composites.....	99
Chemical and structural characterization of carbon nitride and oxide composites.....	106
Morphology and surface area.....	115
Optical properties.....	119
Photocatalytic studies.....	122

4.4 Conclusions.....	131
CHAPTER 5 ENHANCED PHOTOCATALYSIS OF TRANSITION-METAL SURFACE-MODIFIED TITANIUM DIOXIDE	132
5.1 Introduction.....	132
5.2 Experimental.....	134
Reagents.....	134
Modification of TiO ₂ surface with photodeposited transition metals.....	134
Characterization	136
Photocatalytic reactions	137
5.3 Results and Discussion	139
Photochemical M:TiO ₂ synthesis.....	139
M:TiO ₂ structure, composition, and surface analysis.	139
Optical properties.....	146
Photocatalytic reactions	149
5.4 Conclusions.....	164
CHAPTER 6 PRELIMINARY STUDIES ON METAL NITRIDES, SILICA ETCHING, SELECTIVE ORGANIC PHOTO-OXIDATIONS, CONCLUSIONS, AND FUTURE OUTLOOK.....	166
6.1 Introduction.....	166
6.2 Experimental.....	167
Reagents.....	167
Metal nitride formation on C ₃ N ₄	167
Etching of silica from C ₃ N ₄ @SiO ₂	168
Photocatalytic oxidation of small organic molecules	168
Characterization	169
6.3 Results and Discussion	170
Metal nitrides on C ₃ N ₄	170
Etching of SiO ₂ from C ₃ N ₄ @SiO ₂	172
Photocatalytic oxidations in the vapor phase.....	174
6.4 Overall Thesis Summary and Conclusions.....	176
6.5 Future Outlook.....	177
APPENDIX.....	180

A.1 Photocatalytic Hydrogen Evolution	180
Signal calibration	180
Photocatalysis set-up.....	182
A.2 Quantum Yield Calculations	183
A.3 Protocol for CHN Elemental Analysis.....	185
Start-up.....	185
Calibration and sampling (Manual 4-58).....	185
Shutdown	187
Changing the combustion and reduction tubes	187
REFERENCES	189

LIST OF TABLES

Table 1.1. Band gaps and corresponding absorption edges for C ₃ N ₄ , TiO ₂ , and WO ₃	6
Table 2.1. NMR assignments and shifts for TCM-C ₃ N ₄ (S).....	24
Table 2.2. CHN elemental analysis of C ₃ N ₄ products.	27
Table 2.3. XPS signal positions and surface composition for C ₃ N ₄	30
Table 2.4. Rate constants (min ⁻¹) for UV light degradation of MB dye using TCM-C ₃ N ₄ products.	36
Table 2.5. Rate constants (min ⁻¹) for visible light degradation of MB dye using TCM, MA, and DCDA-C ₃ N ₄ products.....	38
Table 2.6. Rate constants (min ⁻¹) for UV and visible light degradation of methyl orange using TCM-C ₃ N ₄ and DCDA-C ₃ N ₄ products.	42
Table 2.7. XPS surface analysis data for metals deposited on TCM-C ₃ N ₄ (P/A).	45
Table 2.8. Average hydrogen production rates (with standard deviation) for Pt, Pd, and Ag deposited C ₃ N ₄ products with ICP-OES quantification of metal loading.	48
Table 3.1. Heats of formation for tested additive salts. ¹⁰⁰	64
Table 3.2. CHN elemental analysis for selected washed TCM-salt C ₃ N ₄ products from 500 °C tube reactions.	73
Table 3.3. Summary of XRD phases observed in different salt mixtures before and after decomposition reaction (major phase in bold).	77
Table 3.4. BET surface areas of C ₃ N ₄ products from TCM and TCM-salt mixtures.	80
Table 3.5. Rate constants (min ⁻¹) for UV light degradation of methyl orange dye using washed C ₃ N ₄ products from TCM-NaCl mixtures.	83
Table 3.6. Rate constants (min ⁻¹) for UV light degradation of methyl orange dye using washed C ₃ N ₄ produced from different TCM-salt mixtures.	85
Table 3.7. Average hydrogen production rates (with standard deviation) for Pt deposited C ₃ N ₄ and ICP-OES quantification of metal loading.	87
Table 4.1. CHN elemental analysis for C ₃ N ₄ metal oxide composite products.....	108
Table 4.2. BET surface areas of C ₃ N ₄ -metal oxide composites.	119

Table 4.3. Rate constants (min^{-1}) for UV and visible light degradation of methyl orange dye using C_3N_4 -metal oxide composites.....	124
Table 4.4. Rate constants (min^{-1}) for UV and visible light degradation of methyl orange dye using C_3N_4 and milled C_3N_4 -metal oxide composites.	126
Table 4.5. Average hydrogen evolution rates for 1 wt% Pt deposited TiO_2 , C_3N_4 , and C_3N_4 -metal oxide composites over 4 1-hour cycles (standard deviation reported in parentheses).....	129
Table 5.1. ICP-OES and XPS compositions and peak positions of $\text{M}(\text{x}\%)\text{TiO}_2$ samples.	142
Table 5.2. XPS analysis of surface chlorine relative to deposited metals on $\text{M}(\text{x}\%):\text{TiO}_2$	146
Table 5.3. First-order rate constants (min^{-1}) for the degradation of methylene blue dye using $\text{M}(2\%):\text{TiO}_2$ products.....	149
Table 5.4. First-order rate constants (min^{-1}) for the degradation of methylene blue dye using $\text{M}(1\%)\text{M}'(1%):\text{TiO}_2$ products.....	151
Table 5.5. Hydrogen evolution rates ($\mu\text{mol/h}$) and quantum yields for $\text{M}:\text{TiO}_2$ materials.....	156
Table 5.6. Comparison of several Ni and Cu modified titania for hydrogen evolution photocatalysis.	157
Table 5.7. Hydrogen evolution rates ($\mu\text{mol/h}$) and quantum yields for select recycled $\text{M}:\text{TiO}_2$ materials.....	158
Table 5.8. XPS data on select $\text{M}:\text{TiO}_2$ products after use in photocatalytic hydrogen evolution.	159
Table 6.1. Summary of XRD phases observed for annealing reactions between C_3N_4 and MCl_2	171
Table 6.2. CHN elemental analysis of $\text{C}_3\text{N}_4@\text{SiO}_2$ and etched products.....	174
Table A.1. Volume additions of hydrogen and corresponding pressure signals for hydrogen and argon used for calibration.	181

LIST OF FIGURES

Figure 1.1 – Franklin’s proposed pathway of deamination products, which lead to the melon polymer.....	2
Figure 1.2 – The generally accepted ideal structure of g-C ₃ N ₄	4
Figure 1.3 – Unit cell structures of TiO ₂ (A) anatase and (B) rutile. Ti atoms are in cyan and O atoms are in red.	5
Figure 1.4 – Generalized mechanism for photocatalysis at a semiconductor particle surface.	7
Figure 1.5 – Chemical structures of (A) methyl orange and (B) methylene blue dyes.....	8
Figure 2.1 – TGA and DTA plots of TCM decomposition under argon flow and a 10 °C/min ramp rate.	20
Figure 2.2 – FT-IR spectrum of gas phase products from TCM decomposition.	21
Figure 2.3 – Decomposition of TCM to an ideal C ₃ N ₄ structure of condensed heptazines.	21
Figure 2.4 – FT-IR spectra of precursors used to prepare C ₃ N ₄ (a) TCM, (b) MA, and (c) DCDA.	22
Figure 2.5 – FT-IR spectra of (a) TCM-C ₃ N ₄ (S), (b) TCM-C ₃ N ₄ (P), (c) TCM-C ₃ N ₄ (T), (d) TCM-C ₃ N ₄ (P/A), (e) DCDA-C ₃ N ₄ (T), and (f) MA-C ₃ N ₄ (T).....	23
Figure 2.6 – CP-MAS-NMR spectra for TCM-C ₃ N ₄ (S), (a) ¹³ C, (b) ¹⁵ N.....	25
Figure 2.7 – Powder X-ray diffraction of C ₃ N ₄ products (a) TCM-C ₃ N ₄ (S), (b) TCM-C ₃ N ₄ (P), (c) TCM-C ₃ N ₄ (T), (d) TCM-C ₃ N ₄ (P/A), (e) MA-C ₃ N ₄ (T), and (f) DCDA-C ₃ N ₄ (T).....	26
Figure 2.8 – XPS C 1s, N 1s, O 1s, and Cl 2p spectra for TCM-C ₃ N ₄ (P/A).....	29
Figure 2.9 – SEM of (A,B) TCM-C ₃ N ₄ (S), (C,D) TCM-C ₃ N ₄ (P), (E,F) TCM-C ₃ N ₄ (T), (G,H) TCM-C ₃ N ₄ (P/A).....	32
Figure 2.10 – Optical microscope images of (a) TCM-C ₃ N ₄ (S), (b) TCM-C ₃ N ₄ (P), (c) TCM-C ₃ N ₄ (T), (d) TCM-C ₃ N ₄ (P/A), (e) MA-C ₃ N ₄ (T), and (f) DCDA-C ₃ N ₄ (T).....	34
Figure 2.11 – DRS UV-vis of C ₃ N ₄ products (a) raw reflectance spectra and (b) Tauc plots.	35

Figure 2.12 – UV light degradation of methylene blue with TCM-C ₃ N ₄ products, (A) degradation plots and (B) linear rate fits.	37
Figure 2.13 – Visible light degradation of methylene blue with C ₃ N ₄ products, (A) degradation plots and (B) linear rate fits.	39
Figure 2.14 – UV light degradation of methyl orange with C ₃ N ₄ products, (A) degradation plots and (B) linear rate fits.	41
Figure 2.15 – Visible light degradation of methyl orange with C ₃ N ₄ products, (A) degradation plots and (B) linear rate fits.	43
Figure 2.16 – XRD TCM-C ₃ N ₄ (P/A) with photodeposited (a) Pt, (b), Pd, and (c) Ag.	44
Figure 2.17 – Photocatalytic hydrogen evolution using TCM-C ₃ N ₄ (P) with and without Pt co-catalyst.	47
Figure 2.18 – Valence band XPS spectra of (A) TCM-C ₃ N ₄ (S), (B) TCM-C ₃ N ₄ (P), (C) TCM-C ₃ N ₄ (T), and (D) TCM-C ₃ N ₄ (P/A).	50
Figure 2.19 – Band structure diagram for TCM-C ₃ N ₄ products based on XPS valence band spectra and calculated band gaps.	51
Figure 3.1 – Method for introducing porosity into C ₃ N ₄ by hard templating with salts.	54
Figure 3.2 – XRD patterns of TCM-KBr mixtures prepared by (a) mortar and pestle, (b) solution mixture, and (c) ball milling.	64
Figure 3.3 – XRD patterns of TCM-KI mixtures prepared by (a) mortar and pestle, (b) solution mixture, and (c) ball milling.	65
Figure 3.4 – XRD patterns of TCM-KSCN mixtures prepared by (a) mortar and pestle, (b) solution mixture, and (c) ball milling.	65
Figure 3.5 – IR spectra of C ₃ N ₄ precursors (a) TCM, (b) TCM-NaCl, (c) TCM-KBr, (d) TCM-KI, (e) TCM-KSCN, and (f) TCM-NH ₄ SCN.	67
Figure 3.6 – C ₃ N ₄ products prepared from (a) 3:1, (b) 2:1, (c) 1:1, and (d) 1:2 mixtures of TCM:NaCl.	69
Figure 3.7 – TGA plots of C ₃ N ₄ products from 1:1 TCM:NaCl mixtures under air flow and a 10 °C/min ramp rate.	71
Figure 3.8 – TGA plots of C ₃ N ₄ products from salt exchange reactions under air flow at a 10 °C/min ramp rate.	72

Figure 3.9 – IR spectra of water washed C_3N_4 products prepared from 500 °C tube decompositions of (a) TCM, (b) TCM-NaCl, (c) TCM-KBr, (d) TCM-KI, (e) TCM-KSCN, and (f) as-synthesized TCM-NH ₄ SCN.....	74
Figure 3.10 – XRD patterns of C_3N_4 products from TCM-KBr (a) mortar and pestle mixtures, (b) solution mixtures, (c) ball milled mixtures, and (d) washed product.....	76
Figure 3.11 – XRD patterns of C_3N_4 products from TCM-KI (a) mortar and pestle mixtures, (b) solution mixtures, (c) ball milled mixtures, and (d) washed product.....	76
Figure 3.12 – SEM images of (A) 3:1 TCM:NaCl product and its (B) water washed C_3N_4 product, (C) 1:1 TCM:NaCl product and its (D) water washed C_3N_4 product, (E) 1:2 TCM:NaCl product and its (F) water washed C_3N_4 product.	78
Figure 3.13 – SEM images of washed C_3N_4 products from (A) TCM-KBr, (B) TCM-KI, (C) TCM-KSCN, and (D) TCM-NH ₄ SCN.	79
Figure 3.14 – Optical microscope images of C_3N_4 products from 500 °C tube decomposition of (A) TCM-NaCl, (B) TCM-KBr, (C) TCM-KI, (D) TCM-KSCN, and (E) TCM-NH ₄ SCN. Scale bar represents 2 mm.	81
Figure 3.15 – UV-vis DRS data for TCM-salt products (A) reflectance data and (B) Tauc plots.	82
Figure 3.16 – UV-vis analysis of the photodegradation of MO dye using C_3N_4 products from TCM-NaCl mixtures (A) UV-light data (B) linear rate data.	84
Figure 3.17 – UV-vis analysis of the photodegradation of MO dye using washed C_3N_4 products from TCM-salt mixtures (A) UV-light degradation data (B) linear rate data.	86
Figure 3.18 – Stacked plots of photocatalytic hydrogen evolution using TCM-salt products. Each catalyst contained a targeted 1 wt% Pt co-catalyst. The UV lamp was turned on for 1 hour cycles, and the reactor was purged with argon for 10 minutes between each cycle.	89
Figure 4.1 – Optical microscope images of (A) $C_3N_4@SiO_2$ (Schlenk), (B) $C_3N_4@SiO_2$ (Tube), (C) $C_3N_4@Al_2O_3$ (Schlenk), (D) $C_3N_4@Al_2O_3$ (Tube), (E) $C_3N_4@TiO_2$ (Schlenk), and (F) $C_3N_4@TiO_2$ (Tube). Scale bar represents 2 mm.....	101
Figure 4.2 – TGA plots of $C_3N_4@SiO_2$ products under air flow, heated at a rate of 10 °C/min.	103

Figure 4.3 – TGA plots of $C_3N_4@Al_2O_3$ products under air flow, heated at a rate of $10\text{ }^\circ\text{C}/\text{min}$.	103
Figure 4.4 – TGA plots of $C_3N_4@TiO_2$ under air flow, heated at a rate of $10\text{ }^\circ\text{C}/\text{min}$.	104
Figure 4.5 – Optical microscope images of (A) $C_3N_4@WO_3$ (Schlenk), (B) $C_3N_4@WO_3$ (Anneal), (C) $C_3N_4@WO_3$ (Tube), and (D) $WO_3@C_3N_4$. Scale bar represents 2 mm.	105
Figure 4.6 – TGA plots of $C_3N_4@WO_3$ and $WO_3@C_3N_4$ under air flow, heated at a rate of $10\text{ }^\circ\text{C}/\text{min}$.	106
Figure 4.7 – IR spectra of (a) $C_3N_4@SiO_2$ (Schlenk) and (b) $C_3N_4@SiO_2$ (Tube). The large broad peak centered at 1100 cm^{-1} is characteristic of SiO_2 .	109
Figure 4.8 – IR spectra of $C_3N_4@TiO_2$ (Schlenk) and (b) $C_3N_4@TiO_2$ (Tube). The large broad peak centered at 800 cm^{-1} is characteristic of TiO_2 .	110
Figure 4.9 – IR spectra of (a) $C_3N_4@$ (Schlenk) and (b) $C_3N_4@$ (Tube). The broad absorptions centered at 700 cm^{-1} are characteristic of Al_2O_3 .	111
Figure 4.10 – IR spectra of (a) $C_3N_4@WO_3$ (Schlenk) (b) $C_3N_4@WO_3$ (anneal) (c) $C_3N_4@WO_3$ (Tube), and (d) $WO_3@C_3N_4$.	112
Figure 4.11 – XRD patterns of (a) $C_3N_4@TiO_2$ (Tube), (b) $C_3N_4@SiO_2$ (Tube), and (c) $C_3N_4@Al_2O_3$ (Tube).	113
Figure 4.12 – XRD patterns of (a) $C_3N_4@WO_3$ (Schlenk), (b) $C_3N_4@WO_3$ (anneal), (c) $C_3N_4@WO_3$ (Tube), and (d) $WO_3-C_3N_4$.	115
Figure 4.13 – SEM images of (A) $C_3N_4@SiO_2$ (Tube), (B) $C_3N_4@Al_2O_3$ (Tube), (C, D) $C_3N_4@TiO_2$ (Tube), (E) $WO_3@C_3N_4$, and (F) $C_3N_4@WO_3$ (Tube).	117
Figure 4.14 – SEM images of ball milled (A, B) $C_3N_4-TiO_2$ and (C, D) $C_3N_4-WO_3$.	118
Figure 4.15 – UV-vis DRS data for C_3N_4 , TiO_2 , and WO_3 (A) reflectance spectra and (B) Tauc plots.	120
Figure 4.16 – UV-vis DRS data for C_3N_4 -metal oxide composites (A) reflectance spectra and (B) Tauc plots.	121
Figure 4.17 – UV-vis analysis of photodegradation of MO dye (A) UV light data and (B) UV linear rate data.	123
Figure 4.18 – UV-vis analysis of photodegradation of MO dye (A) visible light data and (B) visible linear rate data.	125

Figure 4.19 – UV-vis analysis of photodegradation of MO dye using milled C ₃ N ₄ -TiO ₂ and C ₃ N ₄ -WO ₃ composites (A) UV light data and (B) UV linear rate data.	127
Figure 4.20 – UV-vis analysis of photodegradation of MO dye using C ₃ N ₄ -TiO ₂ (milled) and C ₃ N ₄ -WO ₃ (milled) composites (A) visible light data and (B) visible linear rate data.	128
Figure 4.21 – Photocatalytic hydrogen evolution using C ₃ N ₄ @TiO ₂ (Tube) with 1% Pt co-catalyst. The UV lamp was turned on for 1 hour cycles and the reactor was purged with argon for 10 minutes between each cycle.....	130
Figure 5.1 – XRD patterns for select M(2%):TiO ₂ products, rutile phase TiO ₂ is marked with an asterisk.....	140
Figure 5.2 – SEM images of (A) P25 TiO ₂ and (B) Cu(1%):TiO ₂ photoreaction product.....	141
Figure 5.3 – Representative XPS spectra for 2p doublets for Ti from Cu(2%):TiO ₂ , Mn from Mn(2%):TiO ₂ , Fe from Fe(2%):TiO ₂ , Co from Co(2%):TiO ₂ , Ni from Ni(2%):TiO ₂ , and Cu from Cu(2%)TiO ₂	144
Figure 5.4 – UV-vis DRS data on M(2%):TiO ₂ samples (A) reflectance spectra and (B) Tauc plots.....	148
Figure 5.5 – UV-vis analysis of the photodegradation of MB dye with M(2%):TiO ₂ samples (A) UV light data (B) linear rate data.....	150
Figure 5.6 – UV-vis analysis of the photodegradation of MB dye with M(1%)M'(1%):TiO ₂ samples (A) UV light data (B) linear rate data.	152
Figure 5.7 – Real-time hydrogen gas evolution under UV light illumination for (A) M(1%):TiO ₂ and (B) M(1%),M'(1%):TiO ₂ . H ₂ production was measured during one-hour illumination cycles followed by a 10 minute argon flush. The sequential illumination cycles began at the 30, 100, 170, and 240 minute marks.	154
Figure 5.8 – <i>In-situ</i> metal deposition and hydrogen evolution data, average rates for all 4 cycles (μmol/h) are Co 12.2, Ni 15.8, and Cu 28.3. H ₂ production was measured during 1 hour illumination cycles followed by a 10 minute argon flush. Each illumination cycle began at the 30, 100, 170, and 240 minute marks.	161
Figure 5.9 – <i>In-situ</i> copper UV photodeposition and hydrogen evolution in 18 MΩ water. First UV lamp on cycle began near 30 min and ended at 90 min. Reactor headspace was flushed with argon between UV illumination runs. Second UV lamp on cycle began at 100 min and	

ended at 160 min. Methanol is spiked into solution during the argon flush prior to the third cycle.	162
Figure 6.1 – XRD pattern of Ni ₃ N on C ₃ N ₄ prepared from annealing NiCl ₂ ·6H ₂ O on C ₃ N ₄ at 500 °C under argon.	170
Figure 6.2 – IR spectra of (a) C ₃ N ₄ @SiO ₂ and (b) the 6M NaOH washed product to etch the SiO ₂	173
Figure 6.3 – SEM images of C ₃ N ₄ @SiO ₂ after etching with NaOH.	174
Figure 6.4 – Targeted photocatalytic oxidations of small organic molecules using C ₃ N ₄ -based catalysts.	175
Figure 6.5 – IR spectra of benzene vapor before and after 4 hour UV light (450 W Hg) illumination in the presence of C ₃ N ₄ @TiO ₂	176
Figure A.1 – Linear calibration for the quantification of hydrogen using RGA-MS.	181
Figure A.2 – Photo of Schlenk flask inside the photoreactor cabinet. The hose connected to the gas inlet adapter is connected to an argon Schlenk line in the adjacent hood. The side-arm is connected to the sampling capillary from the RGA-MS. The flask is clamped above the stir plate, positioned 20 cm from the UV lamp.	183
Figure A.3 – Photographs of (A) prepared reduction tube and (B) prepared combustion tube.	188

CHAPTER 1

INTRODUCTION AND BACKGROUND

1.1 Introduction

This thesis will describe the synthesis and modification of carbon nitrides (C_3N_4) and titanium dioxide (TiO_2) and their uses in photocatalysis. It is important to first give an appropriate background to the history of the development of these materials, including synthesis, properties, and applications. The general mechanism for photocatalytic processes will also be discussed.

1.2 Carbon Nitrides

The history of carbon nitride materials dates back to 1834 and the synthesis of the polymer melon by Justus Liebig.¹ By heating mercury (II) thiocyanate, a brown polymeric solid formed with the elimination of mercury sulfide and carbon disulfide, a reaction commonly known as the Pharaoh's serpent. In the years following, reports of the composition of this solid varied around the ratio in the formula $H_3C_6N_9$.¹⁻² It was some time before the structure of melon was further investigated. In 1922, work by Edward Franklin looked at the condensation of the class of ammonio carbonic acids.³ Starting with guanidine, heating the solid leads to a chain of ammonia elimination reactions. With each step the structure condensed, forming dimers and eventually cyclizing and expanding to the melon polymer (Figure 1.1). He also proposed the as yet-to-be-isolated "carbonic nitride" as the final stage of the deammonolysis reactions before complete thermal decomposition. In 1937, Linus Pauling followed up on Franklin's work, identifying the heptazine or tri-s-triazine unit (C_6N_7) as the core of several

cyameluric salts.⁴ Work on derivatives of this core structure continued through the years, but the investigation of the extended C-N structures beyond melon had stagnated.⁵⁻⁸

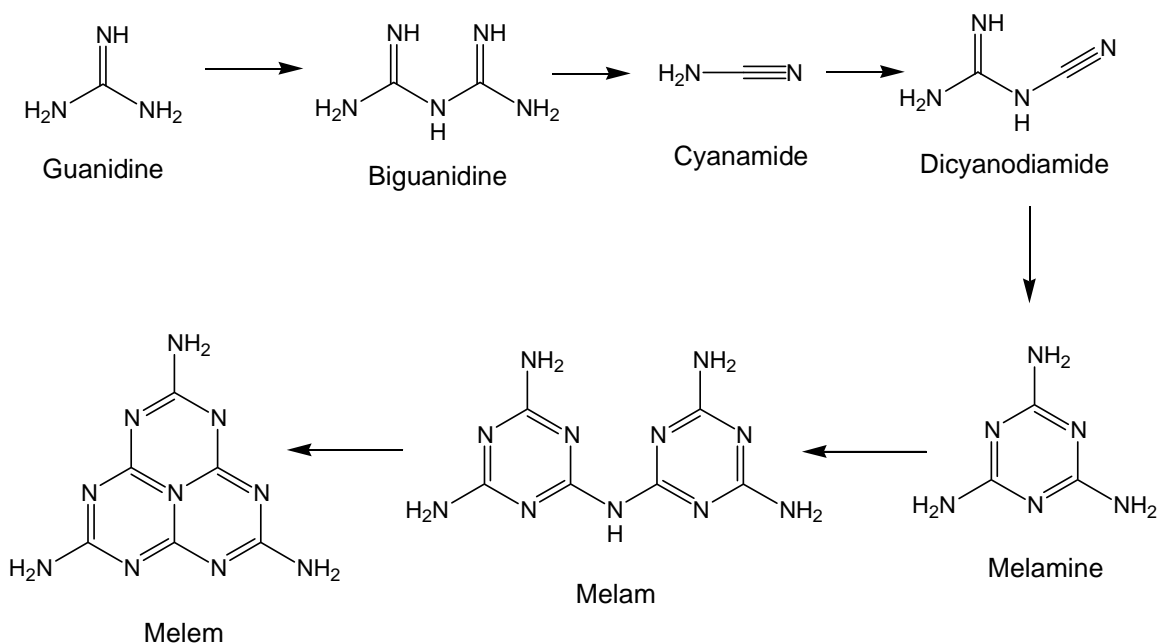


Figure 1.1 – Franklin’s proposed pathway of deamination products, which lead to the melon polymer.

Focus had shifted by the late 1980’s, with Kouvetakis preparing nitrogen-containing graphite thin-film structures from the gas-phase reaction between pyridine and chlorine.⁹ Sekine and co-workers studied high pressure pyrolysis of tetracyanoethylene giving a product with the formula $\text{C}_{4.66}\text{N}$.¹⁰ This led to the consideration of nitrogen in diamond-like structures with carbon. In 1989, a theoretical study by Cohen and Liu proposed the $\beta\text{-C}_3\text{N}_4$ phase based on the structure of $\beta\text{-Si}_3\text{N}_4$.¹¹ Their study predicted this sp^3 covalent structure to have a bulk modulus higher than diamond.¹¹ They proposed using high pressure and temperature reaction conditions to force a phase transition from recently published-amorphous carbon nitride films with the formula C_3N_4 .¹² Early attempts at the formation of $\beta\text{-C}_3\text{N}_4$ found only amorphous, sp^2 structures.¹³⁻¹⁴ Further

computational studies proposed that trying to fit the composition of C_3N_4 into the dense 3-D β - C_3N_4 structure was unfavorable due to N-N repulsions, which could only be relieved at higher C:N ratios (C_4N_3).¹⁵

While research continued on attempts at forming β - C_3N_4 , attention turned to the amorphous sp^2 C_3N_4 products. In a study by Kawaguchi and Nozaki, the polymerization of cyanuric trichloride ($C_3N_3Cl_3$) by itself or mixed with melamine ($C_3N_6H_6$) formed insoluble yellow powders with high thermal stability.¹⁶ They noted similarities in the X-ray diffraction peaks to those of graphite and hexagonal boron nitride, and proposed a structure of linked triazine rings. This graphitic carbon nitride (g- C_3N_4) was prepared from triazines¹⁷⁻²¹ as well as the heptazine derivatives that followed from Pauling's work.²²⁻²³ As g- C_3N_4 could be formed from both triazine and heptazine-based precursors, more studies of the core unit and arrangement of these extended structures were conducted.²⁴⁻²⁵ Solid state NMR studies by the Schnick group were able to show the change of the smaller linear molecules or triazine rings to heptazine from the isolation of the melem ($C_6N_7(NH_2)_3$) intermediate.²⁶⁻²⁷ Further supporting this, Holst in our group showed the base hydrolysis product of g- C_3N_4 , prepared from a triazine precursor, was a crystalline heptazine salt. One possible ideal form of an ordered g- C_3N_4 structure is shown in Figure 1.2, though actual products contain low amounts of hydrogen and are likely to have some degree of defects.

With the generally accepted structure now better understood, studies turned to examinations of chemical and physical properties. In addition to its robust chemical and thermal stability, g- C_3N_4 exhibited interesting optical and luminescent properties.^{16, 28-30} Furthermore, there are aspects of the structure that feature electronic properties and

different types of coordinating sites that have potential in catalytic or coordination applications.³¹ Carbon nitride has a reported band gap of 2.7 eV, though this has been shown to vary slightly depending on the precursors and synthesis conditions.³²⁻³³ It has grown in use in photocatalytic reactions, including water-splitting and oxidation of dyes and other organic compounds.³⁴⁻³⁶ The principles of photocatalysis will be discussed in more detail near the end of this chapter.

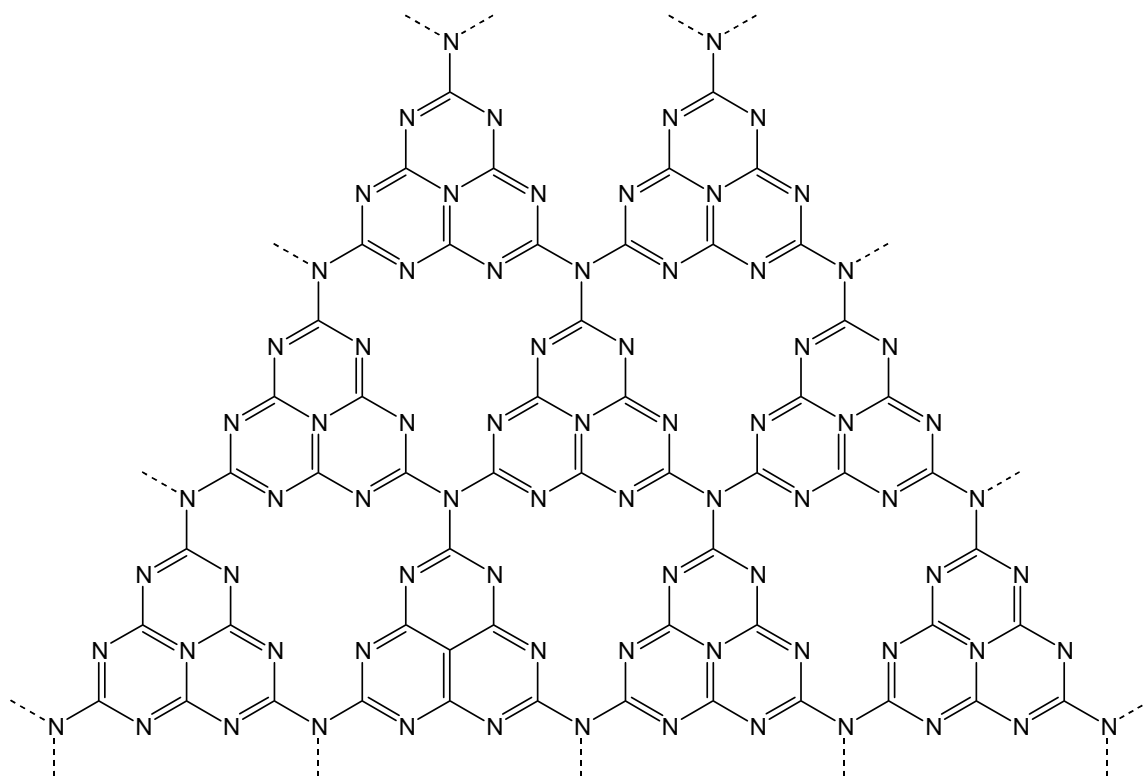


Figure 1.2 – The generally accepted ideal structure of g-C₃N₄.

1.3 Titanium Dioxide

Titanium dioxide (TiO₂) is a white, semiconducting solid, with uses as a catalyst, component in batteries, or pigment.³⁷⁻³⁸ One of the most significant contributions to the study of photocatalysis was the work of Fujishima and Honda, who demonstrated the photolysis of water into hydrogen and oxygen using TiO₂ in an electrochemical cell.³⁹

TiO₂ has two common structures, anatase (Figure 1.3A) and rutile (Figure 1.3B). The band gap for these structures differ between 3.2 eV for anatase and 3.0 eV for rutile.

Though different, both structures are restricted to the absorption of UV light in order to promote electrons from the valence band to the conduction band and utilize this charge separation for a photocatalytic process. To overcome these challenges, structural doping, dye sensitization, or compositing with other light-absorbing semiconductors or metal co-catalysts are methods used.⁴⁰⁻⁴²

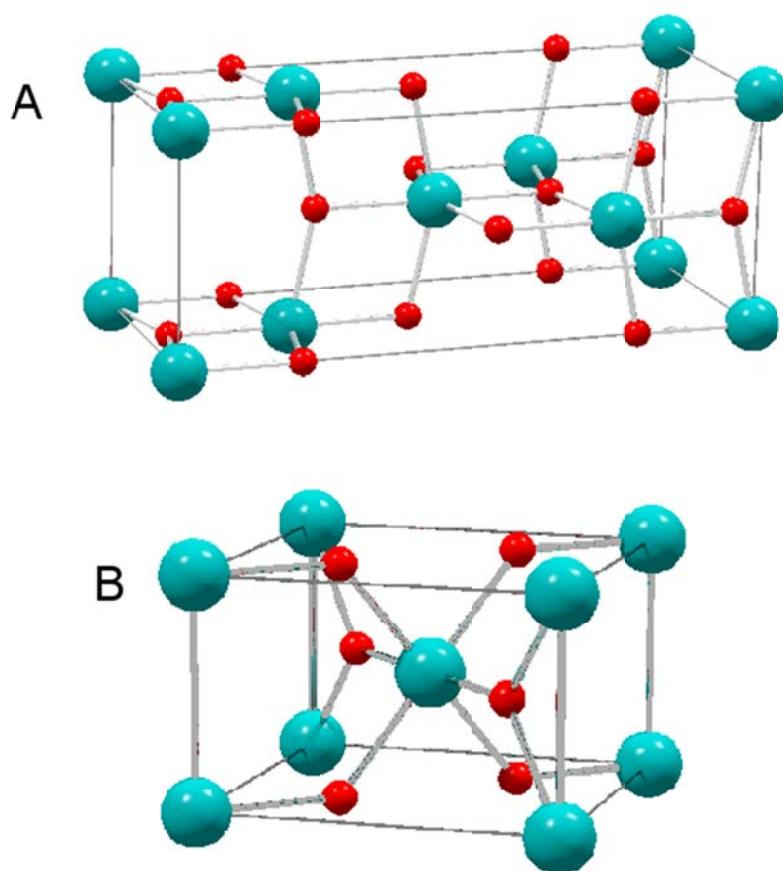


Figure 1.3 – Unit cell structures of TiO₂ (A) anatase and (B) rutile. Ti atoms are in cyan and O atoms are in red.

1.4 Principles of Photocatalysis

Following the work of Fujishima and Honda, many studies have gone into the design of catalysts for the photocatalytic production of hydrogen as a clean, renewable fuel source.⁴³⁻⁴⁴ However, this is only one class of photocatalytic reaction.

Photochemical reactions have been used for many different redox processes.⁴⁵ With a suitable semiconducting substrate, platinum and other precious metals can be photo-reduced onto the surface without the need of a reducing agent such as NaBH₄ or flowing hydrogen.⁴⁶⁻⁴⁷ This photoreduction method has also been used as a way for removing metal ions from wastewater.⁴⁸⁻⁵⁰ So far, all of the reactions described have been reduction processes, but photocatalytic oxidations are just as prominent. Similar to the removal of metal ions, the removal of organic dyes and industrial or pharmaceutical waste can be done with photocatalysis.⁵¹⁻⁵⁴ The oxidative degradation of this waste to more environmentally-benign products presents an alternate method of water remediation.

The requirements for a photocatalyst are a semiconductor (SC) with a band gap suitable to the light source, stability in the reaction media, and favorable charge-separation kinetics. Band gaps for the semiconductors studied in the following chapters are summarized in Table 1.1.

Table 1.1. Band gaps and corresponding absorption edges for C₃N₄, TiO₂, and WO₃.

Semiconductor	Bandgap (eV)	Absorption edge (nm)
C ₃ N ₄	2.7	460
TiO ₂	3.2 (A), 3.0 (R)	388 (A), 413 (R)
WO ₃	2.6-2.8	443

The general mechanism for the function of the catalyst is shown in Figure 1.3. First, the catalyst absorbs light with energy larger than its band gap. This excites an electron from the full valence band (VB) to the empty conduction band (CB). The promoted electron can then be transferred to target chemical reduction to form the intended product. The hole remaining in the valence band is used to oxidize another component, accepting an electron and allowing the cycle to continue. In most cases either the reduction or oxidation is the intended process, and a sacrificial oxidant or reductant will be added to the system to suppress the reverse reaction.

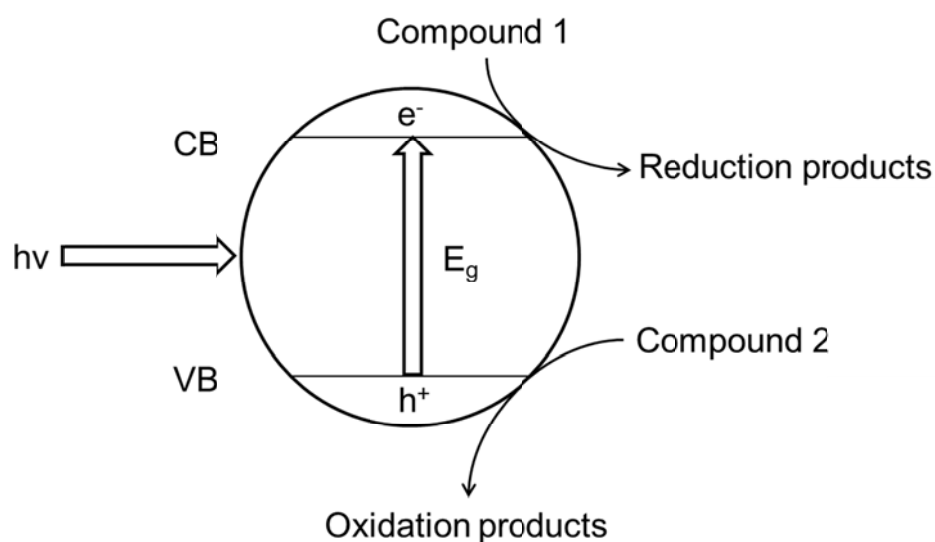
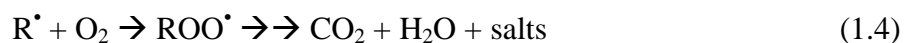


Figure 1.4 – Generalized mechanism for photocatalysis at a semiconductor particle surface.

The photocatalytic oxidative degradation of organic dyes is often attributed to a radical hydroxide mechanism (Equations 1.1-1.4).⁵⁵





The hole produced when the semiconductor is illuminated produces a hydroxyl radical from water. The hydroxyl radical abstracts hydrogen from the organic molecule, forming the radical organic compound. This interacts with atmospheric oxygen to form an organic peroxy radical, and the process continues until complete oxidation to carbon dioxide, with aqueous inorganic salts as byproducts. In the case of the dyes to be studied in this thesis, methyl orange (Figure 1.5A) and methylene blue (Figure 1.5B), these salts will be nitrates and sulfates.

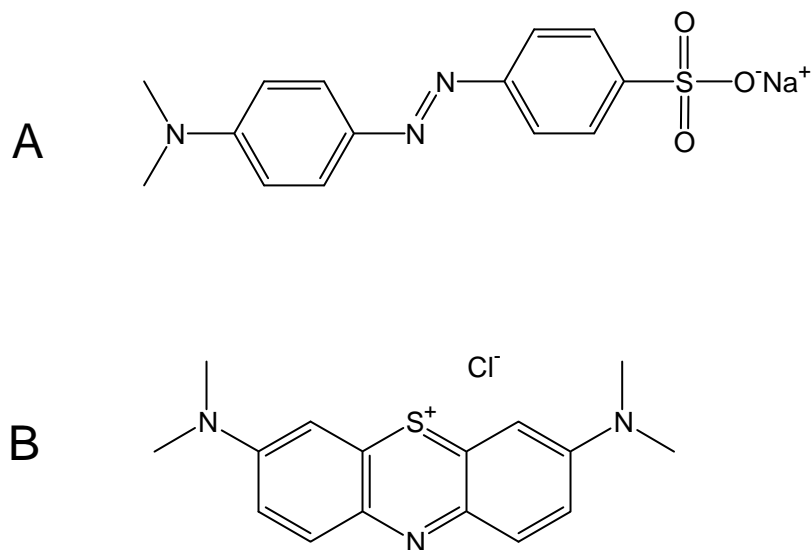


Figure 1.5 – Chemical structures of (A) methyl orange and (B) methylene blue dyes.

The water-splitting reaction is comprised of the reduction of protons to hydrogen and oxidation of water to oxygen (Equations 1.5 and 1.6). Based on the reduction potentials for each half reaction, the semiconductor used as catalyst must have a band gap greater than 1.23 eV.⁴⁴ While the semiconductors described in Table 1.1 all have large enough band gaps, only C₃N₄ and TiO₂ have suitable CB levels to perform the reduction of hydrogen.⁵⁶ Methanol or triethanolamine are commonly used as the sacrificial oxidant for hydrogen evolution.⁴⁴ This limits the production of oxygen during the reaction, instead forming the higher organic oxidation products leading to carbon dioxide.



1.5 Thesis Overview

The remaining chapters of this thesis are as follows. Chapter 2 will detail the synthesis of C₃N₄ from a trichloromelamine (TCM) precursor under several synthesis temperatures and reactor designs. Chapter 3 will detail the modification of the TCM precursor by incorporating different salts as hard templates to increase porosity in the product structure. Chapter 4 will detail the use of different oxides as supports for the formation of C₃N₄. Chapter 5 will detail the modification of TiO₂ by photoreduction of first row transition metals onto its surface. These chapters will feature characterization of the solids by infrared (IR) spectroscopy, thermogravimetric analysis (TGA), elemental analysis, powder X-ray diffraction (XRD), nuclear magnetic resonance (NMR), X-ray photoelectron spectroscopy (XPS), scanning electron microscopy (SEM), and UV-vis diffuse reflectance spectroscopy (UV-vis DRS). Each chapter will also examine the

photocatalytic degradation of dyes and the water-splitting reaction for hydrogen production. Chapter 6 will discuss overall conclusions and research areas with preliminary results that may be starting points for future projects.

CHAPTER 2

SYNTHESIS AND ACTIVATION OF CARBON NITRIDE FROM TRICHLOROMELAMINE DECOMPOSITION

2.1 Introduction

Graphitic carbon nitride (g-C₃N₄) has been extensively studied as a metal-free photocatalyst.^{55, 57-62} It consists of a conjugated nitrogen-rich network that is typically formed through the thermal condensation and ring expansion of nitrogen containing precursors, with cyanamide (NC-NH₂) being one of the simplest precursors.^{3, 31, 58} Early synthetic work to obtain carbon nitrides utilized film growth from triazine-based precursors.^{14, 63} Two precursors commonly used for C₃N₄ growth are dicyandiamide (DCDA, C₂H₄N₄) and melamine (triaminotriazine, C₃N₃(NH₂)₃).⁶⁴⁻⁶⁶ The generally-accepted local structure of sp² hybridized carbon nitride materials is composed of linked tri-s-triazine (heptazine, C₆N₇) units. The heptazine structural model is supported by X-ray and neutron diffraction, IR, NMR, and XPS analysis.^{21, 26, 67-70} These structurally-disordered carbon nitride materials are akin to condensed and crosslinked polymers, and early molecules to materials syntheses studied heptazine polymers as C₃N₄ intermediates.²²⁻²³ As described in Chapter 1, even C₃N₄ grown from triazine-based precursors shows properties consistent a tri-s-triazine extended structure rather than a triazine network. The heptazine core structure is supported by the fact that C₃N₄ chemical degradation in hot KOH yields only the heptazine oxyanion, and this anion has strong luminescent properties.^{69, 71}

Carbon nitride materials have recently found extensive use in photocatalytic oxidation and reduction reactions, including environmental applications such as the

oxidative degradation of aqueous organic model pollutants⁷²⁻⁷³ or gas phase photolysis of NO.⁷⁴ Applications in organic reactions include use as a photoinitiator in radical polymerization⁷⁵ and selective oxidation of alcohol or sulfonate functional groups.⁷⁶⁻⁷⁷ The photocatalytic production of hydrogen from aqueous systems has been demonstrated with carbon nitrides decorated with Pt co-catalysts.^{34, 59, 78-79} This has also extended to the use of C₃N₄ in electrode design for photoelectrochemical hydrogen evolution reactions (HER).^{61, 80} Silica templates have been utilized to generate mesoporous C₃N₄ products with higher surface area that leads to greater photocatalytic activity.⁸¹⁻⁸² Thermal or chemical exfoliation of bulk C₃N₄ produces colloidal nanoflakes that lead to improved photocatalytic activity.⁸³⁻⁸⁴ The level of structural order in the π -stacking direction is often on the order of a few nanometers and can vary with different synthetic methods. Such nanoscale changes influence physical properties of the carbon nitride materials. Given the typical structural disorder associated with these polymer-like structures, recent work has identified and exploited important carbon nitride defects to enhance its catalytic properties.⁸⁵⁻⁸⁷

This Chapter describes the structure and photocatalytic behavior of C₃N₄ produced from the rapid and exothermic self-decomposition of a thermochemically-unstable trichloromelamine (TCM, (C₃N₃(NHCl)₃) and compares its properties with carbon nitride materials produced from melamine and DCDA. Our previous work established the thermochemically-reactive nature of the TCM precursor under external heating (<250 °C) or in contact with a resistively-heated nichrome wire.^{21, 69} These reports also showed that while TCM-derived C₃N₄ is very stable in organic solvents, acids, and bases, it undergoes base hydrolysis when refluxed in 3 M KOH. The local

C_3N_4 structural information was consistent with a network structure built up of interconnected heptazine (C_6N_7) rings. Though TCM has the advantage of a low reaction temperature, higher synthesis temperatures and post-reaction annealing were explored to compare their effect on photocatalytic activity. The rapid combustion-like decomposition and condensation of TCM leads to carbon nitrides that form as large nanoscale to small micrometer-sized plate-like particles made up of smaller fused regions. The TCM-derived C_3N_4 materials were utilized as photocatalysts in the oxidative degradation of methyl orange dye under UV and filtered visible light compared to C_3N_4 from DCDA and melamine. Solution photoreduction reactions were used to add Pt, Pd, or Ag nanoparticle co-catalysts onto the C_3N_4 surface for HER. HER photocatalysis was successfully performed in aqueous solution using triethanolamine as a sacrificial oxidant, and hydrogen gas evolution was conveniently measured in real-time using a portable mass spectrometer.

2.2 Experimental

Reagents

Trichloromelamine ($C_3N_3(NHCl)_3$, TCM, 98%) was purchased from GFS Chemical and stored in an argon atmosphere glovebox. Other reagents used as received were melamine ($C_3H_6N_6$, MA, Aldrich 99+%), dicyandiamide ($C_2H_4N_4$, DCDA, Alfa Aesar, 99%), methanol (ACS certified, Fisher), triethanolamine (Alfa Aesar, 98+%), $H_2PtCl_6 \cdot 6H_2O$ (99.9%, Strem), K_2PdCl_6 (Baker & Co. Inc.), $AgNO_3$ (Aldrich, 99+%), methylene blue (high purity, Alfa Aesar), and methyl orange (85% dye content, Sigma Aldrich). Deionized water (18 M Ω) was prepared using a Photronix MiniQuad system.

Thermal decomposition of TCM

Safety Warning: Most C_3N_4 formation reactions involve the condensation of C-N bonded precursors that can liberate hazardous byproduct gases. Careful hood ventilation must be utilized and pressure calculations should be performed on closed systems that can rapidly increase in pressure during synthesis. Appropriate hood shields and PPE should be employed during synthesis and product workup and isolation.

Rapid heating in Schlenk reactor

TCM (600 mg, 2.6 mmol) was loaded into a 100 mL round bottom flask and connected to a reflux condenser fitted with a gas inlet adapter. The reactor was purged with nitrogen on a Schlenk line prior to heating. The reactor was heated rapidly on a heating mantle to a set temperature of 300 °C. Typically, by 240 °C the decomposition will occur, noted by the color change of the solid in the flask and vigorous gas evolution. The byproduct gases were first sampled via syringe to transfer to a gas IR cell for characterization, and then the remaining gas in the reactor was vented into the fume hood. The bulk tan-orange product was recovered (~23% mass yield). This Schlenk synthesized product from TCM will be referred to as TCM- $C_3N_4(S)$.

Rapid heating in a Parr reactor

Inside a glovebox, TCM (5.0 g, 21.8 mmol) was loaded into a glass-lined stainless steel reactor (Parr Instruments, 125 mL, model 4752). The reactor was sealed using a wrench on the six hex bolts before removal from the glovebox. The reactor was put into a fitted Glass-col heating mantle and heated to 250 °C at 10 °C/min. The external temperature, internal temperature, and internal pressure from the thermocouple and pressure gauge readings were written down at timed intervals as the system was heated.

Near 220 °C there was a spike in internal temperature (from 120 °C to 250 °C) and pressure (1000 psi). As the system cooled, the pressure equilibrated to 350 psi. The reactor was slowly vented into the fume hood and then disassembled. A bright orange, sponge-like solid was collected from the inside of the reactor (20% mass yield). This Parr-synthesized product from TCM will be referred to as TCM-C₃N₄(P).

Single-step high temperature heating in a Schlenk tube

TCM (400 mg, 1.7 mmol) was loaded into a 1.5 cm diameter test tube cut to 5 cm long, and put into a Schlenk tube with and fitted with a gas inlet adapter. An oil bubbler was connected to the side arm for pressure venting and degassed with nitrogen. The tube was clamped in position above a vertically oriented furnace, set to heat to 500 °C at a rate of 10 °C/min and held for 1 hour. Gas evolution was observed from the bubbler near 180°C. After the hold, the tube was cooled and vented of byproduct gases. A porous orange pellet was recovered from the insert (~20% mass yield). This tube-synthesized product from TCM will be referred to as TCM-C₃N₄(T).

Annealing of carbon nitrides

As synthesized C₃N₄ (Schlenk or Parr methods) was treated at higher temperatures to further anneal the structure. Typically, 100-300 mg of product was loaded into an alumina boat, which was put inside a Pyrex tube closed on one end. The tube was connected to a Schlenk line, evacuated, and back-filled with argon. The tube was placed into a clamshell furnace and heated to between 450 °C and 500 °C at a rate of 5 °C/min and held for 1-3 hours. Following annealing, 60-90% of the starting mass was recovered from the boat and a transported film of white material was observed at the cool

end of the tube. These anneals of Schlenk and Parr synthesized products from TCM will be referred to as TCM-C₃N₄(S/A) and TCM-C₃N₄(P/A).

Synthesis of reference carbon nitrides

Melamine (MA) or dicyandiamide (DCDA) (400 mg, 3.2 mmol MA, 4.75 mmol DCDA) was loaded into a 1.5 cm diameter test tube cut to 5 cm long, and put into a Schlenk tube with and fitted with a gas inlet adapter. An oil bubbler was connected to the side arm for pressure venting and degassed with nitrogen. The tube was clamped in position above a vertically-oriented furnace, set to heat to 500 °C at a rate of 10 °C/min and held for 1 hour. After the hold, the tube was cooled and vented of byproduct gases. A hard yellow solid was recovered from the insert (~34% mass yield from MA, ~45% mass yield from DCDA). This tube synthesized product from TCM will be referred to as MA-C₃N₄(T) and DCDA-C₃N₄(T).

Ball milling of carbon nitrides

To examine the effect of macroscopic surface area changes on carbon nitride properties, selected products were ball milled using a high-energy ball mill (FormTech FTS 1000). Solid (100 mg) was loaded into a 5 mL stainless steel milling jar with 2x 5 mm steel balls. Milling was performed at 1200 rpm for a duration of 5 minutes.

Characterization

FT-IR spectra were collected on a Nicolet Nexus 670. Solid samples were prepared as KBr pellets for data collection. Gas samples were analyzed by transferring 5 mL of gas from the reaction vessel into a 10 cm long gas IR cell with KBr windows. Elemental analysis was performed on a Perkin Elmer 2400 Series II CHNS/O Analyzer,

with 1-2 mg of sample in crimped tin capsules. Powder X-ray diffraction was collected on a Bruker D8 system (source Cu K α , 5-80°, 0.050 °/step) with samples deposited on glass slides. Solid state ^{13}C and ^{15}N CP-MAS-NMR spectra were collected on a 500 MHz Bruker spectrometer. Thermogravimetric analysis was performed on a Seiko Exstar 6300 TGA-DTA. Samples were heated up to 1000°C at a rate of 10°C/min under air or argon flow. Scanning electron microscopy images were collected on a Hitachi S-4800 FE-SEM ($v_{\text{acc}}=1.8\text{kV}$). X-ray photoelectron spectra for samples pressed onto indium foil were collected on a Kratos Axis Ultra DLD XPS. Diffuse reflectance spectra were collected on a Cary 5000 Series UV-Vis-NIR Spectrophotometer (300-800 nm, 10 nm/s). Solid samples were loaded into a round compression sample holder with a 1 cm diameter sampling area. Kubelka-Munk conversions were calculated from the Cary software, and Tauc plots were generated using $[F(R)h\nu]^{1/2}$. Indirect band gap values were approximated by extrapolating the linear portion of the absorption edge. BET surface area measurements were collected on a Quantachrome Nova 1200, using 100-200 mg of ground solid sample. ICP-OES data was collected using a Varian 720-ES. Samples (5-10 mg) were dissolved in a heated mixture of 5 mL concentrated H_2SO_4 and 1 mL concentrated HNO_3 and diluted in 25 mL volumetric flasks with 5% HNO_3 .

Photocatalytic reactions

Oxidative degradation of organic dyes

Dyes studied for photochemical reactions were methyl orange ($\text{C}_{14}\text{H}_{14}\text{N}_3\text{NaO}_3\text{S}$) and methylene blue ($\text{C}_{16}\text{H}_{18}\text{ClN}_3\text{S}$). A stock 10^{-3} M dye solution was prepared by dissolving the solid dye in 18 M Ω water. The stock solutions were diluted to $4 \cdot 10^{-5}$ M

for methyl orange and $2 \cdot 10^{-5}$ M for methylene blue to fit the peak at λ_{\max} in the range ($\lambda_{\text{MO}}=504$ nm, $\lambda_{\text{MB}}=665$ nm, $A < 1.50$) of the UV-vis spectrophotometer (Agilent 8453). To 30 mL beakers, 10 mL of dye solution and 10 mg of catalyst was added. An additional beaker containing only dye was used as to evaluate self-degradation in the absence of catalyst. Samples were stirred a minimum of 30 minutes in the dark to allow dye absorption equilibrium to be reached. Samples were exposed to UV light (Ace-Hanovia, 450 W Hg) in 15-30 minute intervals in air. After each irradiation period, the catalysts were separated from the dye solution by centrifugation and the UV-vis spectrum of each solution was collected to quantify the remaining concentration of dye. Experiments were typically carried out for 2 hours of total UV irradiation. For visible light experiments, 400 nm long pass filters (Edmund Optics) were placed between the samples and the lamp to filter light below 400 nm, and total illumination times were extended.

Photocatalytic hydrogen evolution via water-splitting

Catalysts were used as synthesized or with Pt, Pd, or Ag co-catalysts. Metals were photoreduced onto the C_3N_4 surface under UV light using H_2PtCl_6 , K_2PdCl_6 , or AgNO_3 as the metal source. C_3N_4 was suspended in a 50% aqueous MeOH solution containing an amount of the metal salt to target 1-3 wt% of reduced metal on C_3N_4 . The solution was degassed with argon and then exposed to UV light for 2 hours. The solid was collected by centrifugation, rinsed with MeOH, and dried in air.

For hydrogen evolution tests, 10 mg of catalyst (C_3N_4 or $\text{M}(x\%):\text{C}_3\text{N}_4$) was dispersed in a 10 mL solution of 10% aqueous triethanolamine ($\text{C}_6\text{H}_{15}\text{NO}_3$) contained in a 50 mL Schlenk flask. The solution was degassed with argon and connected to a

Residual Gas Analysis Mass Spectrometer (RGA-MS, Stanford Research Systems QMS 300 series) by capillary to the side arm. Data were collected as a pressure vs. time scan, monitoring the masses for nitrogen, argon, hydrogen, water, and oxygen. The reactor was exposed to UV light in 1 hour intervals and was vented with an argon purge between each UV run in order to return hydrogen concentrations to baseline levels. The molar amounts of hydrogen produced were determined using a pressure signal calibration based on known concentration mixtures of H₂/Ar (addition details in the Appendix).⁸⁸

2.3 Results and Discussion

Formation of carbon nitride from the decomposition of TCM

The thermal decomposition of trichloromelamine was studied using three different reaction methods, each suited for different scales or heating methods. In the glass Schlenk reactor, the physical changes were observed directly (e.g. color change and gas evolution) at reaction temperature. In the Parr reactor the internal temperature and pressure were monitored. As the heating mantle reached 250 °C, the interior temperature was 105 °C immediately before the reaction occurred. The internal temperature jumped to 230 °C, but quickly cooled back to 150 °C within a minute, indicating a sudden, brief exothermic decomposition. This temperature change also paired with a pressure increase to 1000 psi at the instant of decomposition, but dropped to 450 psi after the initial shock. Once the reactor had cooled back to room temperature, the internal pressure had equilibrated to 350 psi. Thermogravimetric analysis of TCM under argon flow (Figure 2.1) supports the observations from these reaction methods, showing the first major mass loss paired with an exothermic event near 200 °C. Rapid mass loss continues for the next

20-30 °C as the stable carbon nitride product forms. Mass loss is gradual at higher temperatures due to the slow volatilization of C_xN_y fragments from the solid, until complete decomposition by 700 °C. The thermal behavior of TCM from the TGA data helped to determine suitable conditions for annealing experiments.

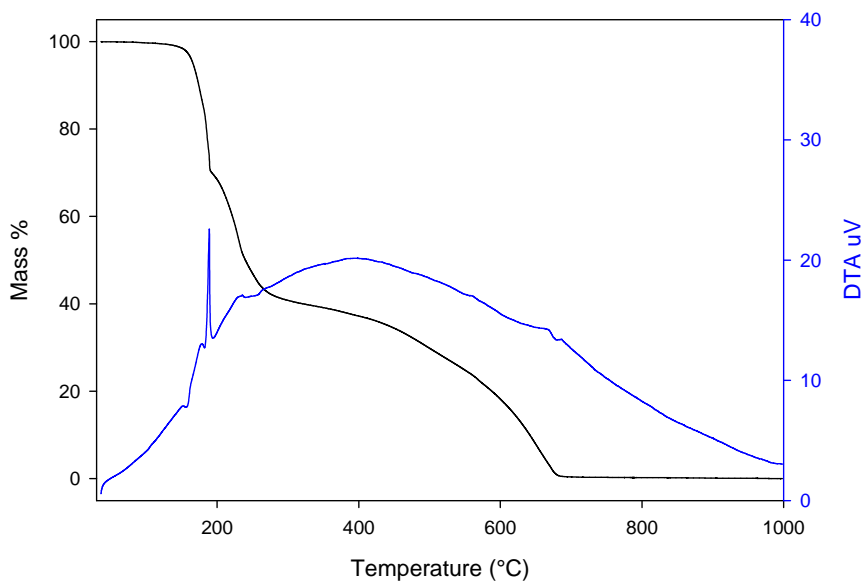


Figure 2.1 – TGA and DTA plots of TCM decomposition under argon flow and a 10 °C/min ramp rate.

The exothermic peak in the DTA matches with the gas evolution that occurs during the decomposition reaction. By transferring this gas to an IR cell, the IR signatures of the gases present could be identified. From the gas phase IR spectrum (Figure 2.2) several sets of peaks were observed. The broad peaks from 3245-3380 cm^{-1} correspond to HCN, the sharp peaks from 2600-3070 cm^{-1} correspond to HCl, the peaks at 2200 cm^{-1} correspond to C_2N_2 , and the peaks at 2100 cm^{-1} correspond to CNCl. Further analysis of the product gases by RGA-MS also showed the presence of Cl_2 (m/z

70 for $^{35}\text{Cl}^{35}\text{Cl}$, m/z 72 for $^{35}\text{Cl}^{37}\text{Cl}$) which could not be observed by IR spectroscopy and also confirmed the presence of the gases observed by IR.

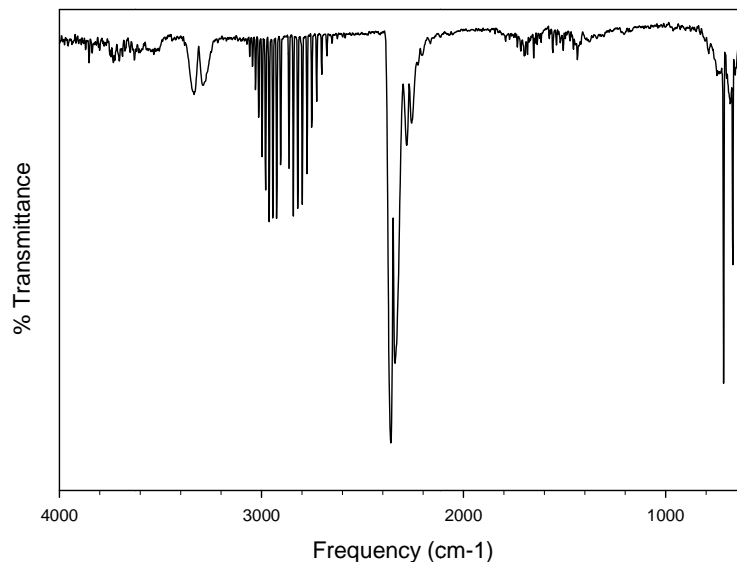


Figure 2.2 – FT-IR spectrum of gas phase products from TCM decomposition.

For the Parr reaction where 22 mmol of TCM was used, ~100 mmol of gaseous products were generated based on the final pressure of the reactor. This mmol estimate is consistent with the expected moles of gaseous C/N/H/Cl containing byproducts shown in Figure 2.3.

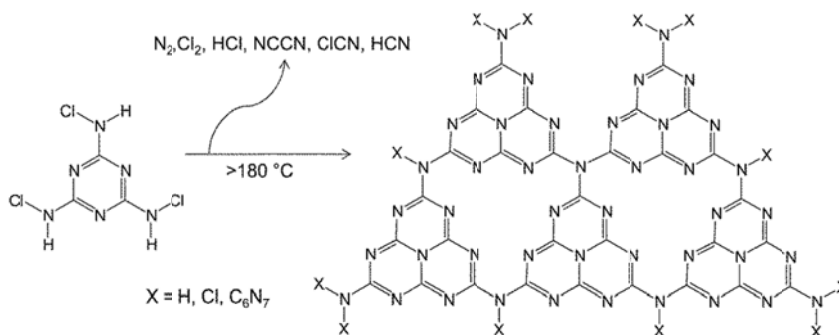


Figure 2.3 – Decomposition of TCM to an ideal C_3N_4 structure of condensed heptazines.

Solid state characterization of carbon nitride from TCM decomposition

Infrared analysis of the different precursors used to prepare carbon nitride show distinct characteristics in some regions (Figure 2.4). Each of the precursors have N-H stretches above 3000 cm^{-1} as well as C-N stretches from $1200\text{-}1700\text{ cm}^{-1}$. Unique to DCDA is the peak at 2100 cm^{-1} for the C-N triple bond of a nitrile group.

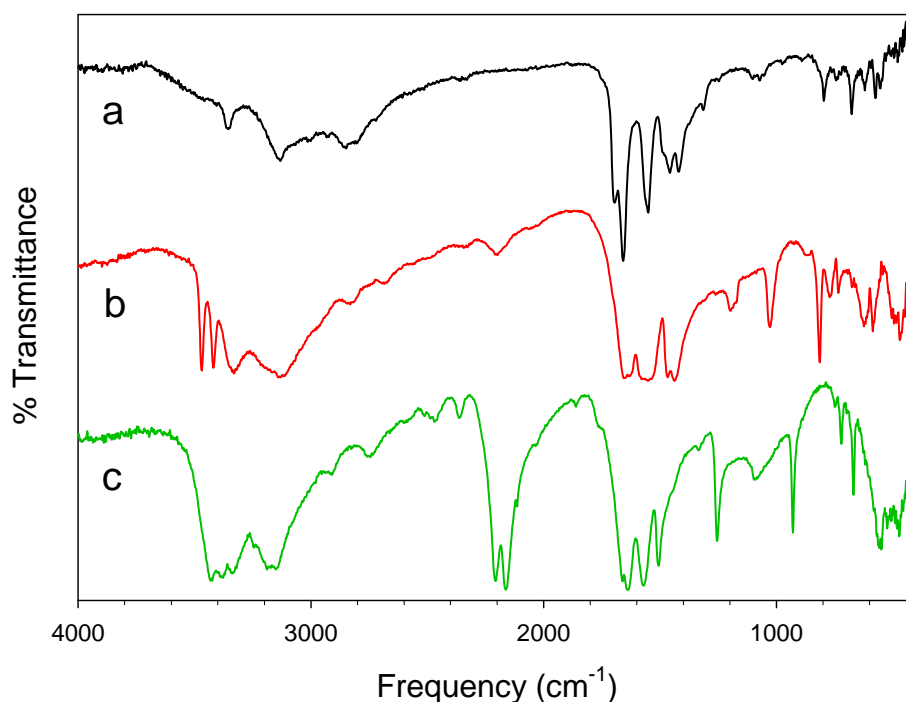


Figure 2.4 – FT-IR spectra of precursors used to prepare C_3N_4 (a) TCM, (b) MA, and (c) DCDA.

The IR spectra of the C_3N_4 products (Figure 2.5) show many similarities between the different decomposition methods and precursors used. The broad band from $3200\text{-}3500\text{ cm}^{-1}$ corresponds to N-H stretches from terminal groups in the C_3N_4 structure. The bands from $1200\text{-}1700\text{ cm}^{-1}$ correspond to C-N ($1200\text{-}1480\text{ cm}^{-1}$) and C=N ($1570\text{-}1640\text{ cm}^{-1}$) stretches in the ring structure. The sharp peak near 810 cm^{-1} is characteristic of the ring breathing mode for conjugated heptazine heterocycles. These peaks are consistent

with those observed for C_3N_4 produced from TCM using rapid, low temperature methods as well as products produced from melamine or cyanamide in air.^{21, 89-90} As compared to Parr TCM, DCDA, and melamine products, the TCM- C_3N_4 (T) product has less well-defined peaks, particularly near 1200 cm^{-1} region, which may indicate some lower structural ordering in this C_3N_4 product.

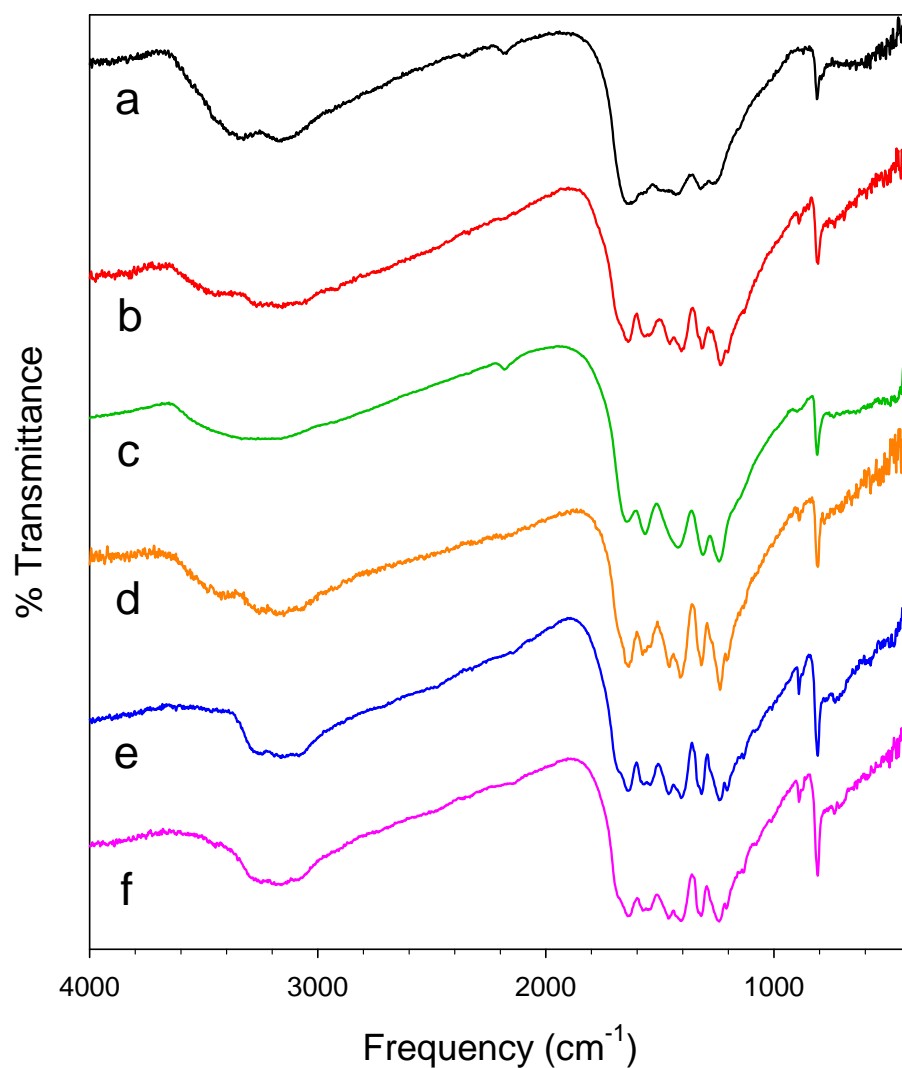
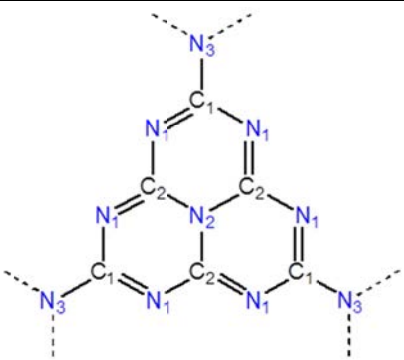


Figure 2.5 – FT-IR spectra of (a) TCM- C_3N_4 (S), (b) TCM- C_3N_4 (P), (c) TCM- C_3N_4 (T), (d) TCM- C_3N_4 (P/A), (e) DCDA- C_3N_4 (T), and (f) MA- C_3N_4 (T).

The similarities in the product spectra are consistent with the literature proposed condensation pathway of the small linear or cyclic molecular precursors. The heptazine fragment, as the core repeat unit of the idealized C_3N_4 structure, is supported by the IR spectra.

Solid state NMR spectra were collected on TCM- $C_3N_4(S)$ for both ^{13}C and ^{15}N nuclei (Figure 2.6). In the ^{13}C spectrum two resonances were present at 156 ppm and 163 ppm. Assigning these signals to the core heptazine unit fits the peak at 156 ppm to the internal ring carbon and the peak at 163 ppm to the external ring carbon. The ^{15}N spectrum showed one well resolved peak at -200 ppm and two overlapping peaks at -250 ppm and -280 ppm. The single peak at -200 ppm can be assigned to the bridging nitrogen (C-N=C) in the heptazine ring. The peak at -250 ppm is assigned to the nitrogen located in the center of the ring, while the remaining peak at -280 ppm is assigned to the nitrogen that links heptazine units. The nitrogen atoms in these last two peaks share a similar sp^2 bonding environment to three carbon atoms, fitting with the proximity of the chemical shifts. Peak assignments with local heptazine repeat unit are summarized in Table 2.1.

Table 2.1. NMR assignments and shifts for TCM- $C_3N_4(S)$.

Local structure	Position	Chemical shift (ppm)	Reference
	C1	163	164.6 ⁶⁹
	C2	156	156.6 ⁶⁹
	N1	-200	-197 to -205 ²⁶
	N2	-250	-234 ²⁶
	N3	-280	-267 to -281 ²⁶

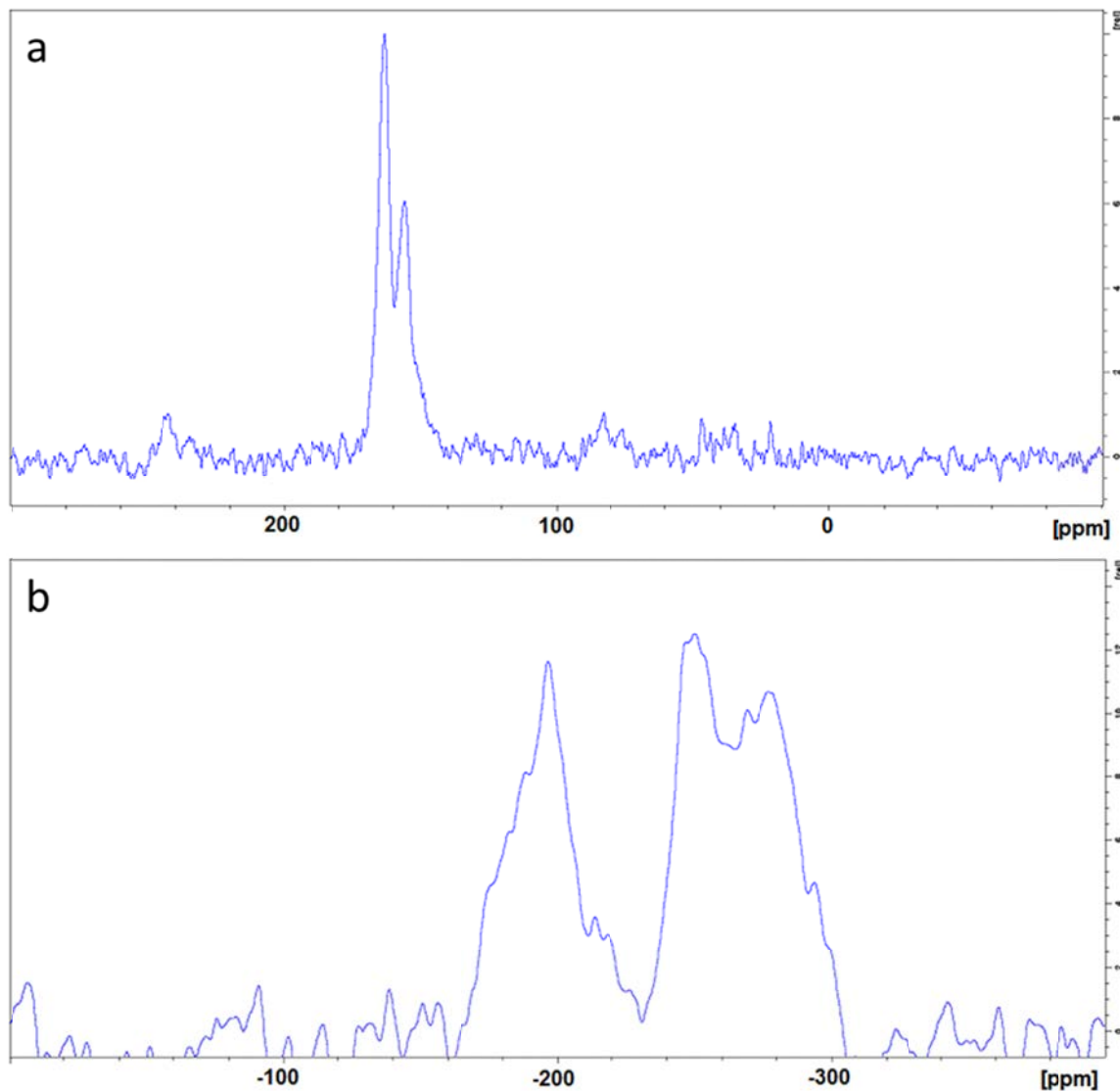


Figure 2.6 – CP-MAS-NMR spectra for TCM- $\text{C}_3\text{N}_4(\text{S})$, (a) ^{13}C , (b) ^{15}N .

Powder X-ray diffraction of the C_3N_4 products from the different methods showed the same level of similarity as the IR spectra (Figure 2.7). The major peak at 27.5° ($d=3.24 \text{ \AA}$) is attributed to the spacing between the tri-s-triazine linked layers or sheets in the C_3N_4 structure. This peak appears sharper in most of the products heated to 500°C , though it was consistently broader for TCM- $\text{C}_3\text{N}_4(\text{T})$. A weaker secondary peak at 13°

($d=6.81 \text{ \AA}$) is sometimes detectable and can be assigned to the in-plane repeat of tri-s-triazine units. The lower intensity or absence of this peak in some samples may indicate that the in-plane ordering is more random during the condensation reactions to form the C_3N_4 structure.

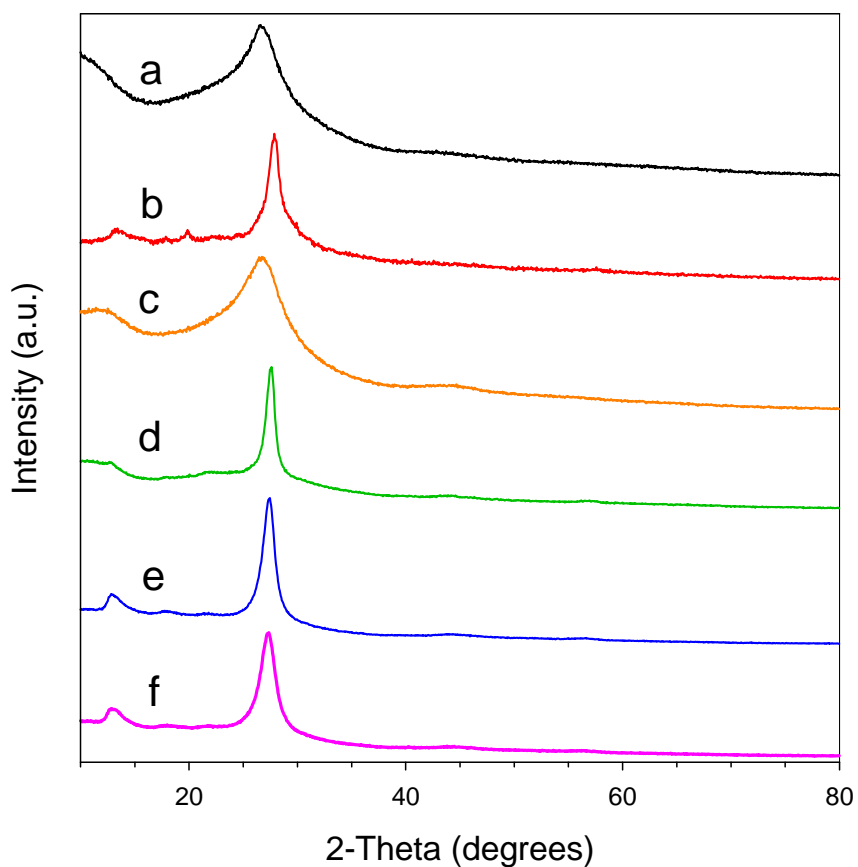


Figure 2.7 – Powder X-ray diffraction of C_3N_4 products (a) TCM- C_3N_4 (S), (b) TCM- C_3N_4 (P), (c) TCM- C_3N_4 (T), (d) TCM- C_3N_4 (P/A), (e) MA- C_3N_4 (T), and (f) DCDA- C_3N_4 (T).

Compositional analysis of carbon nitride

Though carbon nitride is referred to with the formula C_3N_4 , the exact C:N ratio may vary, and some amount of hydrogen usually remains in the product. CHN combustion analysis showed the composition data as shown in Table 2.2. All products

are more nitrogen rich than the general empirical formula for C_3N_4 , instead fitting C_3N_{4+x} ($0.2 < x < 0.8$), consistent with both our previous TCM- C_3N_4 products and C_3N_4 prepared from other precursors.^{21, 69, 83-84, 91} The products also contained hydrogen, likely bound to prevalent NH_2 terminal sites in the structure. The distribution of hydrogen could also cause disruption in the in-plane ordering or conjugation in the long-range structure through formation of secondary NH bridges between heptazine units. The higher-temperature decomposition methods and annealing processes led to C_3N_4 product with a higher total CHN content, indicating that volatile fragments eliminated during heating may contain other elements such as O or Cl. This is consistent with the observed transport of NH_4Cl during annealing experiments, removing chlorine from the low temperature TCM- $C_3N_4(P)$ product. The remaining mass content may be oxygen from either adsorbed water or surface oxidation.

Table 2.2. CHN elemental analysis of C_3N_4 products.

Product (Method)	C wt%	N wt%	H wt%	Total wt % CHN	Formula
TCM- C_3N_4 (S)	30.47	57.15	2.41	90.03	$C_3N_{4.8}H_{2.8}$
TCM- C_3N_4 (S/A)	33.55	58.66	1.81	94.02	$C_3N_{4.5}H_{1.9}$
TCM- C_3N_4 (P)	31.43	55.07	1.93	88.44	$C_3N_{4.5}H_{2.2}$
TCM- C_3N_4 (P/A)	34.27	61.89	1.76	97.92	$C_3N_{4.6}H_{1.8}$
TCM- C_3N_4 (T)	34.41	58.65	1.84	94.90	$C_3N_{4.4}H_{1.9}$
MA- C_3N_4 (T)	33.85	2.16	60.61	96.62	$C_3N_{4.6}H_{2.2}$
DCDA- C_3N_4 (T)	34.03	2.41	60.02	96.46	$C_3N_{4.5}H_{2.5}$

X-ray photoelectron spectroscopy was used to gain additional compositional data as well as information about the bonding environment around carbon (C 1s) and nitrogen (N 1s) as well as oxygen (O 1s) and chlorine (Cl 2p) regions (Figure 2.8). Two peaks were present in the C 1s spectrum at 284.5 eV and 288 eV. The peak at 284.5 eV had a lower intensity and is likely representative of adventitious surface carbon contamination commonly detected in XPS samples. The primary peak at 288 eV agrees with reported C_3N_4 values and can be assigned to carbon in an sp^2 coordination environment as would be expected of an interior or exterior sp^2 carbon in the heptazine subunit (either C1 or C2 from Table 2.1).^{21, 67} The N 1s spectrum shows a major peak at 398 eV with a shoulder at higher energy that is deconvoluted into two peaks at 400 eV and 401 eV. The peak at 398 eV can be assigned to the bridging C-N-C on the exterior of the heptazine ring. The higher energy shoulder peaks fit to $N-(C)_3$, $H-N-(C)_2$, or $(H)_2-N-C$ and potentially some surface N-O further at 404.5 eV.^{21, 67} There are two different three-coordinate nitrogen sites in the ideal layered C_3N_4 structure as shown in Table 2.1, one in the center of the heptazine ring (N2) and the second acting as the linker between heptazine units (N3).

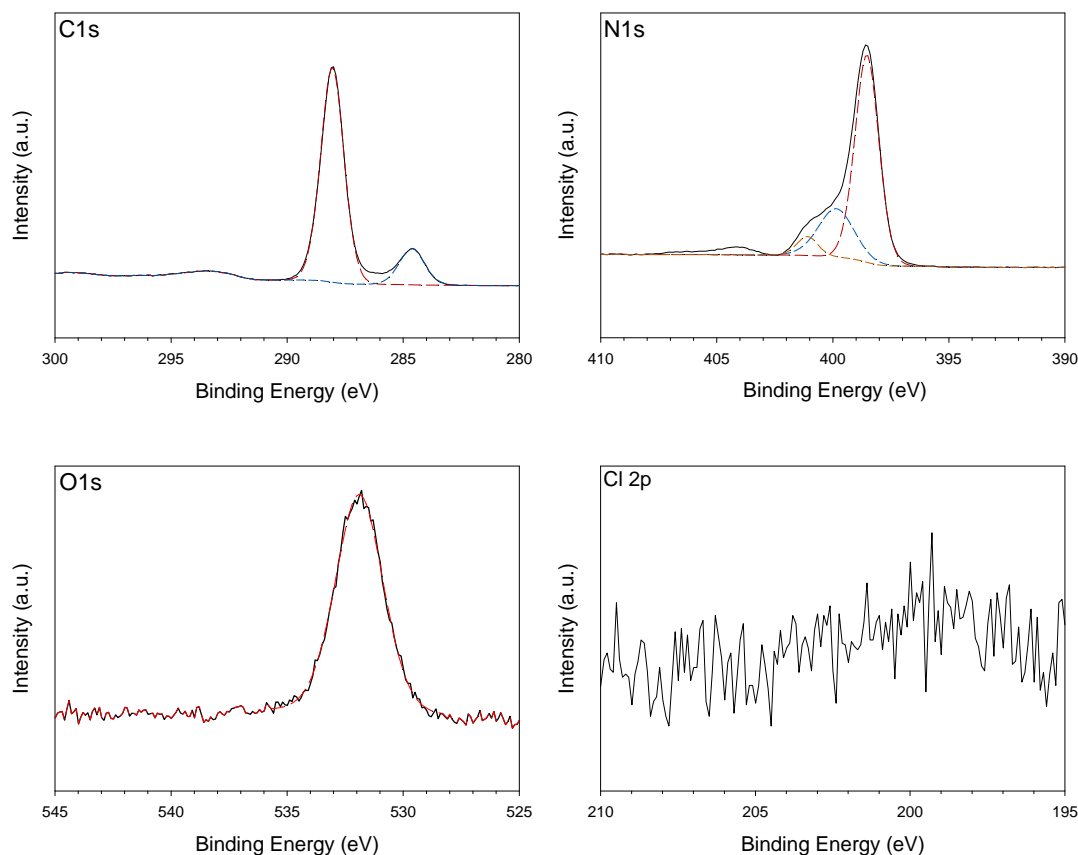


Figure 2.8 – XPS C 1s, N 1s, O 1s, and Cl 2p spectra for TCM-C₃N₄(P/A).

While the bulk elemental analysis data above shows that the C₃N₄ materials are mainly C, N, and H, XPS also showed the presence of surface O and Cl. Products prepared from all methods have some degree of oxygen present on the surface. Trace chlorine was mainly present in TCM-C₃N₄(S) and TCM-C₃N₄(P) products and was generally smaller or absent from the annealed C₃N₄ or product prepared with extended heating at 500 °C. This agrees with the increase of total CHN content in annealed products and observation of NH₄Cl transport. The surface oxygen content also decreased significantly in the TCM-C₃N₄(P/A) product. The surface compositions measured by XPS fit a formula of C₃N_{3+x} (0.4<x<0.6) that has a higher C:N ratio than the bulk

elemental analysis ($\sim\text{C}_3\text{N}_{4+x}$ with $x \geq 0.2$). Since these compositional analysis methods measure different parts of the sample (bulk versus surface), it is not surprising that these values differ. The higher amounts of total carbon on the surface include the small adventitious carbon peak at ~ 284 eV and, if it is removed from the XPS surface composition analysis, then the XPS and CHN data are similar (*e.g.*, for TCM- C_3N_4 (P/A) $\text{C}_3\text{N}_{4.2}$ vs. $\text{C}_3\text{N}_{3.4}$). The low levels of oxygen and chlorine content are also slightly higher than our previously reported values; however, this also represents a difference between bulk and surface compositional analysis.²¹

Table 2.3. XPS signal positions and surface composition for C_3N_4 .

Sample	C1s	N1s	O1s	Cl2p	XPS Composition
TCM- C_3N_4 (S)	284.33, 286.04, 288.09	398.53, 399.73	531.5	197.14, 198.42, 199.81	$\text{C}_3\text{N}_{3.5}\text{O}_{0.4}\text{Cl}_{0.3}$
TCM- C_3N_4 (S/A)	284.5, 286.03, 288.02	398.49, 399.86, 401.07, 404.6	532.04	196.85, 198.4, 200.31	$\text{C}_3\text{N}_{3.4}\text{O}_{0.2}\text{Cl}_{0.01}$
TCM- C_3N_4 (P)	284.34, 288.18	398.34, 399.92	531.38	196.94, 198.34, 199.49	$\text{C}_3\text{N}_{3.6}\text{O}_{0.8}\text{Cl}_{0.2}$
TCM- C_3N_4 (P/A)	284.62, 286.22, 288.05	398.53, 399.86, 404.5, 401.1	531.88	Not detected	$\text{C}_3\text{N}_{3.4}\text{O}_{0.2}$
TCM- C_3N_4 (T)	284.68, 287.94, 288.07, 291.46	398.52, 399.94	532.05, 534.49	197.15, 198.71, 200.83	$\text{C}_3\text{N}_{2.6}\text{O}_{0.8}\text{Cl}_{0.05}$

Microstructure and morphology

The analysis of carbon nitride morphologies by SEM shows that TCM-derived C_3N_4 products form large aggregates above 1 μm (Figure 2.9). These appear to have smooth faces but have fractures along the edges that reveal large nanometer-size features. The produced carbon nitride appears to grow in an aggregated mass of irregularly-shaped plate or sheet-like structures. The TCM- C_3N_4 (S) products have a coral-like appearance of interconnected fragments. The surfaces also appear to have shallow pores formed from the gas evolution during the decomposition reaction. When compared with TCM- C_3N_4 (P), TCM- C_3N_4 (P/A) exhibits many of the same features, including ~100-200 nm sized plate-like particles. There is some opening up of pores and perhaps some smoothing of surface features on some particles. The TCM- C_3N_4 (T) product prepared by direct inert tube heating at 500 °C shows larger, more extended structures on the order of 10-40 μm that contain large pores or depressions on the order of ~500 nm, likely a consequence of rapid gas evolution with precursor condensation to form the carbon nitride. The surfaces of these larger structures contain smooth 1-5 μm fragments with rough edges that are fairly thin (~100 nm).

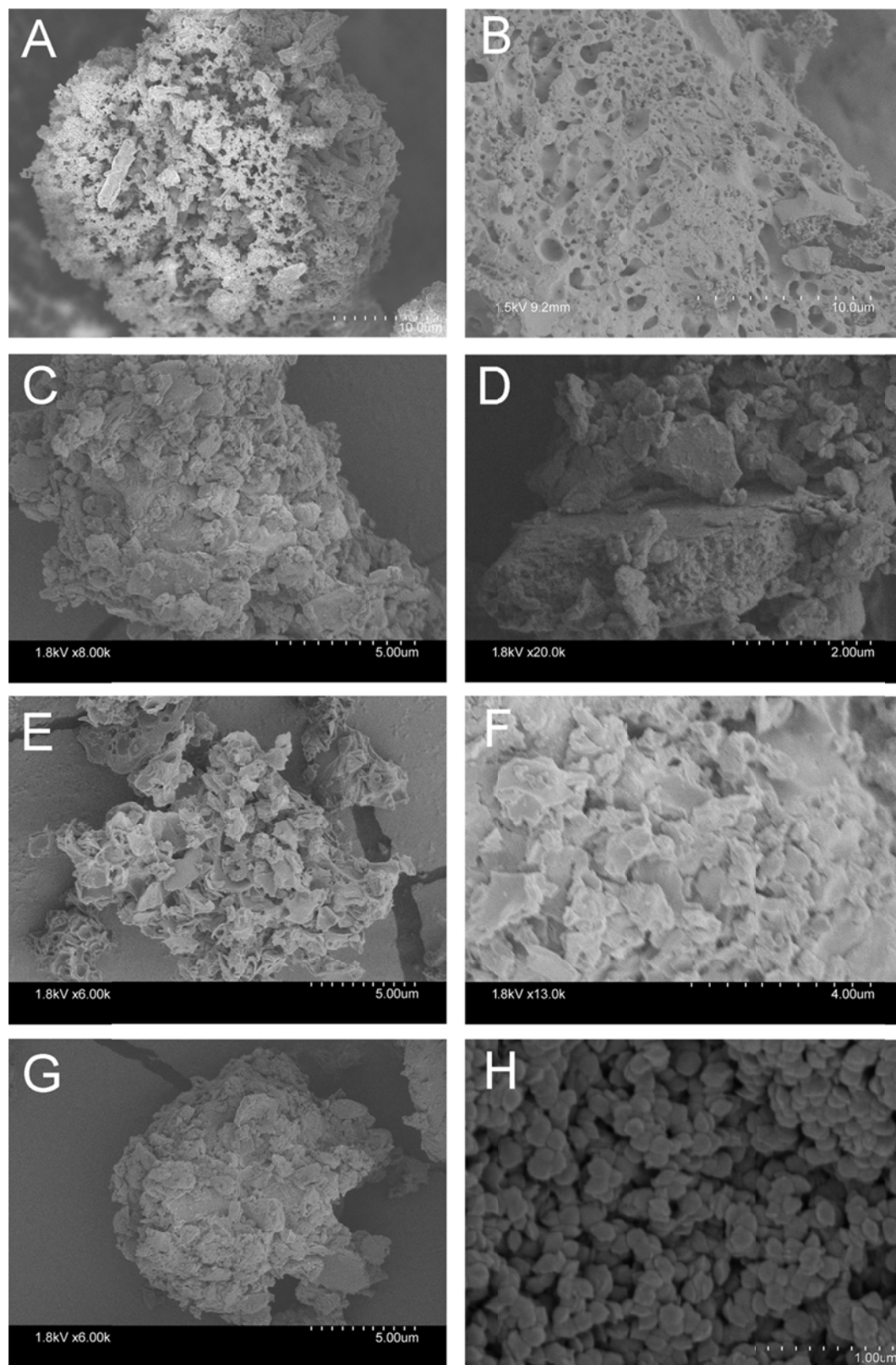


Figure 2.9 – SEM of (A,B) TCM-C₃N₄(S), (C,D) TCM-C₃N₄(P), (E,F) TCM-C₃N₄(T), (G,H) TCM-C₃N₄(P/A).

BET surface area analysis showed that TCM-C₃N₄(P) has a low surface area of 3.3 m² g⁻¹, comparable to our previously reported 5 m² g⁻¹ for a TCM product decomposed via hot wire initiation, and consistent with the packed and aggregated flakes observed.²¹ Following ball-milling, this increased to 6.2 m² g⁻¹. Higher temperature treatment resulted in a slight increase to 4.2 m² g⁻¹ for TCM-C₃N₄(P/A) and 4.1 m² g⁻¹ for TCM-C₃N₄(T). The surface area of TCM-C₃N₄ products are lower than that measured for DCDA-C₃N₄(T) formed in the same experimental setup at 7.6 m² g⁻¹, which is comparable to reported values.⁷⁹

Optical properties

The color of carbon nitride ranges from light yellow to darker orange or tan depending on the synthesis conditions (Figure 2.10). Diffuse reflectance UV-vis was used to determine the optical absorption properties and band gaps of the C₃N₄ products. The reflectance data (Figure 2.11A) can be converted to absorbance data using the Kubelka-Munk function, F(R), and modified to fit a Tauc plot (Figure 2.11B). Plotting this against energy (eV), the band gap of a material can be extracted from an extrapolation of linear regions of the data giving E_g values of 2.2, 2.45, 2.35, 2.42, 2.62, and 2.65 eV for TCM-C₃N₄(S), TCM-C₃N₄(P), TCM-C₃N₄(P/A), TCM-C₃N₄(T), MA-C₃N₄(T), and DCDA-C₃N₄(T), respectively. The band gaps of the DCDA and melamine products are very similar and are comparable to values reported for carbon nitrides,³² and they share a light yellow color as shown in Figure 2.10E and 2.10F. In contrast, the products formed from TCM are consistently darker in color, ranging from bright orange to dark tan. The absorption edges of the TCM products are not as sharp and extend

further into the visible region with low absorbance continuing to ~ 600 nm, consistent with the darker orange colorations of the TCM- C_3N_4 products. A second lower energy absorption event near 2 eV is also observed for the TCM products, which may arise from structural defects giving rise to intermediate band absorption. Similar secondary absorption edges have been reported for annealed carbon nitrides.⁸⁴

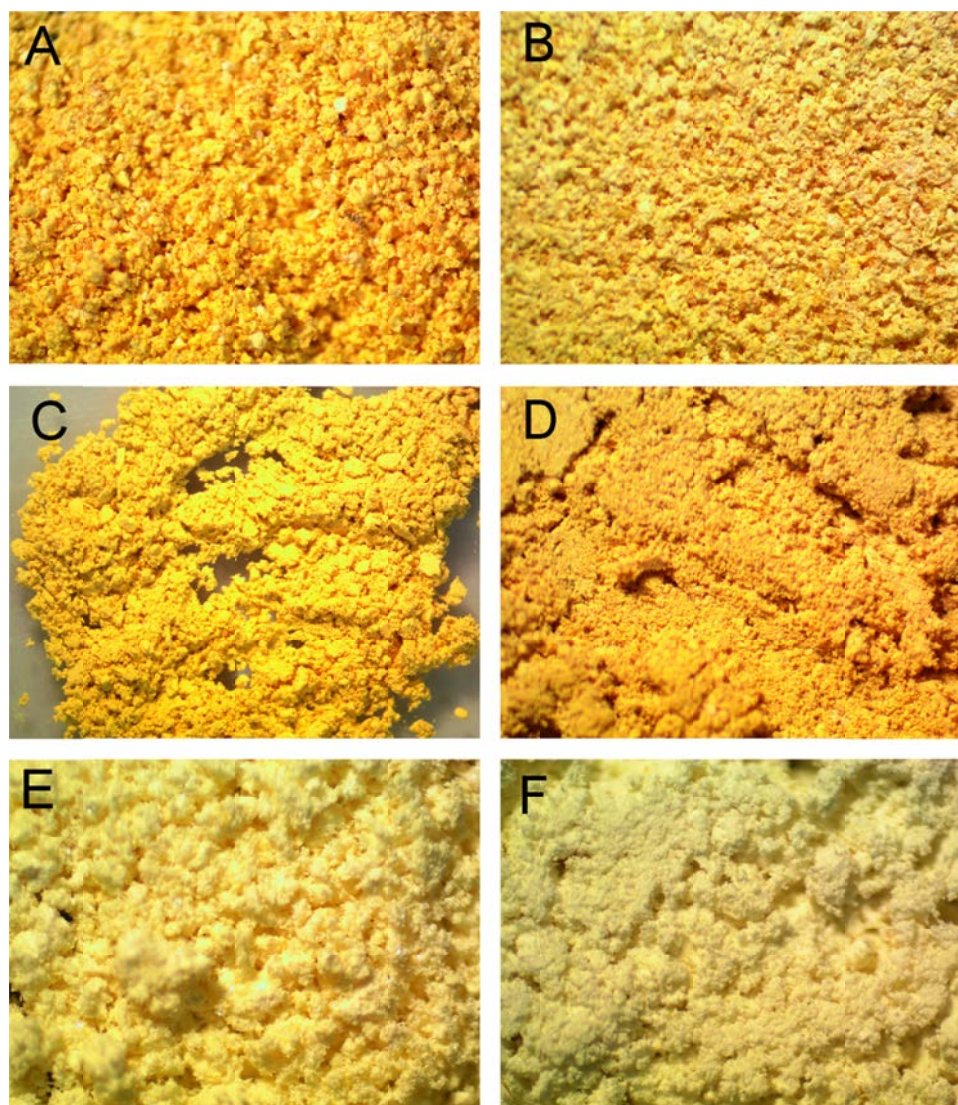


Figure 2.10 – Optical microscope images of (a) TCM- C_3N_4 (S), (b) TCM- C_3N_4 (P), (c) TCM- C_3N_4 (T), (d) TCM- C_3N_4 (P/A), (e) MA- C_3N_4 (T), and (f) DCDA- C_3N_4 (T).

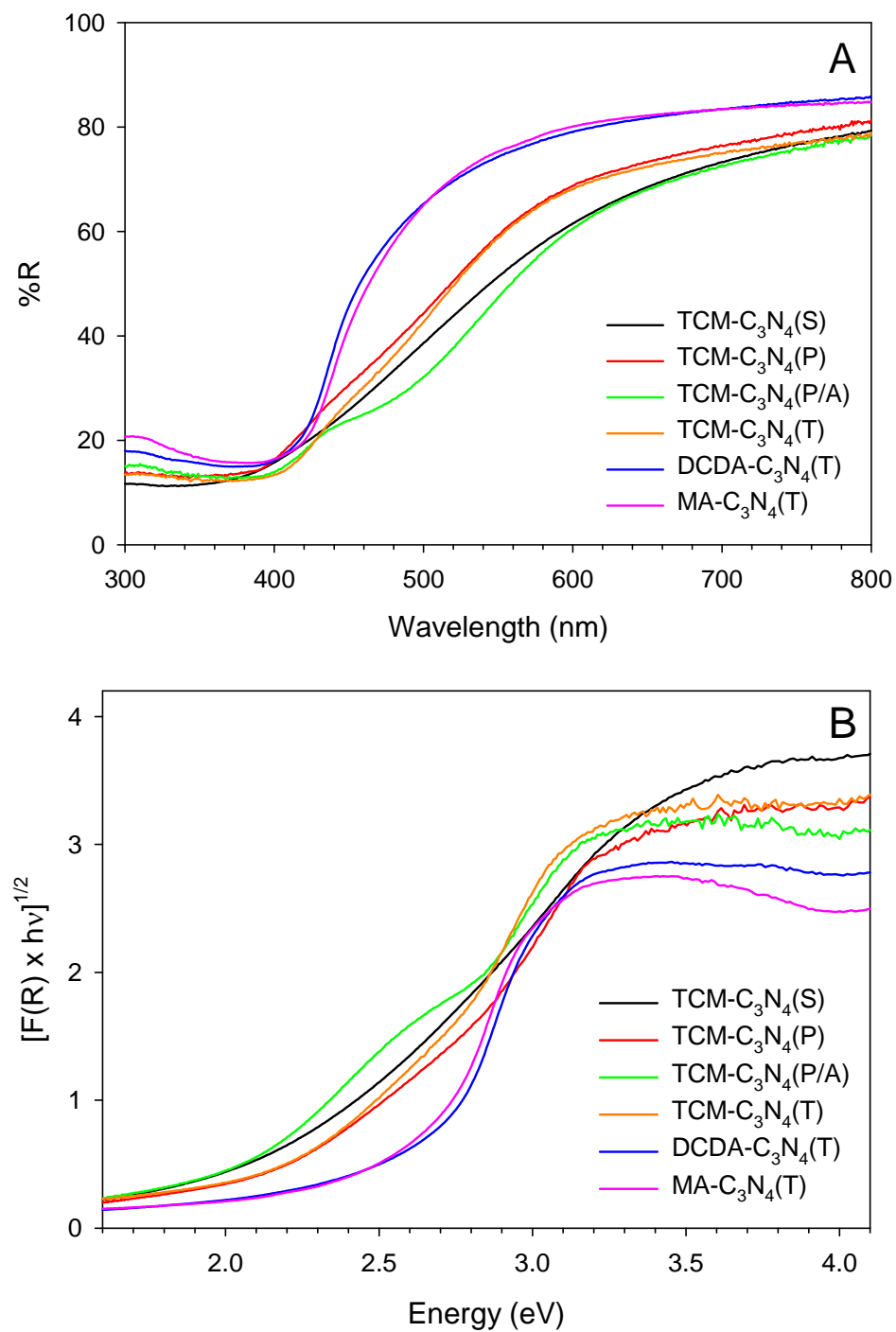


Figure 2.11 – DRS UV-vis of C_3N_4 products (a) raw reflectance spectra and (b) Tauc plots.

*Photocatalytic studies*Photocatalytic oxidation of organic dyes

The degradation of methylene blue was studied to compare the activity of TCM-C₃N₄ products. Following the dark stir, there was a 20-40% lost in initial absorbance intensity (Figure 2.12A). This was also evident in the C₃N₄ powders that developed a green tint (blue dye mixing with the bulk orange color). Upon UV illumination, the carbon nitrides steadily degrade methylene blue, evidenced by solution decolorization. After one hour of total irradiation, the as-synthesized Schlenk and Parr products reduced the dye to below 20% of its initial concentration. The annealed product had higher dark adsorption and a slower initial degradation rate, but reached the same level of total degradation at the end of 100 minutes. The linear rate fits (Figure 2.12B) and calculated rate constants (Table 2.4) show that TCM-C₃N₄(P) was most effective at degradation of MB.

Table 2.4. Rate constants (min⁻¹) for UV light degradation of MB dye using TCM-C₃N₄ products.

	TCM-C₃N₄(S)	TCM-C₃N₄(P)	TCM-C₃N₄(P/A)
UV light	0.0403 (R ² = 0.982)	0.0528 (R ² = 0.991)	0.0175 (R ² = 0.999)

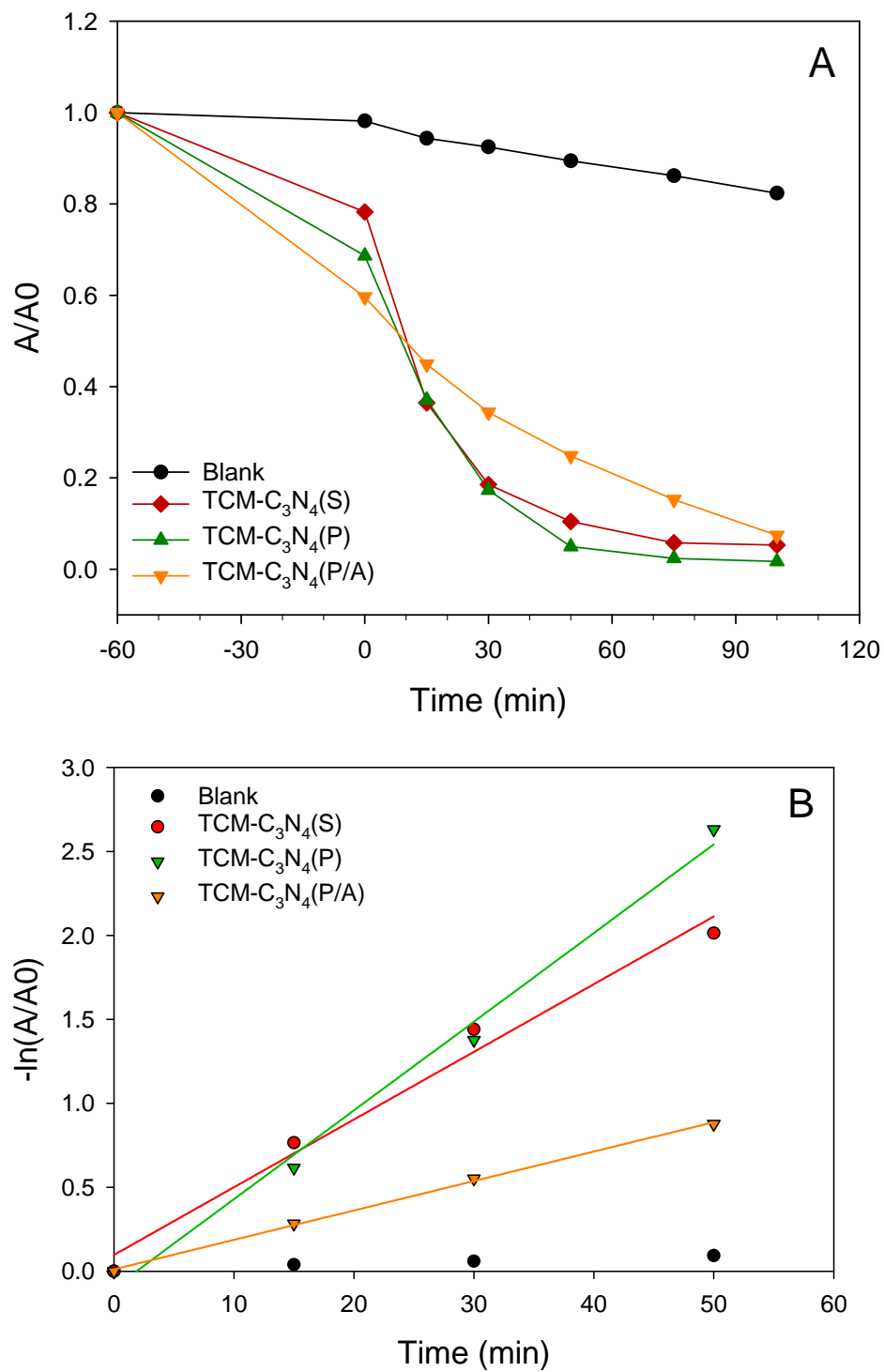


Figure 2.12 – UV light degradation of methylene blue with TCM-C₃N₄ products, (A) degradation plots and (B) linear rate fits.

The TCM-C₃N₄(P) product, being most active under UV light, was tested against MA-C₃N₄(T) and DCDA-C₃N₄(T) under visible light illumination using 400 nm long pass filters. As in the unfiltered experiment, there was some degree of dark adsorption of the dye on the catalyst surface. Activity was lower in the absence of UV light, with all C₃N₄ samples reaching 40-60% of initial dye concentration after 150 minutes (Figure 2.13A). TCM-C₃N₄(P) showed very similar MB dye degradation (~30%) as compared to the DCDA-C₃N₄(T) and MA-C₃N₄(T) products, after account for their higher initial dark adsorption. The self-degradation of methylene blue is minimal here compared to the unfiltered experiment. Estimated rate constants (Table 2.5) based on linear fits (Figure 2.13B) of first order kinetic data for the degradation of methylene blue are between 6.3% of the unfiltered UV experiments for TCM-C₃N₄(P).

Table 2.5. Rate constants (min⁻¹) for visible light degradation of MB dye using TCM, MA, and DCDA-C₃N₄ products.

	TCM-C₃N₄(P)	MA-C₃N₄(T)	DCDA-C₃N₄(T)
Visible (>400 nm)	0.0033 (R ² = 0.962)	0.0038 (R ² = 0.993)	0.0045 (R ² = 0.995)

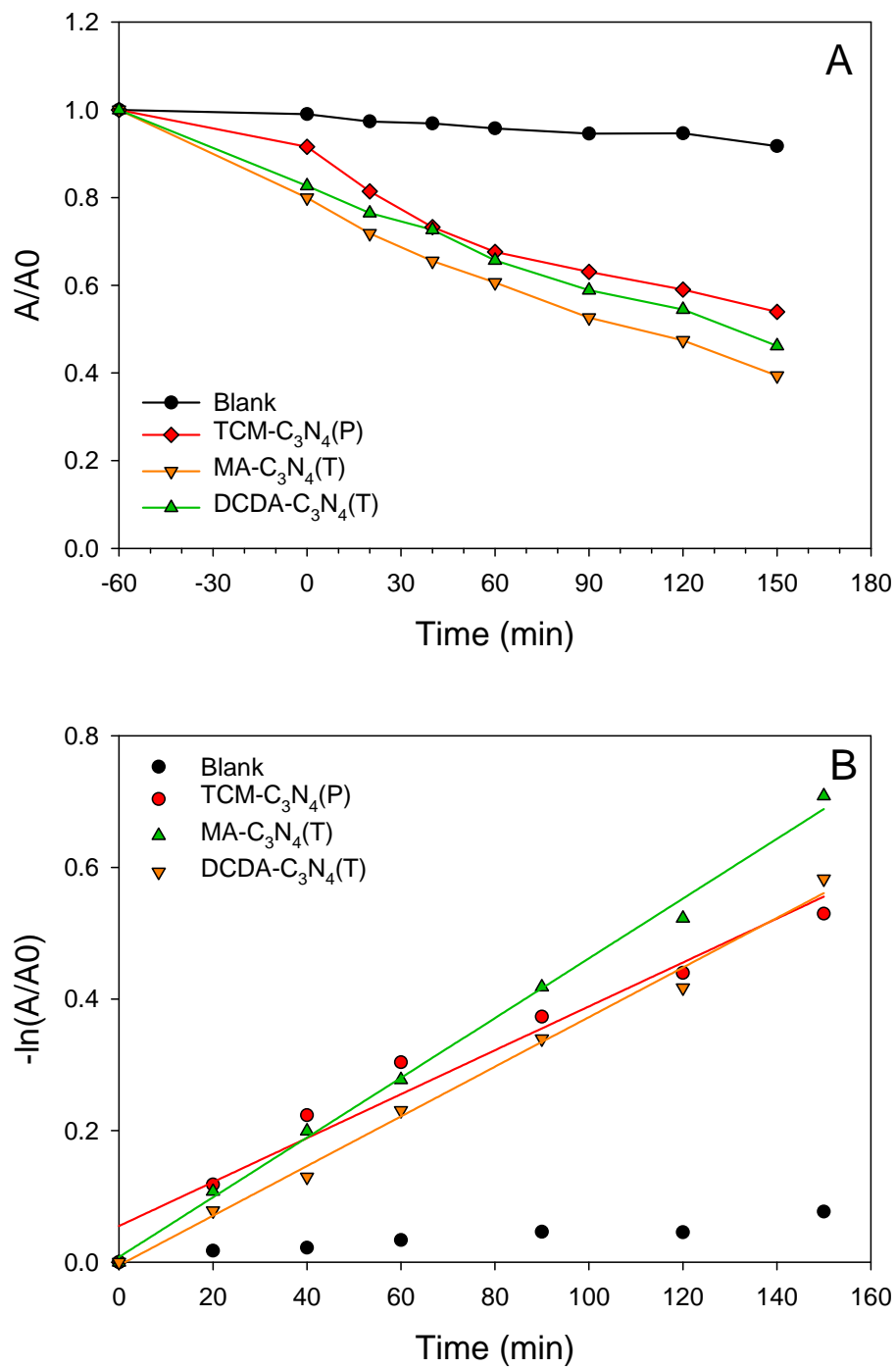


Figure 2.13 – Visible light degradation of methylene blue with C_3N_4 products, (A) degradation plots and (B) linear rate fits.

The activities for the oxidative degradation of methyl orange (MO) dye were compared for the ball-milled TCM-C₃N₄ and DCDA-C₃N₄ products. MO acts as a pH indicator, and its λ_{max} will change when the solution pH is below 4. Initial photooxidation tests with C₃N₄ prepared from TCM were performed in neutral conditions, however, after the dark stir period, the dye solution for some samples changed to a darker red-orange color indicating an increase in solution acidity. The Parr products may contain some residual HCl bound to the surface during the high pressure reactor synthesis, and after stirring in the MO dye it is released and causes the dye to change color. This is consistent with previous tests showing that suspensions of TCM-C₃N₄ in water reduced the pH from 7 to 3.²¹ In order to insure that the dye absorption maximum did not change or move during the oxidation studies, MO dye experiments were performed in a pH 3 solution environment. The MO dye is very stable under UV light illumination in the absence of catalyst, staying above 95% of its initial concentration after 2 hours of UV exposure (Figure 2.14A). The amount of dark adsorption onto the catalyst surfaces varied, with most being less than 10% except for TCM-C₃N₄(P), which adsorbed near 20% of the starting dye concentration. C₃N₄ samples prepared from the different methods performed similarly, with < 30% dye remaining. Both TCM-C₃N₄(P) and DCDA-C₃N₄(T) reached complete decolorization of the solution after 2 hours. TCM-C₃N₄(P) was consistently lower in concentration at each measurement point, though some of this difference is due to the additional amount of dye absorbed during the dark stir. The linearized rates of each catalyst are compared in Figure 2.14B, and calculated rate constants are in Table 2.6.

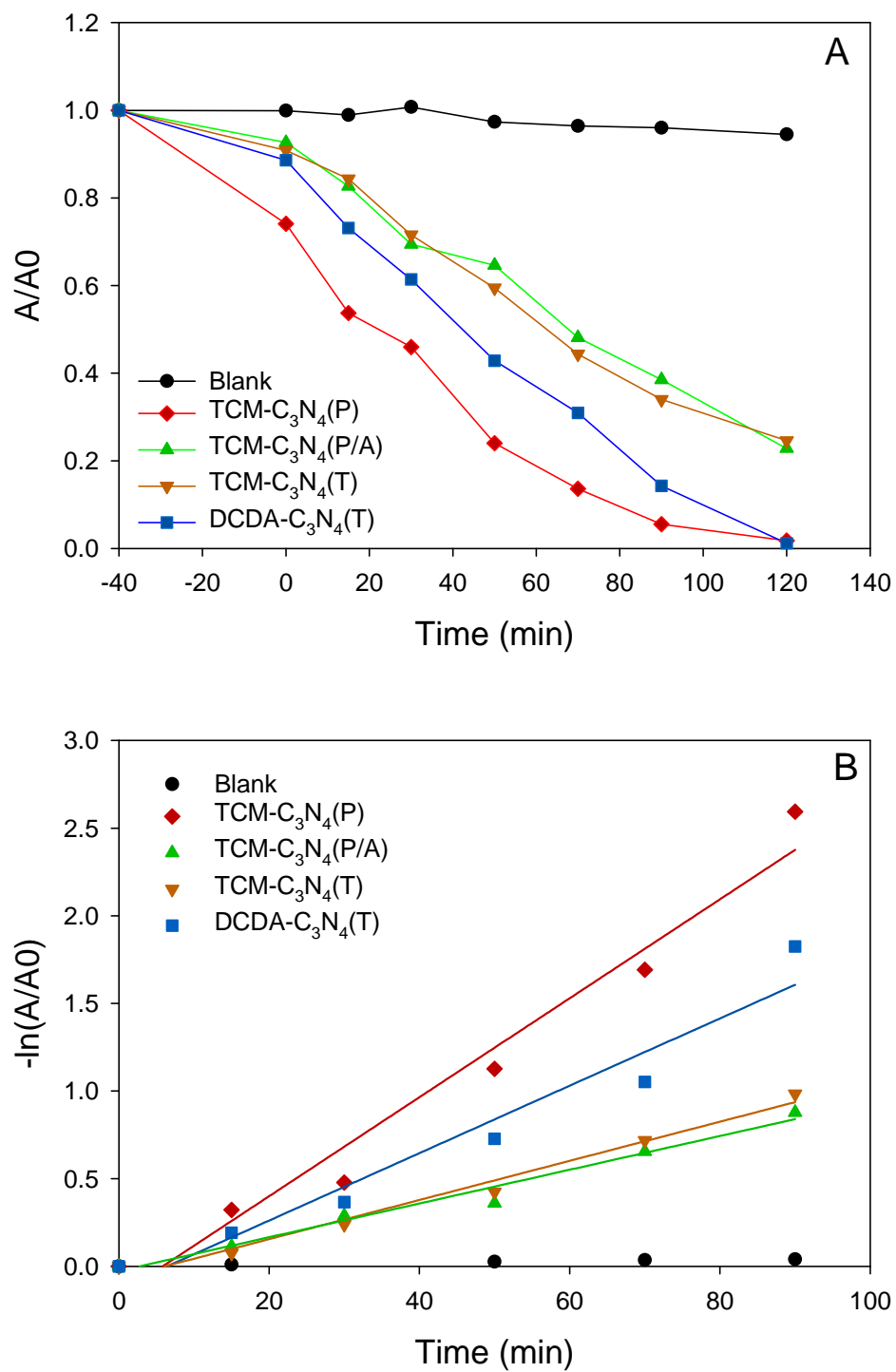


Figure 2.14 – UV light degradation of methyl orange with C_3N_4 products, (A) degradation plots and (B) linear rate fits.

Under visible light illumination, the C_3N_4 photoactivity was lower compared to the unfiltered UV illumination (Figure 2.15A). The remaining MO dye concentration reached 50-80% in 150 minutes. TCM- C_3N_4 (P) still had near 20% initial concentration loss due to dark dye surface adsorption, as well as the lowest concentration of dye remaining at the end of the illumination periods. The estimated rates based on Figure 2.16B for visible light degradation of methyl orange ranged from 8-25% of unfiltered UV light activity. The results also showed that after accounting for the concentration loss due to dark adsorption, TCM- C_3N_4 (P) still showed the highest rate of degradation for methyl orange for both visible (0.0037 min^{-1}) and UV light (0.024 min^{-1}) (Table 2.6). These values are comparable to previously reported visible light C_3N_4 degradation rates for methyl orange.⁹² The approximate photon flux reaching the C_3N_4 catalysts in the dye solution is $3.2 \times 10^{17} \text{ photons s}^{-1}$ for UV light and $1.1 \times 10^{17} \text{ photons s}^{-1}$ for visible light based on our previous work.⁸⁸ Based on the initial degradation rates, there is a loss of 3.05×10^{-4} dye molecules per UV light photon and 1.36×10^{-4} dye molecules per visible light photon. Given that the carbon nitride band gaps are in the near UV region, cutoff filters limit both flux intensity and photons of appropriate wavelength for C_3N_4 electron/hole formation necessary for MO photooxidation.

Table 2.6. Rate constants (min^{-1}) for UV and visible light degradation of methyl orange using TCM- C_3N_4 and DCDA- C_3N_4 products.

	TCM- C_3N_4(P)	TCM- C_3N_4(P/A)	TCM- C_3N_4(T)	DCDA- C_3N_4(T)
UV	0.0242 ($R^2 = 0.977$)	0.0096 ($R^2 = 0.978$)	0.0112 ($R^2 = 0.983$)	0.0152 ($R^2 = 0.993$)
Visible (>400 nm)	0.0037 ($R^2 = 0.971$)	0.0024 ($R^2 = 0.977$)	0.0015 ($R^2 = 0.980$)	0.0018 ($R^2 = 0.951$)

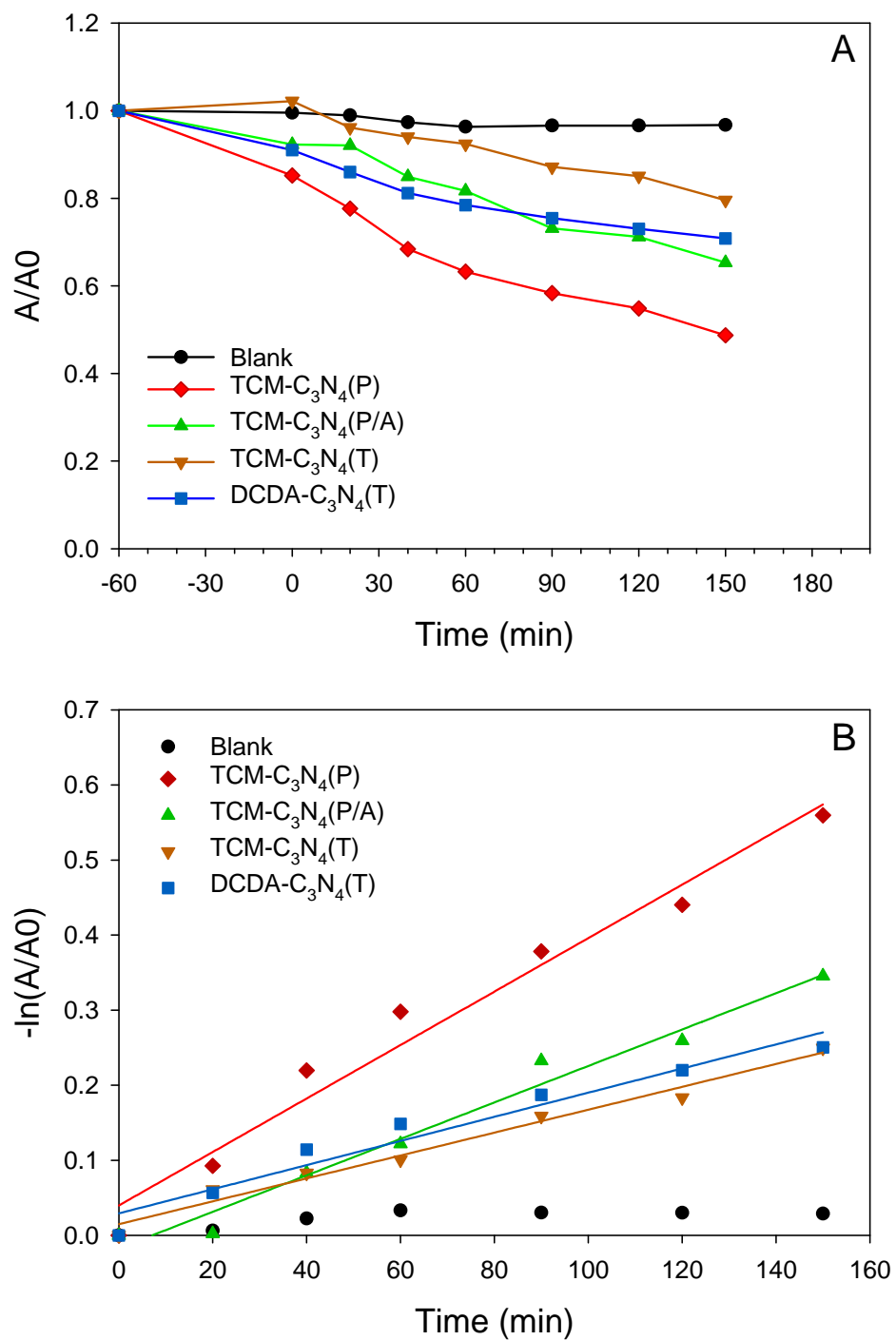


Figure 2.15 – Visible light degradation of methyl orange with C_3N_4 products, (A) degradation plots and (B) linear rate fits.

Photodeposition of metals onto the surface of C_3N_4

Precious metals were photoreduced onto C_3N_4 by exposing a suspension of C_3N_4 containing a metal salt in 50:50 H_2O :methanol to UV light. In reactions using the melamine or DCDA products, a clear change in color was seen from light yellow to grey. This color change was less notable in metal photodepositions using the darker orange TCM products. Some of these products were more brown in color or had a slight grey tint, but most remained close to their starting orange color. At 1-2 wt% loadings, it is not surprising that a visible change might not be prominent. For some of the 2 wt% samples, the reduced metal was detected using powder XRD (Figure 2.16).

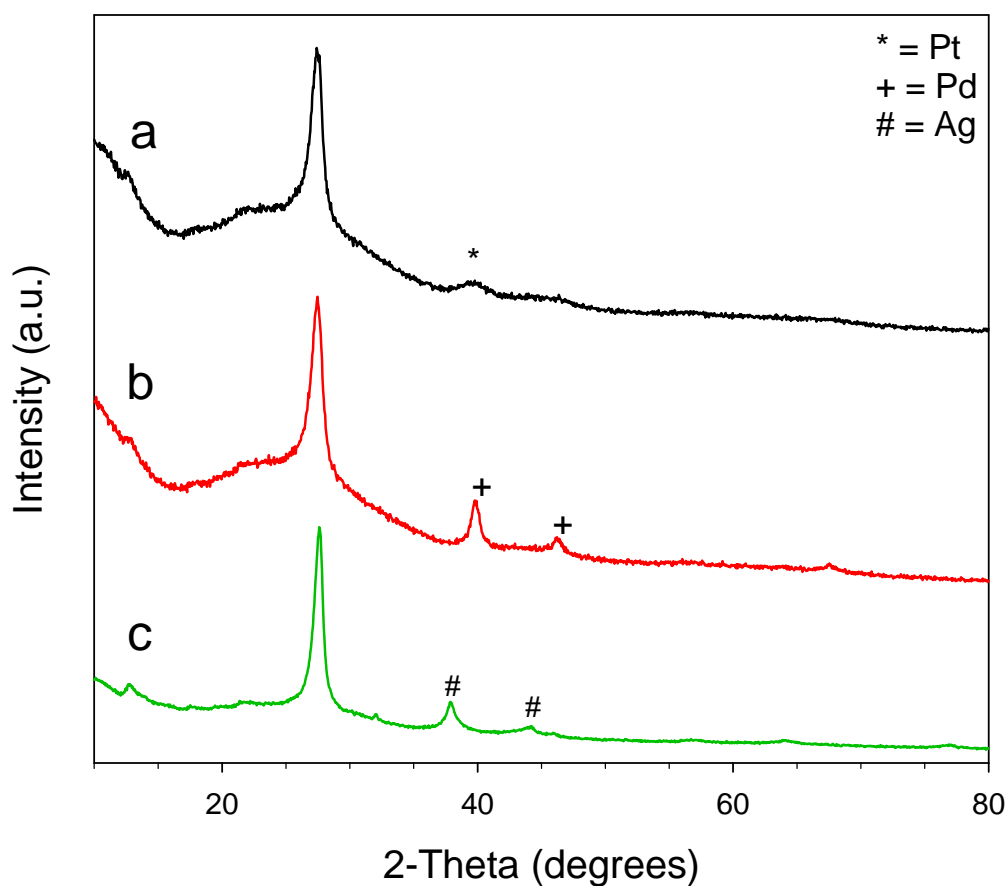


Figure 2.16 – XRD TCM- C_3N_4 (P/A) with photodeposited (a) Pt, (b), Pd, and (c) Ag.

The peaks for these metals, platinum in particular, were very broad and low in intensity. The broad peaks can be attributed to small crystallite sizes (~4-9 nm) for the deposited metals. The low intensity, or absence of peaks in the case of samples with lower metal loadings, is due to being near detection limits. How uniformly the metals deposited on the carbon nitride surface could also impact how well the metals are able to diffract.

The metals were detected on the surface of carbon nitride using XPS (Table 2.7). The XPS data was able to give further information about the oxidation state of the metal. The Pd 4d spectrum showed the major peak at 335.26 eV, with a shoulder at 337.45 eV, indicating the presence of both Pd(0) and Pd(II). Both Ag and Pt spectra showed a single primary peak fitting the position of the reduced metal.

Table 2.7. XPS surface analysis data for metals deposited on TCM-C₃N₄(P/A).

Metal	C (at.%)	N (at.%)	M (at.%)	M (eV)
Pt	50.5	42.1	7.4	71.29 (Pt ⁰ 71.1-3)
Pd	55.4	37.9	6.7	335.26 (Pd ⁰ 335.1-6) 337.45 (PdO 337.1)
Ag	46.3	53.2	0.5	368.05 (Ag ⁰ 368.1-2)

Photocatalytic hydrogen evolution reactions

In many previous hydrogen evolution studies with C₃N₄ materials, the UV photodeposition of a noble metal co-catalyst is performed *in-situ*, followed by H₂ evolution analysis. This can lead to unknown solution environments or redox-active metal species remaining in solution. Instead, sequential metal (Pt, Pd, Ag)

photodeposition and isolation was performed in order to analyze the metal-deposited C_3N_4 catalyst using nominally 1 wt% metal in solution. At nominally 1 wt% concentrations, the crystalline metals were not detectable by XRD, but XPS identified the presence of each metal on the carbon nitride surface. Quantification of the deposited metal co-catalyst by ICP-OES determined that the deposited Pt metal varies widely from ~0.13 to 0.5 wt% (Table 2.8), demonstrating that a nominally 1 wt% metal-coated product contains much less than that amount on its surface, which would leave the remaining metal cations in solution when the catalyst is not isolated before conducting photocatalytic hydrogen evolution studies.

The photocatalytic hydrogen evolution reactions were monitored in real time using the RGA-MS system; four cycles for TCM- C_3N_4 (P) are shown in Figure 2.17. Under this system, the first cycle sometimes showed lower activity than the subsequent cycles. Venting the reactor after the first illumination cycle increased the rate, which then remained stable for at least three additional one-hour cycles. This activating first UV cycle was effective with as little as 10 minutes of UV light. The nature of this photoactivation step is unclear, but it may involve some surface-adsorbed species on the platinum resulting from the methanol photodeposition step that the TEOA solution removes under UV illumination.

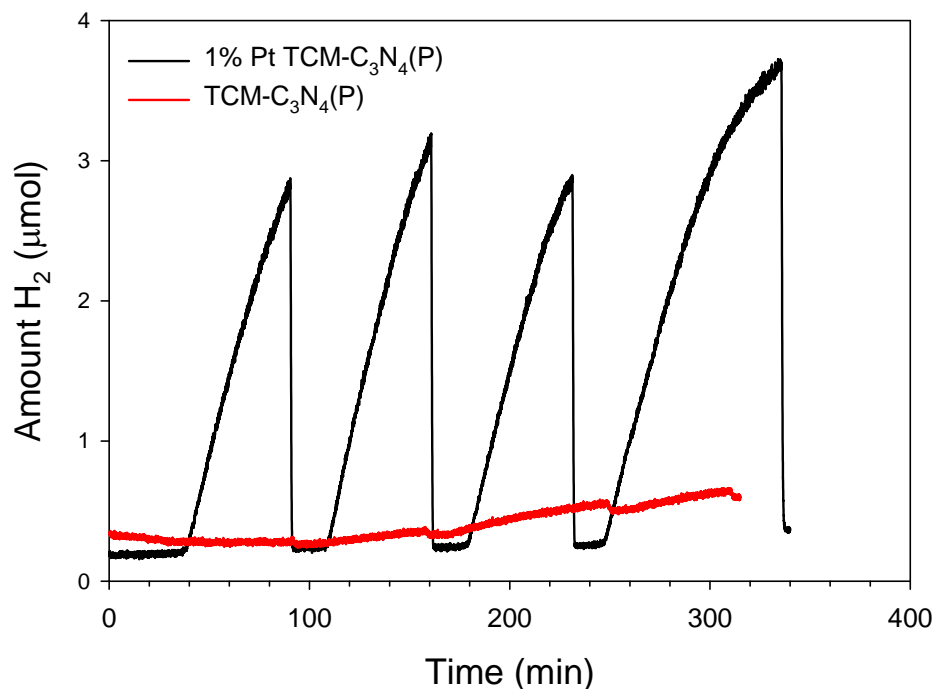


Figure 2.17 – Photocatalytic hydrogen evolution using TCM-C₃N₄(P) with and without Pt co-catalyst.

While rates for the oxidative degradation of methyl orange above were comparable for the TCM, DCDA, and MA derived C₃N₄ photocatalysts, there were clear differences in the hydrogen production rates (Table 2.8), with DCDA-C₃N₄(T) having the highest mass averaged rate of 453 μmol h⁻¹ g⁻¹. Some of these differences can be attributed to catalyst surface area (DCDA-C₃N₄ being highest) and also variations in the amount of Pt deposited on the surface (TCM-C₃N₄(T) being lowest) and, finally, there are differences in C₃N₄ band gaps and band edges (which may relate to structural order/defects). There is a notable improvement in H₂ evolution rates when milling the as-synthesized Parr product before photodeposition (doubles surface area with similar amount of Pt deposited), but less improvement when treating the annealed product in the same manner (see Table 2.8) even though metal deposition amount increases.

Table 2.8. Average hydrogen production rates (with standard deviation) for Pt, Pd, and Ag deposited C₃N₄ products with ICP-OES quantification of metal loading.

Sample	Target wt% M (ICP wt%)	H ₂ Rate (μmol h ⁻¹ g ⁻¹)
TCM-C ₃ N ₄ (P) - milled	None	9 (3)
TCM-C ₃ N ₄ (P)	1% Pt (0.39)	43 (4)
TCM-C ₃ N ₄ (P) - milled	1% Pt (0.40)	260 (30)
TCM-C ₃ N ₄ (P/A)	1% Pt (0.28)	153 (35)
TCM-C ₃ N ₄ (P/A)	1.5% Pt (0.36)	210 (15)
TCM-C ₃ N ₄ (P/A) - milled	1% Pt (0.49)	193 (12)
TCM-C ₃ N ₄ (S/A)	1.5% Pt (0.38)	159 (17)
TCM-C ₃ N ₄ (T)	1% Pt (0.13)	68 (8)
TCM-C ₃ N ₄ (T)	2% Pt (0.46)	42 (4)
DCDA-C ₃ N ₄ (T)	1% Pt (0.33)	453 (67)
MA-C ₃ N ₄ (T)	1% Pt (0.28)	283 (50)
TCM-C ₃ N ₄ (P) - milled	1% Pd (0.37)	127 (15)
TCM-C ₃ N ₄ (P) - milled	1% Ag (0.06)	63 (10)
TCM-C ₃ N ₄ (P)	0.75% Ag (0.158) 0.25% Pd (0.01)	85 (17)

The effect of the co-catalyst metal was also studied and, moving from Ag<Pd<Pt, resulted in roughly doubled hydrogen evolution rates for nominally 1 wt% metal deposition (Table 2.8). The difference in activities for these metals shows similar trends to previously reported data for other precious metal co-catalysts on cyanamide based

products.⁹³ For example, increasing the Pt ion solution concentration to 2 wt% for a TCM-C₃N₄(T) sample increased the metal loading to 0.46 wt% Pt on the C₃N₄ surface, but its mass-averaged HER was ~42 μmol h⁻¹ g⁻¹, similar to that for the nominally 1 wt% sample in Table 2.8. The variability of actual metal deposited on different carbon nitride structures observed here (and corresponding differences in HER photocatalytic activity) highlights the importance of quantitative metal analysis on the exact carbon nitride samples used for catalytic studies, to allow for useful comparisons across different literature reports.

Band structure

As noted above, the extrapolated band gap absorptions (HOMO-LUMO) for the TCM derived C₃N₄ network structures are ~0.3 eV lower than that for DCDA or MA products. In addition, low energy valence band spectra from XPS shows that the TCM products have valence band onset levels near 1.4-1.9 eV, which is similar to those reported for DCDA and MA derived C₃N₄ (Figure 2.18).⁹⁴⁻⁹⁵ Combining the E_g and VB results leads to approximate simplified energy diagrams for TCM derived C₃N₄ materials (Figure 2.19). Even though there are subtle variations in the band gaps and conduction band positions, the TCM-C₃N₄ products are still in a position where the 2H⁺ → H₂ reduction is possible.

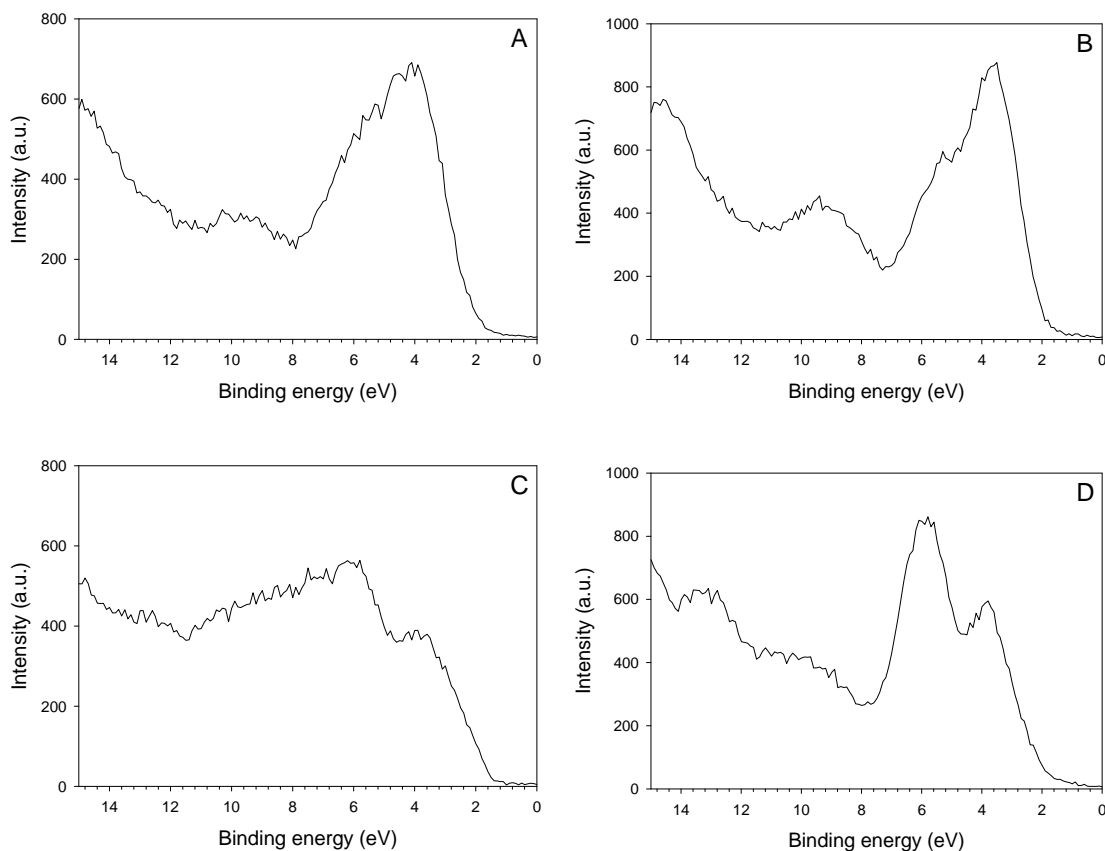


Figure 2.18 – Valence band XPS spectra of (A) TCM-C₃N₄(S), (B) TCM-C₃N₄(P), (C) TCM-C₃N₄(T), and (D) TCM-C₃N₄(P/A).

As expected, the deposition of Pt onto the TCM-C₃N₄ surface leads to electron emission near 0 eV, consistent with facile electron ejection from the surface-deposited metal. This would also place Pt metal states below the C₃N₄ conduction band to readily accept photoexcited electrons from the CB to subsequently use in proton reduction on its surface. The lower structure-ordering of the TCM-C₃N₄(T) product versus TCM-C₃N₄(P) product may be somehow influenced by the latter product forming under moderate pressure in the Parr reactor in the presence of hot HCl gas. This structural disorder for TCM-C₃N₄(T) may influence the lower photocatalytic activity for both Pt metal deposition and hydrogen production. It is expected that in these non-crystalline C₃N₄

structures, solution photodeposition of metal co-catalysts will be very dependent on accessible surface structures that can serve as “antennas” to shuttle photoexcited conduction band electrons from C_3N_4 to the Pt cations for surface reduction. These deposited metal regions are then likely the most readily photoreducing sites for subsequent $H^+ \rightarrow H_2$ photoreduction reactions. As noted earlier, tuning and controlling defects in C_3N_4 can greatly influence its catalytic activity.⁸⁵⁻⁸⁷

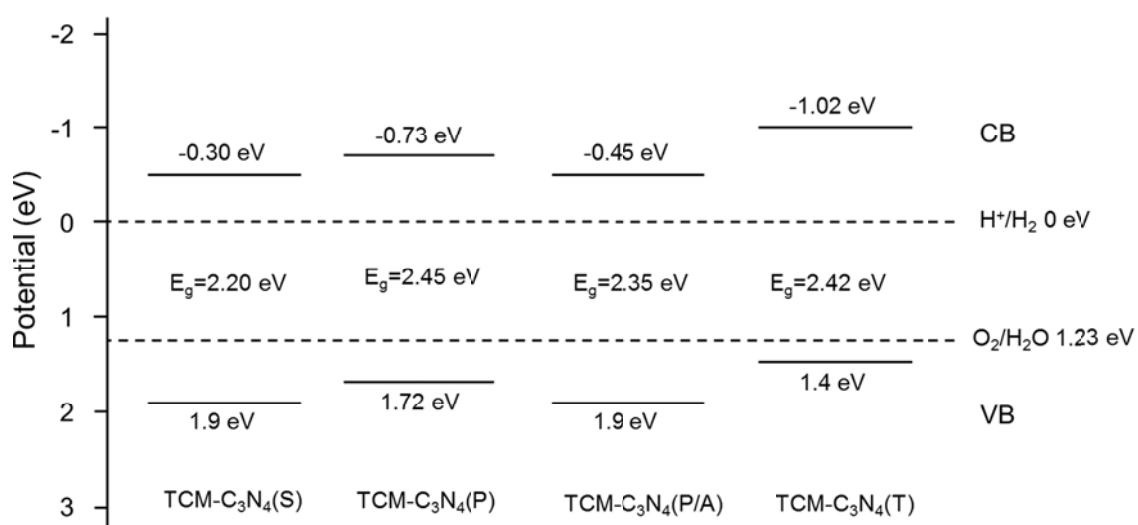


Figure 2.19 – Band structure diagram for TCM- C_3N_4 products based on XPS valence band spectra and calculated band gaps.

2.4 Conclusions

This chapter has described the preparation of semiconducting C_3N_4 networks from a trichloromelamine (TCM) precursor. TCM has a unique precursor feature to undergo a facile and energetic thermochemical decomposition that produces multiple gaseous byproducts, driving the reaction to condensation and completion at lower temperatures than other precursors via self-heating. Rapid self-heating from this triazine precursor leads to effective ring expansion into heptazine-based C_3N_4 networks with large several

hundred nanometer sized plate or sheet-like morphologies, but with only a few nanometers of interlayer ordering. The presence of chlorine in the precursor provides a site for potential functionalization of the precursor that may alter the C_3N_4 product and positively-impact interaction with a Pt cocatalyst.⁸⁶ Though starting with a different precursor, structural analysis shows TCM- C_3N_4 has key features that mirror C_3N_4 products prepared from other precursors. One notable difference is its darker orange product color and smaller band gap. Its photocatalytic activity for oxidative degradation of methyl orange dye was comparable or exceeding that of DCDA- C_3N_4 . Photocatalytic hydrogen evolution rates for TCM- C_3N_4 materials approach those from DCDA and MA precursors, with differences influenced by surface area, metal co-catalyst content, and TCM- C_3N_4 optical absorption properties. Since carbon nitrides are non-crystalline network structures, they can vary in subtle but important structural and electronic ways, and so careful attention should be paid to analysis of the actual amount of metal co-catalyst deposition on catalytically-accessible surface sites as it may vary greatly for different C_3N_4 structures, which can influence catalytic properties.

CHAPTER 3

POROUS ENGINEERING BY SALT MODIFICATIONS TO CARBON NITRIDE SYNTHESIS

3.1 Introduction

The previous chapter has described the synthesis and properties of C_3N_4 prepared from the thermal decomposition of TCM. Though chemically and structurally very similar to carbon nitrides produced from DCDA or melamine, there were differences in the photocatalytic activity for these darker-orange powders. The subtle differences in the band structures play a role in some of the change, so this property would be difficult to tune controllably without the use of dopants or control of defects, structure, or composition. Surface area is a physical property that influences catalytic activity through modification of the amount of accessible surface sites that can be adjusted without making changes to the chemical nature of C_3N_4 .

Hard templating is a common method of producing higher surface area, more porous materials.⁹⁶ By mixing a precursor with a hard inert support that can be chemically separated from the product with a wash step, one can obtain a product containing pores with the negative image of the template. SiO_2 particles are a common template choice available in different sizes and frequently used in the synthesis of mesoporous carbon nitrides.^{82, 97-99} The catalytic activity of these higher surface area carbon nitrides has been shown to improve by factors of 5-10.^{58, 81}

This chapter will describe the synthesis of C_3N_4 from mixtures of TCM with different alkali salt templates (NaCl, KBr, KI). In contrast to SiO_2 , salts can be readily removed at room temperature using water as the wash solvent. As TCM is soluble in

methanol, it can be co-precipitated with the salt prior to reaction for a more intimate mixture. In addition to solution mixtures, TCM was also mixed with the salts using solid state methods using mortar and pestle or ball milling. The bromide and iodide salts can also exchange with the chlorine in TCM and change the reactivity of the precursor and its decomposition, potentially leading to some differences in the product's reactivity. The general scheme for the synthetic steps is shown in Figure 3.1.

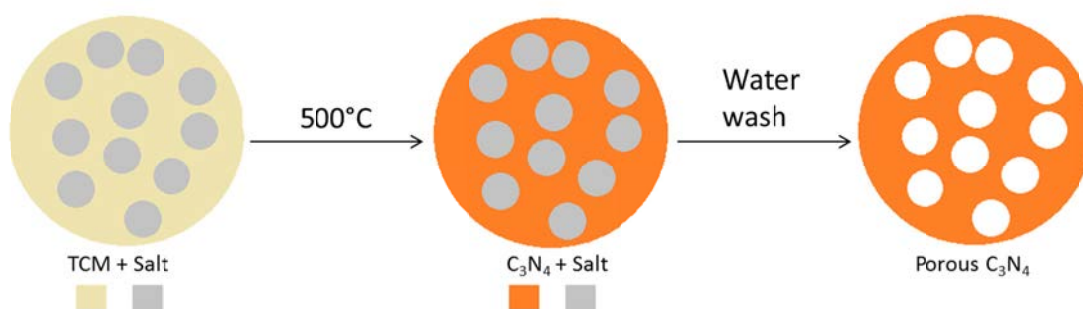


Figure 3.1 – Method for introducing porosity into C_3N_4 by hard templating with salts.

Previous work has treated melon with KSCN as a method for introducing structure defects and modifying catalytic activity.⁸⁶⁻⁸⁷ Mixtures of TCM with KSCN and also NH_4SCN were also investigated. The addition of extra C-N linkages could change the connectivity of the heptazine units and degree of condensation within the C_3N_4 structure.

3.2 Experimental

Reagents

Trichloromelamine ($C_3N_3(NHCl)_3$, TCM, 98%) was purchased from GFS Chemical and stored in an argon atmosphere glovebox. Other reagents used as received were NaCl (EM Science), KBr (Acros, 99+%), KI (J.T. Baker Chemical, reagent grade), KSCN (Aldrich, 98%), NH_4SCN (Sigma Aldrich, 97.5+%), $H_2PtCl_6 \cdot 6H_2O$ (99.9%, Strem), methanol (ACS certified, Fisher), methyl orange (85% dye content, Sigma Aldrich), and triethanolamine (Alfa Aesar, 98+%). Deionized water (18 M Ω) was obtained from a Photronix MiniQuad system.

C_3N_4 synthesis from alkali halide mixtures with TCM

NaCl Mixtures

TCM (300 mg, 1.31 mmol) was dissolved in 40 mL of methanol in a 100 mL Schlenk flask. The flask was purged by bubbling nitrogen through the side arm from a Schlenk line and then capped with a stopper. While maintaining nitrogen flow, the stopper was removed and 0.3, 0.5, 1 or 2 mass equivalents of NaCl were added to the dissolved TCM. The mixture was allowed to stir overnight. The methanol was removed under vacuum by a liquid nitrogen cold trap. The mixed solid was transferred to the Schlenk style reactor described in Chapter 2. The reactor was placed on the heating mantle and set to 300 °C. Unlike the reactions using only TCM, the temperature often reached 300 °C before visible decomposition occurred, as indicated by gas evolution and color change. In the reactions with higher salt content, gas evolution was significantly

less vigorous and the color change was observed to be more gradual. A tan to light brown solid was collected from the reactor.

TCM-NaCl mixtures were also reacted using the tube method. The mixed solid was placed into a 1.5 cm diameter test tube cut to 5 cm length and loaded into a Schlenk tube. An oil bubbler was connected to the side arm and the tube was purged with nitrogen. The tube was immersed in a vertically-oriented furnace and heated to 500 °C at a rate of 10 °C/min and held for 1-2 hours. Gas evolution was observed near 180 °C.

KBr Mixtures

TCM (400 mg, 1.75 mmol) was dissolved in 40 mL of methanol in a 100 mL beaker. While stirring, KBr (630 mg, 5.25 mmol) was added to the solution. Immediately upon addition, a bright yellow color developed, indicating possible reaction between TCM and KBr. The mixture was stirred for 1 hour, then left open in air to allow the methanol to evaporate overnight and deposit the mixed solid. A pale yellow solid was collected and placed into a 1.5 cm diameter test tube cut to 5 cm length, which was loaded into a Schlenk tube. A bubbler was connected to the side arm and the tube was purged with nitrogen. The tube was immersed in a vertically-oriented furnace and heated to 500 °C at a rate of 10 °C/min and held for 1 hour. An orange solid was collected from the tube insert. Evolution of a yellow-brown gas was observed between 160 and 180 °C.

KI Mixtures

TCM (400 mg, 1.75 mmol) was dissolved in 40 mL of methanol in a 100 mL beaker. While stirring, KI (880 mg 5.25 mmol) was added to the solution. Immediately upon addition, a dark red-brown solution color developed. The mixture was stirred for 1 hour, then left open in air overnight to allow the methanol to evaporate and deposit the

mixed solid. A rust red solid was collected and placed into a 1.5 cm diameter test tube cut to 5 cm long, which was loaded into a Schlenk tube. A bubbler was connected to the side arm and the tube was purged with nitrogen. The tube was immersed in a vertically-oriented furnace and heated to 500 °C at a rate of 10 °C/min. As the reaction was heated from 200-300 °C, purple vapors filled the tube and discolored the oil in the bubbler. A dark-purple film deposited around the top of the tube that remained outside the furnace, and some white solids deposited just under the top. The reaction was held at 500 °C for 1 hour, and then the tube was removed from the furnace and allowed to cool. A light brown solid was collected from the tube insert.

C₃N₄ synthesis from thiocyanate mixtures with TCM

KSCN Mixtures

TCM (300 mg, 1.31 mmol) was first dissolved in 40 mL of methanol in a 100 mL beaker. While stirring, KSCN (390 mg 3.93 mmol) was added to the solution. Immediately, upon addition a bright yellow solution color developed. The mixture was stirred for 1 hour, then left open in air overnight to allow the methanol to evaporate and deposit the mixed solid. A bright-yellow solid was collected and placed into a 1.5 cm diameter test tube cut to 5 cm long, which was loaded into a Schlenk tube. The tube was immersed in a vertically-oriented furnace and heated to 500 °C at a rate of 10 °C/min and held for 1 hour. Gas evolution was observed at 160 °C.

NH₄SCN Mixtures

TCM (300 mg, 1.31 mmol) was dissolved in 40 mL of methanol in a 100 mL beaker. While stirring, NH₄SCN (300 mg 3.93 mmol) was added to the solution.

Immediately, upon addition a bright yellow color developed. The mixture was stirred for 1 hour, then left open in air overnight to allow the methanol to evaporate and deposit the mixed solid. A vibrant-yellow solid was collected and placed into a 1.5 cm diameter test tube cut to 5 cm long, which was loaded into a Schlenk tube. The tube was immersed in a vertically-oriented furnace and heated to 500 °C at a rate of 10 °C/min and held for 1 hour. Gas evolution was observed by 200 °C. When the furnace temperature had reached 500 °C, a layer of white solid deposited at the top of the tube that remained outside the furnace.

Solid state mixtures with salts

Mixtures between TCM and the previously-outlined salts were also prepared using a mortar and pestle. The same 1:3 molar ratio for TCM versus KBr, KI, KSCN, NH₄SCN were used. The solids were ground and mixed for 5-10 minutes and then loaded into a Schlenk tube with a glass insert. Solids were also mixed using an addition of 1 mL methanol to aid in grinding or pre-reaction. In these methanol-assisted mixtures, color changes similar to the solution mixtures were observed immediately upon addition of methanol. Color changes during dry mixing were lighter shades than the respective solution mixtures when shorter grinding times were used. The mixed reagents were heated in a Schlenk tube in the same manner as the solution mixed precursors.

Mixtures of TCM with these salts were also prepared using a ball mill. TCM and the additive salt were loaded into a 3 mL screw cap Nalgene bottle with 2 x 5 mm ZrO₂ balls to avoid potential reactivity with the milling jar. This bottle was placed into a 15 mL steel milling jar and milled for various timing intervals at 1000-1200 rpm. The solid

precursor mixtures exhibited color changes similar to their solution-mixed counterparts, typically in under 5 minutes of milling time. The milled solids were loaded into a Schlenk tube purged with nitrogen and heated in the same manner as previous mixtures.

Safety note: The physical mixtures between TCM and the thiocyanate salts, by grinding or milling, occasionally exhibited a violent exothermic reaction. It is important to prepare these mixtures at lower scales and in a fume hood. Always wear gloves when handling thiocyanate salts.

Water wash of C₃N₄-salt composites

All salt-composite products were washed with water to remove the salt, leaving the enhanced porosity C₃N₄ products. The products were lightly ground and placed into a 100 mL beaker with 50 mL of H₂O and sonicated in a BioSonic UC100 for 1 hour. Then the solid was stirred for 1-2 hours following sonication. The suspension was transferred to a centrifuge tube and spun at 4000 rpm to separate the remaining C₃N₄. The solids were washed with 20 mL H₂O and separated by centrifugation again. The solids were rinsed with methanol and left to dry in air.

Characterization

FT-IR spectra were collected on a Nicolet Nexus 670. Solid samples were prepared as KBr pellets for data collection. Gas samples were analyzed by transferring 5 mL of gas from the reaction vessel into a 10 cm long gas IR cell with KBr windows. Elemental analysis was performed on a Perkin Elmer 2400 Series II CHNS/O Analyzer, with 1-2 mg of sample in crimped tin capsules. Powder X-ray diffraction was collected

on a Bruker D8 system (source Cu K α , 5-80°, 0.050 °/step) with samples deposited on glass slides. Thermogravimetric analysis was performed on a Seiko Exstar 6300 TGA-DTA. Samples were heated up to 1000°C at a rate of 10°C/min under air or argon flow. Scanning electron microscopy images were collected on a Hitachi S-4800 FE-SEM ($v_{acc}=1.8kV$). Diffuse reflectance spectra were collected on a Cary 5000 Series Spectrophotometer (200-800 nm, 10 nm/s). Solid samples were loaded into a round compression sample holder with a 1 cm diameter sampling area. Kubelka-Munk conversions were calculated from the Cary software, and Tauc plots were generated using $[F(R)hv]^{1/2}$. BET surface area measurements were collected on a Quantachrome Nova 1200 using 100-200 mg of ground solid sample. Quantification of deposited platinum was determined using a Varian 720-ES ICP-OES. Samples (5-10 mg) were dissolved in a heated mixture of 5 mL concentrated H₂SO₄ and 1 mL concentrated HNO₃ and diluted in 25 mL volumetric flasks with 5% HNO₃.

Photocatalytic reactions

Oxidative degradation of organic dyes

The oxidative degradation of methyl orange dye (C₁₄H₁₄N₃NaO₃S) was studied. A stock 10⁻³ M dye solution was prepared by dissolving the solid dye in 18 M Ω water. The stock solutions were diluted to 4·10⁻⁵ M for methyl orange in order to fit the peak at λ_{max} in the range ($\lambda_{MO}=504$ nm, $A<1.50$) of the UV-vis spectrophotometer (Agilent 8453). In 30 mL beakers 10 mL of dye solution and 10 mg of catalyst were added. An additional beaker containing only dye was used to evaluate self-degradation in the absence of catalyst. Samples were stirred in the dark for a minimum of 30 minutes to

equilibrate dye absorption. Samples were exposed to UV light (Ace-Hanovia, 450 W Hg) in 15-30 minute intervals in air. After each irradiation period, the catalysts were separated from the dye solution by centrifugation, and the UV-vis spectrum of each solution was collected to quantify the remaining concentration of dye. Experiments were typically carried out for 2 hours of total UV irradiation.

Hydrogen evolution via water-splitting

The water washed products were used as catalysts with photodeposited Pt. Pt was photoreduced onto the C_3N_4 surface under UV light (450 W Hg) using H_2PtCl_6 as the metal source. C_3N_4 was suspended in a 50% aqueous MeOH solution containing an amount of the metal salt to target 0.5-2 wt% of reduced metal on C_3N_4 . The solution was degassed with argon and exposed to UV light for 2 hours. The solid was collected by centrifugation, rinsed with MeOH, and dried in air.

For hydrogen evolution tests, 10 mg of catalyst (C_3N_4 or $M(x\%):C_3N_4$) was dispersed in a 10 mL solution of 10% aqueous triethanolamine ($C_6H_{15}NO_3$) contained in a 50 mL Schlenk flask. The solution was degassed with argon and connected to a Residual Gas Analysis Mass Spectrometer (RGA-MS, Stanford Research Systems QMS 300 series) by capillary to the side arm. Data was collected as a pressure vs. time scan, monitoring the masses for nitrogen, argon, hydrogen, water, and oxygen. The reactor was exposed to UV light in 1 hour intervals and was vented with an argon purge between each UV run in order to return hydrogen concentrations to baseline levels. The amount of hydrogen was quantified using a calibration curve referencing known quantities of hydrogen to the argon background.⁸⁸ Additional details about calibration and experimental set-up can be found in the appendix.

3.3 Results and Discussion

Initial reactions between TCM and salt additives

In the solution precursor-salt mixtures, evidence of reaction was immediately clear when using the non-chloride salts in solution. Bright-yellow solution colors for KBr, KSCN, and NH₄SCN and dark-red for KI were observed upon addition of the salt to dissolved TCM. Analysis of the isolated solids by X-ray diffraction showed the formation of KCl from the exchange of the chlorine on TCM with the anion of the salt (Figures 3.2b, 3.3b, and 3.4b).

In the solid mixtures prepared with a mortar and pestle, the color change of the precursor was not as substantial, instead being a lighter shade of the yellow or red color achieved from solution mixtures. Longer grinding times or the addition of 1 mL of methanol to grind as a slurry produced a mixed precursor more-closely resembling the halide-exchanged solution mixture. The X-ray diffraction showed complete exchange of the chlorine in most cases. The incomplete exchange was most notable for KBr physical mixtures that retain more of the starting KBr salt (Figure 3.2a), though the TCM-KI mixture had a small amount of residual KI (Figure 3.3a).

Ball milling provided an alternate, facile approach to the solid state precursor mixtures. As noted, the solids were placed into Nalgene bottles inside the milling jars due to uncertainty of the reactivity between TCM and the different salts under the more energetic conditions. Color change consistent with the solution mixtures were observed between 1 and 5 minutes of total milling time at 1200 rpm. As with the mortar and pestle mixture, the TCM-KBr mixture exhibited the presence of some KCl formation in the

XRD but remained predominantly KBr (Figure 3.2c). The KI and thiocyanate salt mixtures showed complete exchange and KCl formation by XRD (Figure 3.3c and 3.4c)

As to be expected, there was no reaction between TCM and NaCl under any of the mixing methods, as the anions are the same, though chloride exchange could occur. For the remaining salts tested where formation of KCl is observed, the exchange was thermodynamically-favorable based on the heats of formation of the halide salts (Table 3.1). Of the potassium halide salts, KF has the most negative value for ΔH_f and would be unlikely to complete the exchange reaction with TCM. Though the decomposition reaction of a TCM-KF mixture was not investigated for concerns of gaseous fluorinated byproducts, the precursor mixture was prepared in methanol. XRD analysis of the isolated powder showed no formation of KCl and only KF, consistent with the thermochemistry data. In addition to the KX conversion to KCl, the other consideration is the thermodynamics of the formation of N-X bonds in place of N-Cl bonds in TCM.

Table 3.1. Heats of formation for tested additive salts.¹⁰⁰

Salt	ΔH_f (kJ/mol)
KF	-567.3
KCl	-436.5
KBr	-393.8
KI	-327.9
KSCN	-200.2
NH ₄ Cl	-314.4
NH ₄ SCN	-83.4

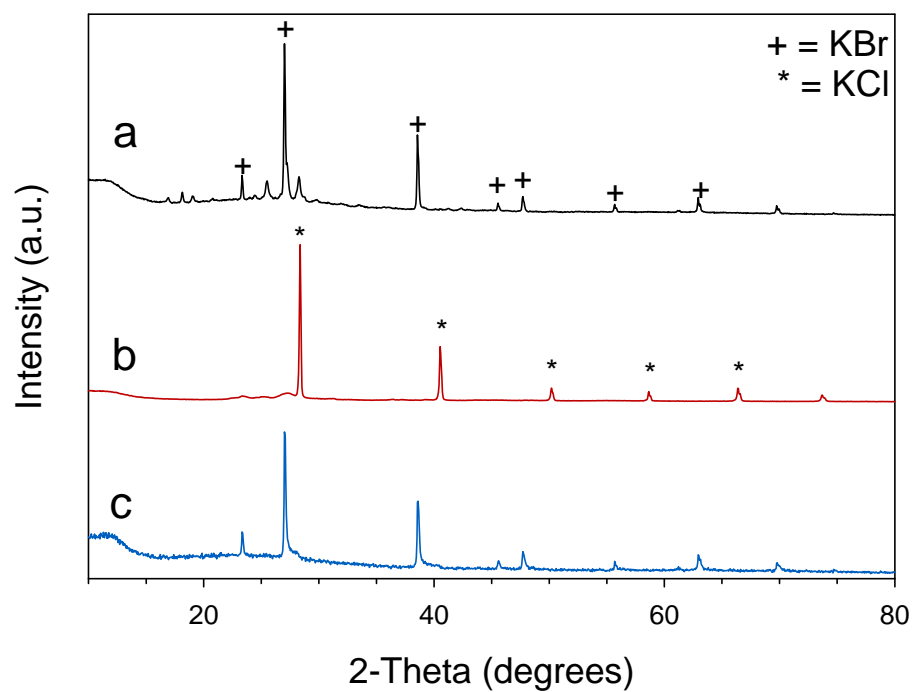


Figure 3.2 – XRD patterns of TCM-KBr mixtures prepared by (a) mortar and pestle, (b) solution mixture, and (c) ball milling.

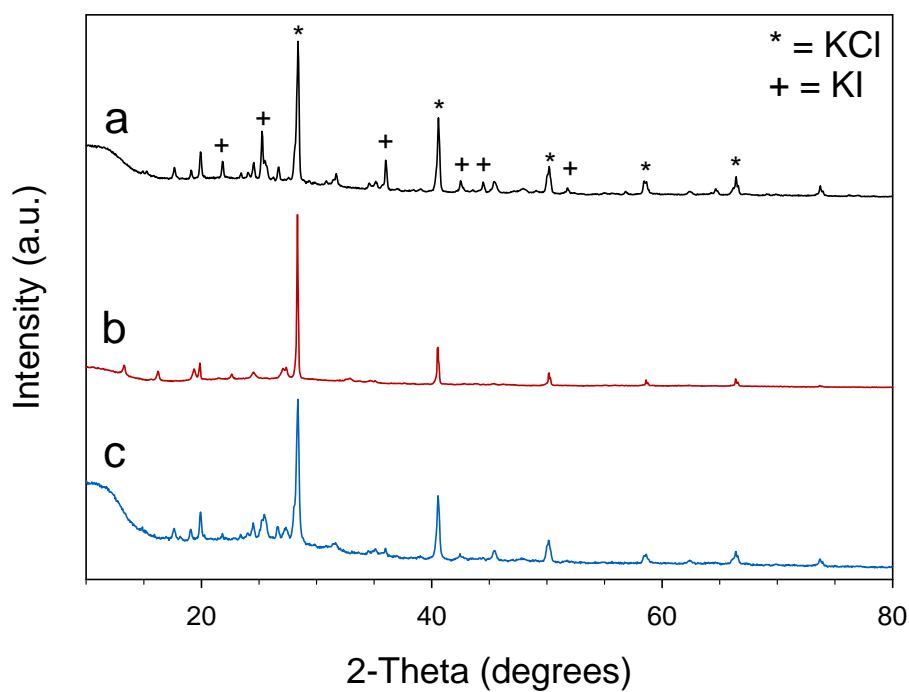


Figure 3.3 – XRD patterns of TCM-KI mixtures prepared by (a) mortar and pestle, (b) solution mixture, and (c) ball milling.

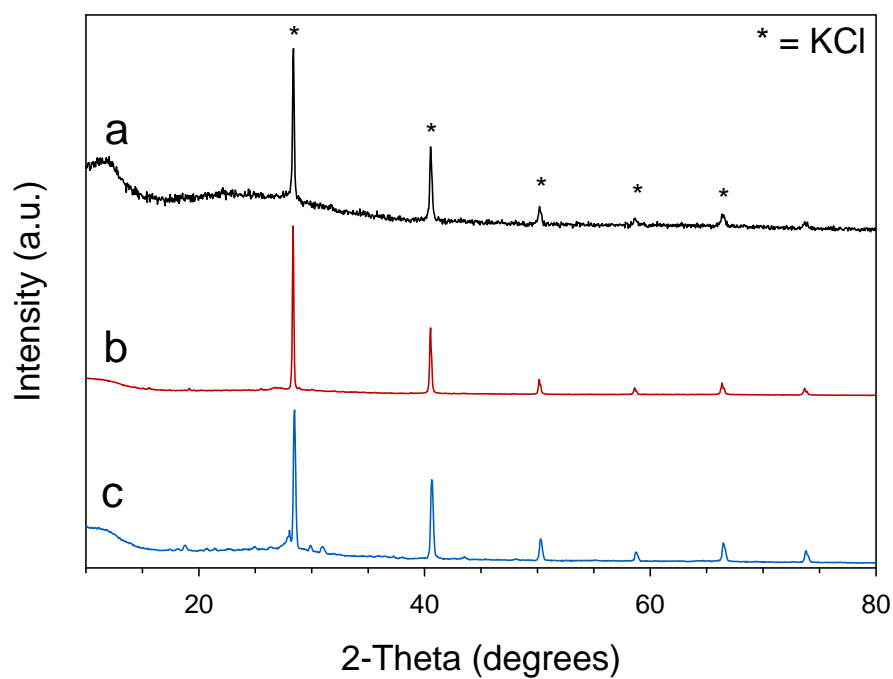


Figure 3.4 – XRD patterns of TCM-KSCN mixtures prepared by (a) mortar and pestle, (b) solution mixture, and (c) ball milling.

The IR spectra of the precursor mixtures are shown in Figure 3.5. Compared with unmodified TCM, the halide mixtures show fewer distinct differences than the thiocyanate mixtures. Nitrogen halide stretches occur at low frequencies near 686 cm^{-1} for an N-Cl stretch in chloro amine functional groups.¹⁰¹ The TCM and TCM-NaCl mixture have a small absorption at 680 cm^{-1} , just below this frequency. As indicated by the XRD data, the exchange of chlorine with the halogen of the KX salt would yield a new N-X bond. The presence of the heavier halogen atom would shift this stretch to an even lower frequency. The TCM-KBr and TCM-KI mixtures show small absorptions below 556 cm^{-1} and at 474 cm^{-1} instead of the absorption near 686 cm^{-1} in support of this exchange. The precursors formed from thiocyanate mixtures show new distinct features. Both the KSCN and NH_4SCN show the thiocyanate stretch near 2050 cm^{-1} , though notably weaker than for the starting salts. The NH_4SCN mixture had more prominent features from $2900\text{-}3200\text{ cm}^{-1}$ for N-H stretches of the ammonium cation. The C-N stretches in the $1400\text{-}1700\text{ cm}^{-1}$ range are overlapped with features from the thiocyanate salts.

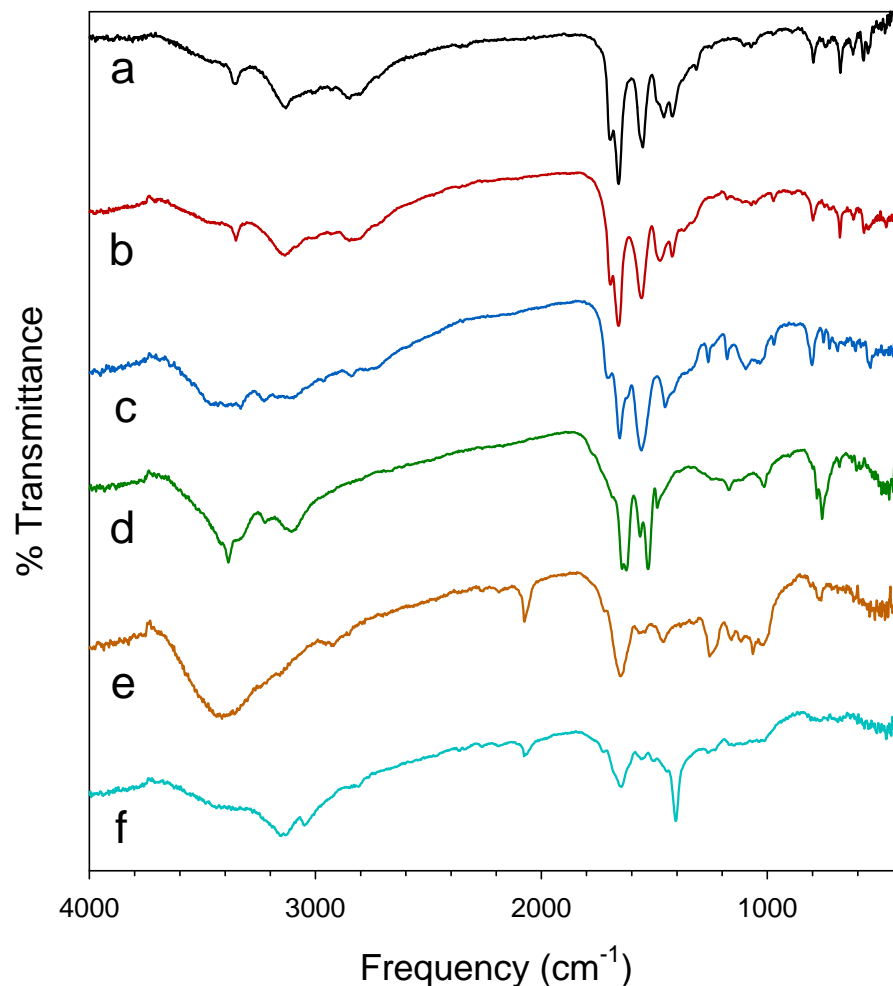


Figure 3.5 – IR spectra of C₃N₄ precursors (a) TCM, (b) TCM-NaCl, (c) TCM-KBr, (d) TCM-KI, (e) TCM-KSCN, and (f) TCM-NH₄SCN.

Carbon nitride formation from decomposition of TCM-salt mixtures

As described in the methods section, the synthesis of carbon nitride using salt mixtures with TCM differed from the decomposition of TCM alone. The early tests using NaCl mixtures in the Schlenk reactor saw higher initiation temperatures, less vigorous decompositions than TCM only reactions, or no reaction at all. Reactions were tested in 3:1, 2:1, 1:1, and 1:2 mass ratios of TCM:NaCl. Initially, the size of the flask was reduced from 250 mL to 50 mL to fit the powder in a more focused area on the

heating mantle. Even with this change, the NaCl-rich reactions had to dwell at 300 °C before reaction would visibly occur. The color of these products varied, typically being a lighter-yellow shade than the orange TCM only product. IR analysis of the TCM-NaCl products is shown in Figure 3.6. Significant differences were seen in the 1200-1700 cm^{-1} region with increasing proportions of NaCl. The 3:1 starting ratio of TCM:NaCl has an even intensity across this IR region, most similar to a TCM only product. As more NaCl is added, the lower-energy end of these bands decreases in intensity. While the peaks are broadened, indicating some degree of the decomposition reaction has taken place, the intensity distribution is closer to that of the TCM precursor. This may indicate the formation of a smaller ring triazine-based network if the typical heptazine-based C_3N_4 could not fully form by thermal rearrangement in the presence of the thermally-insulating salt.

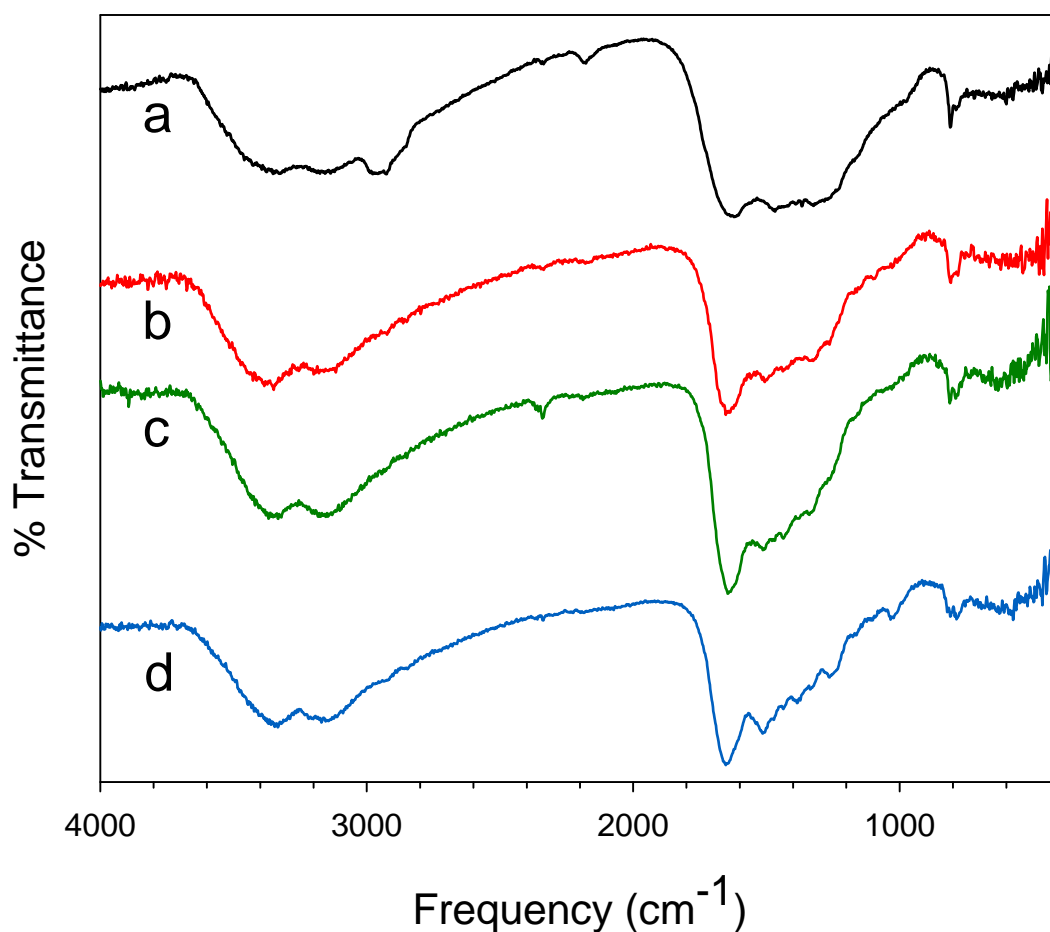


Figure 3.6 – C_3N_4 products prepared from (a) 3:1, (b) 2:1, (c) 1:1, and (d) 1:2 mixtures of TCM:NaCl.

As a next step, small scale reactions in test tubes were used to see if the reactions proceeded to completion at higher temperatures. This was first done using a natural gas torch to heat the bottom of the tube until decomposition occurred. This produced dark brown powders with IR spectra more characteristic of fully formed C_3N_4 , with an additional peak near 2150 cm^{-1} consistent with $\text{C}\equiv\text{N}$ or cumulated double bond $-\text{N}=\text{C}=\text{N}$ stretching frequencies. This method was challenging in order to avoid melting the tube in the presence of the flame and the heat and gas released from the TCM decomposition.

To perform this reaction in a more controlled manner and in larger scales, the Schlenk tube method described in Chapter 2 was developed. By clamping the tube in place inside a vertically-oriented furnace, the decomposition was tested from 400-500 °C. Under this method, the tube reactor was heated from all sides rather than just the base of a flask.

TGA was used to compare the thermal stabilities of the different NaCl-containing products produced in the different reactor set-ups. Figure 3.7 shows the TGA plots for products from reactions starting with 1:1 mass mixtures of TCM:NaCl prepared below 300 °C in 250 mL and 50 mL Schlenk flask reactors, and at 500 °C in the Schlenk tube reactor. The 250 mL product, which received the least-focused heating on the solid, showed mass loss just above 200 °C and continues until 550 °C. The 50 mL product lost mass at a similar temperature, but more gradually. The tube product, having been prepared at 500 °C, shows high stability until after 500 °C where C_3N_4 undergoes complete combustion. The residual mass in each sample is the NaCl, which melts at 801 °C and is volatile enough to be carried away by the air flow. The DTA for these products showed broad exothermic peaks at the end of the C_3N_4 mass loss and a sharp endothermic peak corresponding to the melting of NaCl. The lower-temperature Schlenk products had less relative NaCl mass, this is due to having a less complete condensation to a more stable final C_3N_4 product. From a starting 1:1 mixture, the tube product contains approximately 25% C_3N_4 or 1:3 C_3N_4 :NaCl by mass. Since the mass of NaCl should be unchanged in the reaction, the mass yield of C_3N_4 from TCM should be roughly 33%.

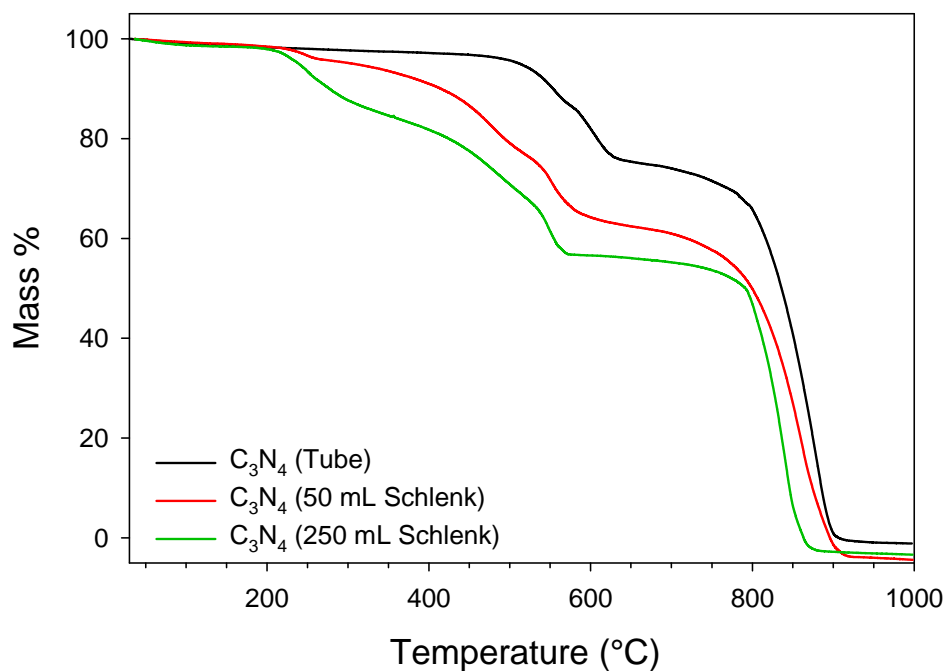


Figure 3.7 – TGA plots of C_3N_4 products from 1:1 TCM:NaCl mixtures under air flow and a $10\text{ }^\circ\text{C}/\text{min}$ ramp rate.

The remaining TCM-salt products were produced at $500\text{ }^\circ\text{C}$ using the tube reactor; the TGA data for these is shown in Figure 3.8. With the exception of the TCM-KI product, the remaining products showed high stability with no significant mass loss until above $500\text{ }^\circ\text{C}$. The TCM-KI product has a gradual 10% mass loss until $500\text{ }^\circ\text{C}$, and after this point showed rapid weight loss like the others. The amount of residual salt mass varies between these samples due to the different starting mass ratios to target the 1:3 TCM:salt molar ratio for complete exchange of chlorine. The decomposition of C_3N_4 in each case is paired with a large broad exothermic peak in the DTA. Since these products formed KCl, the final mass loss occurs near the melting point of KCl at $770\text{ }^\circ\text{C}$. The endothermic peak observed for these in the DTA is broader and less intense than what was observed for the melting of NaCl. The earlier loss of mass for the TCM-KBr

and TCM-KSCN products could be from residual amounts of the original, lower melting point salts. In the case of the TCM-NH₄SCN product, there is no residual salt mass since NH₄Cl is produced as the exchange product (observed from XRD) and sublimates out of the C₃N₄ product during the synthesis.

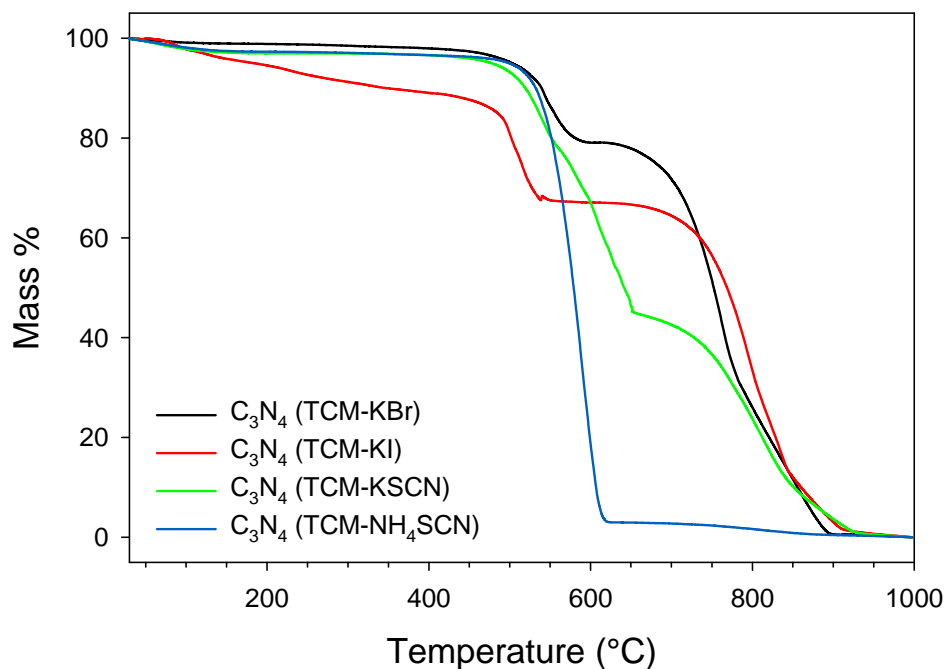


Figure 3.8 – TGA plots of C₃N₄ products from salt exchange reactions under air flow at a 10 °C/min ramp rate.

Chemical and structural characterization of carbon nitride salt composites

Elemental analysis data for the TCM-salt products is shown in Table 3.2. While data was collected on the water-washed products, the total CHN percentages determined were lower than for C₃N₄ produced from TCM only. These differences may indicate presence of some residual salts, which contain elements not quantifiable by this method. Insufficient drying of the samples could also contribute to lower values, as the oxygen present in water or methanol would also go unanalyzed. The exception of this set was the

TCM-NH₄SCN product, which was not washed since the NH₄Cl transports out of the product during its synthesis. Some of the unanalyzed mass in the KSCN and NH₄SCN products could also result from incorporated sulfur. Alternative methods of combustion analysis could confirm and quantify the amount of sulfur present. However the relative atomic C:N ratios are very consistent for the different TCM-salt products, fitting C₃N_{4+x} (0.2 < x < 0.4). This formula ratio is also consistent with those reported in Chapter 2 for the TCM, melamine, and DCDA products, being only slightly-less nitrogen rich on average.

Table 3.2. CHN elemental analysis for selected washed TCM-salt C₃N₄ products from 500 °C tube reactions.

Product	C wt%	N wt%	H wt%	Total wt% CHN	Formula
C ₃ N ₄ (TCM-NaCl)	28.39	48.56	1.87	78.76	C ₃ N _{4.4} H _{2.4}
C ₃ N ₄ (TCM-KBr)	30.46	1.74	51.67	83.87	C ₃ N _{4.4} H _{2.0}
C ₃ N ₄ (TCM-KI)	27.94	46.70	1.60	76.24	C ₃ N _{4.3} H _{2.1}
C ₃ N ₄ (TCM-KSCN)	27.11	44.67	2.14	73.92	C ₃ N _{4.2} H _{2.8}
C ₃ N ₄ (TCM-NH ₄ SCN)	35.15	58.43	1.55	95.13	C ₃ N _{4.3} H _{1.6}

The IR spectra of the TCM-salt products shown in Figure 3.9 are representative of the solution-mixed products for each salt. As with the TCM-only C₃N₄ products in Chapter 2, these salt products have a broad absorption above 3100 cm⁻¹ for N-H stretches, absorptions from 1200-1700 cm⁻¹ for C-N and C=N stretches, and a sharp ring breathing mode at 810 cm⁻¹. There are notable differences in the relative intensities of the absorptions in the 1200-1700 cm⁻¹ region. The TCM-KI product, in particular, has much sharper absorptions in this region, which could indicate a more-ordered local structure.

With the exception of the TCM-NH₄SCN product, these products also show a new absorption at 2150 cm⁻¹, fitting a nitrile stretch. This feature has been observed in C₃N₄ products grown in eutectic mixtures of LiCl, NaCl, and KCl.¹⁰² The IR spectra of these products showed little to no variation regardless of the precursor mixing methods.

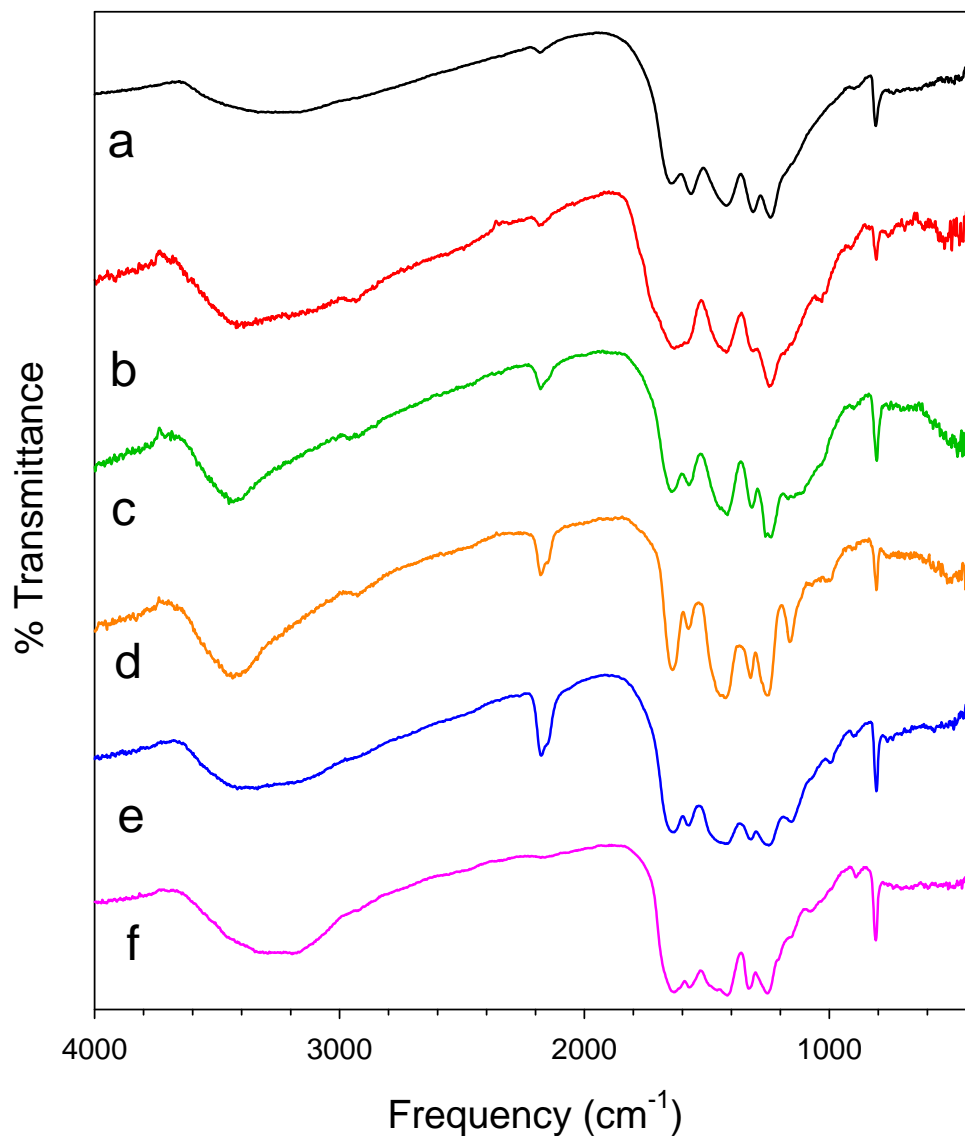


Figure 3.9 – IR spectra of water washed C₃N₄ products prepared from 500 °C tube decompositions of (a) TCM, (b) TCM-NaCl, (c) TCM-KBr, (d) TCM-KI, (e) TCM-KSCN, and (f) as-synthesized TCM-NH₄SCN.

Powder XRD was used on the products before washing with water to identify which salt remained after the reaction and, also, after washing to confirm its removal. While most mixing methods between TCM and the different salts showed an exchange to form KCl or NH_4Cl , some of the products after the thermal decomposition reaction showed the exchange partially reversed. In the case of the TCM-KBr products (Figure 3.10), the solution mix contained primarily KCl, and the mortar and pestle and ball milled products showed mostly KBr. Each of these products also showed different intensities of a peak fitting a solid solution of KBr-KCl rather than the other salt. The KI showed a partial reversal of the halide exchange only for the mortar and pestle and ball milled products (Figure 3.11). Unlike the case with KBr, these did not form a KCl-KI solid solution, but instead reformed KI in close to a 1:1 ratio with KCl based on the most intense peak. The difference in radii between Cl, Br, and I can be used to rationalize why a solid solution was only observed in the KBr-KCl mixtures and not the KI-KCl mixtures. This agrees with phase diagrams for KI-KCl, which shows that solid solutions for a 1:1 ratio can form, but only at temperatures higher than the 500 °C used in tube synthesis.¹⁰³ None of the TCM-KSCN showed the exchange reverse, only having KCl in the XRD. As described earlier, the TCM- NH_4SCN products transported NH_4Cl out of the C_3N_4 product during the decomposition reaction. This product as well as the washed products showed the main peak at 27 ° for spacing between C_3N_4 layers. A summary of the identified crystalline phases is listed in Table 3.3. Though KCl was formed from the different mixing methods between TCM and the different salts, solid state mixtures for the KBr and KI products showed partial re-formation of the original salt. It is possible the hot halide volatiles generated during the synthesis could react with the KCl.

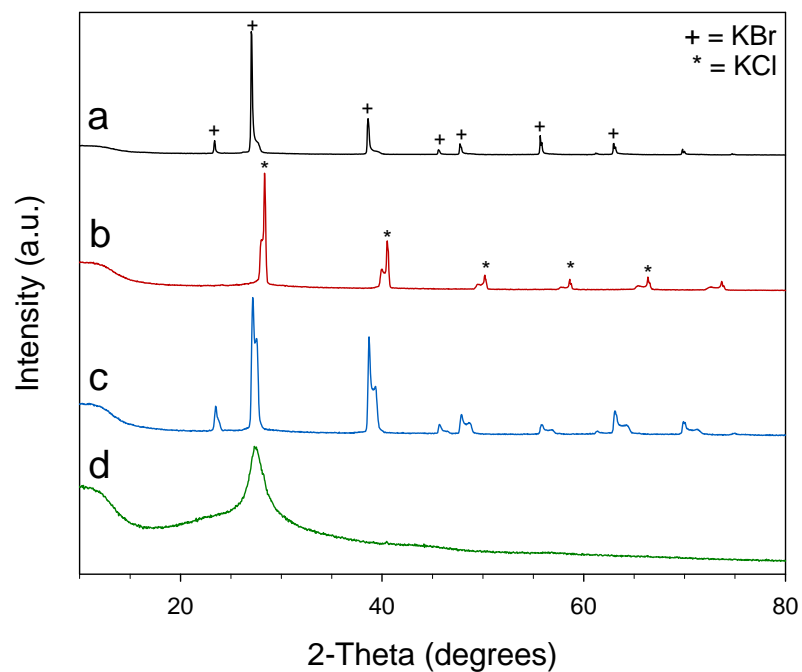


Figure 3.10 – XRD patterns of C_3N_4 products from TCM-KBr (a) mortar and pestle mixtures, (b) solution mixtures, (c) ball milled mixtures, and (d) washed product.

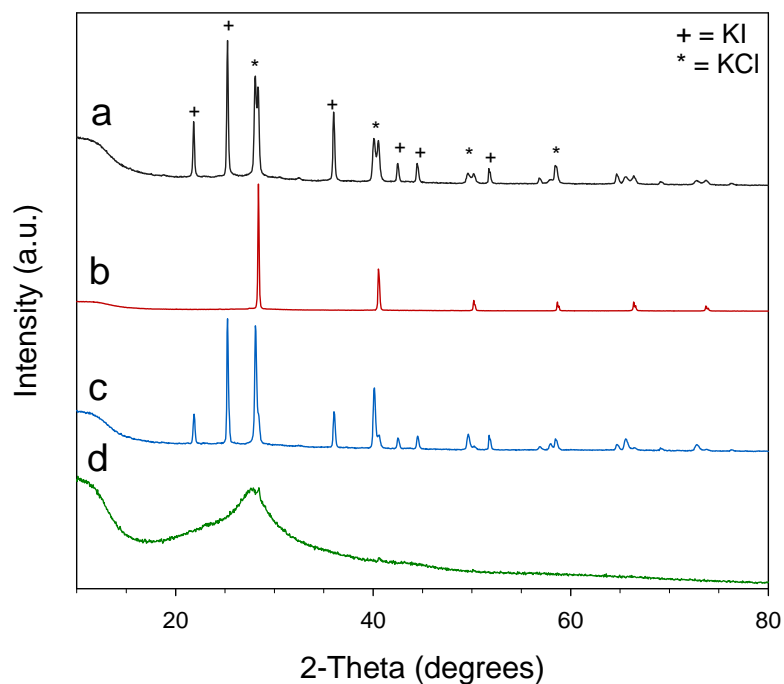


Figure 3.11 – XRD patterns of C_3N_4 products from TCM-KI (a) mortar and pestle mixtures, (b) solution mixtures, (c) ball milled mixtures, and (d) washed product.

Table 3.3. Summary of XRD phases observed in different salt mixtures before and after decomposition reaction (major phase in bold).

Incorporated salt	Mixture method	XRD phases before	XRD phases after
KBr	Methanol solution	KCl	KCl
	Mortar and pestle	KBr	KBr , $\text{KCl}_{0.4}\text{Br}_{0.6}$
	Ball milling	KBr , KCl	KBr, $\text{KCl}_{0.4}\text{Br}_{0.6}$
KI	Methanol solution	KCl	KCl
	Mortar and pestle	KCl , KI	KI, KCl
	Ball milling	KCl	KI, KCl
KSCN	Methanol solution	KCl	KCl
	Mortar and pestle	KCl	KCl
	Ball milling	KCl	KCl
NH_4SCN	Methanol solution	NH_4Cl	No salt
	Mortar and pestle	NH_4Cl	No salt
	Ball milling	NH_4Cl , NH_4SCN	No salt

Morphology and surface area

Expectations are that salt inclusions will serve to spread out C_3N_4 products into a more-accessible solid form for enhanced catalytic activity. Analysis of the product morphologies by SEM showed some differences depending on the quantity and type of salt mixed with TCM prior to the decomposition reaction. The unwashed and washed 3:1, 1:1, and 1:2 products are shown in Figure 3.12. The TCM-rich 3:1 product showed similar aggregates above $10\ \mu\text{m}$, with smooth surfaces and rough, porous edges. Washing added some extra surface roughness, but not in the form of any ordered porosity. This rougher surface was more notable compared to C_3N_4 prepared in the absence of salt. The 1:1 product has shorter regions with smooth surface features and

still had some edge nanoscale roughness. The 1:2 product aggregates were still above 10 μm , but discrete 2 μm chunks could be identified. The washed product has a rough surface with pockets 500 nm and smaller.

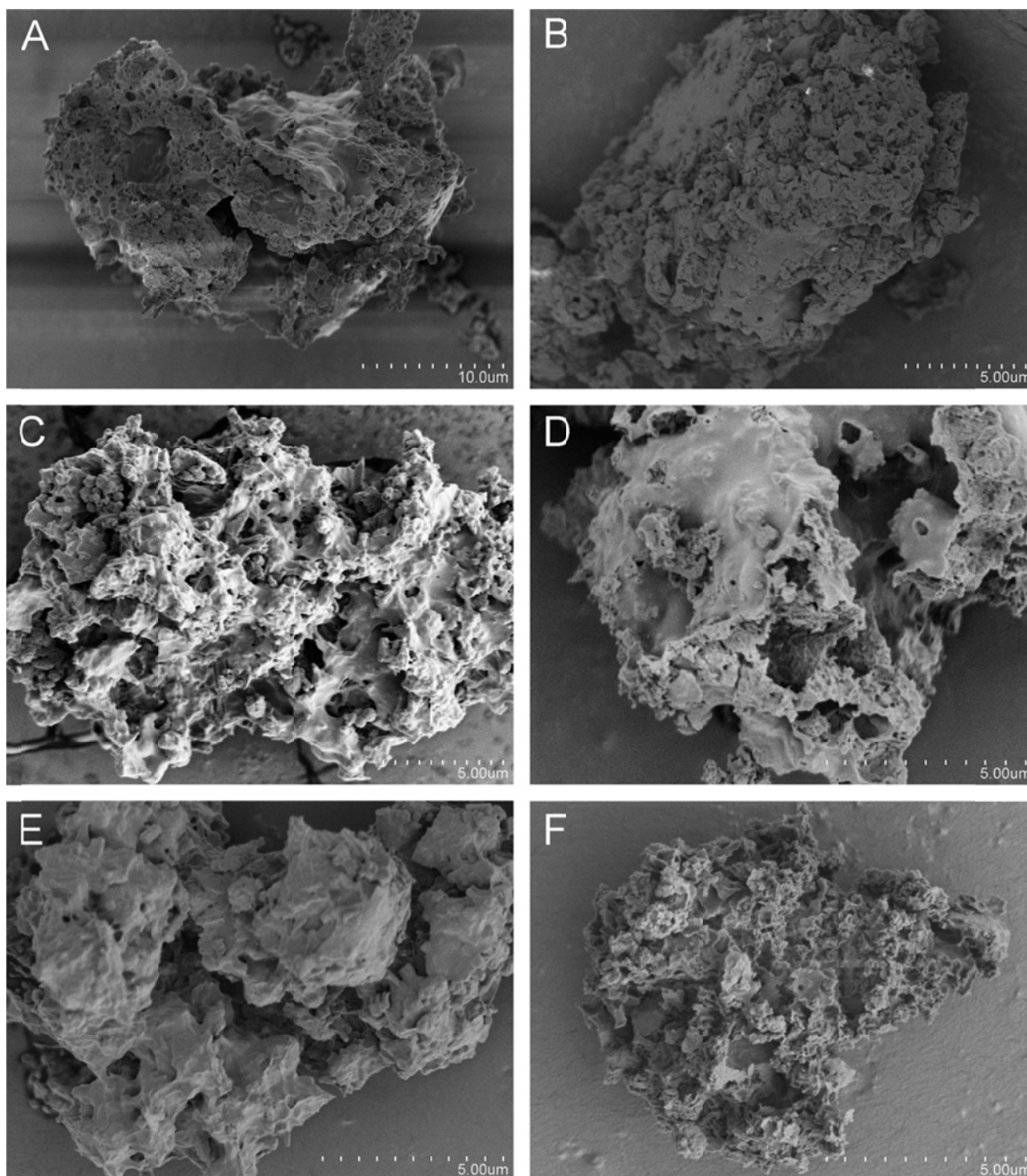


Figure 3.12 – SEM images of (A) 3:1 TCM:NaCl product and its (B) water washed C_3N_4 product, (C) 1:1 TCM:NaCl product and its (D) water washed C_3N_4 product, (E) 1:2 TCM:NaCl product and its (F) water washed C_3N_4 product.

Figure 3.13 shows SEM images of the morphologies of the other salt products. These also show large aggregates, but with very distinct fine features. The TCM-KBr product has a very moss-like appearance, with some walls thinner than 200 nm. The TCM-KI product resembled coral, made up of short interconnected rods with 200-400 nm channels. The KSCN and NH_4SCN products were similar extended aggregates without distinct particle shapes. These did have very rough surfaces with small <100 nm pores.

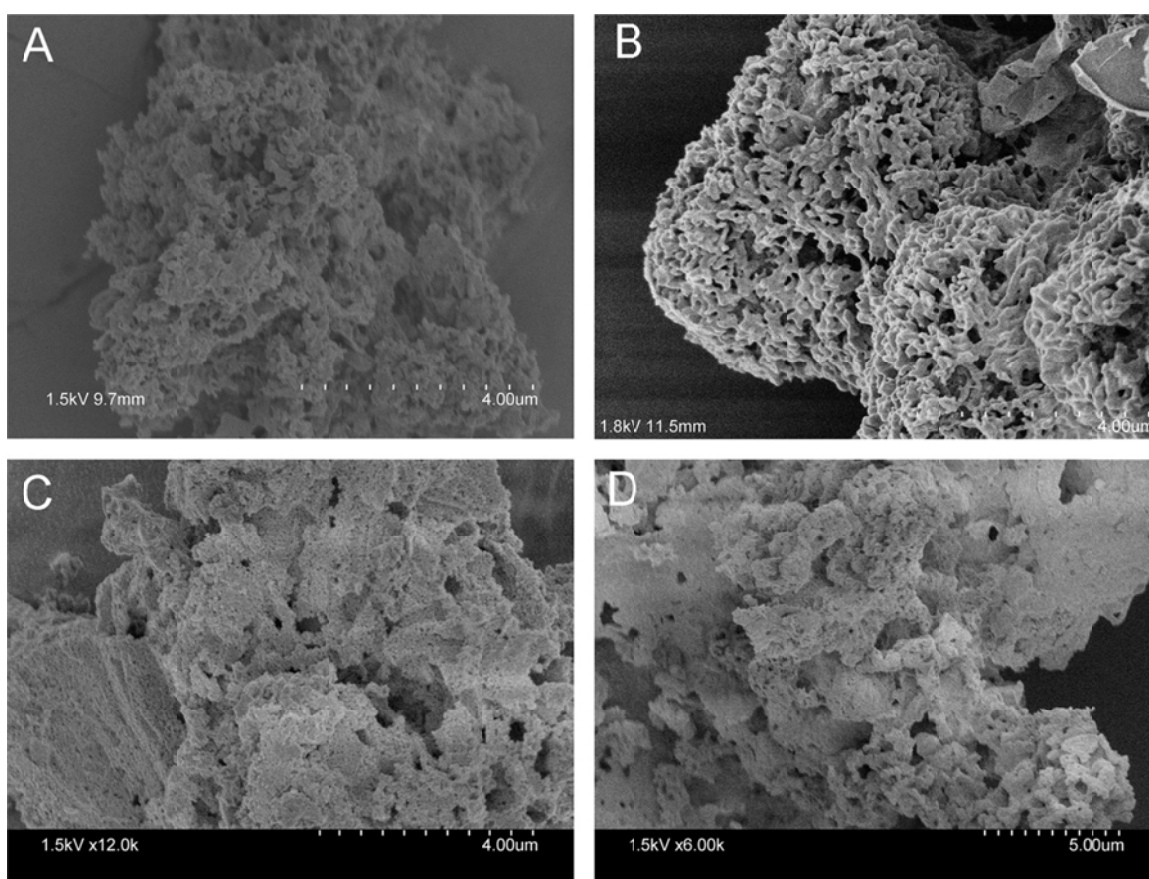


Figure 3.13 – SEM images of washed C_3N_4 products from (A) TCM-KBr, (B) TCM-KI, (C) TCM-KSCN, and (D) TCM- NH_4SCN .

The BET surface areas for the tube reactor products from solution mixed precursors were measured and summarized in Table 3.4. The NaCl and KBr products had similar surface area compared to the equivalent TCM product. The surface areas of

the KI, KSCN, and NH₄SCN products increased 3-4 times. Though not a significant increase, this was higher than the surface area of as-synthesized C₃N₄ products from DCDA or melamine, two commonly used C₃N₄ precursors.

Table 3.4. BET surface areas of C₃N₄ products from TCM and TCM-salt mixtures.

Product	BET Surface Area (m² g⁻¹)
C ₃ N ₄ (TCM)	4.1
C ₃ N ₄ (TCM-NaCl)	3.22
C ₃ N ₄ (TCM-KBr)	3.59
C ₃ N ₄ (TCM-KI)	12.02
C ₃ N ₄ (TCM-KSCN)	10.14
C ₃ N ₄ (TCM-NH ₄ SCN)	16.67

Optical properties

The colors of the TCM-salt C₃N₄ products vary from the orange products described in Chapter 2 (Figure 3.14). Depending on the starting ratio and synthesis method, the TCM-NaCl products ranged from light-tan to orange to very dark-brown. The TCM-KBr products were tan-orange in color, generally close to that of the TCM products. The TCM-KI products were lighter-yellow in color, similar to C₃N₄ produced from DCDA. The KSCN and NH₄SCN products were brown and dark-tan colors, respectively. Diffuse reflectance UV-vis was used to quantify these colors as band gap values. Converting the raw reflectance data (Figure 3.15A) into absorbance data using the Kubelka-Munk function yielded a Tauc Plot (Figure 3.15B). The indirect band gaps (E_g) were approximated by extrapolating the linear region of the absorption edge to the

intercept with the energy axis (in eV). The E_g values for TCM-NaCl, TCM-KBr, TCM-KI, TCM-KSCN, and TCM-NH₄SCN were 2.23, 2.42, 2.7, 2.45, and 2.58 eV respectively. Except for the TCM-KI product, the rest appeared to have a secondary absorption edge at lower energy.



Figure 3.14 – Optical microscope images of C₃N₄ products from 500 °C tube decomposition of (A) TCM-NaCl, (B) TCM-KBr, (C) TCM-KI, (D) TCM-KSCN, and (E) TCM-NH₄SCN. Scale bar represents 2 mm.

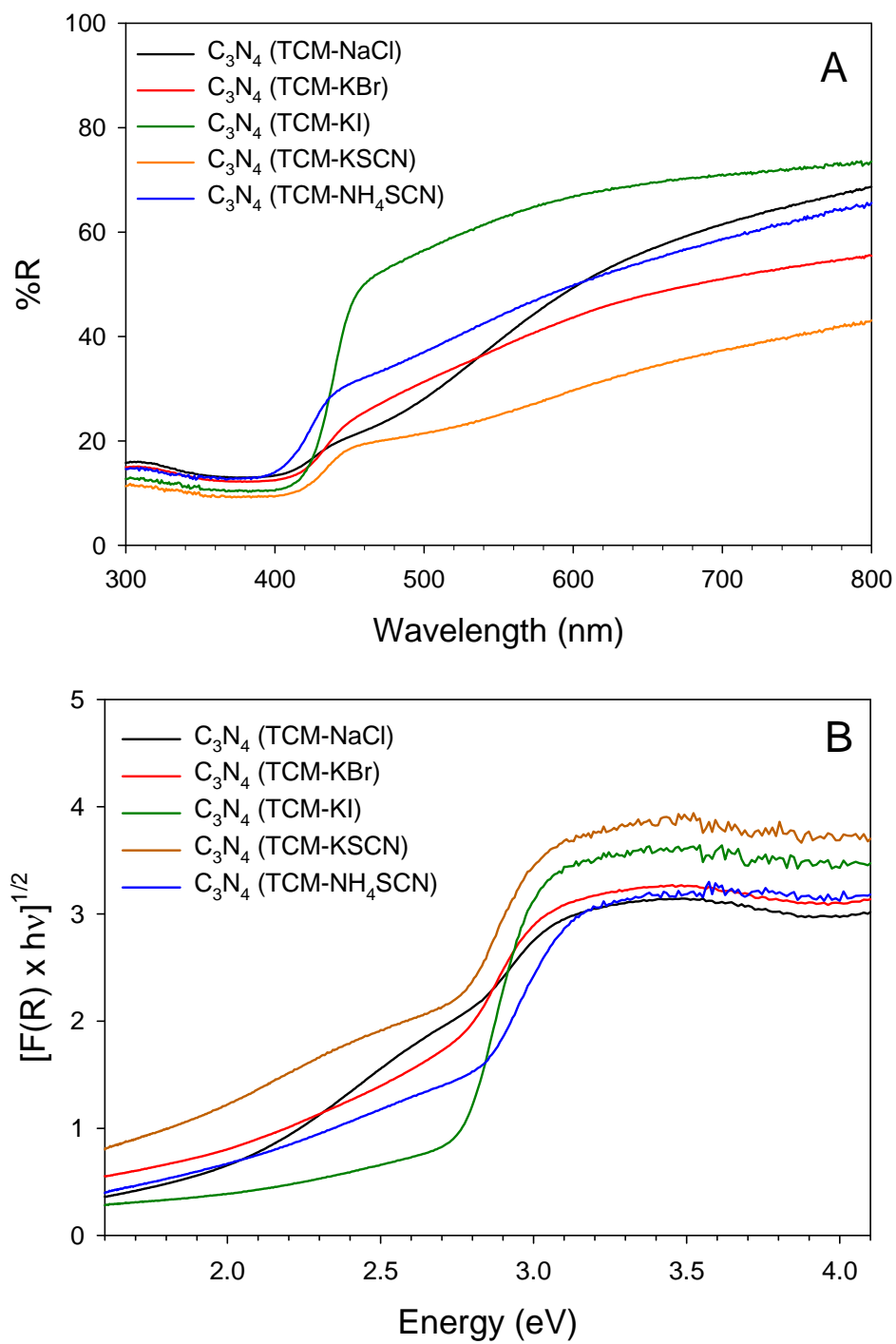


Figure 3.15 – UV-vis DRS data for TCM-salt products (A) reflectance data and (B) Tauc plots.

Photocatalytic studies

Photocatalytic dye oxidation

The degradation of methyl orange dye was studied with the different ratio TCM:NaCl products and the different salt mixtures. Figure 3.16A shows the UV light oxidative degradation in air of MO with C₃N₄ products, for increasing amounts of NaCl had been mixed with TCM. All samples had less than 10% adsorption of dye during the dark stir. At the end of the test, the base C₃N₄ materials (TCM, tube reactor) reached 40% of dye remaining. The 1:1 starting TCM:NaCl product had improved activity to reach under 20% dye remaining. The 2:3 and 1:2 TCM:NaCl products performed nearly identically, the 2:3 product leading by 5% at most time points, but both reached complete degradation by the end of the experiment. The first-order rate fit (Figure 3.16B) and calculated rate constants (Table 3.5) also showed that both the 2:3 and 1:2 TCM:NaCl products were most efficient at degrading MO.

Table 3.5. Rate constants (min⁻¹) for UV light degradation of methyl orange dye using washed C₃N₄ products from TCM-NaCl mixtures.

Sample	C ₃ N ₄ (no NaCl)	C ₃ N ₄ (1:1 TCM-NaCl)	C ₃ N ₄ (2:3 TCM-NaCl)	C ₃ N ₄ (1:2 TCM-NaCl)
UV Rate	0.007 (R ² = 0.997)	0.012 (R ² = 0.992)	0.033 (R ² = 0.95)	0.032 (R ² = 0.96)

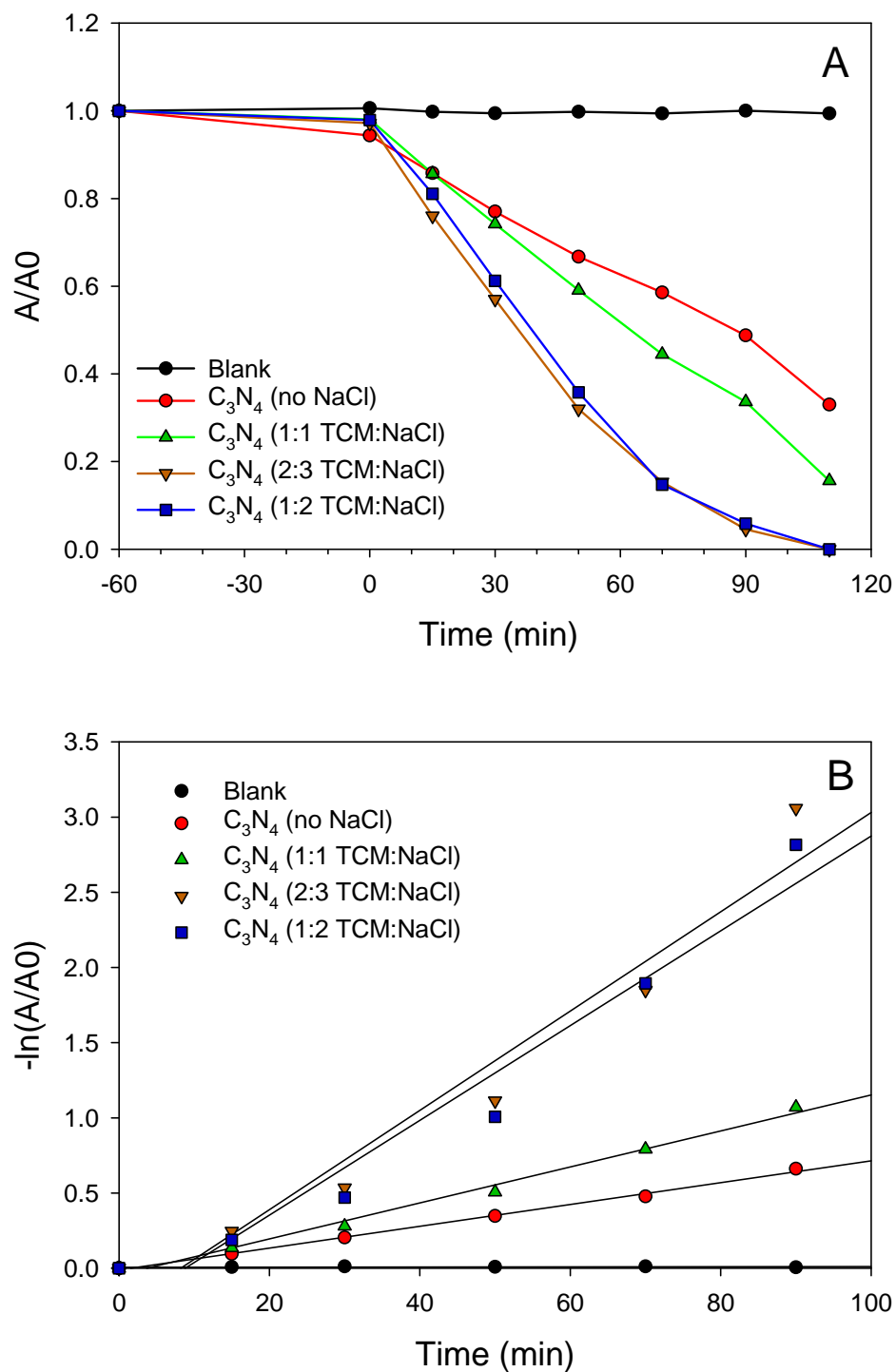


Figure 3.16 – UV-vis analysis of the photodegradation of MO dye using C_3N_4 products from TCM-NaCl mixtures (A) UV-light data (B) linear rate data.

The degradation of methyl orange was also studied with the tube products of each TCM-salt mixture. Figure 3.17A shows the oxidative degradation of MO in air under UV light. Each sample had some degree of dye adsorption during the 60 minute dark stir, the TCM-KI product being the highest near 20%, and the remaining samples at 10% or less. The TCM-KI product was most active reaching near 20% dye remaining by 45 minutes. The TCM-KSCN and TCM-KBr products were different at the first measurement, but from 30 minutes onward had near-identical values. Each of these samples reached 10% of dye remaining by the end of the experiment. The TCM-NH₄SCN and TCM-NaCl products reached 25% and 35% by the end of the experiment, with the TCM-NH₄SCN product leading by 10% and each measurement time. A comparison of the linear rate fits (Figure 3.17B) and first order rate constants (Table 3.6) showed that the TCM-KSCN, TCM-KBr, and TCM-KI C₃N₄ products were most effective within a close margin. The TCM-NaCl and TCM-NH₄SCN products had close rates to each other and were between 34-46% as effective as the other TCM-salt products.

Table 3.6. Rate constants (min⁻¹) for UV light degradation of methyl orange dye using washed C₃N₄ produced from different TCM-salt mixtures.

Sample	C ₃ N ₄ (TCM- NaCl)	C ₃ N ₄ (TCM-KBr)	C ₃ N ₄ (TCM-KI)	C ₃ N ₄ (TCM- KSCN)	C ₃ N ₄ (TCM- NH ₄ SCN)
UV Rate	0.0072 (R ² = 0.979)	0.0224 (R ² = 0.979)	0.0213 (R ² = 0.962)	0.0236 (R ² = 0.972)	0.0099 (R ² = 0.999)

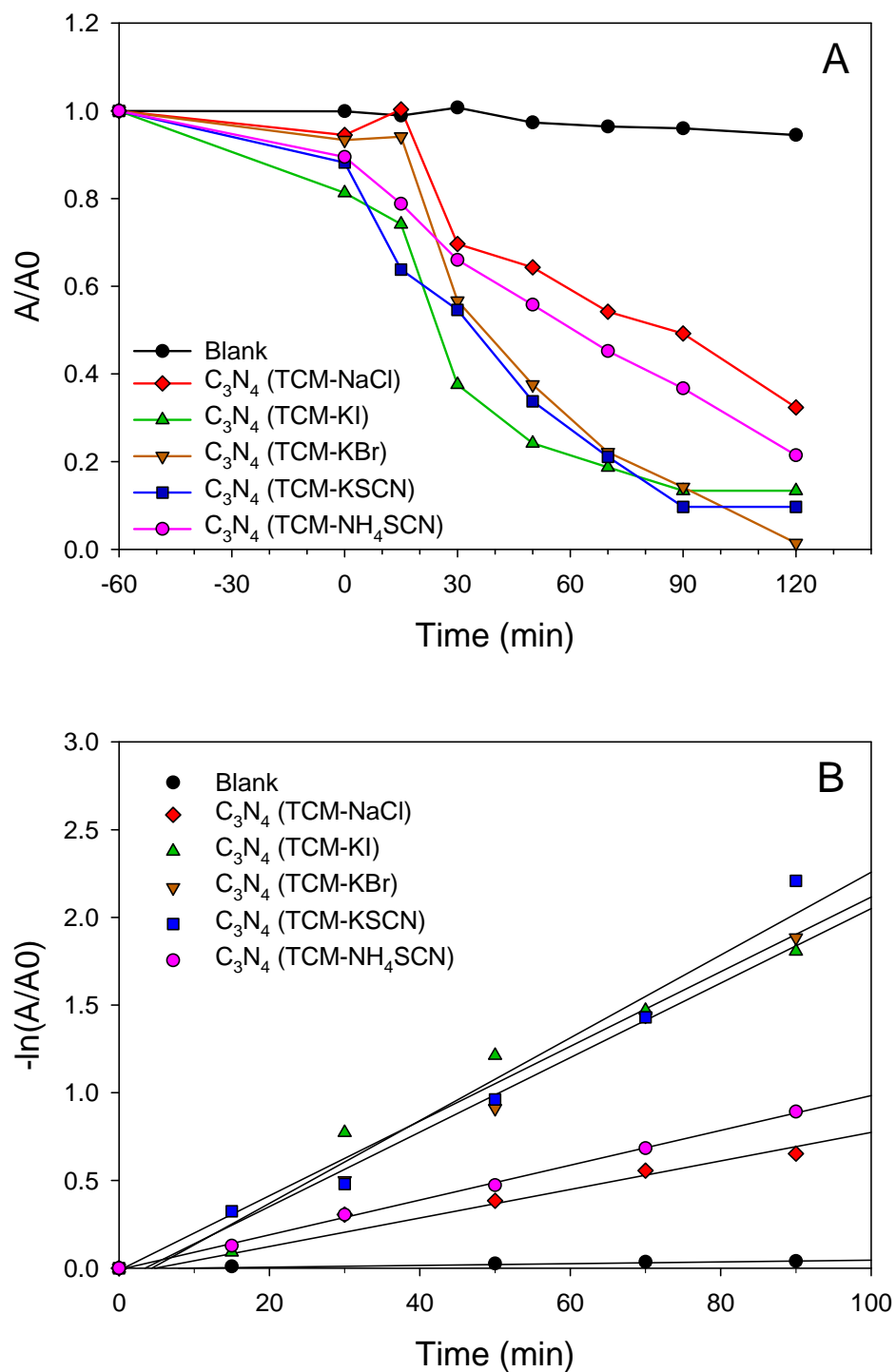


Figure 3.17 – UV-vis analysis of the photodegradation of MO dye using washed C_3N_4 products from TCM-salt mixtures (A) UV-light degradation data (B) linear rate data.

Photocatalytic hydrogen evolution via water-splitting

In the hydrogen evolution studies using the TCM-salt decomposition products, only platinum was studied as a co-catalyst. The target amount was typically 1 wt%, however some tests used between 0.5-1.5 wt% as a target loading. Table 3.7 contains the quantification of Pt content for selected samples by ICP-OES. As in Chapter 2, the actual amount of Pt successfully reduced on the surface was a fraction of the target, typically less than a third. Again, this stresses the importance of proper quantification of the amount of co-catalyst loaded in these experiments.

Table 3.7. Average hydrogen production rates (with standard deviation) for Pt deposited C_3N_4 and ICP-OES quantification of metal loading.

Product source	Target wt% M (ICP wt%)	H₂ Rate ($\mu\text{mol h}^{-1} \text{g}^{-1}$)
TCM (Ch.2)	1% Pt (0.13)	68 (8)
TCM-KBr	1% Pt (0.29)	147 (25)
TCM-KBr	1.52% Pt (0.42)	133 (29)
TCM-KI	0.87% Pt (0.18)	520 (254)
TCM-NH ₄ SCN	0.54% Pt (0.33)	300 (10)
TCM-KSCN	0.89% Pt (0.15)	80 (32)

The photocatalytic production of hydrogen was monitored in real time using the RGA-MS system. Figure 3.18 shows overlays of 1 hour UV illumination cycles for each of the TCM-salt precursor C_3N_4 products. Most notable is the product from the TCM-KI mixture, showing 2-3 times as much hydrogen products as the next most-active sample.

This product has consistently shown a drop in activity after the first cycle, after which the activity stabilizes. While some of this enhanced activity can be attributed to the increased surface area of this product, there are reports of iodine as a dopant in C_3N_4 increasing activity for photocatalytic hydrogen evolution.¹⁰⁴ Since the XRD analysis of the precursor showed the exchange between chloride and iodide, it is possible that some amount of iodide remained in the structure after the decomposition. If this incorporated iodide contributed in some part to this enhanced activity, the decrease after the first cycle could indicate that some may have leached out during the reaction.

The TCM-KBr and TCM-NH₄SCN products performed similarly in the data as shown in Figure 3.18, though the TCM-KBr product exhibited the first-cycle activation step described for some catalysts in Chapter 2. TCM-NH₄SCN products showed fairly consistent activity, even in cases with low target Pt amounts (Table 3.7). The activity of TCM-KBr products was more variable. The rate activity for the test in Figure 3.17 was $293 (\pm 31) \mu\text{mol h}^{-1} \text{g}^{-1}$, double that of previous data for the samples with different amounts of platinum in Table 3.7. Since the total amount of platinum was not quantified on this particular sample, differences in the loading may contribute to the increase in activity. However, even with a difference of 0.13% platinum, the activities of the samples in Table 3.7 were within the standard deviation of each other.

The TCM-NaCl and TCM-KSCN products did not show a significant enhancement as compared to the TCM-C₃N₄(T) product (see Chapter 2), prepared under analogous conditions. This is understandable for the TCM-NaCl product, which did not have a significantly-different surface area. The specific TCM-KSCN product in Figure 3.17 had a hydrogen evolution rate of $143 \mu\text{mol h}^{-1} \text{g}^{-1}$. The activity of this sample

decreased over the four cycles tested, starting at $240 \mu\text{mol h}^{-1} \text{g}^{-1}$ and ending at $77 \mu\text{mol h}^{-1} \text{g}^{-1}$, indicating some chemical change, similar to the TCM-KI product catalysts. A possibility is if residual loosely SCN^- or CN^- fragments remained in the final C_3N_4 product, as these could strongly coordinate to Pt, effectively poisoning the co-catalyst.¹⁰⁵⁻

106

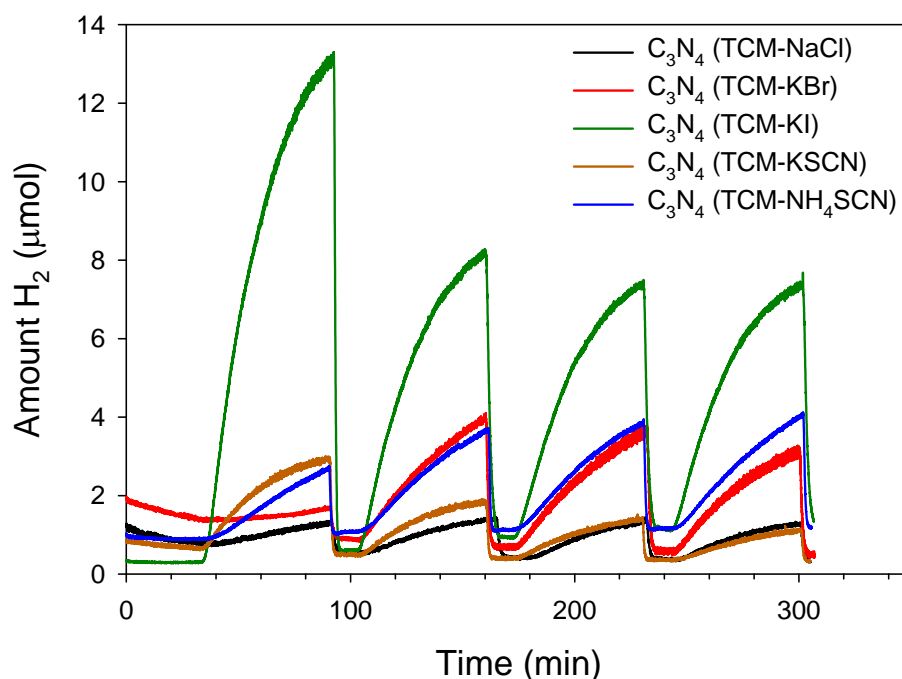


Figure 3.18 – Stacked plots of photocatalytic hydrogen evolution using TCM-salt products. Each catalyst contained a targeted 1 wt% Pt co-catalyst. The UV lamp was turned on for 1 hour cycles, and the reactor was purged with argon for 10 minutes between each cycle.

In regards to surface area, the order from highest to lowest follows TCM- $\text{NH}_4\text{SCN} > \text{TCM-KI} > \text{TCM-KSCN} > \text{TCM-KBr} > \text{TCM-NaCl}$ products. The products of TCM- NH_4SCN and TCM-KI have the highest surface areas and generally the highest rate of hydrogen production. As previously discussed, an iodide-doping effect may be a

cause of the further increased activity for the TCM-KI product. The TCM-KSCN product has the next-highest surface area, but even at its best activity in the first cycle is comparable to rates for TCM-KBr products. The proposed SCN^- or CN^- poisoning may take effect as early as the first cycle in this case. Though the TCM-KBr product does not have a significantly-different surface area from the TCM- $\text{C}_3\text{N}_4(\text{T})$ product, it does have increased activity. The differences in the band gaps for these products could also contribute to the changes in activity.

3.4 Conclusions

This chapter has described the preparation of C_3N_4 products from different mixtures of TCM with halide or thiocyanate salts, with the goal of using the salts as easily removable templates to increase product surface area. The TCM precursor readily reacted with most of these salts, exchanging chlorine for bromine, iodine, or thiocyanate. Use of the low temperature Schlenk reactor set-up for the synthesis of C_3N_4 was met with difficulty in fully propagating decomposition, due to the presence of the thermally insulating salt. The tube reactor decompositions at 500 °C worked for achieving fully-formed products from each TCM-salt mixture. These products formed a more diverse array of colored product than the typical orange product prepared from TCM only, with band gaps ranging from 2.23 to 2.7 eV. Surface areas increased the most for the TCM-KI, TCM- NH_4SCN , and TCM-KSCN products, though SEM displayed new rougher, porous surfaces for the other products. Photocatalytic activity was evaluated for both the degradation of methyl orange dye and hydrogen evolution.

CHAPTER 4

DEPOSITION OF CARBON NITRIDE ONTO METAL OXIDE SUPPORTS

4.1 Introduction

In contrast to the previous chapter where the goal was to utilize different salts as templates to modify and improve the surface area of carbon nitride (C_3N_4), this chapter aims to utilize high surface-area materials as supports for the growth of carbon nitride. Previous work utilized a low melting point cyanamide precursor to infiltrate a silica (SiO_2) host matrix prior to carbon nitride formation.¹⁰⁷⁻¹⁰⁸ A similar approach has been used to incorporate dicyandiamide into alumina (Al_2O_3) foams heated at different temperatures.¹⁰⁹

In addition to utilizing high surface-area supports, using other known metal oxide semiconductors as supports for semiconducting C_3N_4 could enable new synergistic photocatalytic benefits from different absorption properties or differences in band edge positions more suitable to other oxidation or reduction processes.^{55, 110} Titanium dioxide (TiO_2) has a wider band gap ($E_g=3.2$ eV) than C_3N_4 ($E_g=2.6-2.7$ eV), and while limited to using UV light, it can function for a wide variety of photocatalytic reactions including organic molecule oxidation, sterilization, and water-splitting.^{38, 40} C_3N_4 composites with TiO_2 have been prepared by hydrothermal synthesis and calcination of mixed sol-gel precursors,¹¹¹ by electrodeposition of C_3N_4 on a TiO_2 nanotube substrate,¹¹² or by simple solution mixing and evaporation of C_3N_4 with TiO_2 .¹¹³ Tungsten trioxide (WO_3) has a comparable band gap ($E_g=2.6$ eV) to C_3N_4 and is capable of using low wavelength visible light. In contrast to TiO_2 , applications of WO_3 are primarily used for photocatalytic oxidation reactions, rather than both oxidation and reduction.¹¹⁴⁻¹¹⁶ C_3N_4 composites

with WO_3 have been prepared by hydrothermal synthesis with C_3N_4 in a WO_3 precursor solution¹¹⁷ or annealing of dried solution mixtures of C_3N_4 with WO_3 .¹¹⁸⁻¹¹⁹ Low-level doping or composite formation was also achieved by intercalation of WO_4^{2-} between g- C_3N_4 layers.¹²⁰

The work in this chapter explores the use of inert and photoactive oxide supports as a means of improving the photocatalytic activity of TCM-derived carbon nitride. Commercial SiO_2 and Al_2O_3 act as high surface area (300 and 100 m^2/g) supports. Composites with TiO_2 and WO_3 are supports with larger and smaller band gaps, respectively, than C_3N_4 . The methanol-soluble TCM was coated onto the oxide by suspending the oxide in a solution of TCM and evaporating the solvent to deposit TCM on the surface. The coated metal oxide was heated to decomposition conditions in the previously-used reactors. Alternate hybrid composites using C_3N_4 powders were also produced.

4.2 Experimental

Reagents

Trichloromelamine ($\text{C}_3\text{N}_3(\text{NHCl})_3$, TCM, 98%) was purchased from GFS Chemical and stored in an argon atmosphere glovebox. Other reagents used as received were; SiO_2 Aerosil 300 (Degussa), Al_2O_3 Aluminoxid (Degussa), P25 TiO_2 Titanoxid (Degussa), H_2WO_4 (Alfa Aesar), $\text{Na}_2\text{WO}_4 \cdot 2\text{H}_2\text{O}$ (99.0%, Alfa Aesar), $\text{H}_2\text{PtCl}_6 \cdot 6\text{H}_2\text{O}$ (99.9%, Strem), methanol (ACS certified, Fisher), methyl orange (85% dye content, Sigma Aldrich), and triethanolamine (Alfa Aesar, 98+%). Deionized water (18M Ω) was prepared using a Photronix MiniQuad system.

Coating of C₃N₄ onto SiO₂, TiO₂ and Al₂O₃ oxide supports

The mixture of the TCM precursor and the oxide support was prepared both under inert conditions and in air. TCM (300 mg, 1.31 mmol) was dissolved in 40 mL of methanol in a 100 mL Schlenk flask. The flask was purged with nitrogen by connecting the side arm to a Schlenk line and capped with a stopper. While maintaining nitrogen flow, the stopper was removed, and 0.5 or 1 mass equivalents of SiO₂, TiO₂ or Al₂O₃ was added to the dissolved TCM. The mixture was stirred overnight. The methanol was then removed under vacuum by a liquid nitrogen cold trap. The mixed precursor remained white in color but was notably denser than the bare metal oxide. Alternatively, the precursor mixture was prepared in air by dissolving TCM (300-500 mg, 1.31-2.18 mmol) in 50 mL of methanol in a 100 mL beaker. Once completely dissolved, 0.5 or 1 mass equivalent of either oxide was added to the solution. The solution was stirred for two hours and then left to evaporate in air overnight to deposit the mixed solid.

Schlenk heating

The mixed solid was transferred to the Schlenk style reactor described in Chapter 2. The reactor was placed on the heating mantle and set to 300 °C. The decomposition reaction was less vigorous than for TCM only, with the color change not occurring until higher temperatures and lower or slower gas evolution. Depending on the reaction, the reactor was allowed to dwell at 300 °C for up to 5 minutes. Products from this method will be identified as C₃N₄@SiO₂(Schlenk), C₃N₄@Al₂O₃(Schlenk), and C₃N₄@TiO₂(Schlenk).

Tube heating

The decomposition reaction was also performed using the tube reactor set-up. The TCM deposited oxide precursor was loaded into a Schlenk tube with a test tube insert. An oil bubbler was connected to the side arm to allow pressure release, and the tube was purged with nitrogen. The tube was clamped in place above a vertical tube furnace and heated to 500 °C at a rate of 10 °C with a 1 hour dwell time. Gas evolution typically occurred between 180 and 200 °C. Products from this method will be identified as $C_3N_4@SiO_2(\text{Tube})$, $C_3N_4@Al_2O_3(\text{Tube})$, and $C_3N_4@TiO_2(\text{Tube})$.

Preparation of $C_3N_4-WO_3$ composite materials

$C_3N_4-WO_3$ composites were prepared using two different approaches; coating TCM onto WO_3 and performing the decomposition, or depositing a soluble WO_3 precursor onto already made C_3N_4 and completing the metal oxide formation at lower temperature.

C_3N_4 formation on WO_3

For the first method, crystalline WO_3 was first prepared from tungstic acid (H_2WO_4). H_2WO_4 (1 g, 4 mmol) was placed into a crucible, which was loaded into a muffle furnace. The furnace was heated to 300 °C at a rate of 10 °C min^{-1} in air and held overnight. The conversion of H_2WO_4 to WO_3 was verified by XRD. TCM (200 mg, 0.87 mmol) was dissolved in 40 mL of methanol in a 100 mL beaker, then 0.3 or 0.5, mass equivalents of the prepared WO_3 was added to the solution. The mixture was briefly sonicated and then stirred for 2 hours. The beaker was left open in air to allow the methanol to evaporate overnight and deposit the mixed solid.

Schlenk heating

The mixed precursor was loaded into the Schlenk style reactor and put under nitrogen. The reactor was placed onto a heating mantle and set to heat to 300 °C. The decomposition initiated between 240 and 265 °C. An orange to light-brown powder was collected after cooling the reactor (~42-53% mass yield from total precursor mass). Products from this method will be identified as C₃N₄@WO₃(Schlenk).

Tube heating

The decomposition reaction was performed using the tube reactor set-up. The TCM deposited oxide precursor was loaded into a Schlenk tube with a test tube insert. An oil bubbler was connected to the side arm to allow pressure release, and the tube was purged with nitrogen. The tube was clamped in place above a vertical tube furnace, heated to 500 °C at a rate of 10 °C, and held for 1 hour. Gas evolution typically occurred between 180-200 °C. After cooling and venting the tube, a dark brown-black powder was collected from the insert (~18% mass yield from total precursor mass). Products from this method will be identified as C₃N₄@WO₃(Tube).

WO₃ formation on C₃N₄

In the alternate method of preparing C₃N₄-WO₃, Na₂WO₄ · 2H₂O (200 mg, 0.61 mmol) was dissolved in 10 mL of water. C₃N₄ product (150 mg) from a Parr TCM decomposition reaction (Chapter 2) was added into the solution and the mixture stirred. The solution was acidified with 2 mL of concentrated HCl, after which a yellow color developed indicating the formation of H₂WO₄. After precipitation, the solids were isolated by centrifugation. The yellow solids were then rinsed over a Büchner funnel to ensure complete removal of by-product NaCl. The solid was allowed to dry in air. After

drying, the solid was placed into a covered crucible. The crucible was placed into a muffle furnace, heated to 300 °C in air at a rate of 10 °C/min, and held for 3 hours. A yellow-orange powder was collected from the crucible (~91% mass yield based on dry composite before heating). Products from this method will be identified as $\text{WO}_3@C_3N_4$.

Annealing of C_3N_4 -metal oxide composites

Higher-temperature treatments of the Schlenk reactor products were investigated. Typically, 100-200 mg of the solid was placed into an alumina boat that was then placed inside a Pyrex tube closed on one end. The tube was connected to a Schlenk line, evacuated, and refilled with argon. The tube was placed into a clamshell furnace, heated to 450-500 °C at a rate of 10 °C/min, and held for 1-2 hours. Mass recovery ranged from 37-76% depending on the initial ratio of C_3N_4 to oxide support.

Reaction of a physical mixture of C_3N_4 and metal oxide support

Physical mixtures of C_3N_4 (Parr TCM product) and TiO_2 or WO_3 were prepared via ball-milling. 100 mg of C_3N_4 and 50 mg of TiO_2 or WO_3 were loaded into 5 mL stainless steel milling jars with 2 x 5 mm steel balls. The solids were milled for 5 minutes at 1200 rpm in a FormTech FTS 1000. The composites were used without any additional heat treatment. Products from this method will be identified as C_3N_4 - $\text{TiO}_2(\text{mill})$ and C_3N_4 - $\text{WO}_3(\text{mill})$.

Characterization

FT-IR spectra were collected on a Nicolet Nexus 670. Solid samples were prepared as KBr pellets for data collection. Gas samples were analyzed by transferring 5 mL of gas from the reaction vessel into a 10 cm long gas IR cell with KBr windows. Elemental analysis was performed on a Perkin Elmer 2400 Series II CHNS/O Analyzer, with 1-2 mg of sample in crimped tin capsules. Powder X-ray diffraction was collected on a Bruker D8 system (source Cu K α , 5-80°, 0.050 °/step) with samples deposited on glass slides. Thermogravimetric analysis was performed on a Seiko Exstar 6300 TGA-DTA. Samples were heated up to 1000°C at a rate of 10°C/min under air or argon flow. Scanning electron microscopy images were collected on a Hitachi S-4800 FE-SEM ($v_{acc}=1.8$ kV). Diffuse reflectance spectra were collected on a Cary 5000 Series Spectrophotometer (200-800 nm, 10 nm/s). Solid samples were loaded into a round compression sample holder with a 1 cm diameter sampling area. Kubelka-Munk conversions were calculated from the Cary software, and Tauc plots were generated using $[F(R)hv]^{1/2}$. BET surface area measurements were collected on a Quantachrome Nova 1200 using 100-200 mg of ground solid sample.

Photocatalytic reactions

Oxidative degradation of organic dyes

The degradation of methyl orange (C₁₄H₁₄N₃NaO₃S) dye was studied using the materials prepared in this chapter. A stock 10⁻³ M dye solution was prepared by dissolving the solid dye in 18 M Ω water. The stock solution was diluted to 4·10⁻⁵ M for methyl orange to fit the peak at λ_{max} in the range ($\lambda_{MO}=504$ nm, $A<1.50$) of the UV-vis

spectrophotometer (Agilent 8453). To 30 mL beakers, 10 mL of dye solution and 10 mg of catalyst were added. An additional beaker containing only dye was used as to evaluate self-degradation in the absence of catalyst. Samples were stirred a minimum of 30 minutes in the dark to equilibrate dye absorption. Samples were exposed to UV light (Ace-Hanovia, 450 W Hg) in 15-30 minute intervals. After each illumination period, the catalysts were separated from the dye solution by centrifugation (3000 rpm), and the UV-vis spectrum of each solution was collected to quantify the remaining concentration of dye. Experiments were typically carried out for 2 hours of total UV irradiation. For visible light experiments, 400 nm long pass filters (Edmund Optics) were placed between the lamps and samples and irradiation times were extended.

Photocatalytic hydrogen evolution via water-splitting

The composite products were examined as HER catalysts. Pt was photoreduced onto the C_3N_4 surface under UV light using H_2PtCl_6 as the metal source. C_3N_4 was suspended in a 50% aqueous MeOH solution containing the metal salt to target 1-2 wt% of reduced metal on C_3N_4 . The solution was degassed with argon and exposed to UV light for 2 hours. The solid was collected by centrifugation, rinsed with MeOH, and dried in air.

For hydrogen evolution tests, 10 mg of catalyst (C_3N_4 or $M(x\%):C_3N_4$) was dispersed in a 10 mL solution of 10% aqueous triethanolamine ($C_6H_{15}NO_3$) contained in a 50 mL Schlenk flask. The solution was degassed with argon and connected to a Residual Gas Analysis Mass Spectrometer (RGA-MS, Stanford Research Systems QMS 300 series) by capillary to the side arm. Data were collected as a pressure vs. time scan, monitoring the masses for nitrogen, argon, hydrogen, water, and oxygen. The reactor was

exposed to UV light in 1 hour intervals and was vented with an argon purge between each UV run in order to return hydrogen concentrations to baseline levels. The moles of hydrogen produced were determined using a pressure signal calibration based on known concentration mixtures of H₂/Ar.⁸⁸ Additional details about calibration and experimental set-up can be found in the appendix.

4.3 Results and Discussion

Decomposition reaction and thermal stability of C₃N₄ in oxide composites

C₃N₄ with SiO₂, Al₂O₃, and TiO₂

Prior to decomposition reactions, the TCM precursor was mixed with commercial SiO₂, Al₂O₃, and TiO₂ in solution to coat the reactive precursor onto the oxide surface. The oxides used were very fine, high surface area powders (SiO₂ ~300 m²/g, Al₂O₃ ~100 m²/g, TiO₂ ~45 m²/g), and were highly dispersible. Once coated in TCM, these oxides appeared denser and less susceptible to static cling. The color remained unchanged, unlike the reactive mixtures between TCM and the halide and thiocyanate salts described in Chapter 3. The IR spectra showed no change in the signature absorptions of TCM. The only new feature was the appearance of a large broad absorption for the respective M-O stretches (M = Si, Al, Ti).

Using the Schlenk flask and heating mantle reactor, visible decomposition did not take place until reaching higher temperatures than TCM without an additive. The SiO₂ products reached 250-270 °C before decomposition occurred, as indicated by gas evolution and a color change of the solid to a sandy, light-yellow-orange color (Figure 4.1A). The Al₂O₃ composite reactions were unique in that the decomposition occurred

without violent gas evolution and a more gradual color change to an orange solid by 260 °C (Figure 4.1C). These reactions were allowed to dwell at this temperature for 10 minutes after the color changed, but there were no indications of further reaction. The TiO₂ products behaved similarly, reaching 250 °C to yield a light-sand colored solid (Figure 4.1E). When SiO₂ reactions were tested at larger scales, the temperature was allowed to reach 300 °C with no gas evolution, but some change in product color was observed. As with the NaCl reactions described in Chapter 3, reducing the flask size used for the reactor, from 250 mL to 50 mL, helped to focus the heat from the mantle on the solids. This resulted in gas evolution from the decomposition by 290 °C. The presence of the inert oxides was thermally insulating, reducing the reactivity of TCM and allowing decomposition to fully propagate.

Higher temperature annealing of the C₃N₄@SiO₂(Schlenk) products was explored to see if the reaction would continue after a second heating step. Heating to 450 °C under argon did result in a darker product; however some exposed SiO₂ surfaces could begin to be seen. While C₃N₄@SiO₂(Schlenk) composites would contain up to 40% C₃N₄ by mass, following annealing this decreased to 10%. While TGA-DTA analysis of C₃N₄ from TCM only showed that the product could be stable up to 600 °C, higher temperature heating of the poorly-formed product in the oxide composite resulted in a greater breakdown of the residual C₃N₄ components.

The formation of C₃N₄ composite products from single-step high temperature heating in the tube reactor led to reactions that behaved similarly to the decomposition of TCM in the absence of additive. Gas evolution was observed in the lower temperature range of 180-200 °C. The products were darker than their respective Schlenk versions

(Figure 4.1 B, D, and F). The more uniform and encompassing heating method using a furnace rather than a heating mantle resulted in a more typical TCM decomposition reaction.

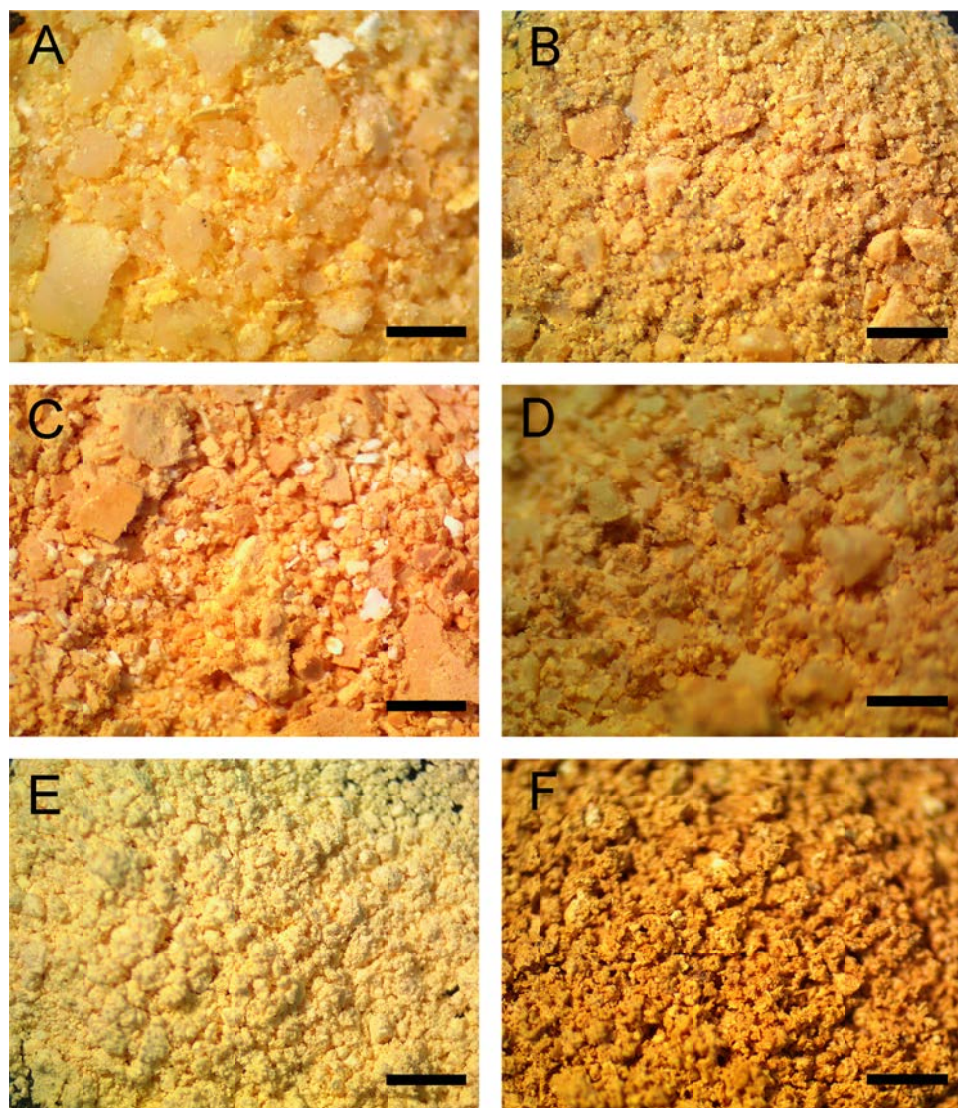


Figure 4.1 – Optical microscope images of (A) $C_3N_4@SiO_2$ (Schlenk), (B) $C_3N_4@SiO_2$ (Tube), (C) $C_3N_4@Al_2O_3$ (Schlenk), (D) $C_3N_4@Al_2O_3$ (Tube), (E) $C_3N_4@TiO_2$ (Schlenk), and (F) $C_3N_4@TiO_2$ (Tube). Scale bar represents 2 mm.

Comparisons between the thermal stabilities of the Schlenk and tube synthesis methods are shown in the TGA plots in Figures 4.2, 4.3 and 4.4. The $C_3N_4@SiO_2$ (Schlenk) composite has a low rate of mass loss until 225 °C, where an increased rate of mass loss begins and continues steadily until 550 °C; at this point, the C_3N_4 has fully decomposed leaving only SiO_2 (57% residual mass). The tube product (heated to 500 °C during synthesis) started with mass loss at the same low rate as the Schlenk products, but this rate continued until 425 °C before the rapid mass loss occurred, leaving only SiO_2 (Figure 4.2). The $C_3N_4@SiO_2$ products had weak broad exothermic peaks near 550 °C in the DTA. The $C_3N_4@Al_2O_3$ (Schlenk) product showed an increased mass loss just above 200 °C, until a slight inflection point near 250 °C where the rate was steady, but slower until reaching 450 °C. This product had a broad exothermic peak in the DTA near 500 °C. The $C_3N_4@Al_2O_3$ (Tube) product had a low rate of mass loss until 430 °C, leading to complete decomposition of the C_3N_4 component by 550 °C (Figure 4.3), and showed a sharper exothermic peak near 500 °C in the DTA. Both the $C_3N_4@TiO_2$ (Schlenk) and $C_3N_4@TiO_2$ (Tube) products exhibit very similar behavior, each having a steady mass loss until 420 °C, followed by complete decomposition of C_3N_4 by 550 °C (Figure 4.4). Both $C_3N_4@TiO_2$ products had broad exothermic peaks near 480 °C, and the $C_3N_4@TiO_2$ (Tube) product had a clear second peak at 520 °C. The differences in the amount of mass remaining after 600 °C were due to different amounts of TiO_2 mixed with TCM in the composite.

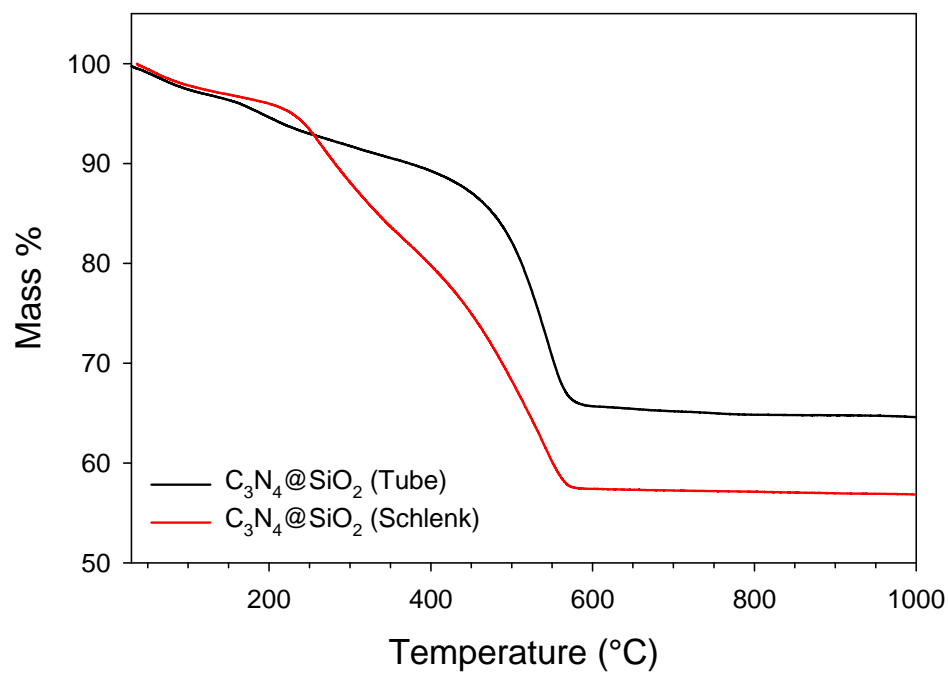


Figure 4.2 – TGA plots of $C_3N_4@SiO_2$ products under air flow, heated at a rate of 10 °C/min.

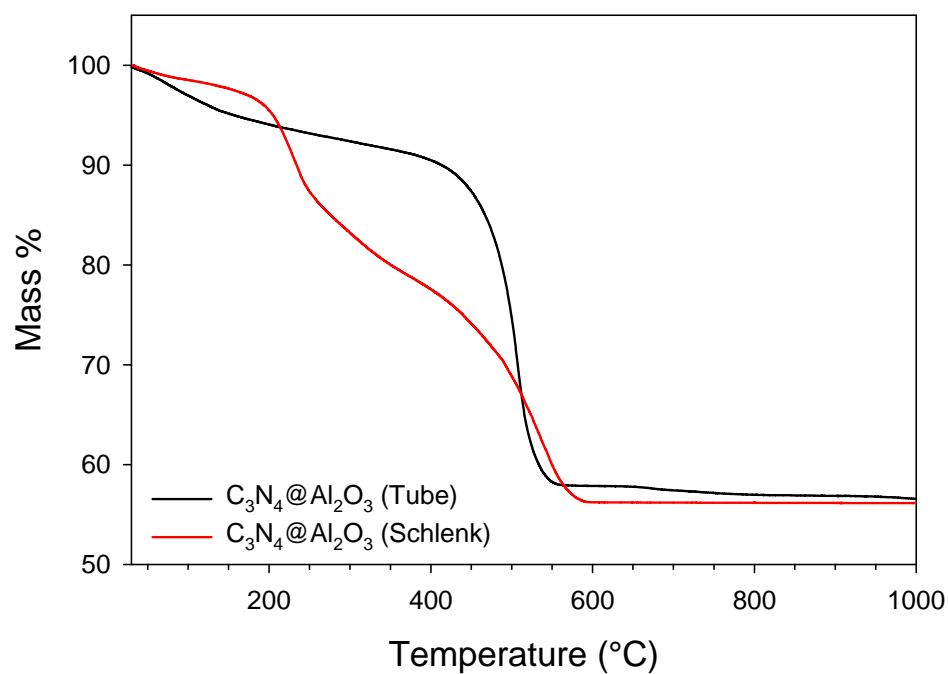


Figure 4.3 – TGA plots of $C_3N_4@Al_2O_3$ products under air flow, heated at a rate of 10 °C/min.

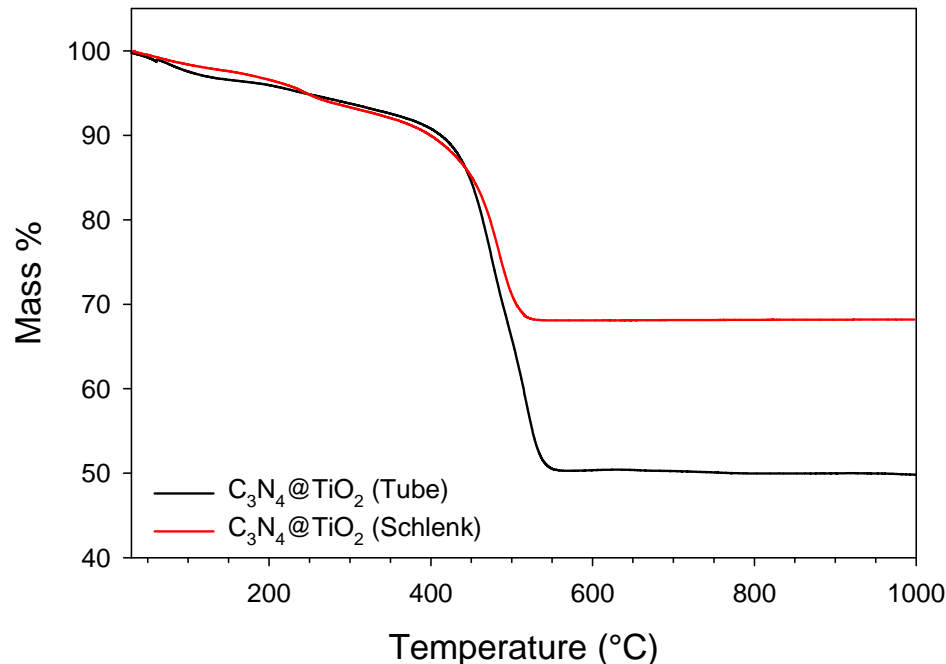


Figure 4.4 – TGA plots of $C_3N_4@TiO_2$ under air flow, heated at a rate of 10 °C/min.

C_3N_4 with WO_3

The synthesis of the $C_3N_4@WO_3$ composites differed from those of the other oxides. Starting with the Schlenk decomposition reactions of TCM coated on WO_3 , gas evolution and product color change occurred in the range of 240-265 °C. These reactions used lower relative amounts of WO_3 to TCM compared to the other oxides, and were put in the smaller 50 mL volume reactor to receive more focused heat from the mantle.

Though the low temperature formation of these products seemed well behaved, higher temperature annealing was explored. When the starting orange product (Figure 4.5A) was heated to 500 °C under argon, a very dark brown, nearly black solid formed (Figure 4.5B). This dark product also formed from annealing a physical mixture of C_3N_4 and WO_3 under the same conditions. The synthesis was also tested in the tube reactor,

starting with TCM on WO_3 and heating to $500\text{ }^\circ\text{C}$ in a single step. This also produced the dark product (Figure 4.5C).

Given that heating WO_3 at high temperatures in the presence of C_3N_4 , whether from TCM or pre-formed, led to an unusual dark product, an alternate approach was taken to form the composite. Starting with Na_2WO_4 dissolved in water, HCl was used to precipitate hydrated WO_3 onto pre-formed C_3N_4 . This was then heated at $300\text{ }^\circ\text{C}$ to dehydrate and ensure complete oxidation in air, without losing significant amounts of C_3N_4 . The products from this method were the more typical yellow-orange powders (Figure 4.5D).

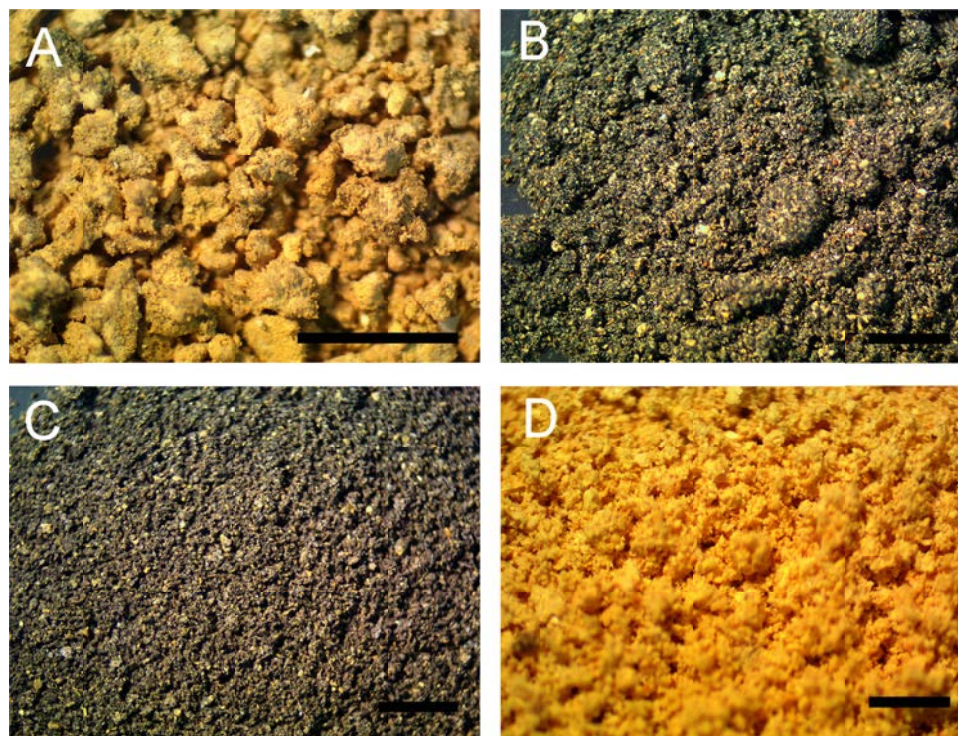


Figure 4.5 – Optical microscope images of (A) $\text{C}_3\text{N}_4@\text{WO}_3$ (Schlenk), (B) $\text{C}_3\text{N}_4@\text{WO}_3$ (Anneal), (C) $\text{C}_3\text{N}_4@\text{WO}_3$ (Tube), and (D) $\text{WO}_3@\text{C}_3\text{N}_4$. Scale bar represents 2 mm.

Figure 4.6 shows the TGA plots of the final products from these two approaches. The dark $C_3N_4@WO_3$ product exhibits continuous mass loss at lower temperatures followed by rapid loss after 450 °C. There was a very weak, broad exothermic peak in the DTA near 480 °C, fitting the more gradual decomposition of the C_3N_4 component of the composite. The $WO_3@C_3N_4$ product is more stable, only beginning to show some mass loss after 450 °C and full decomposition of the C_3N_4 component by 600 °C. This product showed a sharp exothermic peak near 550 °C in the DTA.

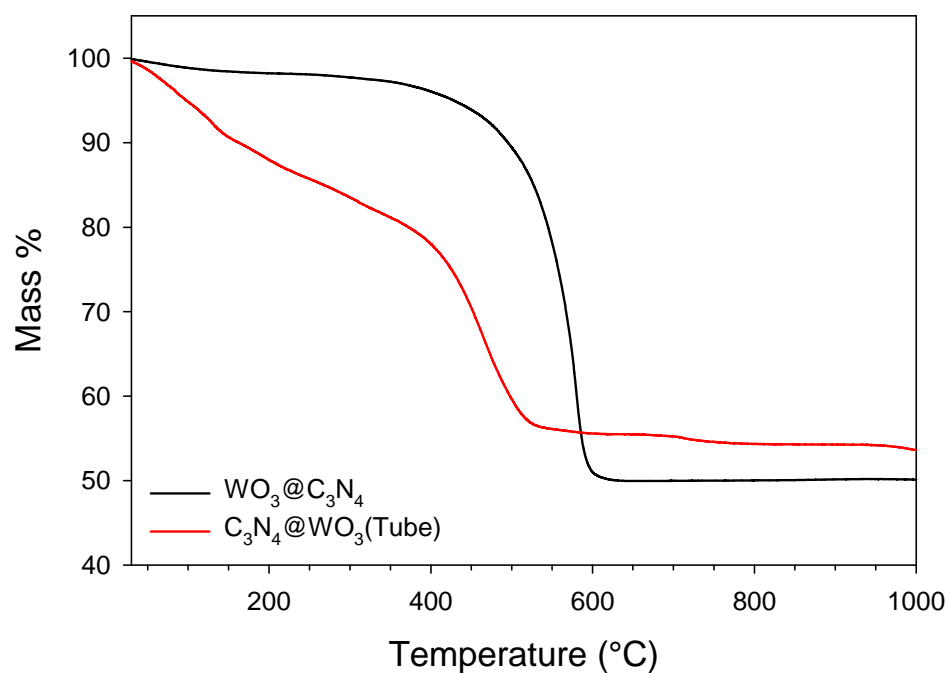


Figure 4.6 – TGA plots of $C_3N_4@WO_3$ and $WO_3@C_3N_4$ under air flow, heated at a rate of 10 °C/min.

Chemical and structural characterization of carbon nitride and oxide composites

Elemental analyses of the C_3N_4 -metal oxide composites are shown in Table 4.1.

Data were collected for both the Schlenk and tube products to compare the compositions

and find correlation with the less-complete reactions. The $C_xN_yH_z$ components of $C_3N_4@TiO_2$ products from each method had nearly identical compositions. As described earlier, compared to the other composites the $C_3N_4@TiO_2$ composites had similar thermal stability and likely achieved the same degree of structural condensation. The $C_3N_4@Al_2O_3$ (Schlenk) composite had a higher N:C ratio than the tube counterpart. This is closer to the starting C_3N_6 of TCM, indicating less condensation to the ideal C_3N_4 structure by retaining extra nitrogen. The $C_3N_4@SiO_2$ composites had similar compositions to each other but with slightly higher N:C ratios than other products. Both preparation methods of the $C_3N_4@Al_2O_3$ and $C_3N_4@SiO_2$ composites had higher relative hydrogen content than other products. Since the hydrogen is typically located in terminal amine sites, these products may be smaller oligomers rather than a more extended structure, in order to incorporate more of these sites, or have high surface adsorption of H_2O due to their high surface areas. The $WO_3@C_3N_4$ composite maintained its starting composition of the C_3N_4 used as the support. Heating to C_3N_4 300 °C in the presence of a WO_3 precursor had no impact on its composition. The $C_3N_4@WO_3$ composite from heating TCM with WO_3 showed higher relative amounts of both nitrogen and hydrogen. Unlike the Al_2O_3 or SiO_2 composites, this is not due to incomplete lower temperature reaction as it was heated and held at 500 °C. There is, instead, some other reaction between the C_3N_4 and WO_3 , as evidenced by the black solid formed.

Table 4.1. CHN elemental analysis for C₃N₄ metal oxide composite products.

Sample	C wt%	N wt%	H wt%	Total wt% CHN (% loss by TGA)	Formula
C ₃ N ₄ @TiO ₂ (Schlenk)	12.13	21.94	1.49	35.56 (32.1)	C ₃ N _{4.6} H _{4.4}
C ₃ N ₄ @TiO ₂ (Tube)	14.45	25.98	1.78	42.21 (49.9)	C ₃ N _{4.6} H _{4.3}
C ₃ N ₄ @Al ₂ O ₃ (Schlenk)	9.06	18.68	1.09	28.83 (43.8)	C ₃ N _{5.3} H _{4.3}
C ₃ N ₄ @Al ₂ O ₃ (Tube)	10.47	19.07	1.78	31.32 (43.4)	C ₃ N _{4.7} H _{6.1}
C ₃ N ₄ @SiO ₂ (Schlenk)	9.65	18.08	1.80	29.53 (43.1)	C ₃ N _{4.8} H _{6.7}
C ₃ N ₄ @SiO ₂ (Tube)	8.65	16.53	2.01	27.19 (35.4)	C ₃ N _{4.9} H _{8.4}
C ₃ N ₄ @WO ₃ (Schlenk)	11.60	21.38	1.23	34.21 (53.5)	C ₃ N _{4.7} H _{3.8}
C ₃ N ₄ @WO ₃ (Tube)	8.65	18.81	2.17	29.63 (46.4)	C ₃ N _{5.6} H _{9.0}
C ₃ N ₄ @ WO ₃	14.63	25.93	2.17	42.02 (49.9)	C ₃ N _{4.6} H _{3.6}

The IR spectra of the $C_3N_4@SiO_2$ composites are shown in Figure 4.7. Both feature N-H stretching absorptions above 3100 cm^{-1} , though there are two absorptions for the Schlenk product as opposed to one broad absorption for the tube products. The C-N and C=N absorptions in the $1200\text{-}1700\text{ cm}^{-1}$ region partly overlap with the intense Si-O stretch from $1000\text{-}1200\text{ cm}^{-1}$. Though this masks the lower energy C-N absorptions, it is clear that the Schlenk product has higher intensity for the absorptions at higher frequency resembling absorption shapes of TCM more than the C_3N_4 product (see Chapter 2 IR spectra). The ring breathing mode at 800 cm^{-1} is present for each, and a sharp absorption for Si-O bend appears below 500 cm^{-1} .

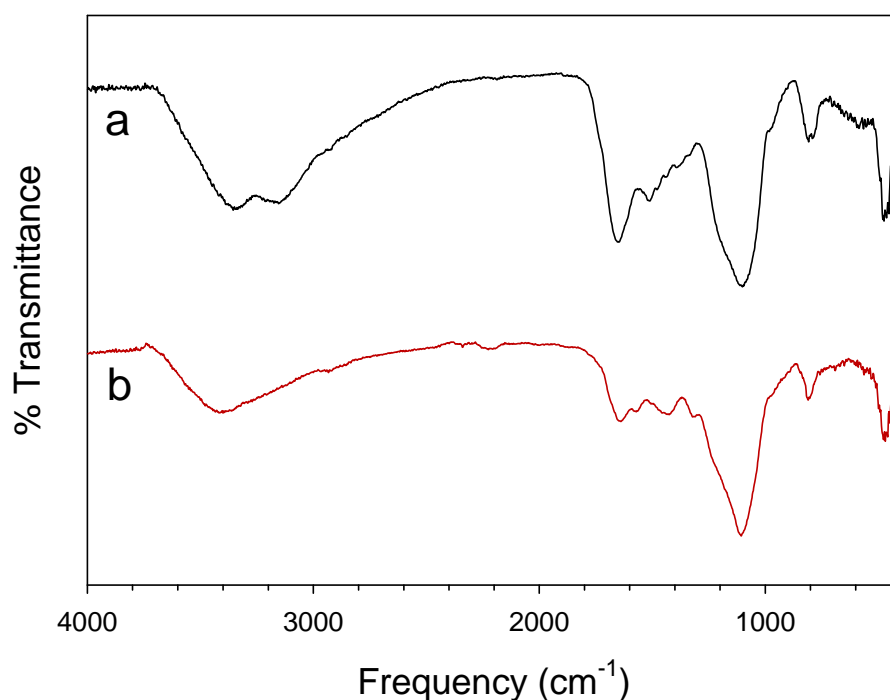


Figure 4.7 – IR spectra of (a) $C_3N_4@SiO_2$ (Schlenk) and (b) $C_3N_4@SiO_2$ (Tube). The large broad peak centered at 1100 cm^{-1} is characteristic of SiO_2 .

The IR spectra of the $C_3N_4@TiO_2$ composites are shown in Figure 4.8. Both spectra feature a single broad N-H stretching absorption above 3100 cm^{-1} . There is some

difference in the relative intensities of the C-N and C=N absorptions in the 1200-1700 cm^{-1} . The absorptions for the Schlenk product are less resolved and higher intensity at the higher frequency end. The tube product has more distinct absorptions in this region, as well as an extended shoulder absorbance towards 1000 cm^{-1} . The ring breathing mode at 800 cm^{-1} is visible for the tube product, but is overshadowed by the Ti-O stretching absorption in the Schlenk product's spectrum.

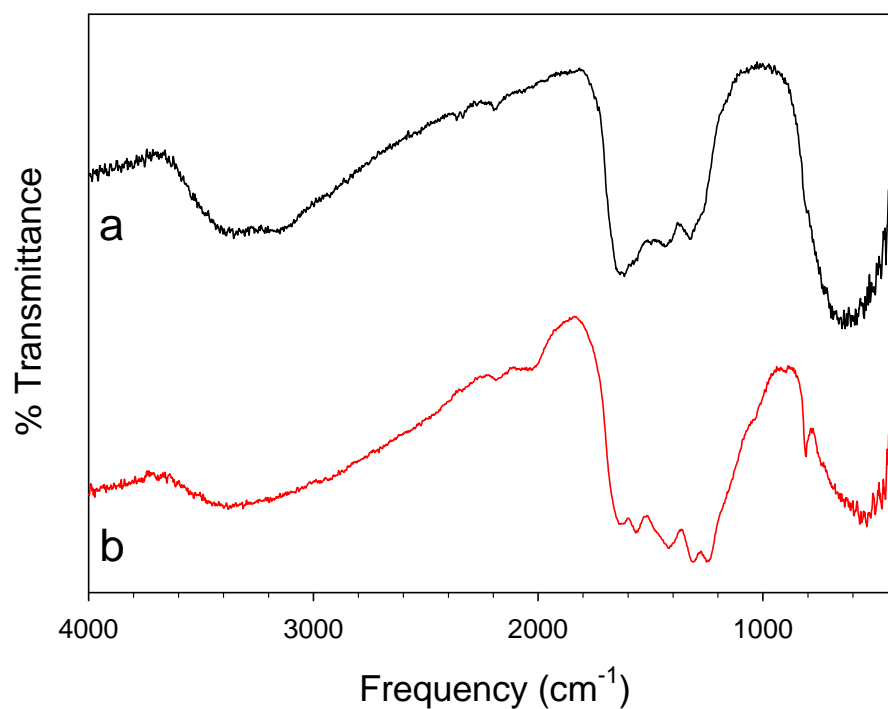


Figure 4.8 – IR spectra of $\text{C}_3\text{N}_4@\text{TiO}_2$ (Schlenk) and (b) $\text{C}_3\text{N}_4@\text{TiO}_2$ (Tube). The large broad peak centered at 800 cm^{-1} is characteristic of TiO_2 .

The IR spectra of the $\text{C}_3\text{N}_4@\text{Al}_2\text{O}_3$ composites are shown in Figure 4.9. The N-H stretching absorptions above 3100 cm^{-1} appeared for each product, though the Schlenk has two absorptions. The relative intensities of the C-N and C=N absorptions in the

1200-1700 cm^{-1} differ significantly for the two products. The Schlenk product has one intense absorption at 1650 cm^{-1} with a broad shoulder feature extending to 1200 cm^{-1} . This higher intensity at 1650 cm^{-1} could either be the result of more TCM like character or from an O-H bend from the hydroxylated Al_2O_3 surface. The tube product has the evenly intense absorptions in this region consistent with the other high-temperature tube products. The large broad absorption from 500-900 cm^{-1} represents Al-O-Al bend and Al-O stretches, and covers the C-N ring mode normally observed at 800 cm^{-1} .¹²¹

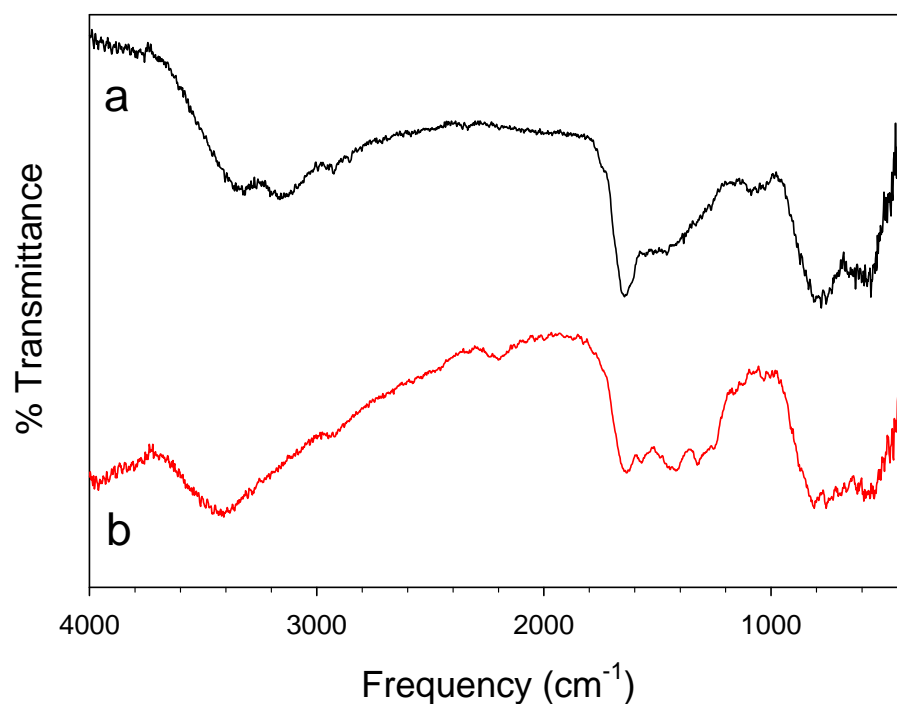


Figure 4.9 – IR spectra of (a) C_3N_4 @(Schlenk) and (b) C_3N_4 @(Tube). The broad absorptions centered at 700 cm^{-1} are characteristic of Al_2O_3 .

The IR spectra of the different C_3N_4 @ WO_3 and WO_3 @ C_3N_4 composites are shown in Figure 4.10. The absorption intensities of C_3N_4 @ WO_3 (anneal) in Figure 4.10b were low due to the need to reduce the sample concentration in the pellet in order to

maintain transmission through the dark product. All products had the broad absorption above 3100 cm^{-1} for N-H stretches. The C-N and C=N absorptions from $1200\text{--}1700\text{ cm}^{-1}$ varied slightly in intensity and shape. The Schlenk product had broader, less resolved absorptions consistent with the other Schlenk C_3N_4 products. The same set of absorptions in Figure 4.10d are fairly sharp, however, since this started with previously synthesized C_3N_4 , no significant changes were expected from only heating to $300\text{ }^\circ\text{C}$. The tube $\text{C}_3\text{N}_4@\text{WO}_3(\text{Tube})$ product is similar to the Schlenk, though there is an extended shoulder absorbance towards 1000 cm^{-1} . The 800 cm^{-1} ring absorption is visible in each, but is partially overlapped with the O-W-O stretching at lower frequency.¹¹⁸

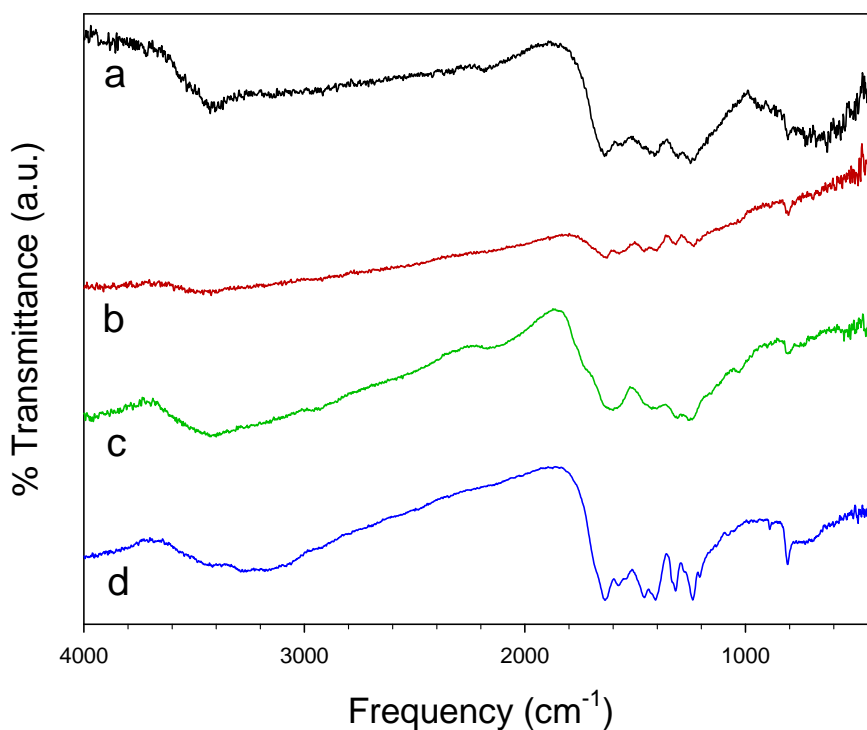


Figure 4.10 – IR spectra of (a) $\text{C}_3\text{N}_4@\text{WO}_3$ (Schlenk) (b) $\text{C}_3\text{N}_4@\text{WO}_3(\text{anneal})$ (c) $\text{C}_3\text{N}_4@\text{WO}_3(\text{Tube})$, and (d) $\text{WO}_3@\text{C}_3\text{N}_4$.

Powder XRD patterns for the $C_3N_4@SiO_2(\text{Tube})$, $C_3N_4@TiO_2(\text{Tube})$, and $C_3N_4@Al_2O_3(\text{Tube})$ products are shown in Figure 4.11. The $C_3N_4@TiO_2$ composite shows primarily anatase with some rutile TiO_2 . The first peak for rutile overlaps with where the major C_3N_4 peak would be, however the peak for crystalline TiO_2 phase is much more intense and the C_3N_4 peak is lost in the background. The $C_3N_4@SiO_2$ pattern shows the C_3N_4 peak 27.5 degrees on the shoulder of the broad peak for amorphous SiO_2 near 20 degrees. The C_3N_4 peak is also visible in the $C_3N_4@Al_2O_3$ composite, while the remaining broad peaks fit to nanoscale $\gamma-Al_2O_3$.

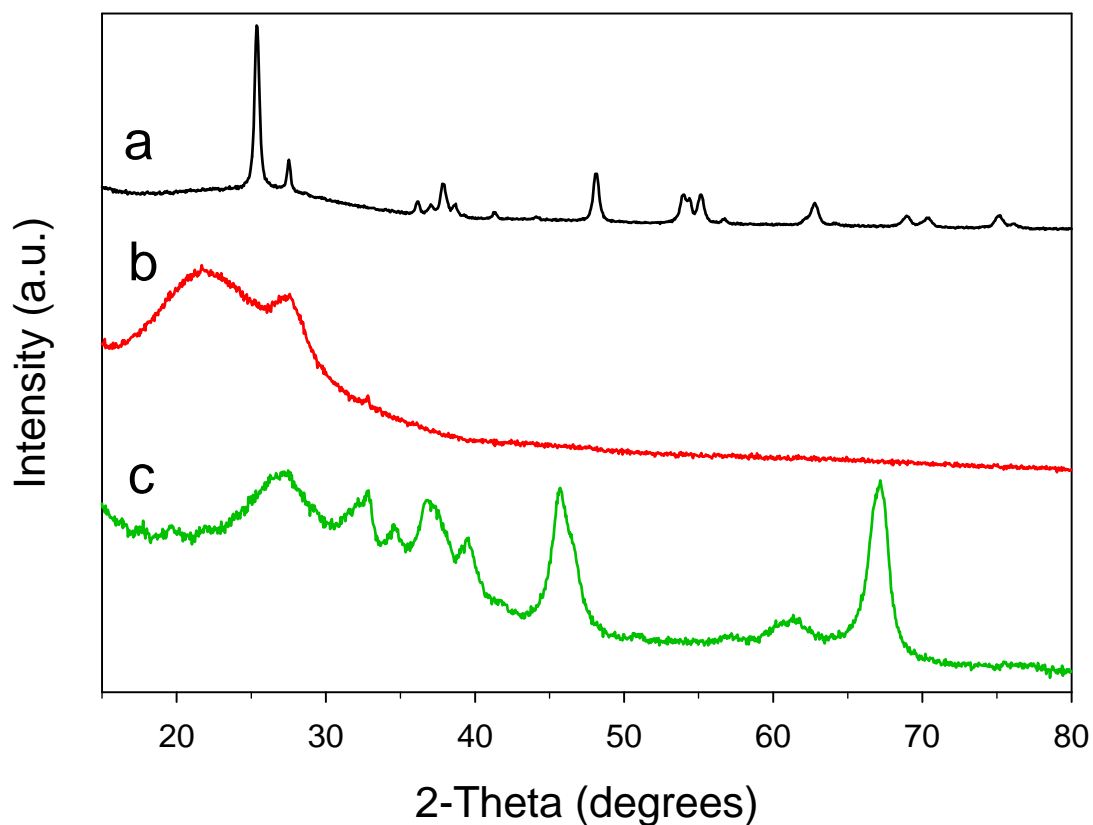


Figure 4.11 – XRD patterns of (a) $C_3N_4@TiO_2(\text{Tube})$, (b) $C_3N_4@SiO_2(\text{Tube})$, and (c) $C_3N_4@Al_2O_3(\text{Tube})$.

The XRD patterns for the $C_3N_4@WO_3$ and $WO_3@C_3N_4$ products are shown in Figure 4.12. The low temperature $C_3N_4@WO_3$ (Schlenk) product (Figure 4.12a) and $WO_3@C_3N_4$ product (Figure 4.12d) both show monoclinic phase WO_3 . The peak for carbon nitride at 27.5 degrees is visible only in the product from $WO_3@C_3N_4$. Since this product started with premade C_3N_4 , the structure was already well formed, having this clearly resolved peak. The $C_3N_4@WO_3$ (Schlenk) product, starting with TCM to form C_3N_4 around WO_3 , may not have grown as well ordered around the oxide support. The $C_3N_4@WO_3$ (anneal) (Figure 4.12b) and $C_3N_4@WO_3$ (Tube) (Figure 4.12c) show the formation of a different phase. This phase was found to match hydrogen tungsten bronze ($H_{0.23}WO_3$). The amount of hydrogen can vary in these H_xWO_3 structures ($0.1 < x < 0.6$), which have previously been prepared by heating above 400 °C under hydrogen,¹²² milling under high pressure hydrogen atmosphere,¹²³ or electrodeposition from Na_2WO_4 in H_2SO_4 .¹²⁴ H_xWO_3 products are described as dark blue or black versus the yellow WO_3 , which is consistent with the dark color of these products. Since it is known that C_3N_4 transports NH_4Cl as a by-product when annealed, this hydrogen incorporation into the structure of WO_3 may come from volatile NH_3 or HCl .

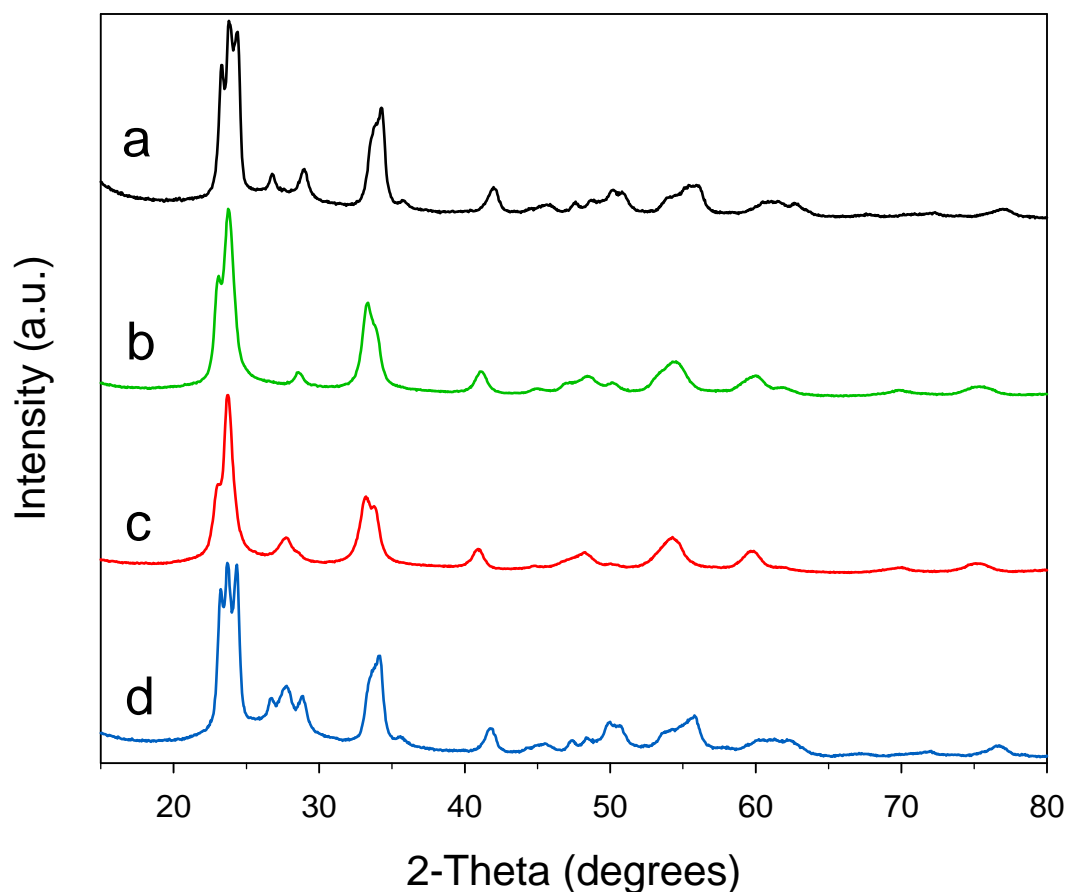


Figure 4.12 – XRD patterns of (a) C₃N₄@WO₃(Schlenk), (b) C₃N₄@WO₃(anneal), (c) C₃N₄@WO₃(Tube), and (d) WO₃-C₃N₄.

Morphology and surface area

The morphologies of the C₃N₄ composites were investigated with SEM. The C₃N₄@SiO₂(Tube) composite (Figure 4.13A) shows a cluster of 3-5 μm aggregates. Compared to unmodified C₃N₄, the composite had a very rough surface with small particle features less than 200 nm. The C₃N₄@Al₂O₃(Tube) composite (Figure 4.13B) shows a 5 μm aggregate particle. This has a similar rough surface as the C₃N₄@SiO₂(Tube) composite, though the smaller 100-300 nm particulate features are more distinct. The C₃N₄@TiO₂(Tube) composite (Figure 4.nC,D) shows a 10 μm

aggregate. The smaller segments are more irregularly shaped and feature void spaces as small as 100 nm in diameter. The walls of these pieces are smoother, and small individual particles are not distinguishable as in the $C_3N_4@SiO_2$ (Tube) and $C_3N_4@Al_2O_3$ (Tube) composites. The $WO_3@C_3N_4$ composite (Figure 4.13E) was made up of particles varying in size from 400 nm to 2 μ m. These pieces appear dense, with no pores, and aggregate in 5-10 μ m clusters. The $C_3N_4@WO_3$ (Tube) composite (Figure 4.13F) formed aggregates 10 μ m and larger. These had very rough surface features including 150-300 nm particles on extended surfaces and 300-500 nm pores along edges.

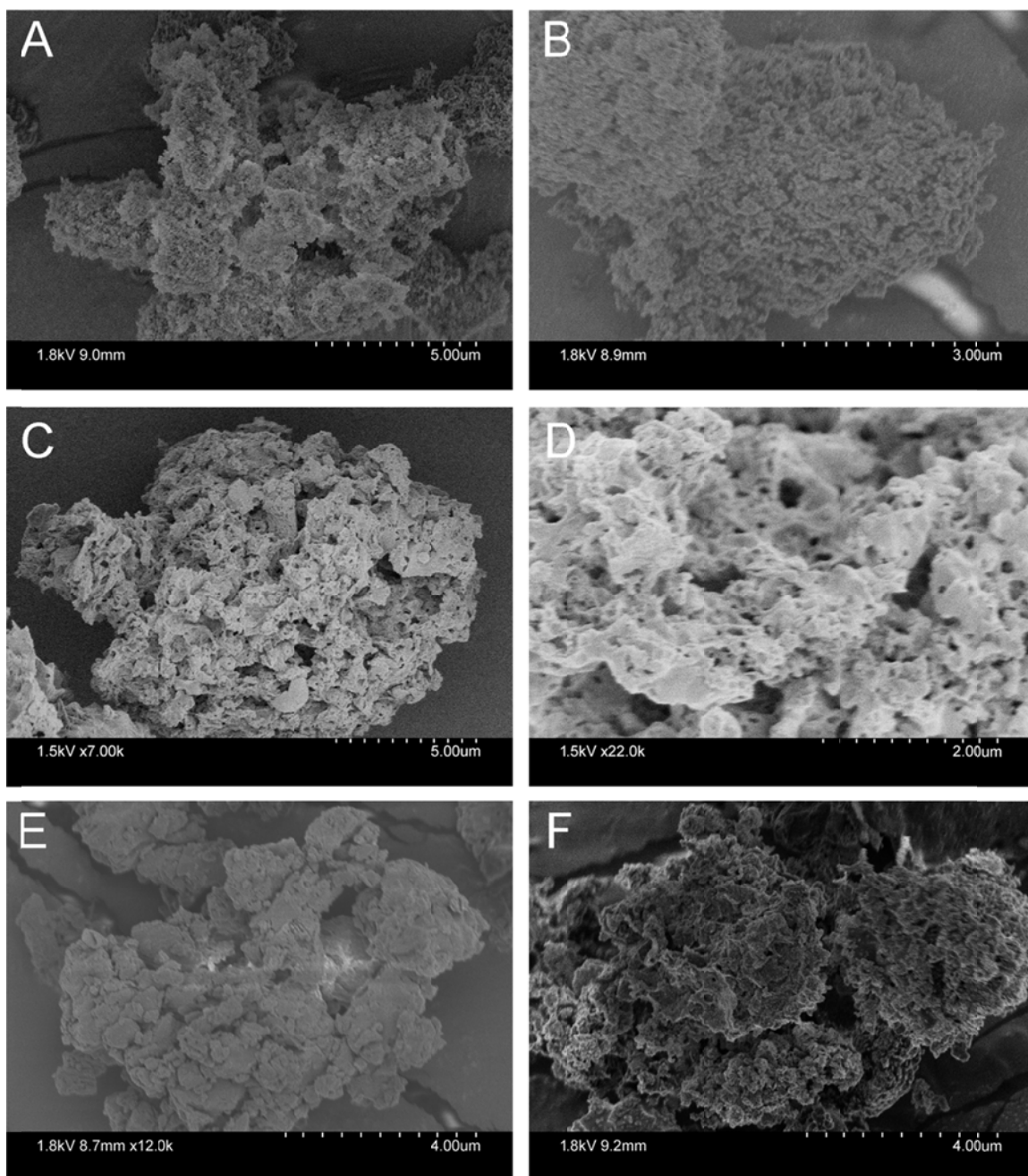


Figure 4.13 – SEM images of (A) $C_3N_4@SiO_2$ (Tube), (B) $C_3N_4@Al_2O_3$ (Tube), (C, D) $C_3N_4@TiO_2$ (Tube), (E) $WO_3@C_3N_4$, and (F) $C_3N_4@WO_3$ (Tube).

Physical mixtures of C_3N_4 with TiO_2 and WO_3 were prepared by ball milling. The physically-mixed C_3N_4 - TiO_2 composite (Figure 4.14A,B) featured a large 5-10 μm aggregate. This had some small 1-2 μm segments and had particles visibly embedded on

the surface. Figure 4.14B gives a higher magnification of these 100-200 nm particles embedded on a very contoured wall. The physical C_3N_4 - WO_3 composite (Figure 4.14C,D) showed highly textured 1-4 μm segments on a larger aggregate. Figure 4.14D gives a close view of the disordered thin 100 nm plates of WO_3 . These plates appear to be embedded on a wall made up of C_3N_4 particles.

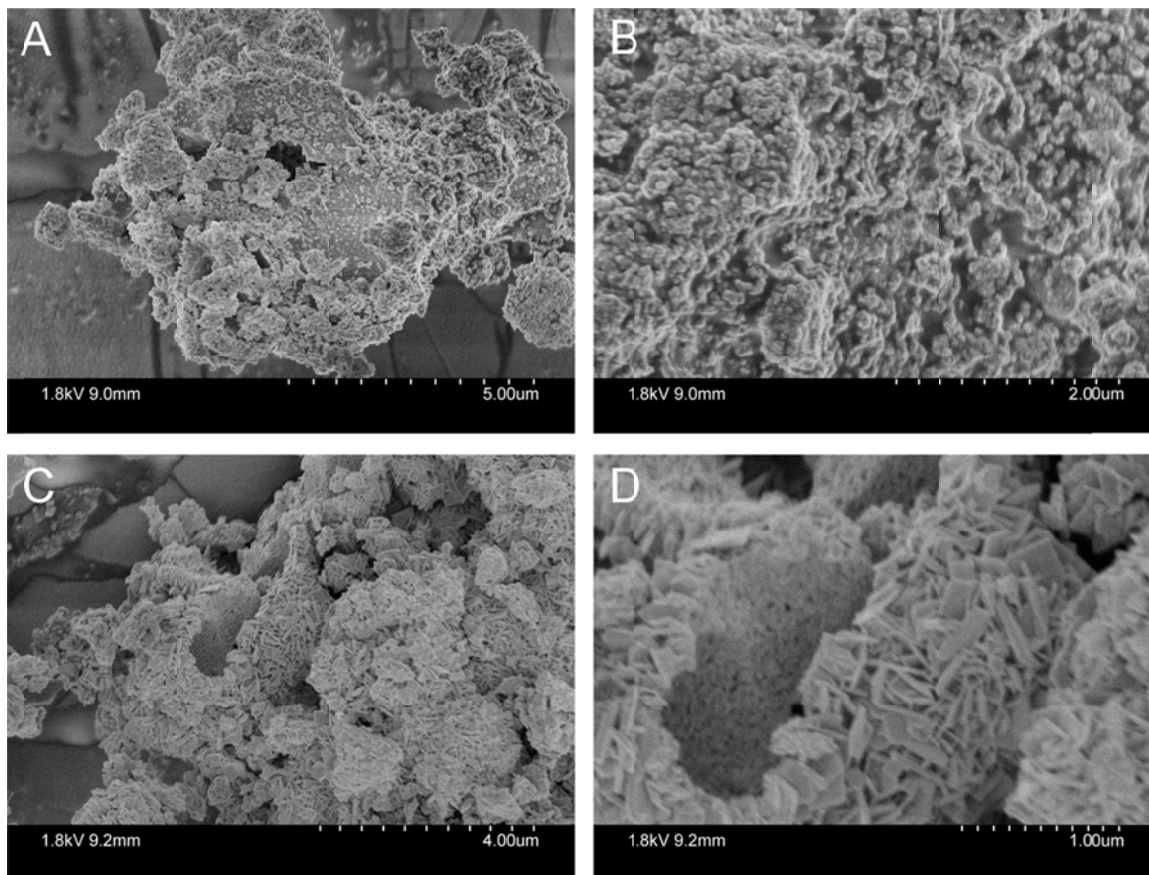


Figure 4.14 – SEM images of ball milled (A, B) C_3N_4 - TiO_2 and (C, D) C_3N_4 - WO_3 .

The BET surface area for oxide products from tube reactions are summarized in Table 4.2 and compared to the bare metal oxides. While these oxide-supported composites had a higher surface area C_3N_4 material, the growth of C_3N_4 as a coating around the oxide reduced its natural surface area. This reduction in surface area was

roughly by a factor of three for each of the oxides. This loss could be dependent on how thick the C_3N_4 coating on the oxide surface was.

Table 4.2. BET surface areas of C_3N_4 -metal oxide composites.

Product	Composite Surface Area ($m^2 g^{-1}$)	Oxide Surface Area ($m^2 g^{-1}$)
$C_3N_4@SiO_2$ (Tube)	135.1	300
$C_3N_4-Al_2O_3$ (Tube)	33.7	100
$C_3N_4-TiO_2$ (Tube)	16.3	44.8

Optical properties

The optical absorption properties and band gaps of the composite materials were explored with UV-vis diffuse reflectance spectroscopy and compared with those of bare C_3N_4 , TiO_2 , and WO_3 (Figure 4.15A and B). The raw reflectance data (Figure 4.16A) showed some level of increased reflectance for wavelengths above 380 nm, except for the $C_3N_4-H_xWO_3$ sample due to its very dark color. The reflectance data was converted into absorbance data using the Kubelka-Munk function and plotted against energy to give the Tauc Plot (Figure 4.16B). The indirect band gaps (E_g) can be approximated by extrapolating the linear region of the absorption edge to the energy axis (in eV). The E_g values for $C_3N_4@SiO_2$, $C_3N_4@Al_2O_3$, $C_3N_4@TiO_2$, and $WO_3@C_3N_4$ were 2.3, 2.45, 2.7, and 2.25 eV respectively. These values are lower than the component semiconducting metal oxides and comparable or slightly lower than bare C_3N_4 . $C_3N_4@WO_3$ (Tube) does not have a clear absorption edge in the range measured. H_xWO_3 is known to be a

conducting material, and its high visible light absorbance overshadows the contribution of C_3N_4 by this measurement.

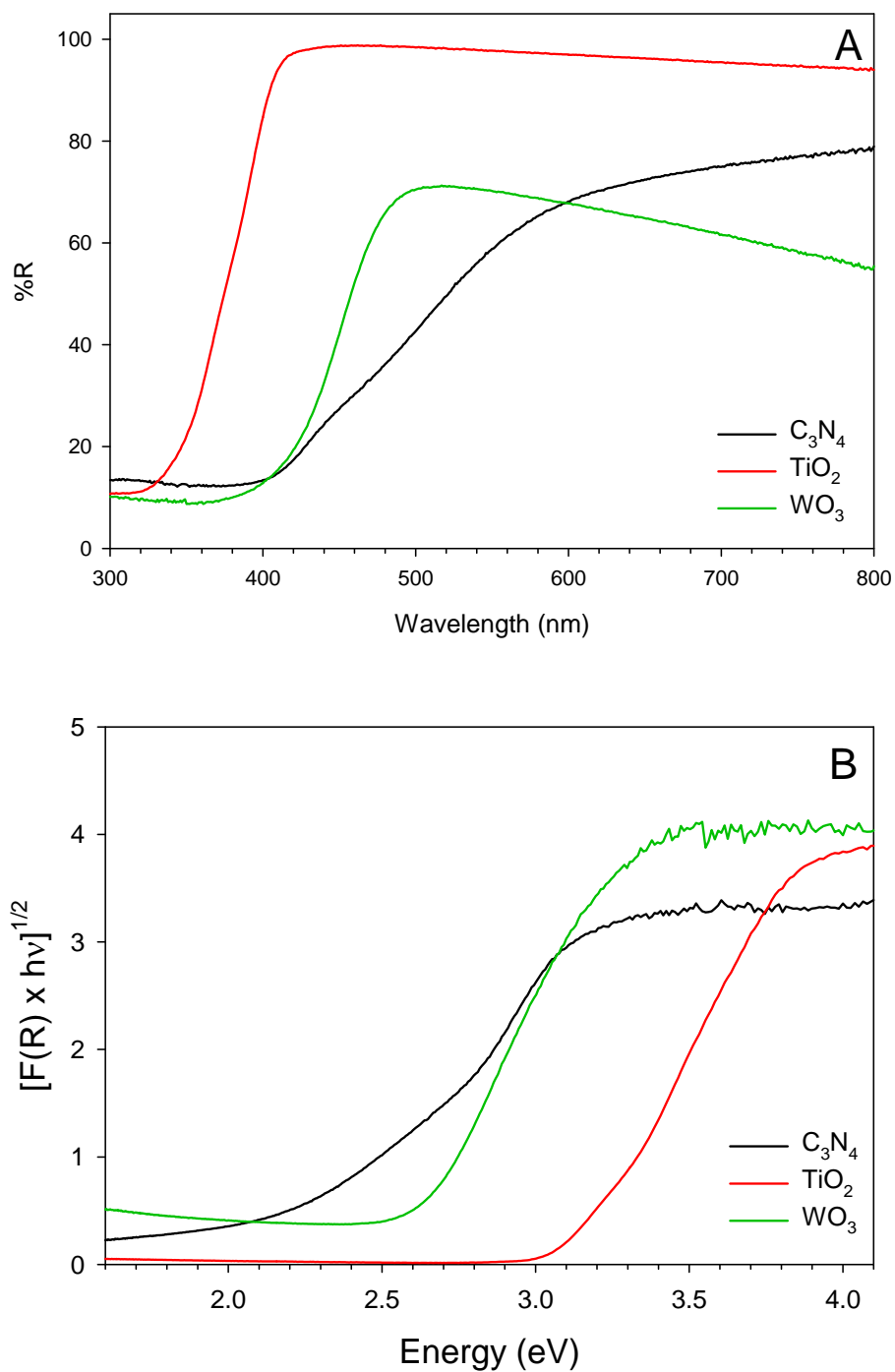


Figure 4.15 – UV-vis DRS data for C_3N_4 , TiO_2 , and WO_3 (A) reflectance spectra and (B) Tauc plots.

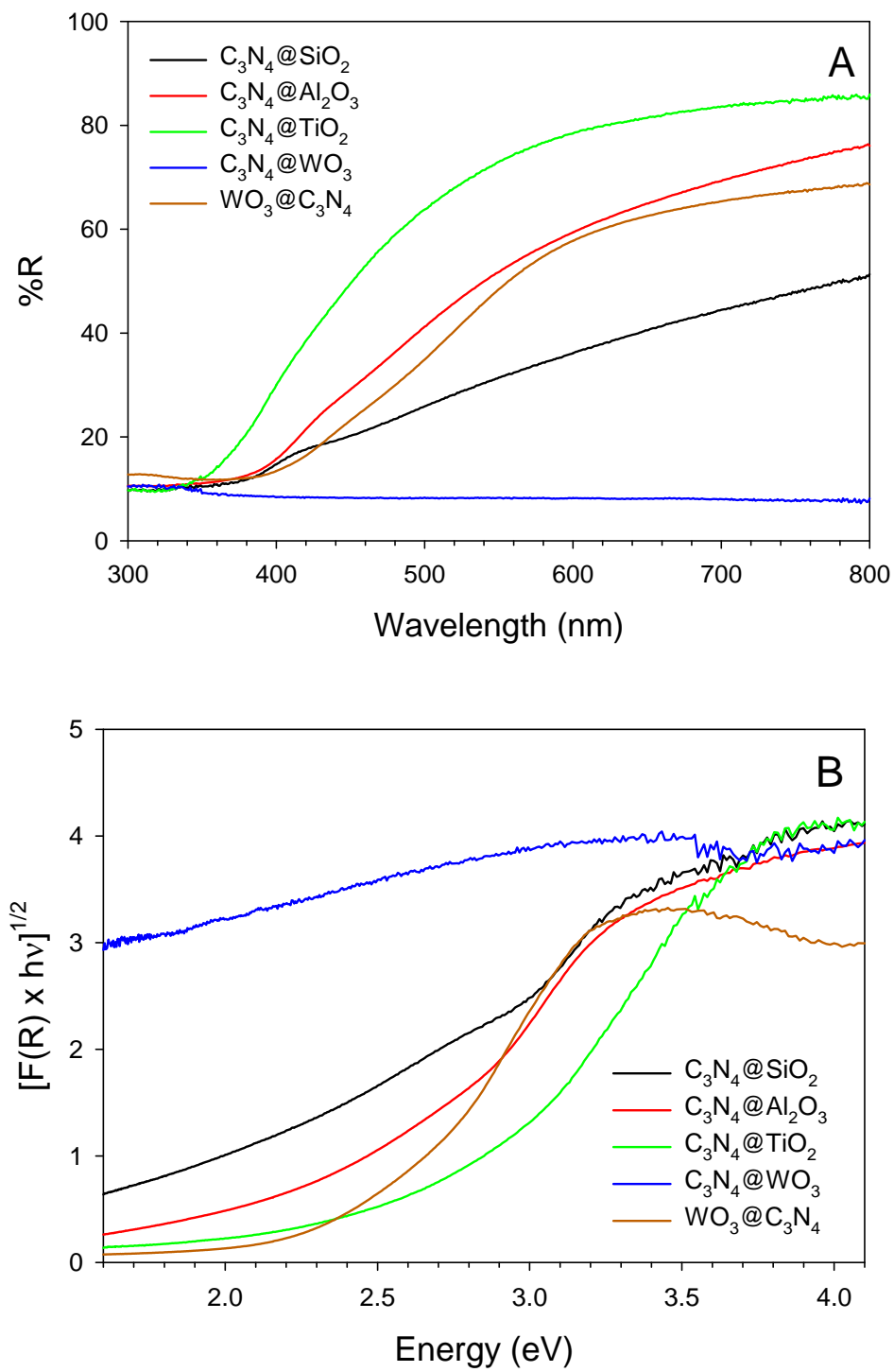


Figure 4.16 – UV-vis DRS data for C_3N_4 -metal oxide composites (A) reflectance spectra and (B) Tauc plots.

*Photocatalytic studies*Photocatalytic dye oxidation

The degradation of methyl orange dye was studied with the tube products of the C_3N_4 -metal oxide composites. Figure 4.17 shows the UV light oxidative degradation in air of methyl orange with each composite. These samples absorbed different amount of the dye during the dark stir, up to 50% for $C_3N_4@Al_2O_3$ and $C_3N_4@WO_3$, nearly 30% for $C_3N_4@SiO_2$, and less than 20% for $C_3N_4@TiO_2$ and $WO_3@C_3N_4$. Bare SiO_2 and Al_2O_3 were stirred in the dye solution to test if this high degree of absorption was just a factor of their high surface areas. After allowing these to stir for up to 2 hours, Al_2O_3 absorbed less than 5% and SiO_2 absorbed 15%. The extra absorption on the composites must be due to the combination of high surface area and the presence of C_3N_4 . This could be from interactions with residual amino functional groups on C_3N_4 . Accounting for the dark absorption, the $C_3N_4@SiO_2$ and $C_3N_4@Al_2O_3$ composites still had the highest activity, reaching less than 10% dye remaining by 45 minutes. The $C_3N_4@TiO_2$, $WO_3@C_3N_4$, and $C_3N_4@WO_3$ reached 40%, 50%, and 30% dye remaining, respectively, after 2 hours of total UV illumination. Comparing the rates (Table 4.3 and Figure 4.17B), $C_3N_4@Al_2O_3$ is slightly higher than $C_3N_4@SiO_2$ and 7-8 times more active than the remaining composites.

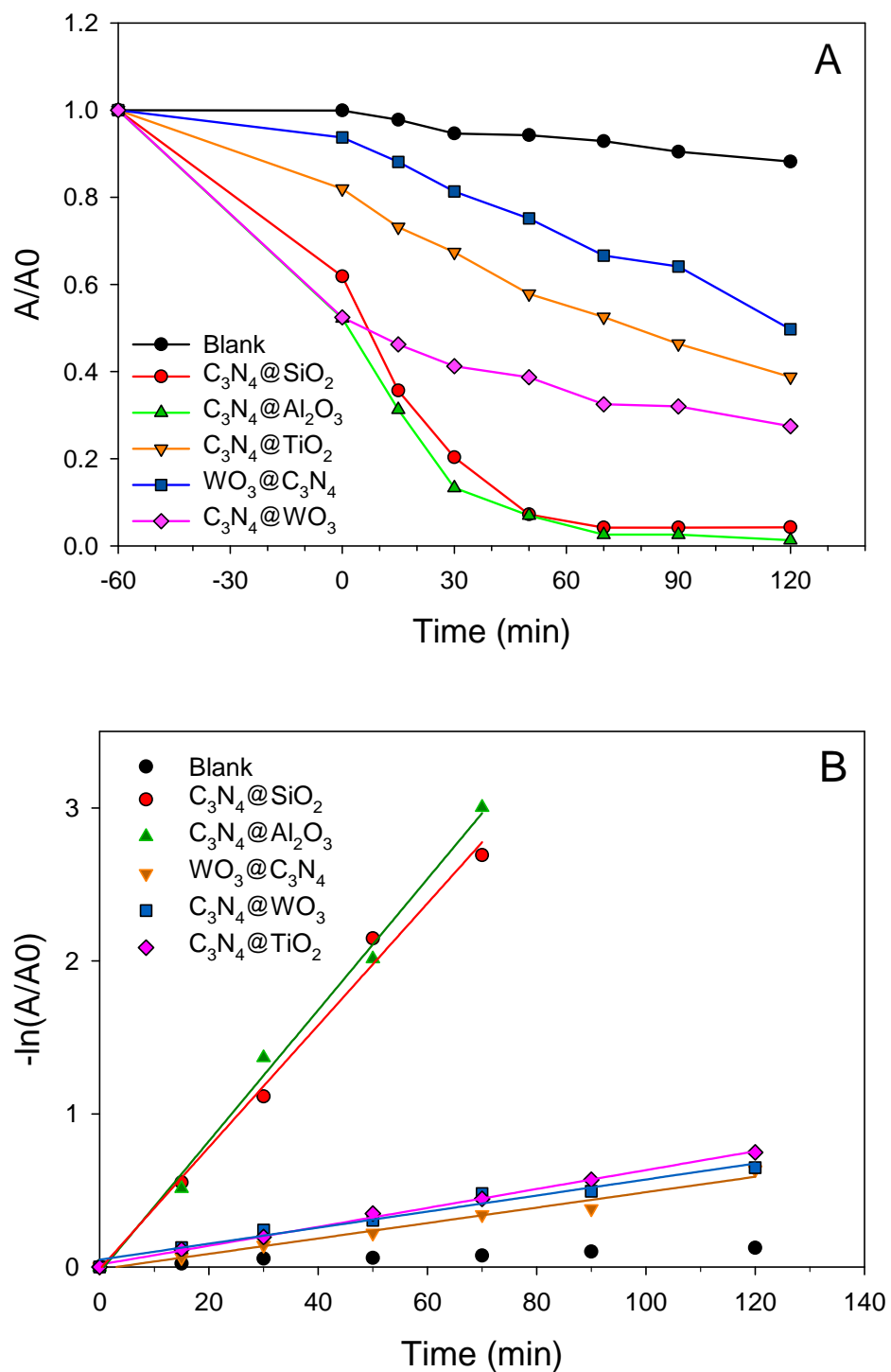


Figure 4.17 – UV-vis analysis of photodegradation of MO dye (A) UV light data and (B) UV linear rate data.

Visible light degradation using the same catalysts was tested using 400 nm cut-off filters. Dark absorption behavior was similar, though $C_3N_4@SiO_2$ only absorbed near 30% of the initial dye in this test. Total activity was lower using visible light, with samples ranging from 10-40% decrease in dye concentration after 150 minutes of illumination. In contrast, $C_3N_4@TiO_2$ maintained a visible rate similar to what was observed under UV light (Figure 4.18B and Table 4.3). The remaining rates decreased from $C_3N_4@Al_2O_3$, $C_3N_4@SiO_2$, $C_3N_4@WO_3$, and $WO_3@C_3N_4$.

Table 4.3. Rate constants (min^{-1}) for UV and visible light degradation of methyl orange dye using C_3N_4 -metal oxide composites.

	$C_3N_4@SiO_2$	$C_3N_4@Al_2O_3$	$C_3N_4@TiO_2$	$WO_3@C_3N_4$	$C_3N_4@WO_3$
UV	0.0399 ($R^2 = 0.992$)	0.0429 ($R^2 = 0.994$)	0.0062 ($R^2 = 0.998$)	0.0052 ($R^2 = 0.970$)	0.0050 ($R^2 = 0.979$)
Visible (>400 nm)	0.0033 ($R^2 = 0.980$)	0.0045 ($R^2 = 0.999$)	0.0063 ($R^2 = 0.982$)	0.0004 ($R^2 = 0.43$)	0.0025 ($R^2 = 0.86$)

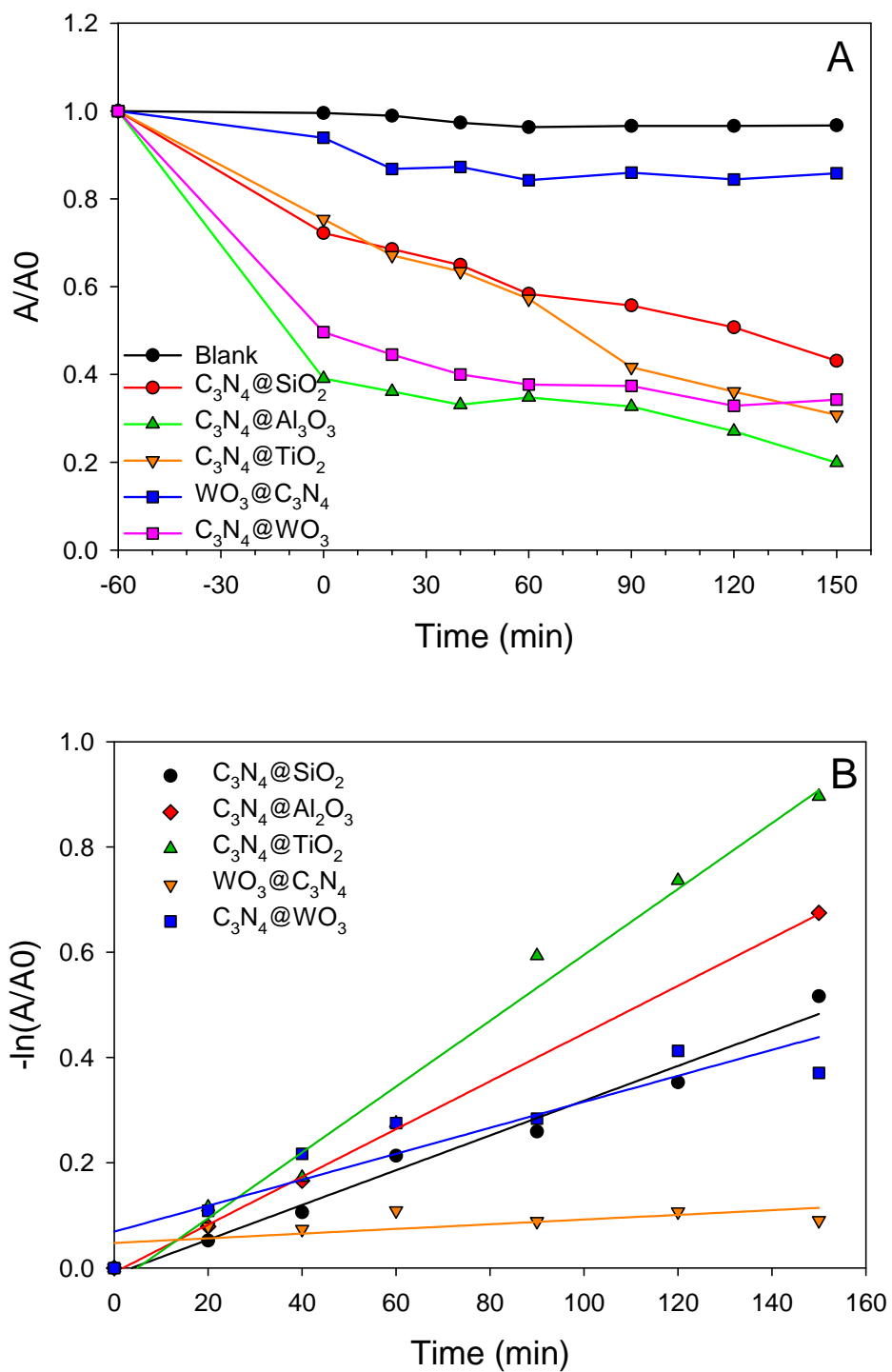


Figure 4.18 – UV-vis analysis of photodegradation of MO dye (A) visible light data and (B) visible linear rate data.

The UV and visible light degradation of methyl orange were also tested using ball milled mixtures of C_3N_4 with TiO_2 or WO_3 . The milled composites showed slightly higher dark absorption of the dye, nearing a 15-20% loss compared to 5% for unmodified C_3N_4 . Since the composites were milled, they were finer powders than the C_3N_4 used in this experiment, giving more potential surface sites for the dye to adsorb. The C_3N_4 - TiO_2 composite was most active, reaching less than 10% of dye remaining by 100 minutes of illumination. The C_3N_4 - WO_3 reduced the dye concentration to 20%, and C_3N_4 made it to 40% in the same time. The plots for the linear rate fits and rate constants are shown in Figure 4.19B and Table 4.4. Since TiO_2 benefits from higher activity under UV light due to its band gap (3.2 eV), its having the highest rate is unsurprising.

The visible light experiment is shown in Figure 4.20A. The dark absorption varied slightly from the UV experiment, with each milled composite showing only a 10% loss. After 150 minutes of visible light illumination, each composite reached 70% of dye remaining, while C_3N_4 reached 20%. The rate fits and rate constants are shown in Figure 4.20B and Table 4.4. C_3N_4 - TiO_2 and C_3N_4 - WO_3 had identical visible light rates, which were 6.6% of the UV rate for C_3N_4 - TiO_2 and 14.6% of the rate for C_3N_4 - WO_3 . The rate for C_3N_4 was 17.0% of its UV activity.

Table 4.4. Rate constants (min^{-1}) for UV and visible light degradation of methyl orange dye using C_3N_4 and milled C_3N_4 -metal oxide composites.

	C_3N_4 (Parr)	C_3N_4 - TiO_2	C_3N_4 - WO_3
UV	0.0094 ($R^2 = 0.986$)	0.0317 ($R^2 = 0.988$)	0.0144 ($R^2 = 0.992$)
Visible (>400nm)	0.0016 ($R^2 = 0.993$)	0.0021 ($R^2 = 0.984$)	0.0021 ($R^2 = 0.980$)

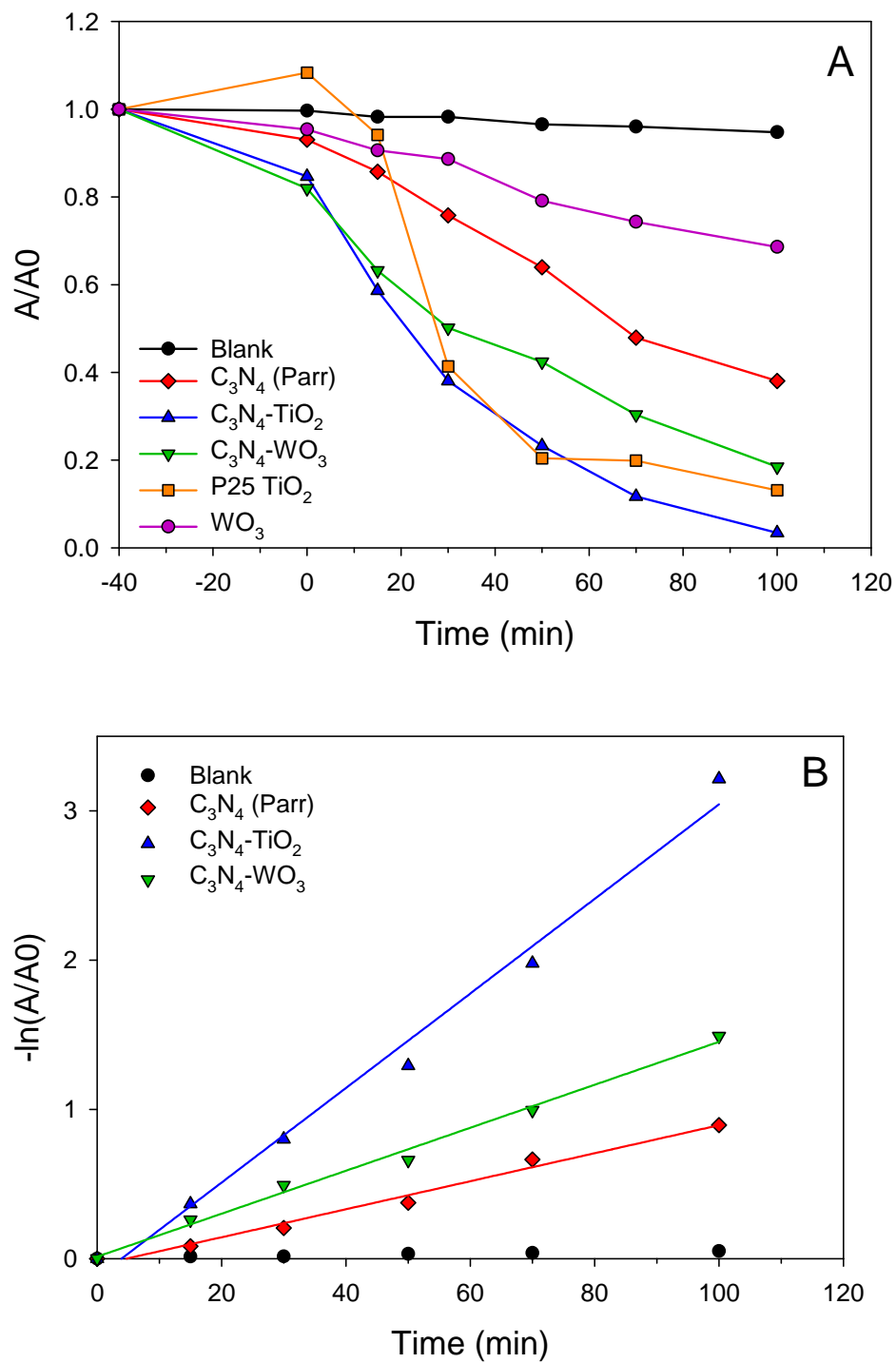


Figure 4.19 – UV-vis analysis of photodegradation of MO dye using milled C_3N_4 - TiO_2 and C_3N_4 - WO_3 composites (A) UV light data and (B) UV linear rate data.

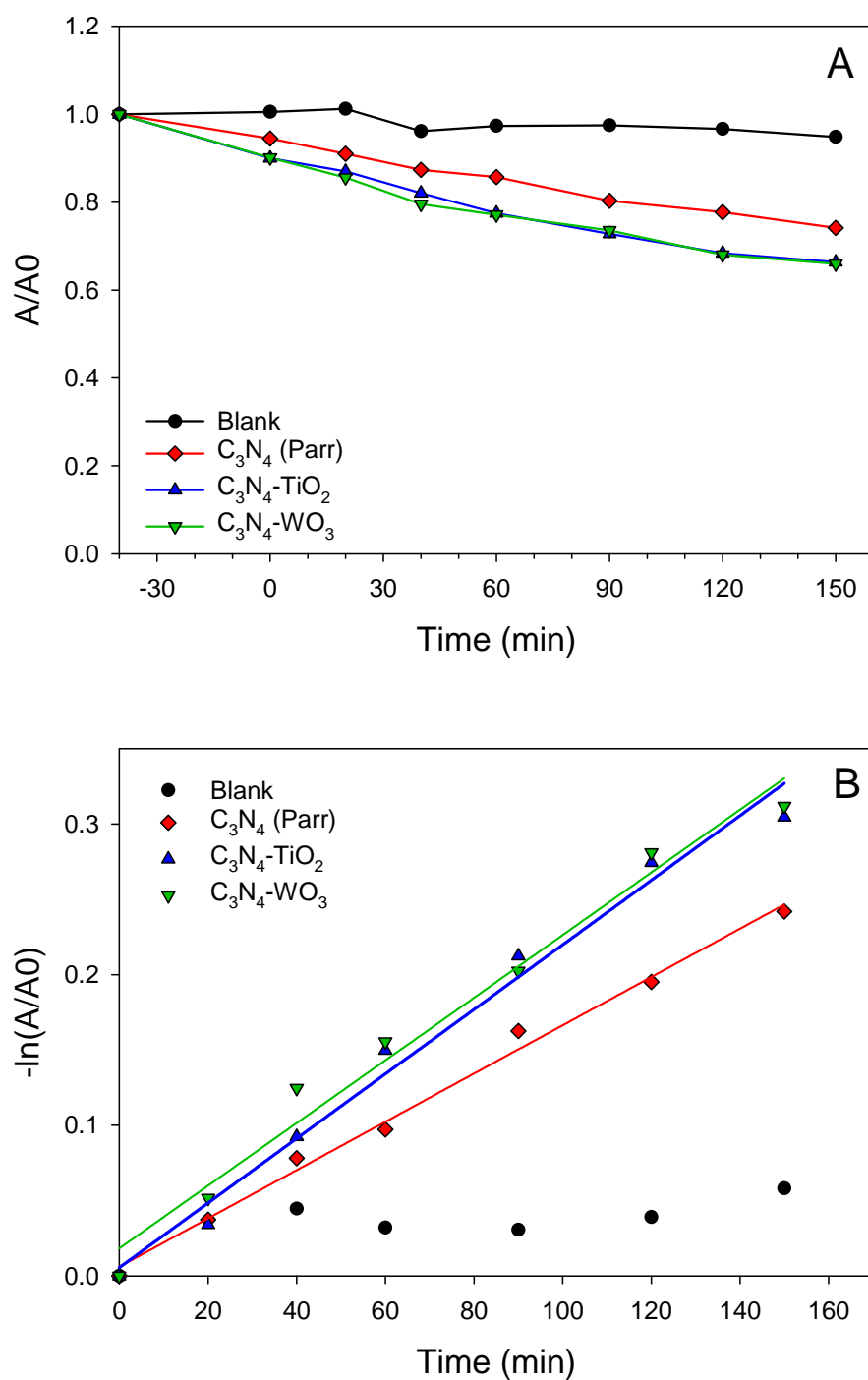


Figure 4.20 – UV-vis analysis of photodegradation of MO dye using C_3N_4 - TiO_2 (milled) and C_3N_4 - WO_3 (milled) composites (A) visible light data and (B) visible linear rate data.

Photocatalytic hydrogen evolution via water-splitting

Photocatalytic hydrogen evolution tests using C₃N₄-metal oxide composites contained a target 1 wt% platinum as co-catalyst. The tests used RGA-MS to monitor the amount of hydrogen produced in real time. Figure 4.21 shows the activity for C₃N₄@TiO₂(Tube) over 4 1 hour illumination cycles. The activity remained stable from cycle to cycle and did not exhibit a first hour activation step like other C₃N₄ products described in the previous chapters. The rate of 190 μmol h⁻¹ g⁻¹ for C₃N₄@TiO₂(Tube) was nearly 3 times that of C₃N₄ without a support, but significantly lower than the activity of unmodified P25 TiO₂ (Table 4.5). Since C₃N₄ was formed on the surface of TiO₂, it is likely blocking the UV photons from being absorbed by TiO₂. In this case, C₃N₄ would be the primary light absorber, and any charge transferred to the TiO₂ core would not be accessible to facilitate hydrogen reduction. The increased activity over unsupported C₃N₄ could be from a smaller contribution from TiO₂ or a result of the surface area increase.

Table 4.5. Average hydrogen evolution rates for 1 wt% Pt deposited TiO₂, C₃N₄, and C₃N₄-metal oxide composites over 4 1-hour cycles (standard deviation reported in parentheses).

Sample	H ₂ Rate (μmol h ⁻¹ g ⁻¹)
P25 TiO ₂	20,000 (1,400)
C ₃ N ₄ (Tube)	68 (8)
C ₃ N ₄ @TiO ₂ (Tube)	190 (11)
C ₃ N ₄ -TiO ₂ (mill)	106 (38)
C ₃ N ₄ @SiO ₂ (Tube)	44 (14)
C ₃ N ₄ @Al ₂ O ₃	0

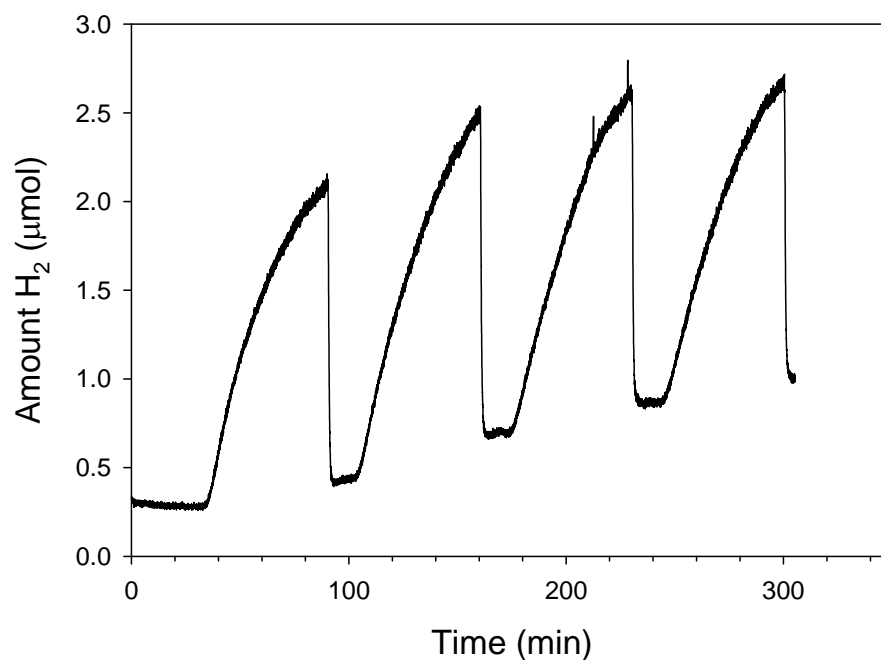


Figure 4.21 – Photocatalytic hydrogen evolution using $C_3N_4@TiO_2$ (Tube) with 1% Pt co-catalyst. The UV lamp was turned on for 1 hour cycles and the reactor was purged with argon for 10 minutes between each cycle.

The ball-milled $C_3N_4-TiO_2$ mixture was less active than the surface-coated $C_3N_4@TiO_2$ with a rate of $110 \mu\text{mol h}^{-1} \text{g}^{-1}$ (Table 4.5). This was still an improvement over unsupported C_3N_4 , but remained much less than the activity of TiO_2 . This physical mixture was prepared with a 2:1 ratio of C_3N_4 to TiO_2 . While it should be an intimate mixture, it is possible that the particles of TiO_2 embedded into C_3N_4 . This could mask the ability of TiO_2 to absorb light as in the case with $C_3N_4@TiO_2$.

The $C_3N_4@SiO_2$ (Tube) and $C_3N_4@Al_2O_3$ (Tube) product showed a decrease in activity compared to the unsupported C_3N_4 , with a rate of $44 \mu\text{mol h}^{-1} \text{g}^{-1}$ and no hydrogen production observed respectively (Table 4.5). Unlike the TiO_2 composites, both SiO_2 and Al_2O_3 are photochemically inert, so any enhancement activity would be solely linked to their increased surface areas. The surface of these products was shown to

be much higher than unsupported C_3N_4 in Table 4.2. These products were from the 500 °C tube reactions and, based on IR and elemental analysis, should be fully formed C_3N_4 . Their band gaps were also in the range of some of the products shown in Chapter 2. The presence of these oxides may have interfered with successful surface deposition of platinum. The absence or diminished amount of co-catalyst could account for a drop in activity of these samples.

4.4 Conclusions

This chapter has described the synthesis of C_3N_4 on the surface of several metal oxide supports (SiO_2 , Al_2O_3 , TiO_2 , and WO_3) and the synthesis of WO_3 on a C_3N_4 support. Low temperature synthesis conditions in the Schlenk reactor set-up yielded poorly-formed products, which had difficulty initiating the decomposition. Heating the coated precursors in the 500 °C tube reactor showed more typical reactions, and gave products with properties similar to unsupported C_3N_4 . Heating C_3N_4 with WO_3 under these conditions led H_xWO_3 , hydrogen tungsten bronze, from the reaction between WO_3 with hydrogen containing volatiles. Because of this, the alternate approach to prepare WO_3 on a C_3N_4 support was used. Photocatalytic activity was evaluated for both the degradation of methyl orange dye and hydrogen evolution. The high surface area $C_3N_4@SiO_2$ and $C_3N_4@Al_2O_3$ showed a high degree of surface adsorption for the dye, not matched by either of the individual components. The higher amount of surface adsorption seemed to contribute to the UV light degradation activity for these to composites. By strongly adsorbing to the C_3N_4 surface, the dye could be more readily oxidized.

CHAPTER 5

ENHANCED PHOTOCATALYSIS OF TRANSITION-METAL SURFACE-MODIFIED TITANIUM DIOXIDE

5.1 Introduction

Titanium dioxide (TiO_2) is a well-studied semiconducting material for photocatalysis and has promise in solar energy conversion.^{37-38, 40, 42} Anatase TiO_2 ($E_g = 3.2$ eV) can perform the photolysis of water into hydrogen and oxygen gases in an electrochemical cell.³⁹ The deposition of platinum metal on the surface of anatase TiO_2 forms a highly-active UV photochemical water-splitting catalyst.^{46-47, 125} Platinum metal regions on titania act as a surface catalyst that funnel photoexcited TiO_2 conduction band electrons to protons in solution, that are then reduced to H_2 . In these types of photocatalytic reactions, a sacrificial oxidant is needed to remove photogenerated holes from the semiconductor's valence band and maintain overall charge balance.¹²⁶⁻¹²⁷ However, even in low ~ 1 wt% co-catalyst concentrations, platinum has disadvantages related to its high cost and low abundance.

There are extensive efforts to improve the photochemical properties of TiO_2 -based materials that do not involve noble metal co-catalysts and also may enable absorption of solar radiation for water-splitting hydrogen production.¹²⁸ A wide range of metals (Cu,¹²⁹⁻¹³⁰ Ni,¹³¹ Co,¹³² Cr, Fe, Mo, V, and W¹³³) and non-metals (N,¹³⁴ F,¹³⁵ P,¹³⁶ S¹³⁷) have been doped into the bulk structure of TiO_2 by solution or solid-state methods in order to modify the bulk titania band structure and improve visible light absorption or electron-hole charge recombination kinetics. Most prior work has used gas phase H_2 or solution phase NaBH_4 reduction of metal ions mixed with TiO_2 precursors. Previous

work by Coleman from our group incorporated ~5-10 at% of several 3d metals into rutile TiO₂ via exothermic solid-state metathesis reactions.¹³⁸ These metathesis-derived titanias showed lower photoactivity versus undoped materials, though the 3d metals gave visible color to the products. Modifying TiO₂ with two metals in its bulk structure, such as Co-Ni or Cu-Ce, has been studied for photocatalytic applications in dye degradations and water-splitting.¹³⁹⁻¹⁴⁰ CuO coatings or intimate copper oxide mixtures with TiO₂ exhibit partial reduction of the copper oxide during observed enhanced photocatalytic hydrogen evolution.¹⁴¹⁻¹⁴²

Photodeposition has been utilized for removal of metal ions from aqueous environments with semiconducting WO₃ or TiO₂ as photoactive substrates.^{48, 50, 143-146} In addition to environmental remediation, photo-assisted deposition can also function as a potentially facile, low-temperature method to modify photoactive surfaces such as TiO₂ with metal or metal oxide co-catalysts.⁴⁷ Copper and nickel have shown promise as photodeposited co-catalysts or *in-situ* catalysts for photocatalytic hydrogen evolution using high surface area titania nanotubes or mesoporous structures.¹⁴⁷⁻¹⁴⁹

This Chapter describes the UV photodeposition of several 3d metals (Mn, Fe, Co, Ni, Cu) onto the surface of photoactive commercial Degussa P25-TiO₂ (primarily anatase) using a method analogous to noble metal (*e.g.*, Ag, Pt) photoreduction processes, and is an expansion of published work.⁸⁸ The bulk titania structure and particle morphologies after 3d metal surface modification are unchanged. The surface and optical properties of the modified TiO₂ were investigated using X-ray photoelectron (XPS) and UV-vis spectroscopies. XPS surface compositions were compared to bulk chemical analysis by inductively-coupled plasma optical emission spectroscopy (ICP-OES) to

better inform the metal deposition process. Real-time reactor headspace gas analysis by portable residual gas analysis mass spectrometry (RGA-MS) was used to quantify the photoactivity of these catalysts for hydrogen production. The 3d metal surface-modified TiO₂ materials show significant improvements in the photoreduction of water to hydrogen gas to levels approaching half that of similarly prepared platinum coated titanias.

5.2 Experimental

Reagents

Reagents used as received were TiO₂ (Degussa P25, ~50 nm size and 45 m²/g), MnCl₂ (Aldrich, 98%), FeCl₂·4H₂O (Aldrich, 99%), CoCl₂·6H₂O (Aldrich, reagent grade), NiCl₂·6H₂O (Aldrich, ReagentPlus), CuCl₂·2H₂O (Aldrich, 99+%), H₂PtCl₆·6H₂O (99.9%, Strem), methanol (ACS certified, Fisher), and methylene blue (Alfa Aesar, high purity). Deionized water (18 MΩ) was prepared using a Photronix MiniQuad system.

Modification of TiO₂ surface with photodeposited transition metals

Single metal (1%) modified TiO₂. In a 50 mL Erlenmeyer flask, 4 mg (0.017 mmol) of MCl₂·6H₂O (M = Co or Ni) or 3 mg (0.017 mmol) of CuCl₂·2H₂O was dissolved in 30 mL of 50 vol% aqueous methanol. TiO₂ (100 mg, 1.25 mmol) was added to the solution. The flask was covered with a septum and the solution degassed with argon while stirring. The flask was exposed to a water-jacketed UV light (450 W Hg lamp, Ace-Hanovia) for 90 minutes under an argon blanket. Solids were isolated by

centrifugation (3000 rpm), washed with 5-10 mL of methanol, centrifuged again from methanol, and then dried in air. The product from nominally 1 wt% metal relative to TiO_2 was denoted as $\text{M}(1\%):\text{TiO}_2$.

Single metal (2%) modified TiO_2 . In a 50 mL Erlenmeyer flask, 5 mg (0.039 mmol) of MnCl_2 , 7 mg (0.035 mmol) of $\text{FeCl}_2 \cdot 4\text{H}_2\text{O}$, 8 mg (0.034 mmol) of $\text{MCl}_2 \cdot 6\text{H}_2\text{O}$ ($\text{M} = \text{Co}$ or Ni) or 6 mg (0.034 mmol) of $\text{CuCl}_2 \cdot 2\text{H}_2\text{O}$ was dissolved in 30 mL of 50 vol% aqueous methanol. TiO_2 (100 mg, 1.25 mmol) was added to the solution. The flask was covered with a septum and the solution degassed with argon while stirring. The flask was exposed to a water-jacketed UV light (450 W Hg lamp, Ace-Hanovia) for 90 minutes under an argon blanket. Solids were isolated by centrifugation (3000 rpm), washed with 5-10 mL of methanol, centrifuged again from methanol, and then dried in air. The product from nominally 2 wt% metal relative to TiO_2 was denoted as $\text{M}(2%):\text{TiO}_2$.

Mixed metal modified TiO_2 . In a 50 mL Erlenmeyer flask, a combination using two of these metals: 6 mg (0.035 mmol) of $\text{CuCl}_2 \cdot 2\text{H}_2\text{O}$, 8 mg (0.034 mmol) of $\text{CoCl}_2 \cdot 6\text{H}_2\text{O}$, or 8 mg (0.034 mmol) of $\text{NiCl}_2 \cdot 6\text{H}_2\text{O}$, was dissolved in 30 mL of 50 vol% aqueous methanol. TiO_2 (200 mg, 2.5 mmol) was added to the solution. The flask was covered with a septum and the solution degassed with argon while stirring. The flask was exposed to UV light for 90 minutes under an argon blanket. Solids were isolated by centrifugation (3000 rpm), washed with 5-10 mL of methanol, centrifuged again from methanol, and then dried in air. These mixed metal products each had nominally 1 wt% metal relative to TiO_2 and were denoted $\text{M}(1\%)/\text{M}'(1%):\text{TiO}_2$.

Platinum modified TiO_2 . In a 50 mL Erlenmeyer flask, 2.4 mg (0.006 mmol) of H_2PtCl_6 was dissolved in 30 mL of 50 vol% aqueous methanol. TiO_2 (100 mg, 1.25

mmol) was added to the solution. The flask was covered with a septum, and the solution was degassed with argon while stirring. The flask was exposed to UV light (450 W Hg) for 90 minutes under an argon blanket. Solids were isolated by centrifugation (3000 rpm), rinsed with methanol, and dried in air. This platinum loading is nominally 1 wt% Pt relative to TiO₂ and is denoted Pt(1%):TiO₂.

Characterization

A Bruker D8 DaVinci powder X-ray diffractometer was used for analysis of powders uniformly placed on glass slides (Cu K α , 0.050°/s step). X-ray photoelectron spectroscopy (XPS) was performed on a Kratos Axis Ultra XPS (Al K α) with samples mounted on carbon tape. XPS peak analysis was performed using CasaXPS software (www.casaxps.com). Inductively-coupled plasma optical emission spectroscopy (ICP-OES, Perkin Elmer Optima DV 7000) was used for bulk elemental analysis. Samples were dissolved in a heated 5:1 mixture of concentrated H₂SO₄:HNO₃ and diluted with 5% HNO₃. Calibration standards were prepared from 1000 ppm commercial ICP standards for Ti, Co, Cu (Alfa Aesar), and Ni (Fluka). Diffuse reflectance UV-vis data was collected on a Cary 5000 Series Spectrophotometer (300-800 nm, 10 nm/s). Solid samples were loaded into a round compression sample holder with a 1 cm diameter sampling area. Raw reflectance data was converted to Kubelka-Munk units $[(F(R))]$, and band gaps were calculated using $[(F(R)hv)]^{1/2}$ extrapolations of linear regions of curve. Scanning electron microscopy (SEM) images were collected on a Hitachi S-4800 FE-SEM with an accelerating voltage of 1.3 kV. Samples were mounted on aluminum stubs using carbon tape and were not coated prior to analysis. BET surface area measurements

were collected on a Quantachrome Nova 1200 using approximately 50 mg of solid sample.

Photocatalytic reactions

Oxidative degradation of organic dyes

The photodegradation of methylene blue ($C_{16}H_{18}ClN_3S$) was studied using the M(2%)TiO₂ and M(1%)M'(1%):TiO₂ samples. A stock 10^{-3} M dye solution was prepared by dissolving the solid dye in 18 MΩ water. The stock solution was diluted to $2 \cdot 10^{-5}$ M to fit the peak at λ_{max} in the range ($\lambda_{MB}=665$ nm, $A < 1.50$) of the UV-vis spectrophotometer (Agilent 8453). To 30 mL beakers, 10 mL of dye solution and 10 mg of catalyst were added. An additional beaker containing only dye was used to evaluate self-degradation in the absence of catalyst. Samples were stirred in the dark for a minimum of 30 minutes to equilibrate dye absorption. Samples were exposed to UV light (Ace-Hanovia, 450 W Hg) in 5 minute intervals. After each irradiation period, the catalysts were separated from the dye solution by centrifugation and the UV-vis spectrum of each solution was collected to quantify the remaining concentration of dye. Experiments were typically carried out for less than 1 hour of total UV light illumination before total degradation of the dye.

Photocatalytic hydrogen evolution.

Reactions were carried out in a 50 mL Schlenk flask containing 10 mg (0.125 mmol) of the titania catalyst suspended in 10 mL of 50 vol% aqueous methanol solution. The reactor was purged with argon and connected to the capillary of a Stanford Research Systems quadrupole mass spectrometer 300 series Residual Gas Analyzer via the flask

side arm. Masses corresponding to N₂ (28), Ar (40), H₂ (2), O₂ (32), CO₂ (44), and H₂O (18) were monitored as a function of time. The flask remained under a constant blanket of argon for the entire experiment, supplied from a Schlenk line with an oil bubbler. Following a 30 minute period for instrument and background stabilization, the flask was illuminated with a UV lamp in 60 minute cycles with an approximate photon flux of 4.0×10^{17} photon s⁻¹. Between each cycle, the reactor was opened briefly and its headspace flushed with argon. Pressure signals were converted to molar amounts of evolved H₂ based on a calibration curve created using known concentration H₂/Ar mixtures. Additional details about calibration and experimental set-up can be found in the appendix.

In-situ metal photodeposition and hydrogen evolution.

This experiment used the same reactor/analysis setup as described in the previous section. Here, 10 mg (0.125 mmol) of Degussa P25-TiO₂ was suspended in 10 mL of 50 vol% of aqueous methanol containing 0.4 mg (0.0017 mmol) of MCl₂·6H₂O (M = Co, Ni) or 0.3 mg (0.0017 mmol) of CuCl₂·2H₂O. The reactor was purged with argon and connected to the RGA as described above. Following a 30 minute period for instrument and background stabilization, the flask was illuminated with a UV lamp in 60 minute cycles. The reactor headspace was flushed with argon between each cycle. In order to verify the critical nature of the methanol sacrificial oxidant in metal deposition and hydrogen evolution, 10 mg (0.125 mmol) of Degussa P25-TiO₂ was suspended in a 10 mL solution 18 MΩ H₂O with 3 mg (0.017 mmol) of CuCl₂·2H₂O and was UV irradiated for two cycles, and then 2 mL of methanol was added for the third UV cycle onward.

5.3 Results and Discussion

Photochemical M:TiO₂ synthesis.

Commercial Degussa P25-TiO₂ nanoparticles (~50 nm, 80:20 anatase:rutile) were surface-modified with the 3d metal ions manganese, iron, cobalt, nickel, and copper using solution UV photoreduction in the presence of a sacrificial methanol oxidant. P25-TiO₂ was dispersed in a 50 vol% aqueous methanol solution containing dissolved metal dichlorides. The solution was degassed with argon prior to UV irradiation to favor inert (non-oxidizing) conditions. The initial solutions contained sufficient metal chloride to deposit either 1 wt% or 2 wt% metal onto the suspended titania powder. Following UV exposure, the titania suspension had darkened in color (*e.g.*, grey Ni:TiO₂, purple Cu:TiO₂), and the washed and dried M:TiO₂ solids were white (Mn), light yellow (Fe), light grey (Ni), or light blue (Co and Cu). When two different metals were present in the photodeposition solution (Co/Ni, Co/Cu, Ni/Cu), the M:TiO₂ products had a light blue coloration similar to the Cu and Co products. Comparable visible titania colorations was observed for the nominally 1 wt% and 2 wt% metal loadings.

M:TiO₂ structure, composition, and surface analysis.

Powder X-ray diffraction (XRD) of the photodeposited M:TiO₂ products showed predominately anatase TiO₂ with a small rutile component in ratios that were unchanged from the starting P25-TiO₂ (Figure 5.1). No additional XRD peaks corresponding to other metals or metal oxide phases were observed, suggesting they are present in amounts below the few percent XRD detection limits, or that they are on the surface in a non-crystalline form.

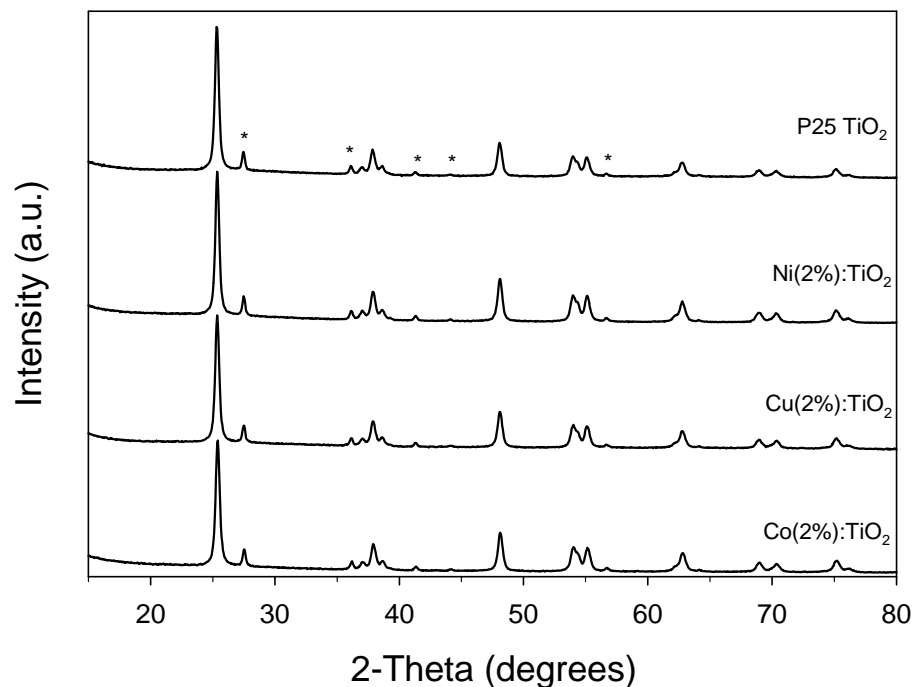


Figure 5.1 – XRD patterns for select M(2%):TiO₂ products, rutile phase TiO₂ is marked with an asterisk.

The photochemical reactions between P25-TiO₂ and metal halide solutions also did not lead to detectable physical changes in the titania powders. A BET surface area of 44.8 m²/g was measured for P25-TiO₂, which is essentially the same as the 44.6 m²/g surface area measured for a surface-modified Cu(1%):TiO₂ sample. Scanning electron microscopy (SEM) analysis also showed that the original TiO₂ particle sizes near 50 nm were retained in the Cu(1%):TiO₂ photoproduct (Figure 5.2). Aggregated small particles near 50 nm were similarly observed for Ni and Co deposition products.

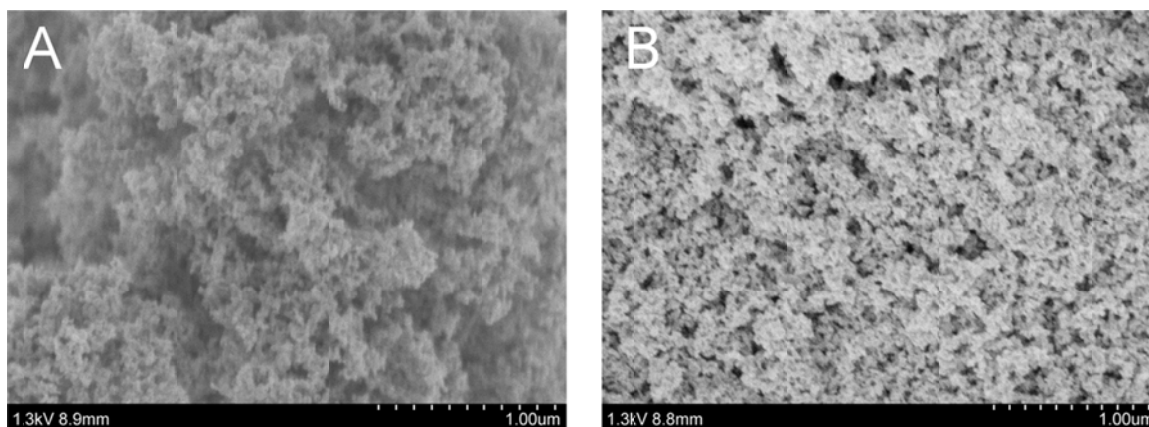


Figure 5.2 – SEM images of (A) P25 TiO₂ and (B) Cu(1%):TiO₂ photoreaction product.

Bulk elemental analysis using ICP-OES showed the metals deposited onto TiO₂, and the M:Ti atomic ratios are summarized in Table 5.1. At the targeted 1 wt% metal loading, the ideal M:Ti atomic ratio would be 1.3 : 98.7 (2.6 : 97.4 for 2 wt%) if all of the metal present in solution was deposited onto the P25-TiO₂ particle surface. Cobalt and nickel were detected at less than 10% of the ideal 1 wt% loading value, while copper approached half of the ideal loading. In the mixed-metal samples, the cobalt and nickel content remained low (<0.07 at% vs. Ti), while the amount of copper was closer to its ideal content based on solution concentrations; thus, the photodeposition of copper onto semiconducting TiO₂ is favored over the other metals. A doubling of the metal chloride solution concentration to 2 wt% did not result in a doubling of metal product content. Similar metal deposition trends have been observed in related photochemical contexts.¹⁴⁹ These surface deposition results are consistent with metal activity series trends and reduction potentials ($M^{2+} + 2e^- \rightarrow M$ with ease of reduction $Cu > 2H >> Ni > Co > Fe > Mn$); for example copper is the most easily-reduced of the metal cations and protons.¹⁵⁰ Copper is also the only one of the metal cations that is easier to reduce than H⁺ to H₂. In

the photo-assisted solution reduction process, it is generally accepted that a sacrificial methanol oxidant interacts with the valence band holes in photoexcited TiO₂, while the photoexcited conduction band electrons in TiO₂ are used for solution H⁺ to H₂ reduction and also surface metal reduction (e.g., Cu²⁺ → Cu⁺/Cu⁰).^{40, 126} This catalytic redox cycle parallels the mechanisms used for platinum-coated titanias produced by UV photoreduction of PtCl₆²⁻ in methanol solutions.

Table 5.1. ICP-OES and XPS compositions and peak positions of M(x%)TiO₂ samples.

Sample	M : Ti (at%) ICP	M : Ti (at%) XPS	M 2p _{3/2} (eV) ^a	Ti 2p _{3/2} (eV)
Mn(2%):TiO ₂	n/a	0.9 : 99.1	641.5	458.5
Fe(2%):TiO ₂	n/a	1.4 : 98.6	710.2	457.9, 458.9
Co(1%):TiO ₂	0.04 : 99.96	0.3 : 99.7	780.0	458.5
Co(2%):TiO ₂	0.07 : 99.93	1.3 : 98.7	780.8, 786.6	458.6
Ni(1%):TiO ₂	0.08 : 99.92	0.5 : 99.5	855.3, 861.5	458.5
Ni(2%):TiO ₂	0.08 : 99.92	3.4 : 96.6	855.8, 860.9	458.6, 461.3
Cu(1%):TiO ₂	0.44 : 99.56	1.7 : 98.3	932.3	458.4
Cu(2%):TiO ₂	0.64 : 99.36	3.5 : 96.5	932.6	458.4
Co(1%)/Ni(1%):TiO ₂	<u>Co/Ni : Ti</u> 0.05/0.06 : 99.89	<u>Co/Ni : Ti</u> 0.6/0.4 : 99.0	Ni: 855.8 Co: 782.0	458.5
Co(1%)/Cu(1%):TiO ₂	<u>Co/Cu : Ti</u> 0.02/0.97 : 99.01	<u>Co/Cu : Ti</u> 0/5.2 : 94.8	Cu: 932.2	458.4
Ni(1%)/Cu(1%):TiO ₂	<u>Ni/Cu : Ti</u> 0.03/1.02 : 98.95	<u>Ni/Cu : Ti</u> 0/6.0 : 94.0	Cu: 933.0	458.8

a) Literature values for M 2p_{3/2} from NIST XPS database:¹⁵¹ Mn(0/+2/+4) 639.0/641.9/642.2, Fe(0/+2/+3) 706.9/710.6/711.3, Co(0/+2/+3) 778.1/780.2/781.3,¹⁵²⁻¹⁵³ Ni(0/+2) 852.8/853-856,¹⁵⁴ Cu(0/+1/+2) 932.4/932.5/933.7.¹⁵⁴

Surface composition and chemical environment were examined for select M:TiO₂ products using surface-sensitive X-ray photoelectron spectroscopy (XPS). For the nominal 1-2 wt% metal concentrations, signals were observable for Co, Ni, and Cu, though the Co and Ni contents were low and required longer sampling times in order to detect weak signals for these metals above the baseline. Figure 5.3 shows 2p_{3/2} spectra for Ti, Mn, Fe, Co, Ni, Cu peaks in representative M(2%):TiO₂ samples. Table 5.1 summarizes XPS peak positions and relative atomic ratios of the surface metal species. As compared to the bulk ICP composition results, XPS shows higher M:Ti surface atomic ratios. Since the metal species are photodeposited on the surface, rather than being homogeneously distributed through the TiO₂ structure, it is not surprising that the XPS surface composition yields a higher M:Ti atomic ratio than bulk analysis. Though the amounts of metal in the Mn(2%) and Fe(2%):TiO₂ samples were not quantified by ICP, the XPS compositions were similar to the other M(2%):TiO₂ samples. For the mixed metal samples, Co(1%)/Ni(1%):TiO₂ have Co and Ni contents similar to that observed for the individual Co(1%) and Ni(1%):TiO₂ samples. In contrast, the mixed-metal samples containing Cu showed no detectable Co or Ni, which is consistent with the bulk ICP results showing decreased photodeposition of Co and Ni when Cu is present in solution. The mixed-metal results provide further support for the ease of copper ion photoreduction onto semiconducting TiO₂ as compared to Co and Ni ions.

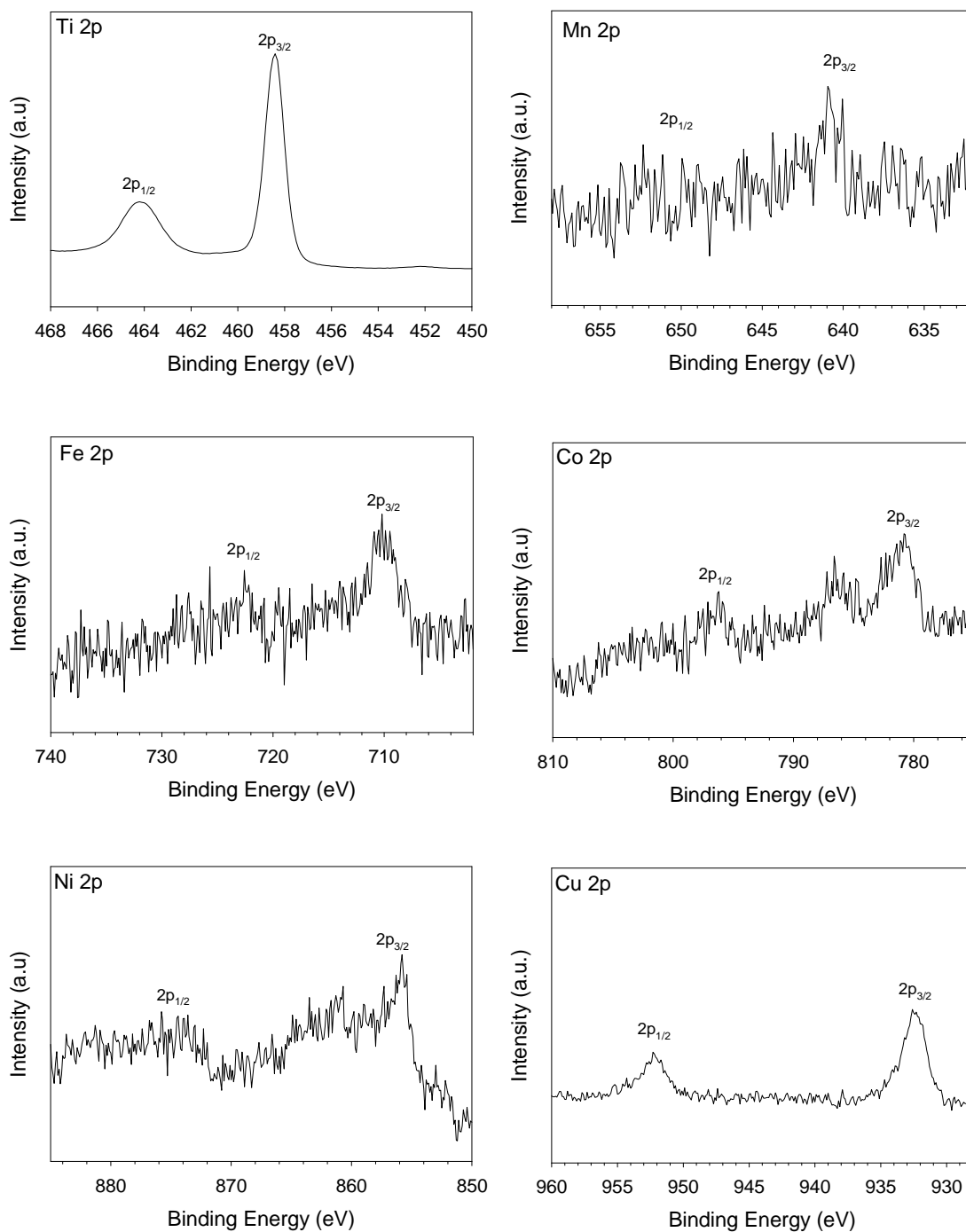


Figure 5.3 – Representative XPS spectra for 2p doublets for Ti from Cu(2%):TiO₂, Mn from Mn(2%):TiO₂, Fe from Fe(2%):TiO₂, Co from Co(2%):TiO₂, Ni from Ni(2%):TiO₂, and Cu from Cu(2%):TiO₂.

In addition to surface-sensitive compositions, XPS provides useful information about the nature of the metals deposited on the surface. As shown in the results from Table 5.1, in all M:TiO₂ samples, the Ti 2p_{3/2} peak is between 458.4 and 459.0 eV, agreeing with a Ti⁴⁺ environment for TiO₂. For reference, the starting P25-TiO₂ has a Ti 2p_{3/2} peak centered at 458.2 eV. The O 1s spectra show a major peak at 530.2 eV in all samples, also consistent with the oxide anion for TiO₂. The other metal peak positions were used to help determine their chemical state on the TiO₂ surface. The 2p_{3/2} peaks positions of Mn, Fe, Co and Ni on P25-TiO₂ are close to their M²⁺ reference positions (e.g., MO, M(OH)₂, or MCl₂) with a small peak near M³⁺ reference energies in the Co case. In contrast, the 2p_{3/2} peak in Cu samples indicates the metal has been reduced on the surface to Cu⁰/Cu⁺ states (e.g., Cu₂O or CuCl), which is consistent with related work on copper coated titanias.^{141, 154} As noted above, Cu is more readily photodeposited onto P25-TiO₂ than Co or Ni, and XPS compositional analysis supports the idea that the ease of Cu²⁺ reduction leads to higher surface deposition. The Co(1%)/Ni(1%):TiO₂ sample has a nickel peak position similar to comparable Ni²⁺ peaks observed in the Ni:TiO₂ samples, but the cobalt peak appeared at slightly higher energy near a Co³⁺ state. The mixed metal samples show Cu is still in a Cu⁰/Cu⁺ state, though the Ni(1%)/Cu(1%):TiO₂ sample may have some Cu²⁺ character. In related studies, chemically-precipitated Cu(OH)₂ or Ni(OH)₂ clusters added to the P25-TiO₂ surface show similar 2p_{3/2} shifts from 935 to 933 eV as surface Cu²⁺ transforms to metallic Cu, and a Ni peak at 856 eV is attributed to surface Ni²⁺.¹⁵⁵⁻¹⁵⁶ Chlorine is also present on the titania surface after photoreaction with metal chloride solutions, and higher surface chlorine is detected for Mn, Co and Ni cations versus partially reduced Cu products (Table 5.2). This is

consistent with metal cations deposited or reacted with oxide surface sites that are accompanied by chloride anions while reduced Cu on the titania surface requires less chloride anion charge balance.

Table 5.2. XPS analysis of surface chlorine relative to deposited metals on M(x%):TiO₂.

Sample	M (at%)	Cl (at%)
Mn(2%):TiO ₂	50.28	49.72
Fe(2%):TiO ₂	65.36	34.64
Co(1%):TiO ₂	25.5	74.5
Co(2%):TiO ₂	40.59	59.41
Ni(1%):TiO ₂	37.1	62.9
Ni(2%):TiO ₂	56.11	43.89
Cu(1%):TiO ₂	66.8	33.2
Cu(2%):TiO ₂	69.9	30.1
Co(1%)/Ni(1%):TiO ₂	22.13 / 15.86	62.01
Co(1%)/Cu(1%):TiO ₂	0 / 67.92	32.08
Ni(1%)/Cu(1%):TiO ₂	0 / 70.95	29.05

Optical properties

Diffuse reflectance UV-vis spectra for the M:TiO₂ samples relative to P25-TiO₂ show that the 3d metal surface modification leads to visible colors and apparent new absorption events in the red or orange regions as well as a slightly lower energy band gap absorption energy (E_g). Figure 5.4 shows the raw reflectance data and Tauc plot for the P25-TiO₂ along with M(2%):TiO₂ products. Each of the M:TiO₂ samples shows a band gap absorption shift to lower E_g near 2.9 eV from 3.2 eV for P25-TiO₂. Cu:TiO₂ samples

show a decrease in reflectance at wavelengths above 600 nm, correlating with its light-blue color. For comparison, a blue CuCl_2 solution has an absorbance maximum at 800 nm corresponding to d-d electronic transitions. Similar absorption near 700-800 nm are observed for $\text{Cu}(\text{OH})_2$ deposited onto TiO_2 .¹⁵⁶ The $\text{Co}:\text{TiO}_2$ samples show decreased reflectance from 520 to 680 nm, similar to CoCl_2 solutions with an absorbance maximum near 500 nm. The light-grey colored $\text{Ni}:\text{TiO}_2$ samples exhibit a broad decrease in total reflectance across the visible spectrum relative to P25- TiO_2 . The spectra for $\text{M}(1\%):\text{TiO}_2$ and $\text{M}(1\%)/\text{M}'(1%):\text{TiO}_2$ samples show similar absorption events and trends. The increase in visible absorptions and band gap decrease may be due to nanoscale surface plasmon resonance effects,^{148, 157} while others have ascribed these optical transitions to charge transfer between TiO_2 bands and the surface deposited metal species.¹⁵⁵⁻¹⁵⁶

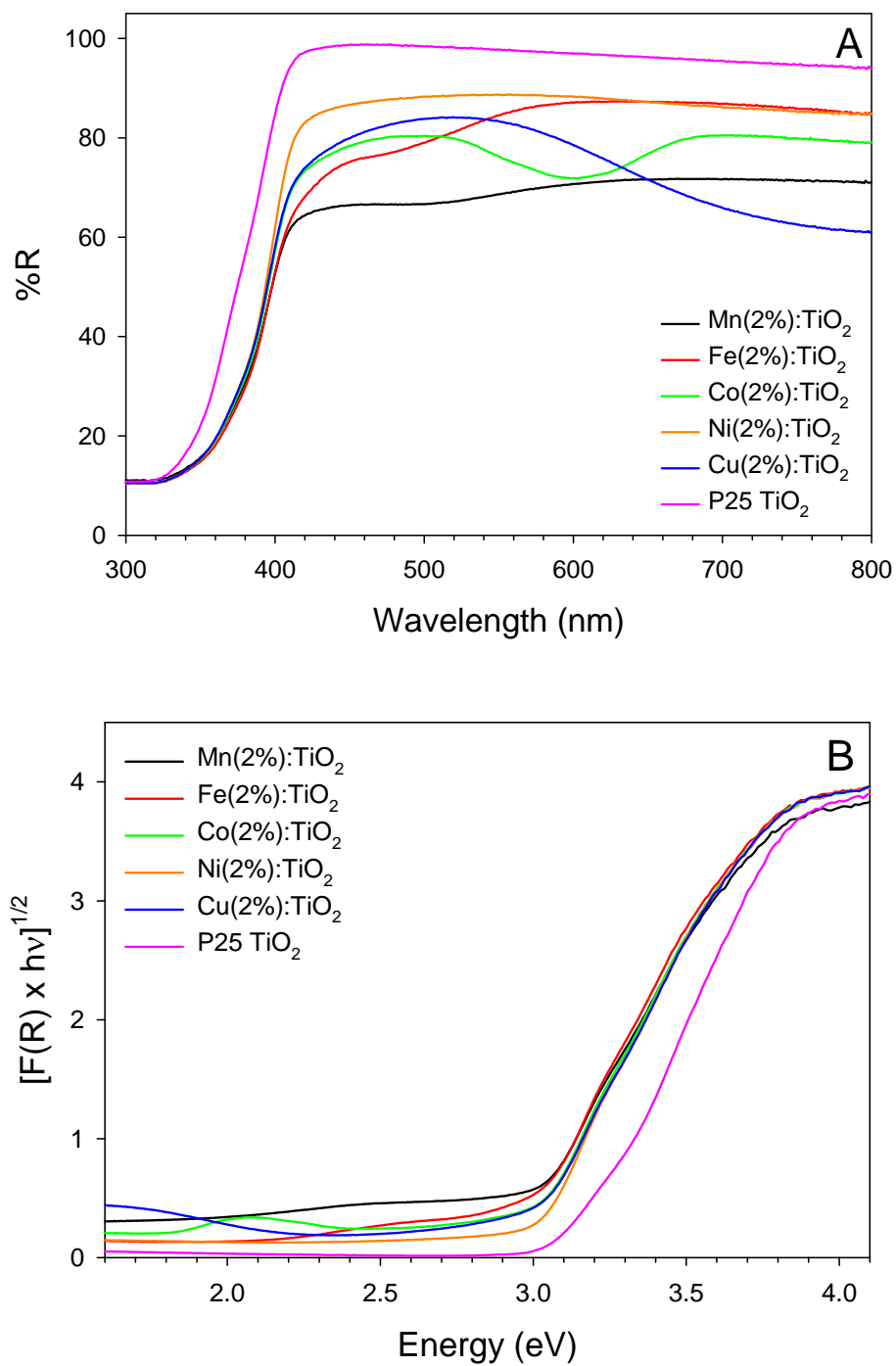


Figure 5.4 – UV-vis DRS data on M(2%):TiO₂ samples (A) reflectance spectra and (B) Tauc plots.

*Photocatalytic reactions*Photocatalytic dye oxidation

The photodegradation of methylene blue was first tested using the M(2%):TiO₂ samples. Following the dark stir, many of the samples saw an increase in absorbance signal due to scattering from fine particles remaining suspended in the dye solution. The degradation of the dye for each sample was compared with unmodified P25 TiO₂ (Figure 5.5). Most of the M(2%):TiO₂ fully decolorized the dye by the end of 30 minutes, with the exception of Cu(2%):TiO₂. Many of the samples tracked closely with the degradation of MB by P25 at each time point leading up to this, most notably Fe(2%):TiO₂. The linear rate fits (Figure 5.5) and first-order rate constants (Table 5.3) show that Fe(2%):TiO₂ is nearly as effective as P25. This is followed by Co(2%):TiO₂, then Mn(2%):TiO₂ and Ni(2%):TiO₂ with the same rate, and Cu(2%):TiO₂ with the lowest rate. The degradation of MB dye is an oxidative process, and as described earlier copper is the most reduced of these metals on the surface of TiO₂. This would make Cu(2%):TiO₂ the least suitable for oxidizing MB, consistent with its low degradation activity. The loss of activity for the other metal-modified TiO₂ products could be due to similar redox processes, but not as notable a loss since these metals maintained higher oxidation states than Cu.

Table 5.3. First-order rate constants (min⁻¹) for the degradation of methylene blue dye using M(2%):TiO₂ products.

Sample	Mn(2%): TiO₂	Fe(2%): TiO₂	Co(2%): TiO₂	Ni(2%): TiO₂	Cu(2%): TiO₂	P25 TiO₂
UV Rate	0.074	0.123	0.091	0.074	0.015	0.127
R ²	0.952	0.986	0.993	0.944	0.973	0.993

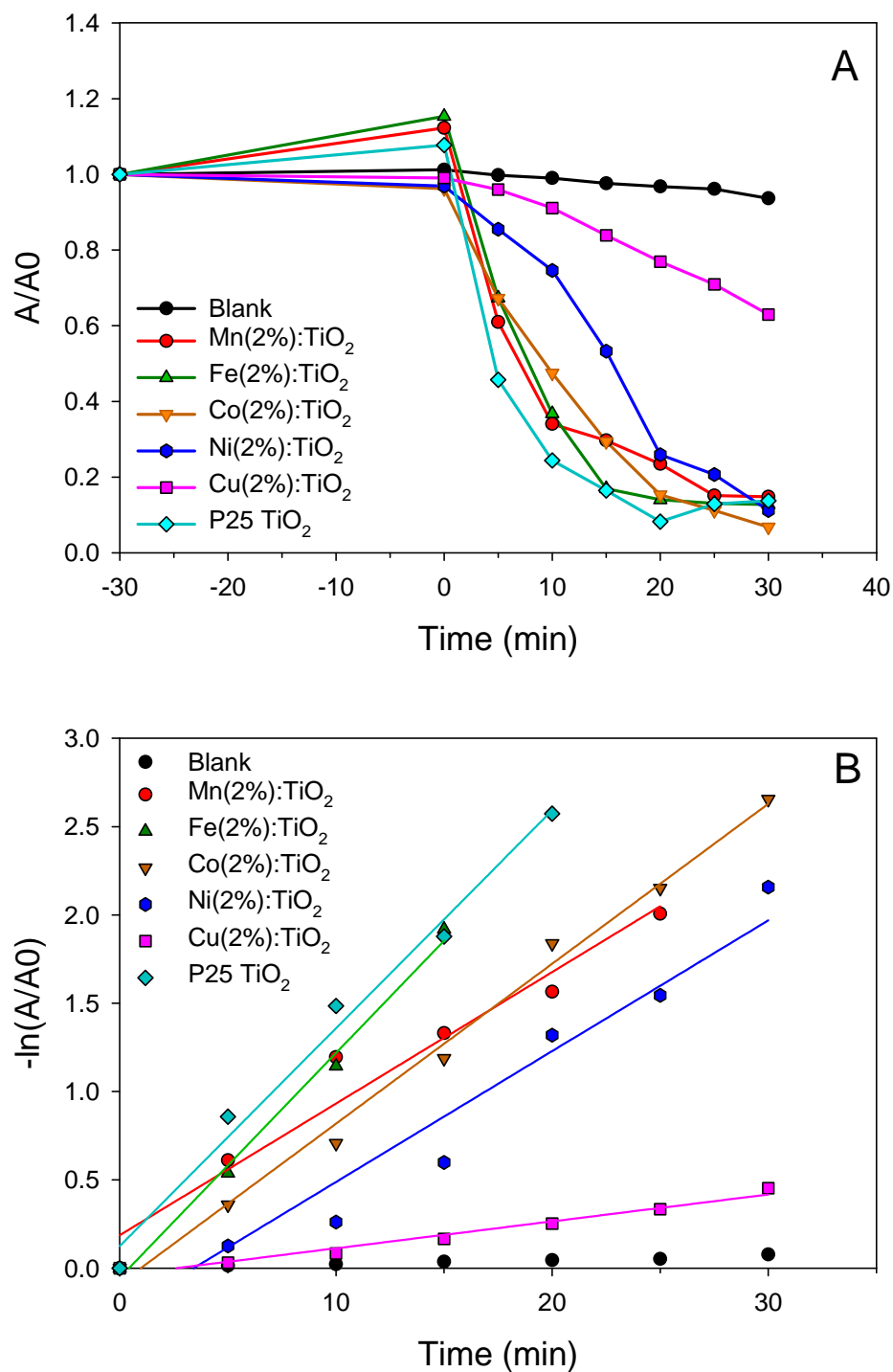


Figure 5.5 – UV-vis analysis of the photodegradation of MB dye with M(2%):TiO₂ samples (A) UV light data (B) linear rate data.

The M(1%)M'(1%):TiO₂ products were also tested for the degradation of MB dye. Similar to the M(2%):TiO₂ samples, there was some initial light scattering from suspended particles following the dark stir. Only Co(1%)Ni(1%):TiO₂ approached the same level of dye degradation as P25 TiO₂. Both of the Cu-containing catalysts performed worse, reaching only 35% and 50% of the initial dye concentration in the 35 minute illumination time. These also had less activity than the individual Co(2%):TiO₂ and Ni(2%):TiO₂ catalysts, further showing the negative effects from the addition of Cu. The linear fits are shown in Figure 5.6, and rate constants are in Table 5.4. The rate for Co(1%)Ni(1%):TiO₂ is 52.6% of that for P25 TiO₂, while Co(1%)Cu(1%):TiO₂ and Ni(1%)Cu(1%):TiO₂ are 9.7% and 6.2% respectively.

Table 5.4. First-order rate constants (min⁻¹) for the degradation of methylene blue dye using M(1%)M'(1%):TiO₂ products.

Sample	Co(1%)Ni(1%): TiO₂	Co(1%)Cu(1%): TiO₂	Ni(1%)Cu(1%): TiO₂	P25 TiO₂
UV rate	0.1216	0.0225	0.0144	0.2311
R ²	0.985	0.988	0.999	0.999

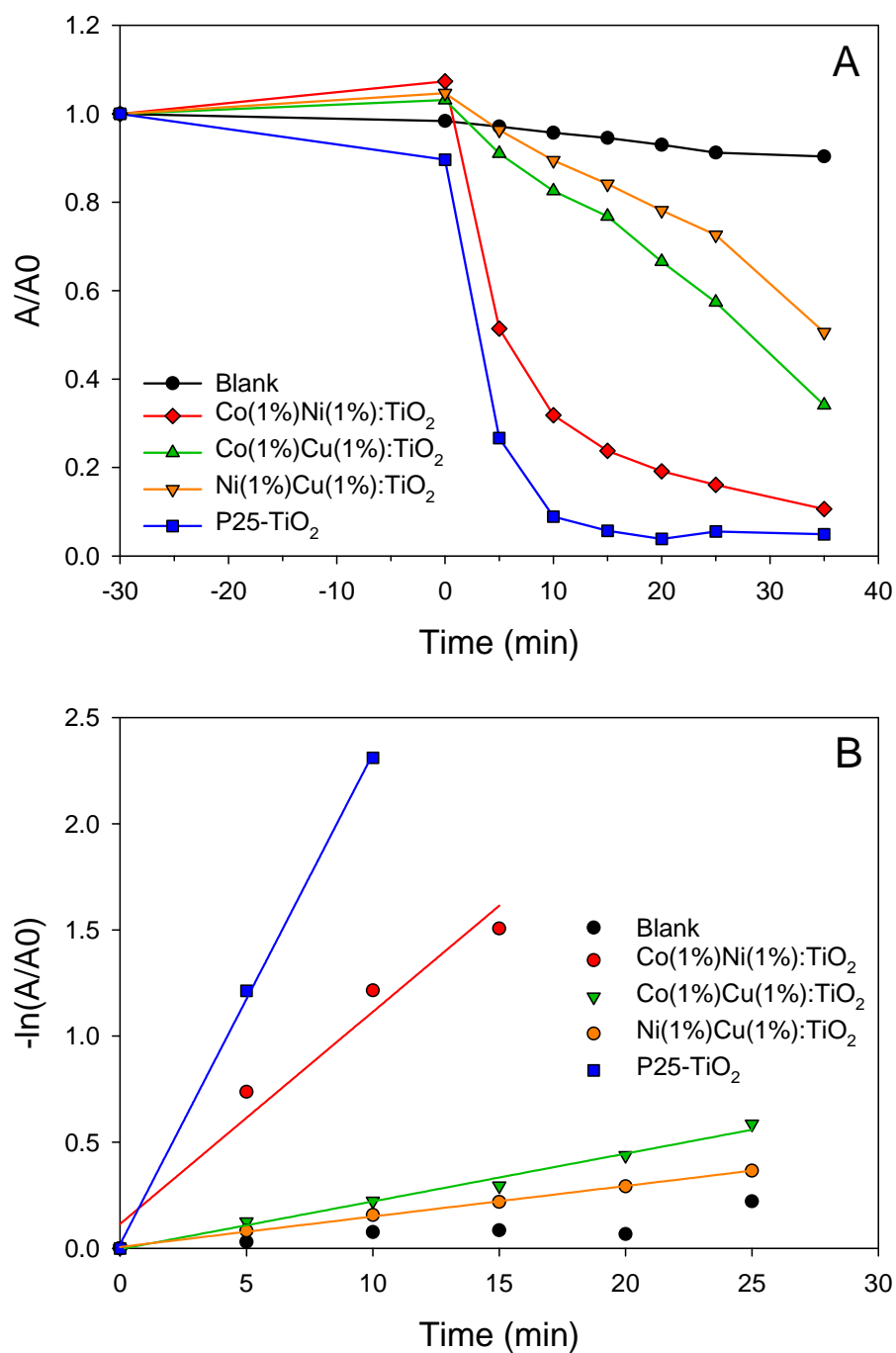


Figure 5.6 – UV-vis analysis of the photodegradation of MB dye with $M(1\%)M'(1\%):TiO_2$ samples (A) UV light data (B) linear rate data.

Photocatalytic hydrogen evolution with M:TiO₂.

Photocatalytic hydrogen gas evolution from aqueous methanol solutions was quantified in real-time using RGA-MS for different M:TiO₂ samples under UV irradiation, with methanol serving as a sacrificial oxidant. Calibration curves for the H₂/Ar headspace mass analysis data allowed direct conversion to molar quantities of evolved hydrogen (see Appendix). The use of direct mass quantification by RGA-MS allowed rates of H₂ produced to be measured continuously, and it yielded similar evolution rates for Pt(1%):TiO₂ reported by GC analysis.¹⁵⁸ For comparison, photocatalytic hydrogen gas evolution was determined for highly-active platinum coated titania, Pt(1%):TiO₂, and unmodified P25-TiO₂, which yielded average H₂ evolution rates of 200 and 5 μmol/h, respectively (for 10 mg samples: 20,000 μmol h⁻¹ g⁻¹ and 500 μmol h⁻¹ g⁻¹). Each M:TiO₂ sample showed considerably-higher H₂ evolution rates than the P25-TiO₂ starting material and multiple cycle data for M(1%):TiO₂ samples is shown in Figure 5.7.

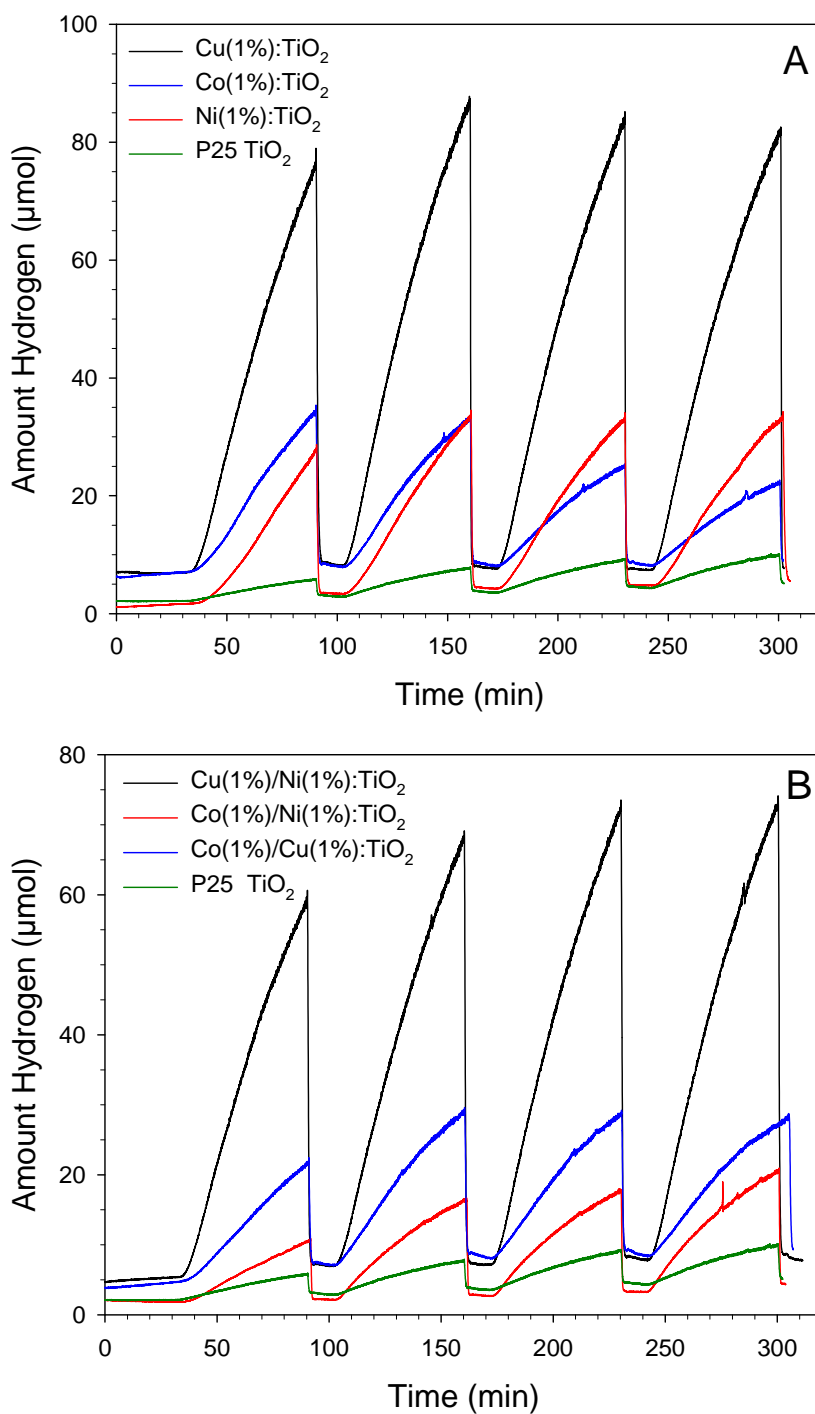


Figure 5.7 – Real-time hydrogen gas evolution under UV light illumination for (A) $M(1\%):\text{TiO}_2$ and (B) $M(1\%),M'(1\%):\text{TiO}_2$. H_2 production was measured during one-hour illumination cycles followed by a 10 minute argon flush. The sequential illumination cycles began at the 30, 100, 170, and 240 minute marks.

Each M:TiO₂ catalyst was tested in several one-hour cycles of UV exposure in the same aqueous methanol solution, and the average hourly hydrogen evolution data is summarized in Table 5.5. The hourly H₂ evolution rates for most samples across the multiple cycles showed small deviation. The samples with the least stability were the Co(1%):TiO₂ and Ni(2%):TiO₂, where H₂ evolution dropped by 30-50% after the third cycle. The Cu(1%):TiO₂ sample had the highest hydrogen evolution rate of 85 μmol/h (8,500 μmol h⁻¹ g⁻¹) that is comparable to or greater than prior studies of copper deposition on porous or nanoscale titanias, with H₂ evolution in range from 1,500 - 8,000 μmol h⁻¹ g⁻¹,^{141, 148-149} or to the structural incorporation of Cu or Ni with 1,100 - 4,300 μmol h⁻¹ g⁻¹.^{131, 142} Though Cu(1%):TiO₂ was more active than Cu(2%):TiO₂, both Cu modified samples had very stable H₂ production for several cycles. The Cu:TiO₂ samples show higher activity than the Co:TiO₂ and Ni:TiO₂ photocatalysts, though this may be due to the higher amount of Cu deposition based on ICP results. Scaling hydrogen evolution activity to the amount of metal cocatalyst indicate that Co(1%):TiO₂ is most active at 8,400 μmol h⁻¹ mg⁻¹ Co, while Cu(1%):TiO₂ had an activity of 2,400 μmol h⁻¹ mg⁻¹ Cu. The calculated quantum yields from the broad spectrum UV illumination were generally similar (~1-20% range) to those reported in other Cu or Ni surface modified titanias.^{149, 155-156}

Table 5.5. Hydrogen evolution rates ($\mu\text{mol/h}$) and quantum yields for M:TiO₂ materials.

Sample	Average H ₂ rate (std. dev)	Quantum Yield (%)
P25-TiO ₂	5.3 (1.1)	0.4
Pt(1%):TiO ₂	200 (14)	16.6
Mn(2%):TiO ₂	4.2 (1.2)	0.3
Fe(2%):TiO ₂	5.7 (0.6)	0.5
Co(1%):TiO ₂	24.8 (8.7)	2.1
Co(2%):TiO ₂	14.9 (1.3)	1.2
Ni(1%):TiO ₂	33.9 (2.2)	2.8
Ni(2%):TiO ₂	33.1 (6.4)	2.8
Cu(1%):TiO ₂	84.7 (4.0)	7.0
Cu(2%):TiO ₂	53.0 (2.8)	4.4
Co(1%)/Ni(1%):TiO ₂	15.6 (4.5)	1.3
Co(1%)/Cu(1%):TiO ₂	23.3 (2.5)	1.9
Ni(1%)/Cu(1%):TiO ₂	70.2 (3.1)	5.8

There was no synergistic photocatalyst effect observed for the titania surface-modified with both Ni and Co, as the activity for the mixed metal sample was similar or lower than that of the individual M(1%):TiO₂ products. While the addition of a second photodeposited metal (Co or Ni) species onto TiO₂ does enhance copper photodeposition, this may lead to higher surface metal coatings that inhibit hydrogen evolution activity by favoring redox reactions of the surface metal species (*e.g.*, Cu⁺/Cu) or blocking illumination of the titania core. Based on Table 5.5 results for M(1%)/Cu(1%):TiO₂, addition of Ni²⁺ to the Cu⁺/Cu photodeposited coating has less negative impact on hydrogen production versus the Co²⁺ additions. There are many variables that prevent

direct comparisons with other related metal coated heterojunction titanias, but Table 5.6 compares several other studies with the current work.

Table 5.6. Comparison of several Ni and Cu modified titania for hydrogen evolution photocatalysis.

Sample Meas. mol% M ^a	TiO ₂ source, surf. area, metal depn.	Conditions	H ₂ rate in μmol h ⁻¹ g ⁻¹ (QY)	Ref.
Ni(1%):TiO ₂ 0.08 mol% Ni	P25, 45 m ² /g MCl ₂ photorxn	50% MeOH, 450 W Hg lamp	3,390 (2.8%)	this work
Ni(OH) ₂ on TiO ₂ 0.23 mol% Ni	P25, 45 m ² /g solution ppt	25% MeOH, 3 W 365 nm UV-LEDs	3,056 (12.4%)	155
0.5% Ni on TiO ₂ , 0.67 mol% Ni	P25, 45 m ² /g H ₂ reduction	10% EtOH, 100 W 365 nm UV lamp	11,600	131
0.25% Ni on TiO ₂ 0.34 mol% Ni (ideal)	mesoporous, 130 m ² /g <i>in-situ</i> photorxn, NiCl ₂	95% EtOH, 1000 W Hg lamp	700 (20%)	149
Cu(1%):TiO ₂ 0.44 mol% Cu	P25, 45 m ² /g MCl ₂ photorxn	50% MeOH, 450 W Hg lamp	8,470 (7%)	this work
Cu(OH) ₂ on TiO ₂ , 0.29 mol% Cu	P25, 43 m ² /g solution ppt.	0.09M ethylene glycol, 3 W 365 nm UV- LEDs	3,418 (13.9%)	156
0.25% Cu on TiO ₂ 0.31 mol% Cu (ideal)	mesoporous, 130 m ² /g <i>in-situ</i> photorxn, CuCl ₂	95% EtOH, 1000 W Hg lamp	1,600 (50%)	149
10% Cu on TiO ₂ , 12.4 mol% Cu (ideal)	P25, 45 m ² /g H ₂ reduction	10% glycerol, 300 W Xe lamp	5,700	141
10% Cu on TiO ₂ , 12.4 mol% Cu (ideal)	P25, <i>in-situ</i> photorxn CuSO ₄	MeOH, 125 W Hg lamp	1,748	148

a) Ideal mol% metal noted based on ideal M/TiO₂ solution content, if bulk analysis not reported.

For the results shown in Table 5.6, some cases note the ideal amount of metal that could be deposited onto TiO₂ from solution where bulk chemical analysis was not available. The metal salt solutions vary from using non-oxidizing chloride anions to potentially reducible sulfate and nitrate anions. As P25-TiO₂ alone only yields ~500 $\mu\text{mol h}^{-1} \text{g}^{-1}$ of H₂ in aqueous UV photocatalytic reactions with a methanol sacrificial oxidant, the wide range of surface deposition strategies in Table 5.4 all show enhanced H₂ evolution abilities with various illumination strategies and oxidants.

Recycling tests were performed after recovering M(1%):TiO₂ samples and testing activity in new aqueous methanol solutions. All M:TiO₂ samples retained enhanced hydrogen evolution, though at lower activity than the initial cycling tests. As an example, Cu(1%):TiO₂ had an average rate of 62 $\mu\text{mol/h}$ during a recycle test, roughly 73% of the average activity of the initial cycles. During several catalyst recycle runs, the individual cycles were fairly consistent (Table 5.7).

Table 5.7. Hydrogen evolution rates ($\mu\text{mol/h}$) and quantum yields for select recycled M:TiO₂ materials.

Sample	Average H ₂ rate (std. dev)	% of initial activity	Quantum Yield (%)
Co(1%):TiO ₂	14.3 (2.9)	58	0.9
Ni(1%):TiO ₂	16.5 (2.6)	49	1.4
Cu(1%):TiO ₂	61.6 (6.4)	73	4.8
Co(1%)Cu(1%):TiO ₂	19.3 (4.1)	83	1.1
Ni(1%)Cu(1%):TiO ₂	33.4 (5.8)	48	2.2

Post-reaction XPS analysis was used to check for changes to the catalyst surface composition (Table 5.8). Cu(2%):TiO₂ showed a ~70% decrease in the Cu:Ti atomic

ratio to 1.1 : 98.9, but no change in Cu 2p_{3/2} peak position. The Co(2%) and Ni(2%) samples did not show clearly identifiable surface metal peaks in the post-reaction analysis, though the solids retained some of their initial color. This loss of surface metal may relate to the decrease in activity over the initial cycles as well as the drop in activity during the recycle tests for these catalysts. In related CuO/TiO₂ photocatalytic systems, it was determined that photocorrosion of chemically-deposited copper occurs during UV hydrogen evolution photocatalysis along with possible competing reverse photodeposition of some dissolved copper.¹⁴⁷

Table 5.8. XPS data on select M:TiO₂ products after use in photocatalytic hydrogen evolution.

Sample	M:Ti:O:Cl (at%)	M 2p _{3/2} (eV)	Ti 2p _{3/2} (eV)
Co(2%):TiO ₂	0 : 31.2 : 68.8 : 0	n/a	458.34
Ni(2%):TiO ₂	0 : 29.21 : 70.79 : 0	n/a	458.50
Cu(2%):TiO ₂	0.34 : 29.45 : 70.22 : 0	Cu: 932.61	458.31
Ni(1%)/Cu(1%):TiO ₂	0 / 0.45 : 30.73 : 68.64: 0.15	Cu: 932.4	458.50

In the Ti 2p_{3/2} XPS spectrum of Ni(1%)/Cu(1%):TiO₂, a small peak appeared at 454.9 eV that is consistent with the presence of reduced Ti³⁺ on the surface of this sample.¹⁵¹ The presence of Ti³⁺ sites on TiO₂ has been associated with enhanced photoreduction abilities.¹⁵⁹⁻¹⁶⁰ As noted earlier, the copper photodeposition preference may be due to its ease in reduction relative to Co²⁺, Ni²⁺, or H⁺. The Ti⁴⁺/Ti³⁺ reduction is slightly less favored than H⁺ reduction and control experiments with P25-TiO₂ alone under UV illumination in methanol solution undergoes no visible change in color or enhanced hydrogen evolution activity (see P25-TiO₂ sample in Figure 5.7).¹⁵⁰ Thus, if

present, Ti^{3+} is not generated in the absence of other metals under the conditions of this work. Given that chloride ions are present on the surface after photodeposition reactions in metal halide solutions, another control experiment with P25- TiO_2 was performed in the presence of $\text{NaCl}(aq)$ under the same aqueous methanol/UV conditions. No detectable changes in H_2 evolution were observed for P25- TiO_2 , indicating that the presence of chloride is not a determining feature of enhanced H_2 evolution from the M: TiO_2 materials.

In-situ photodeposition and hydrogen evolution studies.

Several *in-situ* photocatalytic hydrogen evolution experiments were run with P25- TiO_2 in the presence of MCl_2 in 50% methanol, equivalent to the 1% photodeposition experiments. Cycling data is presented in Figure 5.8 for these single-step deposition/hydrogen evolution experiments. These tests showed that even without the metal previously deposited onto the TiO_2 surface, hydrogen gas is produced very quickly, once some metal surface photodeposition occurs. After the first *in-situ* cycle for CuCl_2 , the titania catalyst developed its characteristic blue color. The *in-situ* copper chloride photocatalytic test showed an average hydrogen evolution rate of $29 \mu\text{mol/h}$ ($2,900 \mu\text{mol h}^{-1} \text{g}^{-1}$, 5 times higher than P25- TiO_2 alone) that is higher than observed in other *in-situ* Cu: TiO_2 studies ($\sim 1,500 \mu\text{mol h}^{-1} \text{g}^{-1}$),¹⁴⁹ but about one-third of that observed for the isolated Cu(1%): TiO_2 material described above. Related titania experiments have shown that the addition of copper sulfate to a titania suspension also improves the rate of hydrogen evolution to $2,200 \mu\text{mol h}^{-1} \text{g}^{-1}$.¹⁴⁸ The initial rates for the *in-situ* Co and Ni tests were comparable to values for the isolated Co(1%) and Ni(1%): TiO_2 materials, but dropped in activity over four cycles. This loss of activity is comparable to that observed

for the isolated Co(1%):TiO₂ sample, but the activity of the isolated Ni(1%):TiO₂ catalyst was more stable under UV photocatalytic cycling than shown by the *in situ* test.

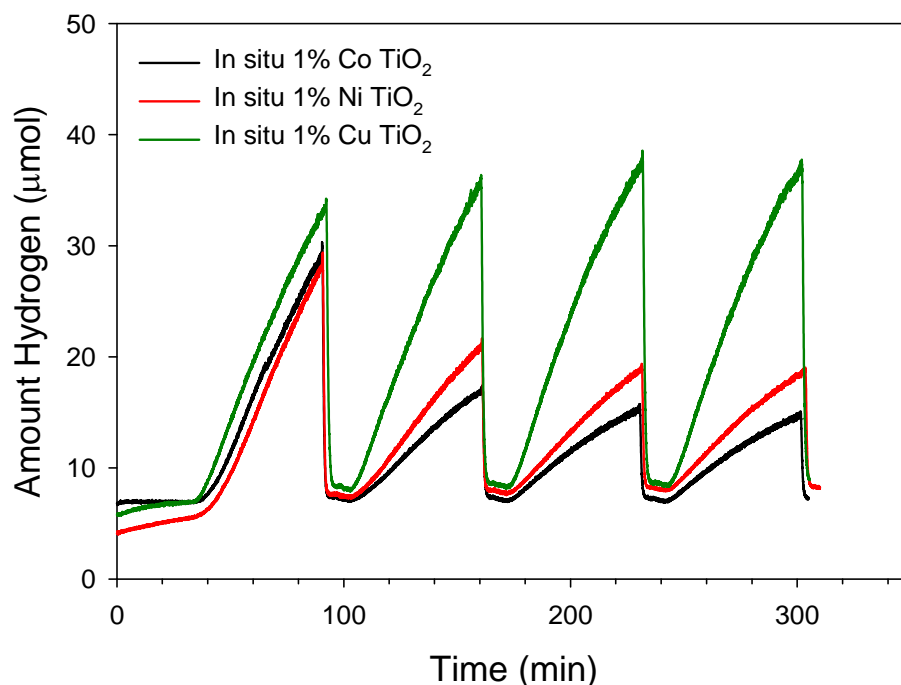


Figure 5.8 – *In-situ* metal deposition and hydrogen evolution data, average rates for all 4 cycles (μmol/h) are Co 12.2, Ni 15.8, and Cu 28.3. H₂ production was measured during 1 hour illumination cycles followed by a 10 minute argon flush. Each illumination cycle began at the 30, 100, 170, and 240 minute marks.

An *in-situ* Cu(1%):TiO₂ experiment was also performed in 18 MΩ water to verify the importance of methanol as a sacrificial oxidant in this photochemical reaction. Two UV illumination cycles (P25-TiO₂, 1 wt% CuCl₂, pure water) were run without methanol, and there was no visible titania color change and no detectable H₂ production by RGA-MS analysis (Figure 5.9). After the second illumination cycle, methanol was spiked into solution and this produced detectable H₂ evolution, and a titania color change was

observed during a third UV illumination cycle. This test confirmed the importance of a sacrificial oxidant for both the photo-assisted copper surface deposition/reduction and hydrogen generation processes.

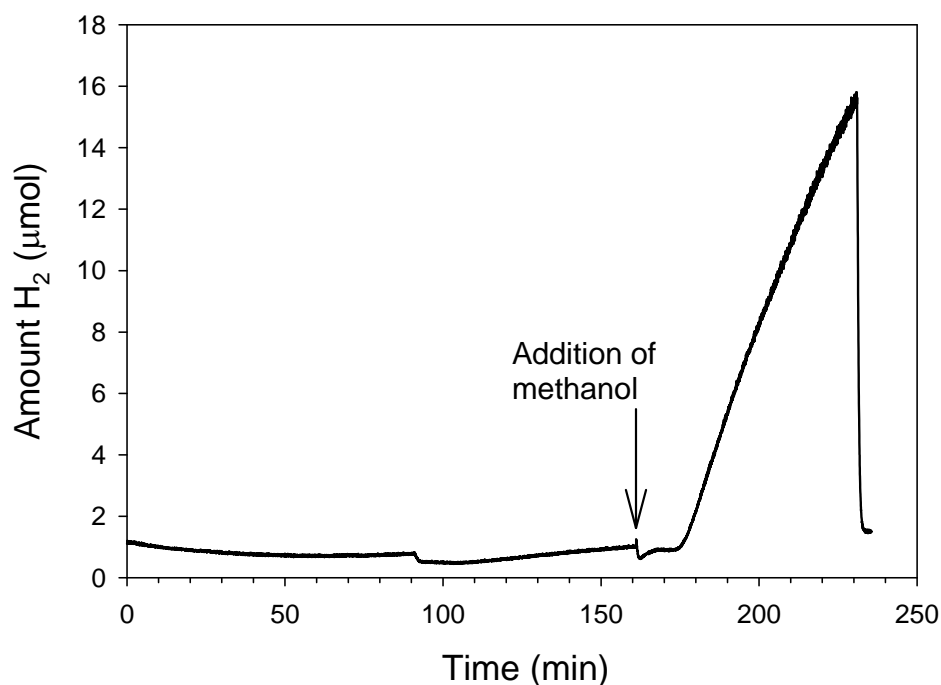
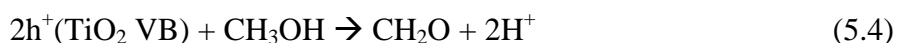
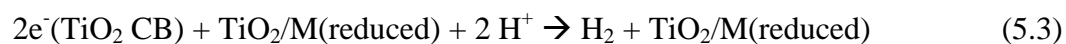
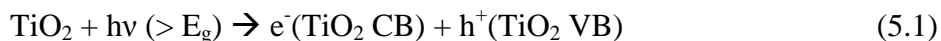


Figure 5.9 – *In-situ* copper UV photodeposition and hydrogen evolution in 18 MΩ water. First UV lamp on cycle began near 30 min and ended at 90 min. Reactor headspace was flushed with argon between UV illumination runs. Second UV lamp on cycle began at 100 min and ended at 160 min. Methanol is spiked into solution during the argon flush prior to the third cycle.

Photocatalytic considerations.

The conduction band energy for anatase TiO₂ is energetically well-suited for the solution reduction of H⁺ to H₂. One of the primary limitations on its activity is the fast charge recombination of photoexcited electrons in the conduction band (CB) with holes in the valence band (VB), before they are utilized in external redox reactions. The addition of metal or metal oxide to the TiO₂ surface provides a pathway to transfer

photogenerated electrons from the TiO₂ CB to the surface-bound metal (or metal ion) co-catalyst that facilitates hydrogen reduction. In the absence of a photocatalyst, the overall reaction of CH₃OH with water to produce CO₂ and H₂ is a thermochemically uphill process, with a calculated ΔH_{rxn} of +53 kJ/mol using standard enthalpy of formation values. One study estimated the endothermic free energy of +16 kJ/mol for this reaction in the absence of a catalyst.¹³⁰ Based on the relatively-low energy redox processes for Co, Ni, and Cu ions in solution and metals on titania particles, the enhanced photocatalytic activity of these heterojunction semiconductor composites is usually attributed to the 3d metal engaging in surface redox reactions that lead to H⁺ to H₂ reduction. During UV illumination, there is a continuous flow of conduction band electrons from TiO₂ to the surface metal co-catalyst that enables reduction processes, which could transiently involve the metal (e.g., metal oxide to metal particles) as well as the H⁺/H₂ reduction. Given the different reduction potentials for Co and Ni versus Cu, there may be different surface reactions occurring, for example, H₂ from Ni or Co systems via transient production of nanoscale metals that reoxidize during H₂ production versus H₂ production from metallic copper particle surfaces. These general heterojunction photoreactions have been proposed in several related previous systems.^{148-149, 155-156} The general reaction steps described for these photocatalytic redox reactions are given in Equations 5.1 through 5.4.



In this work, the lower activity of our photodeposited M:TiO₂ samples for Co or Ni versus Cu can be attributed to the (a) differing amounts of metal species on the TiO₂ surface and (b) differences in metal ion redox activity versus hydrogen reduction. In this photocatalytic metal species deposition, there appears to be an upper limit for metal deposition that competes with hydrogen gas formation. Other studies have also shown that catalytic activity of surface-deposited metals or metal oxides/hydroxides peaks at low metal content (~0.2-0.5 mol% M) and then drops in activity overlap of reactive surface sites, such as with Ni(OH)₂ and Cu(OH)₂ cluster depositions on TiO₂.¹⁵⁵⁻¹⁵⁶ As demonstrated in the *in-situ* test, the presence of methanol plays a crucial supporting role in the overall photocatalytic reaction. While hydrogen is reduced, methanol is oxidized stepwise to formaldehyde and formic acid by holes in the valence band of TiO₂, eventually forming CO₂.^{130, 161} This occurs in preference to the oxidation of water, which would limit overall hydrogen production due to back reaction between hydrogen and oxygen.

5.4 Conclusions

This chapter has described a facile method of modifying commercial P25-TiO₂ to improve its activity for photocatalytic hydrogen production. The photodeposition of Mn, Fe, Co, Ni, or Cu onto the surface of TiO₂ led to visible optical absorption properties. Compositional analysis showed that low metal contents (~0.04 - 1 at% of bulk material, highest for copper) are photodeposited onto the TiO₂ surface, but this surface modification is sufficient to show beneficial effects on the utilization of titania conduction band electrons for photocatalytic hydrogen reduction using methanol as a

sacrificial oxidant. The rate of UV photocatalytic hydrogen production was improved to as high as $8,500 \mu\text{mol h}^{-1} \text{g}^{-1}$ (7% QY) for Cu(1%):TiO₂ versus $500 \mu\text{mol h}^{-1} \text{g}^{-1}$ (0.4% quantum yield) for P25-TiO₂. Direct atmospheric-pressure headspace gas sampling by portable mass spectrometry was demonstrated as a useful portable tool for real-time monitoring of reactor headspaces and quantification of hydrogen gas production.

CHAPTER 6

PRELIMINARY STUDIES ON METAL NITRIDES, SILICA ETCHING, SELECTIVE ORGANIC PHOTO-OXIDATIONS, CONCLUSIONS, AND FUTURE OUTLOOK

6.1 Introduction

Transition metal nitrides have applications in battery materials and a number of catalytic and electrocatalytic reactions, including hydrogen and oxygen evolution reactions.¹⁶²⁻¹⁶⁶ Nickel nitride (Ni_3N), cobalt nitride (Co_4N), and copper nitride (Cu_3N) can be prepared from the reaction between the reduced metal, halide, or amide salts with ammonia.^{163-164, 167-168} However, these materials are metastable and decompose to the reduced metal and nitrogen gas between temperatures of 300-400 °C.¹⁶⁷

C_3N_4 is a potential nitrogen reagent for the formation of metal nitrides. Al-Ga-N and Ti-V-N have been formed from their respective chlorides using C_3N_4 as a reactive nitrogen support.¹⁶⁹ Ta_3N_5 has been prepared using C_3N_4 as a template, but also utilized ammonia during synthesis.¹⁷⁰ However, this work utilized the full decomposition of C_3N_4 at 800 °C to generate a reactive nitrogen containing atmosphere for nitridation. Considering the previously-described transition metal nitrides both formed and decomposed at lower temperatures, it may be possible to use C_3N_4 as the nitrogen source and keep it as an intact support after the synthesis.

Chapter 4 described the preparation of carbon nitride on a silica support ($\text{C}_3\text{N}_4@\text{SiO}_2$) to take advantage of its high surface area. The removal of this support should further increase available surface area by generating new pores into the morphology of C_3N_4 , as shown by the salt templating described in Chapter 3. The

removal of the SiO₂ template often utilizes HF as an etchant, giving ordered porous materials with surface areas on the order of 100 m² g⁻¹.^{81, 107, 171}

The photocatalytic reactions discussed in the previous chapters have either been the oxidative degradation of dyes or hydrogen evolution from water-splitting. C₃N₄ has also been used as a catalyst or photocatalyst in the functionalization of benzene,^{98, 172} cyclization of nitriles and alkynes,⁹⁹ and different organic coupling and oxidation reactions.^{76, 173-175}

6.2 Experimental

Reagents

Trichloromelamine (C₃N₃(NHCl)₃, TCM, 98%) was purchased from GFS Chemical and stored in an argon atmosphere glovebox. Other reagents used as received were TiO₂ (Degussa P25), FeCl₂·4H₂O (Aldrich, 99%), CoCl₂·6H₂O (Aldrich, reagent grade), NiCl₂·6H₂O (Aldrich, ReagentPlus), CuCl₂·2H₂O (Aldrich, 99+%), H₂PtCl₆·6H₂O (99.9%, Strem), methanol (Fisher, ACS certified), benzene (Fisher, laboratory grade), toluene (Fisher, ACS certified), and hexanol (Aldrich, 98%). Deionized water (18 MΩ) was prepared using a Photronix MiniQuad system. Sodium hydroxide solution (6 M) was prepared from dissolving 48 g of sodium hydroxide pellets (Macron Fine Chemical) in 200 mL of deionized water.

Metal nitride formation on C₃N₄

FeCl₂·4H₂O, CoCl₂·6H₂O, NiCl₂·6H₂O, and CuCl₂·2H₂O were used as potential precursors for metal nitride formation. The MCl₂ salt (150 mg) was dissolved in 20 mL

of methanol. C_3N_4 (150 mg, TCM Parr product, see Chapter 2) was added to this solution and the mixture was stirred for 2 hours. The solution was left open in air overnight to allow the methanol to evaporate and deposit the MCl_2 onto C_3N_4 . The dry-coated solid was transferred into an alumina boat and was placed in a Pyrex tube closed on one end. The tube was connected to a Schlenk line, evacuated, and refilled with argon. The tube was placed into a clamshell furnace and heated to 500 °C at a rate of 10 °C/min and held for 1 hour. A dark brown solid was recovered (~38-50% by mass).

Etching of silica from $C_3N_4@SiO_2$

$C_3N_4@SiO_2$ prepared from the Schlenk reactor method (detailed in Chapter 4) was washed with sodium hydroxide to remove the SiO_2 support. $C_3N_4@SiO_2$ (150-300 mg) was put into a 100 mL round bottom flask and the mixture was stirred in 50 mL of 6 M NaOH overnight. Centrifugation (3000 rpm) was used to isolate the solid. The solid was rinsed with additional water over a Büchner funnel, followed by a methanol rinse, and allowed to dry in air. The color of the recovered solid varied, but was usually darker than the initial $C_3N_4@SiO_2$. Mass recovery ranged from 5-30%.

Photocatalytic oxidation of small organic molecules

C_3N_4 , $C_3N_4@TiO_2$, and TiO_2 were used as catalysts in the attempted vapor-phase oxidations of different organic molecules. The catalyst (10-20 mg) was either placed into a 1 cm diameter glass cup or deposited onto a microscope slide from an acetone slurry, and then placed inside a gas IR cell. The assembled cell was first purged with nitrogen in order to collect a background. Then oxygen saturated with hexanol, benzene, or toluene

vapors was flowed through the cell. A spectrum was collected to observe the initial peak signals of the organic species. The cell was exposed to UV by two different methods. The first used a 25 W UV pen lamp kept in the IR sample chamber with the gas cell. The lamp was turned on and spectra were collected every 15 minutes for up to 3 hours. The second method used a larger UV lamp (Ace-Hanovia, 450 W Hg), which required the gas cell to be moved from the lamp cabinet in order to collect spectra. The lamp was turned on in 30 minute intervals for up to 4 hours of total illumination. An IR spectrum of the catalyst was taken after the reaction to check for adsorbed organics.

Characterization

FT-IR spectra were collected on a Nicolet Nexus 670. Solid samples were prepared as KBr pellets for data collection. Photocatalytic vapor measurements were collected in a 10 cm long gas IR cell with KBr windows. Elemental analysis was performed on a Perkin Elmer 2400 Series II CHNS/O Analyzer, with 1-2 mg of sample in crimped tin capsules. Powder X-ray diffraction was collected on a Bruker D8 system (source Cu K α , 5-80°, 0.050 °/step) with samples deposited on glass slides. Solid state ^{13}C and ^{15}N CP-MAS-NMR spectra were collected on a 500 MHz Bruker spectrometer. Thermogravimetric analysis was performed on a Seiko Exstar 6300 TGA-DTA. Samples were heated up to 1000°C at a rate of 10°C/min under air or argon flow.

6.3 Results and Discussion

Metal nitrides on C₃N₄

The inert annealing of different metal chlorides (Fe, Co, Ni, Cu) deposited on the surface of C₃N₄ produced several dark-brown or black products. In addition to the white film of NH₄Cl observed from the annealing of C₃N₄, condensation of water droplets was observed on the cool end of the tube from the waters of hydration from the starting metal chloride. XRD of these products only showed the formation of a crystalline nitride phase for the reaction with nickel (Figure 6.1). Ni₃N is reported to degrade above 440 °C to Ni metal and nitrogen gas.¹⁷⁶ Since this Ni₃N remained crystalline up to 500 °C, it is possible that the presence of the volatiles from C₃N₄ during the annealing reaction stabilized it at the higher temperature. The remaining metals did not show any crystalline peaks, even for the starting chloride.

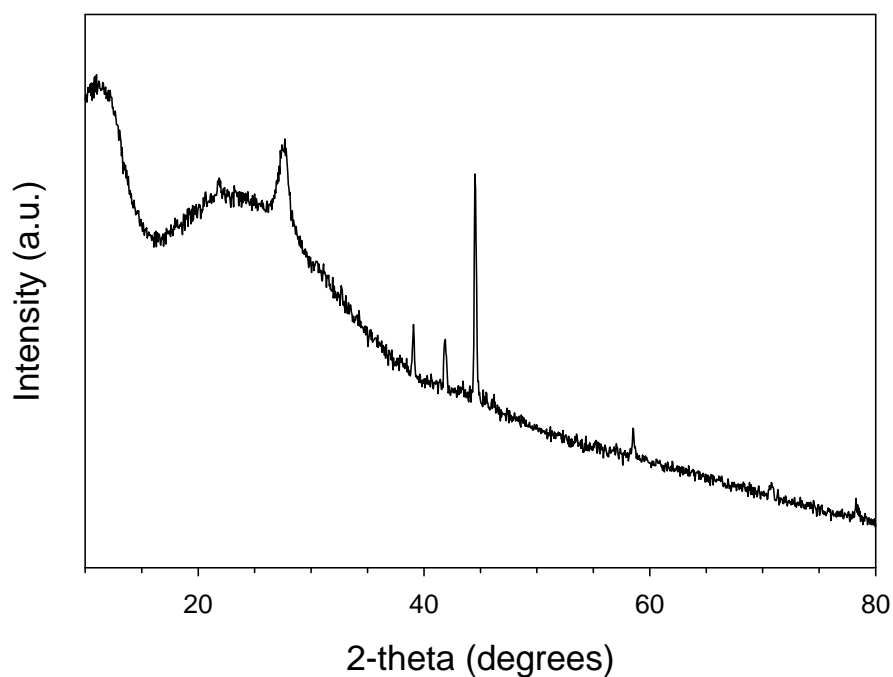


Figure 6.1 – XRD pattern of Ni₃N on C₃N₄ prepared from annealing NiCl₂·6H₂O on C₃N₄ at 500 °C under argon.

Considering the significant color change from annealing, it is likely that the metals underwent some degree of reduction, even if not to the nitride. It is possible that the nitrides may have formed at lower temperatures, but unlike Ni_3N , decomposed by the annealing temperature at 500 °C. TGA analysis showed residual mass for the samples after heating to 1000 °C in air, and the remaining residues were collected from the TGA pan. XRD analysis of these residues showed formation of the respective metal oxides. These phases and colors of the initial products and oxidation residues are summarized in Table 6.1. The presence of the metal oxide in this residue confirms the metal is on the surface of C_3N_4 in some form after the inert anneal. Since there are no identifiable peaks, it is possible that the metals reduced to a nanocrystalline form. If the crystallite size was small enough, the peaks in the XRD could have broadened enough to be lost in the baseline.

Table 6.1. Summary of XRD phases observed for annealing reactions between C_3N_4 and MCl_2 .

Sample	XRD after argon anneal	Color	XRD after air TGA	Residue color	% Mass remaining in TGA
$\text{C}_3\text{N}_4 + \text{NiCl}_2$	Ni_3N	Dark brown	NiO	Green or brown	28.7
$\text{C}_3\text{N}_4 + \text{CuCl}_2$	n/a	Dark brown	CuO	Black	35.6
$\text{C}_3\text{N}_4 + \text{FeCl}_2$	n/a	Brown	Fe_2O_3	Red-brown	37.8
$\text{C}_3\text{N}_4 + \text{CoCl}_2$	n/a	Dark brown	Co_3O_4	Black	19.1

Etching of SiO₂ from C₃N₄@SiO₂

As described in Chapter 4, the starting C₃N₄@SiO₂ Schlenk products were light-yellow in color and required higher reaction temperatures than TCM in the absence of SiO₂. These products also had features in the IR spectrum resembling more triazine-like properties (Figure 6.2a). Washing these in NaOH was successful in removing the SiO₂ support, but there were distinct changes in the remaining C₃N₄. The washed products were notably darker than the original C₃N₄@SiO₂, and had a mass recovery lower than what was expected based on the estimated C₃N₄ content from elemental analysis and TGA. The IR spectrum of the washed product (Figure 6.2b) confirmed the removal of the SiO₂ due to the absence of the large peak at 1000 cm⁻¹. The broad peak above 3200 cm⁻¹ is representative of N-H stretching. Unlike unmodified C₃N₄, there was a single broad signal from 1200-1700 cm⁻¹ for the C-N and C=N stretches. The peak at 1600 cm⁻¹ is slightly more pronounced than the rest of this broad signal. This lack of sharply-defined features in this region may indicate poorly-defined structural ordering. The peak at 800 cm⁻¹ for the ring breathing mode remained intact after the wash.

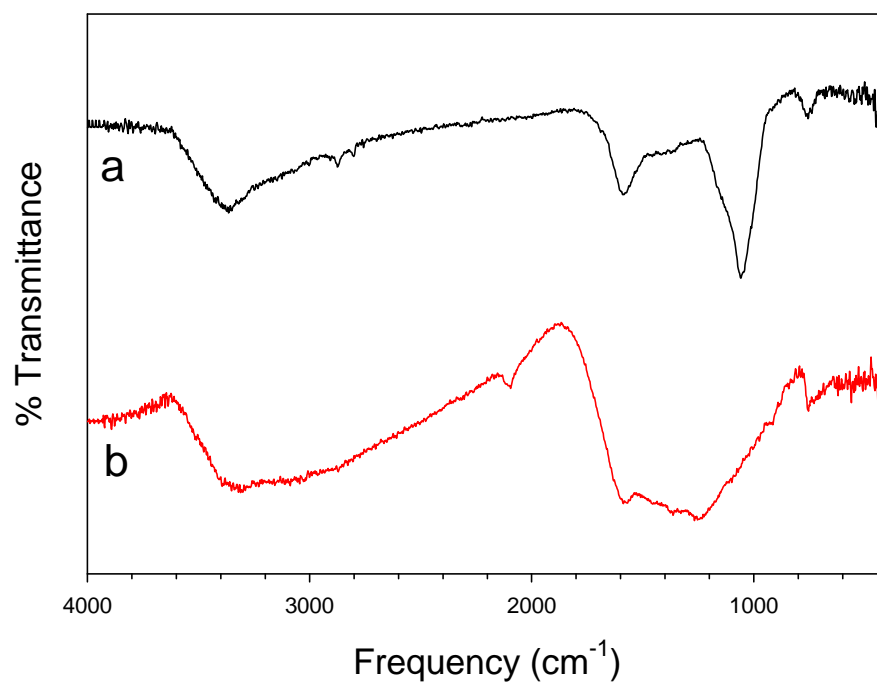


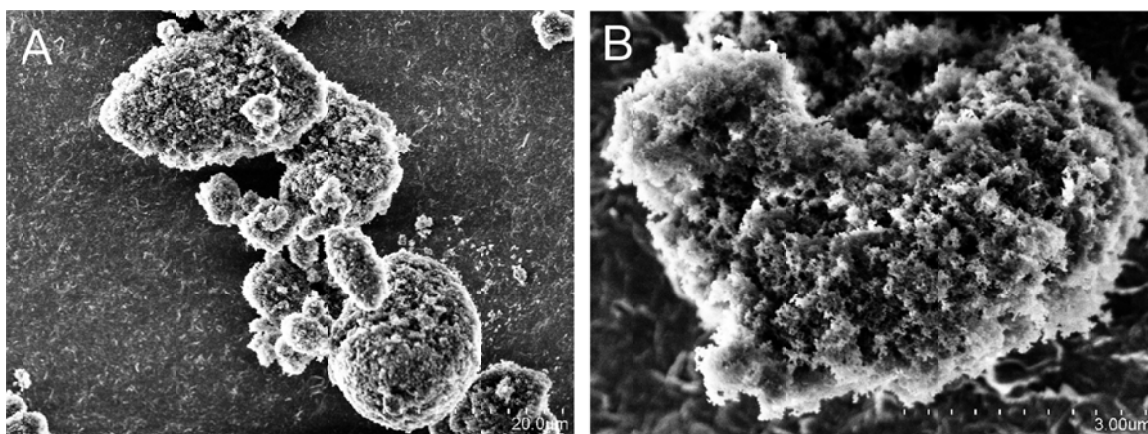
Figure 6.2 – IR spectra of (a) C₃N₄@SiO₂ and (b) the 6M NaOH washed product to etch the SiO₂.

Elemental analysis of two sets of C₃N₄@SiO₂ and etched products is summarized in Table 6.2. Each washed product showed a similar change of total CHN content after the removal of SiO₂, increasing from ~27% to above 70%. There was still a large amount of unanalyzed mass, which could be from additional oxygen content. C₃N₄ products have been shown to undergo base hydrolysis at high temperatures.⁶⁹ Since C₃N₄@SiO₂ has been shown to have difficulty reaching reaction completion, it is possible this product was more susceptible to hydrolysis at room temperature. In addition to the change in total CHN content, the composition also changed. The washed products contained less nitrogen and hydrogen than the starting products. If the products did undergo hydrolysis, a loss of terminal NH₂ sites could account for the decrease in nitrogen and hydrogen.

Table 6.2. CHN elemental analysis of $C_3N_4@SiO_2$ and etched products.

Sample	C wt%	N wt%	H wt%	Total wt%	Composition
$C_3N_4@SiO_2$	8.60	17.09	1.93	27.62	$C_3N_{5.1}H_8$
Etched C_3N_4	24.76	45.20	3.42	73.38	$C_3N_{4.7}H_{5.0}$
$C_3N_4@SiO_2$	8.90	17.44	1.23	27.57	$C_3N_{5.0}H_{5.0}$
Etched C_3N_4	25.83	42.03	3.54	71.40	$C_3N_{4.2}H_{4.9}$

The morphology of the etched C_3N_4 product was investigated using SEM (Figure 6.3). Similar to other C_3N_4 products, these formed 5-20 μm aggregates. The surface of these particles has a very moss-like appearance. The thin component flakes have dimensions less than 100 nm.

Figure 6.3 – SEM images of $C_3N_4@SiO_2$ after etching with NaOH.

Photocatalytic oxidations in the vapor phase

The photocatalytic oxidations of different organic molecules in the vapor phase were attempted. The reagents and targets molecules are summarized in Figure 6.4.

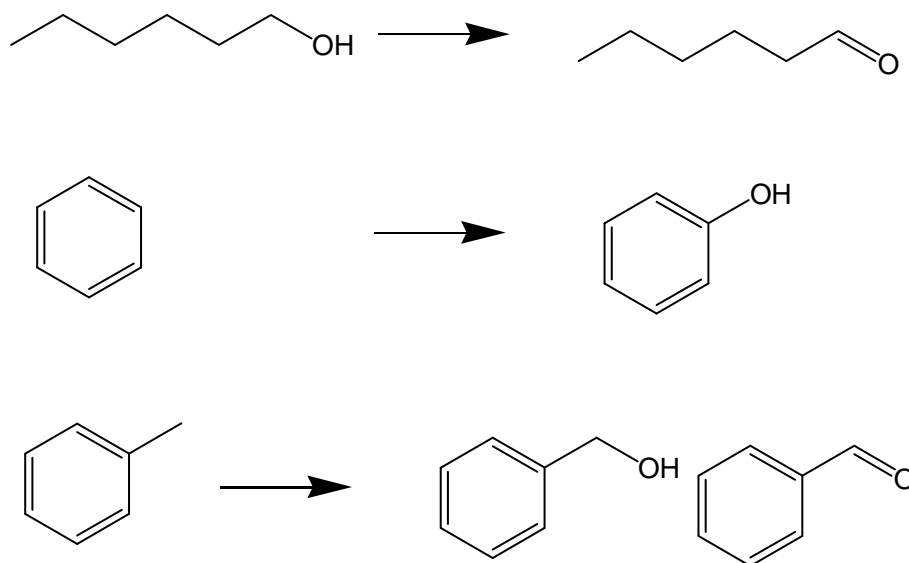


Figure 6.4 – Targeted photocatalytic oxidations of small organic molecules using C_3N_4 -based catalysts.

The reactions were attempted at room temperature using two different intensities of UV light. Very little change was observed for any of the catalyst and starting reagent combinations in the reaction set-up using the 25 W UV lamp. When reactions were illuminated with the 450 W lamp, the absorption for carbon dioxide grew in at 2380 cm^{-1} , indicating the formation of the total oxidation product rather than the target intermediates. Figure 6.5 shows the initial and final IR spectra of benzene using $C_3N_4@TiO_2$ catalyst with the 450 W lamp. While there was some conversion, the photocatalytic reaction was not selective. In order to achieve better selectivity for the partial oxidation products, a milder oxidant might be more suitable rather than performing the reaction in oxygen atmosphere. Depending on how accessible the surface of C_3N_4 is to adsorption of the analyte, catalysis in the vapor phase might not be efficient.

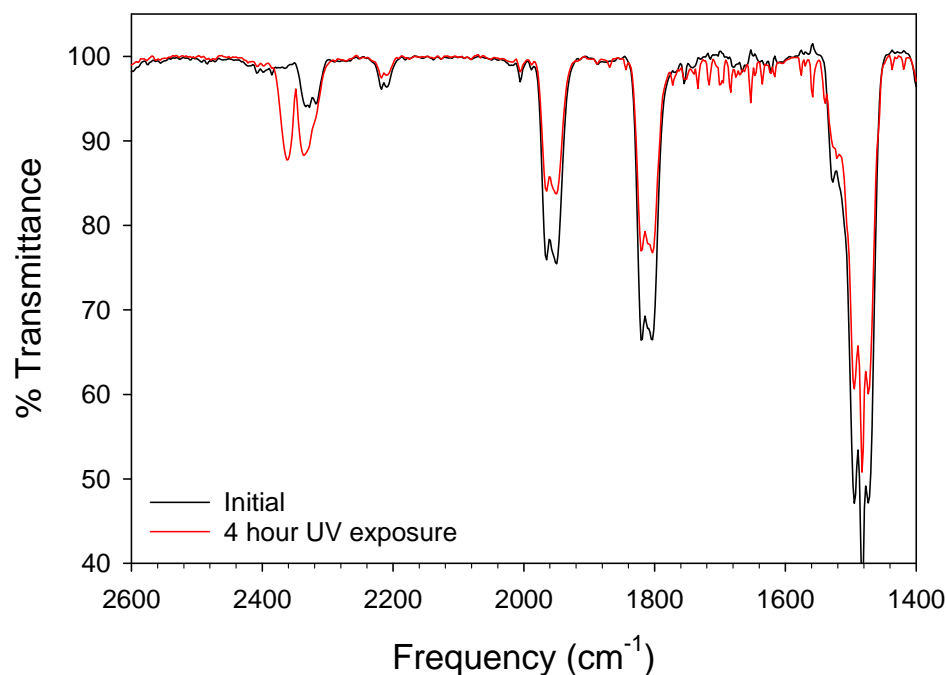


Figure 6.5 – IR spectra of benzene vapor before and after 4 hour UV light (450 W Hg) illumination in the presence of $C_3N_4@TiO_2$.

6.4 Overall Thesis Summary and Conclusions

C_3N_4 can be prepared under several different reaction conditions from a trichloromelamine precursor. These products share many properties with those produced from other common literature precursors. There are some clear differences in the band structure, which accounts for some of the observed differences in photocatalytic activity. Other differences include variations in surface area and the quantity of platinum co-catalyst successfully deposited. Increasing amounts of platinum (up to 0.5 wt%) on C_3N_4 from a given synthetic method showed an increase in hydrogen evolution activity. If higher amounts of platinum loading can be achieved, a more optimal loading could be identified. Higher surface area also increased catalytic rates, though even samples with comparable surface areas differed in activity depending on the synthetic route.

The use of salt templates was successful in generating C_3N_4 products with rougher, more porous surface morphologies. Several of the salts completed an exchange reaction with TCM, which resulted in different colored products than using the unmodified precursor. The products formed from TCM mixtures with KI and NH_4SCN salts showed the greatest improvement for the photocatalytic production of hydrogen over unmodified C_3N_4 , mostly attributed to the increase in surface area.

C_3N_4 composites supported on different metal oxides required higher synthesis temperatures in order to ensure complete reactions. Higher-temperature synthesis using WO_3 as a support resulted in a phase change to H_xWO_3 . To work around this phase change, C_3N_4 was used as the support for the formation of WO_3 at lower temperatures. The composites with SiO_2 and Al_2O_3 showed a notable increase in surface area over unmodified C_3N_4 , which contributed to a higher degree of dye adsorption during the dark stir in dye degradation tests. This adsorption contributed to a higher rate of oxidation in the presence of UV light.

The surface modification of TiO_2 provided very-active photocatalysts for hydrogen evolution. This presents an attractive alternative to the use of platinum as a co-catalyst. Modification with copper, even with lower than the targeted quantities, had the greatest effect on hydrogen evolution, which is very promising considering copper's much higher abundance than platinum.

6.5 Future Outlook

C_3N_4 materials present continued opportunities in future photocatalytic reactions. Besides the dye degradation and hydrogen evolution reactions detailed in this thesis,

there are many other reactions to explore. The preliminary oxidation reactions discussed in this chapter are in need of optimization. Besides adjustments to the reaction parameters, the other composite and salt templates C_3N_4 products could also be active in these reactions. Investigation of the luminescent properties of C_3N_4 could give insights to the life-time of the photo-excited electrons. A shorter excitation life-time would support the low hydrogen evolution activity in the absence of co-catalyst to aid in charge carrier separation. This could show additional differences between the TCM-salt derived C_3N_4 products.

Work on the formation of transition metal nitrides on the surface of C_3N_4 should be continued. Ni_3N has been observed from 500 °C inert heating between C_3N_4 and $NiCl_2$, but these conditions did not work for Fe, Co, or Cu. Lower-temperatures should be tested to see if the nitride phase can form before higher-temperature decomposition. If the remaining nitrides can be formed, this opens up additional catalytic systems to study. Since the metal nitrides are more conductive than C_3N_4 , they can be tested for electrochemical applications. With C_3N_4 as a photoactive support, photoelectrochemical reactions could be tested, where C_3N_4 can provide photogenerated electrons and the conducting nitride can better transport the charge. Even if the metal nitride cannot be stabilized, the presence of the reduced metal may still have use as a co-catalyst on the surface of C_3N_4 in photocatalytic reactions. The presence of the conducting metal could also be useful in electrochemical applications. The $C_3N_4@H_xWO_3$ composite could also be useful in these applications.

The modification of TiO_2 by surface photoreduction of first-row transition metals provided highly-active catalysts for hydrogen evolution. This work only modified

commercial TiO₂. Since our group has prepared TiO₂ using botanical and other natural templates, exploring the same surface modification with these unique morphological structures could show further enhancement of catalytic activity.

APPENDIX

A.1 Photocatalytic Hydrogen Evolution*Signal calibration*

Residual gas analysis mass spectrometry was used as the method of measuring the amount of hydrogen produced during photocatalytic reactions. The raw signal reported from the instrument was pressure (in Torr), while hydrogen quantification is typically reported in μmol or mmol . In order to convert this pressure signal to μmol , a signal calibration method was developed using known mixtures of hydrogen and argon within the reaction flask used for photocatalysis.

A 50 mL Schlenk flask was filled with 10 mL of water in order to account for the liquid volume present during photocatalytic reactions. The flask was capped with a septum and purged with argon. A second flask was filled with hydrogen, and a syringe was used to transfer 0.5, 1, 2, and 5 mL volumes to the argon-filled Schlenk flask. The gas mixture in the flask was sampled with the RGA capillary while scanning on Pressure vs. Time mode (mass 40 and 2). The flask was re-purged with argon before each addition of a different volume of hydrogen.

While a 50 mL Schlenk flask was used for this calibration, the true total volume including the headspace in the neck of the flask was 70 mL. Accounting for the 10 mL of water added to the flask, the total gas volume available was 60 mL. The volume % of hydrogen within the flask was determined for each volume addition used. The ratio of the partial pressures for hydrogen and argon (p_{H_2} and p_{Ar}) were also calculated. These values are presented in Table A.1. Plotting $p_{\text{H}_2}/p_{\text{Ar}}$ against the vol.% H_2 gave the linear calibration in Figure A.1.

Table A.1. Volume additions of hydrogen and corresponding pressure signals for hydrogen and argon used for calibration.

vol H ₂	vol% H ₂	pH ₂	pAr	pH ₂ /Ar
0.5	0.83	2.34×10^{-7}	1.04×10^{-6}	0.225
1	1.67	4.42×10^{-7}	1.04×10^{-6}	0.426
2	3.33	8.22×10^{-7}	1.04×10^{-6}	0.791
5	8.33	2.06×10^{-6}	9.91×10^{-7}	2.08

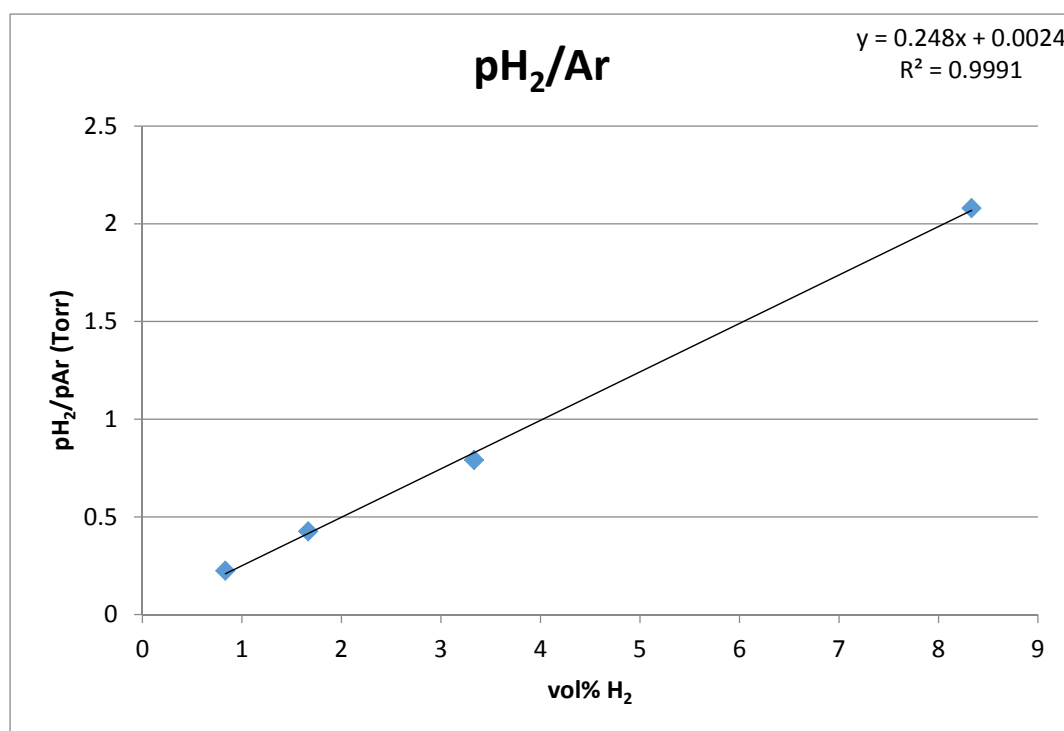


Figure A.1 – Linear calibration for the quantification of hydrogen using RGA-MS.

With this calibration fit, data from each photocatalytic hydrogen evolution experiment can be used to calculate the μmol amount of hydrogen. First the pressure signals in each experiment and the calibration fit can give a value for the volume% of hydrogen. The volume% multiplied by the headspace volume of 60 mL gives the volume

of hydrogen detected. The moles of gas can be calculated from the volume using the ideal gas law.

Photocatalysis set-up

While the main chapters of the thesis have described the methods used for photocatalytic hydrogen evolution, a more detailed description of the reactor design will be given here. Once the methanol or triethanolamine solution and catalyst were placed into the Schlenk flask, the solution was degassed by bubbling argon through a needle for 5-10 minutes. After this the flask was placed into the reactor cabinet and connected via gas inlet adapter to the Schlenk line (Figure A.2). The capillary from the RGA was connected to the side-arm of the flask using a quick connect fitting. During this time, data was collected in broad spectrum mode to observe the stabilization of the argon background and reduction of other atmospheric signals (N_2 , O_2 , H_2O , CO_2). When the background stabilized, the instrument was switched to a Pressure vs Time scan, selecting masses 28, 40, 2, 1, 18, 32, and 44, and changing from triggered to continuous scanning. In between illumination cycles, the produced hydrogen was vented from the flask by disconnecting the quick connect between the flask and RGA. It is important to keep the capillary close to the side arm while venting the hydrogen, in order to maintain the argon background and minimize the amount atmospheric gases that could leak in.

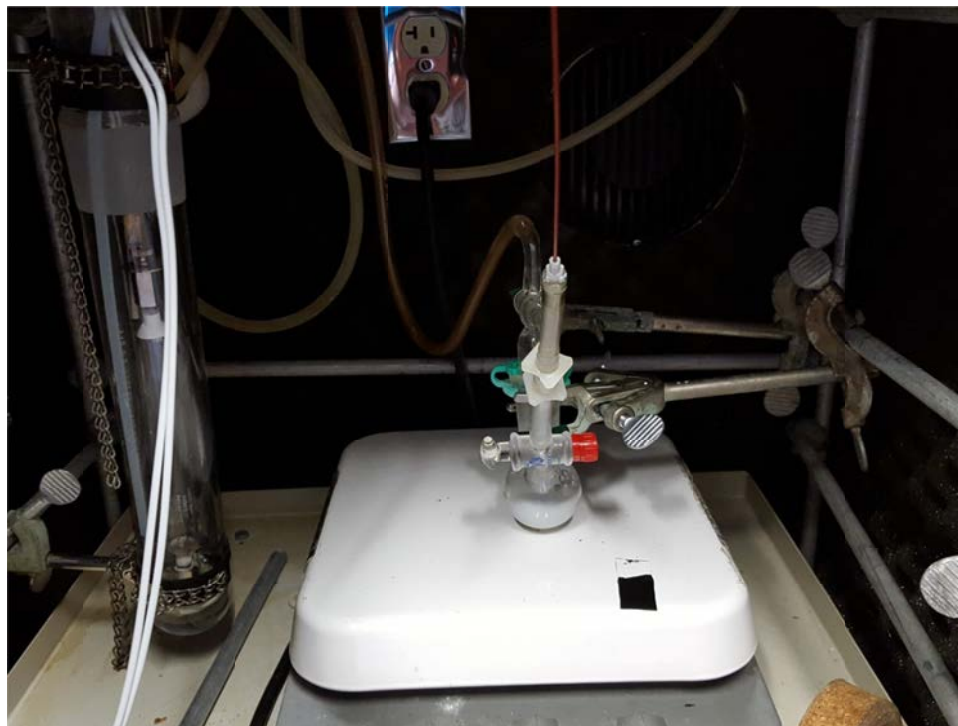


Figure A.2 – Photo of Schlenk flask inside the photoreactor cabinet. The hose connected to the gas inlet adapter is connected to an argon Schlenk line in the adjacent hood. The side-arm is connected to the sampling capillary from the RGA-MS. The flask is clamped above the stir plate, positioned 20 cm from the UV lamp.

A.2 Quantum Yield Calculations

Quantum yield is defined by the ratio between the number of molecules produced or converted per time and the number of incident photons per time (photon flux).

Equation 1 gives an example for the quantum yield of photocatalytic hydrogen production.

$$QY(\%) = \frac{2 \times \text{Hydrogen molecules produced } s^{-1}}{\text{number of incident photons } s^{-1}} \quad (\text{A.1})$$

Photon flux was determined using the manufacturer's reported energy distribution of the radiated mercury lines for a 450 W Ace-Hanovia UV lamp on the exterior surface of the glass cooling jacket. The total power density at the exterior of the water cooling

jacket for wavelengths absorbed greater than the TiO₂ bandgap was 0.426 W cm⁻². Using the energy for mercury emission wavelengths, the power can be converted to number of photons (Equation 2).

$$\Phi(\text{photons } s^{-1} \text{ cm}^{-2}) = \frac{\text{Power density (W cm}^{-2}\text{)}}{\text{Photon energy (J)}} \quad (\text{A.2})$$

Totaled for the reported mercury emission wavelengths, this gives 6.81 x 10¹⁷ photons s⁻¹ cm⁻². The reactor has an illumination area of 19.6 cm² and was a distance of 20 cm from the lamp (17 cm from the jacket exterior). The light intensity decay over this distance was determined using a digital light meter sensitive to the 550 nm emission line (Extech Instruments, LT300), giving a scaling factor of 0.0301. The total number of photons s⁻¹ was then calculated using equation 3.

$$\begin{aligned} 6.81 \times 10^{17} \text{ photons } s^{-1} \text{ cm}^{-2} \times 19.6 \text{ cm}^2 \times 0.0301 \\ = 4.02 \times 10^{17} \text{ photons } s^{-1} \end{aligned} \quad (\text{A.3})$$

An example of calculating the QY for Cu(1%):TiO₂ (data from Chapter 5) is given in Equations 4 and 5.

$$\begin{aligned} 84.7 \mu\text{mol } h^{-1} \times \frac{1 \text{ mol}}{10^6 \mu\text{mol}} \times \frac{6.022 \times 10^{23} \text{ molecules}}{1 \text{ mol}} \times \frac{1 \text{ h}}{3600 \text{ s}} \\ = 1.41 \times 10^{16} \text{ molecules } s^{-1} \end{aligned} \quad (\text{A.4})$$

$$QY(\%) = \frac{2 \times 1.41 \times 10^{16} \text{ molecules } s^{-1} \text{ hydrogen}}{4.02 \times 10^{17} \text{ photons } s^{-1}} \times 100\% = 7.01\% \quad (\text{A.5})$$

A.3 Protocol for CHN Elemental Analysis

Start-up

1. Check gas connections and that the three gas supplies are open and flowing at the correct pressures (Nitrogen 60 psi, Helium 20 psi, Oxygen 20 psi).
2. Turn on the Perkin Elmer 2400 CHNS/O Analyzer. Enter time (24 hour format), date (dd/mm/yy), and press enter through the rest of the start-up parameters. Press yes when prompted for helium purge and enter 60. Repeat for oxygen. Make sure the exhaust fan is running.
3. Under diagnostics, select gas, then leak tests, and enter "1" to run combustion zone leak test. Repeat, entering "2" for mixing zone leak test. If leak tests fail check connections or manually actuate valves.
4. Enter Parameter 12 and press "1" to turn on the furnace. Wait 2-3 hours for temperatures to stabilize before continuing.

Calibration and sampling (Manual 4-58)

1. Run a minimum of three blanks, until H, N, and C read reproduce within $C \pm 30$, $H \pm 100$, $N \pm 16$. If the instrument has not been in operation for an extended period of time additional runs will be needed as adsorbed water vapors are removed from the gas lines. If the nitrogen blank does not stabilize and significantly increases in magnitude, the reduction tube needs to be changed. Depending on usage, this may occur before the run counters indicate.
2. Weigh samples and standards on microbalance. Use between 1-2 mg for best results.

- a. Tare the balance with empty tin capsules on the weigh pan and the reference pan.
 - b. Add powder into the sample capsule, targeting 1-2 mg.
 - c. Fold capsule shut using tweezers according to the diagram in manual (4-57).
3. Run acetanilide standard, values should fall within tolerances theoretical values (71.09% C, 10.36% N 6.71% H).
- a. If measured values for the standard do not match, a full calibration sequence must be run. For full calibration after first standard, run blank, standard, blank, and three k-factors. Check manual for detailed steps and tolerance values (4-63).
4. Run samples by single run or auto run
- a. Single Run: Load Sample, Enter sample name (letters entered by .xx corresponding to order in alphabet A= .01, Z= .26), enter sample weight, press start
 - b. Auto run: Load samples into carousel and enter name and weight for each sample, then press start. If running more than five samples, leave a space after the fifth sample in the carousel, and insert a blank run in the run sequence.
 - c. Optimize combustion: If samples are graphite-like or are largely inorganic with less than 5% total CHN, enter parameter 9 to optimize combustion timing. Enter 1 and change OXYFILL to 3, enter 2 and change COMB to 10, enter 3 and change OXB1 to 1. Additional recommended values are in

the manual (5-34). After analyzing samples with optimized combustion, return OXYFILL, COMB, and OB1 to default value of 1.

Shutdown

1. Enter parameter 12 and press “2” to turn off the furnace.
2. Enter parameter 22 and press “1” to turn on Gas Saver. Enter a start time 2-3 hours after when the furnace was shut off. Enter an arbitrarily distant end time.
3. If the instrument will not be in immediate use, shut off main power, only if the furnace has reached room temperature. Close all gas valves at the tanks.

Changing the combustion and reduction tubes

1. When the instrument is powered on it will display the remaining run counts for the combustion and reduction tubes. Depending of the parameters of the runs until this point, the reduction tube may need to be replaced before the remaining counts reaches zero.
2. Page 4-6 in the manual describes the necessary reagents and filling method for each tube.
3. Figures A.3A and A.3B show photos of correctly prepared tubes.
4. A full calibration sequence should be run before the next analysis after replacing either the combustion or reduction tubes.

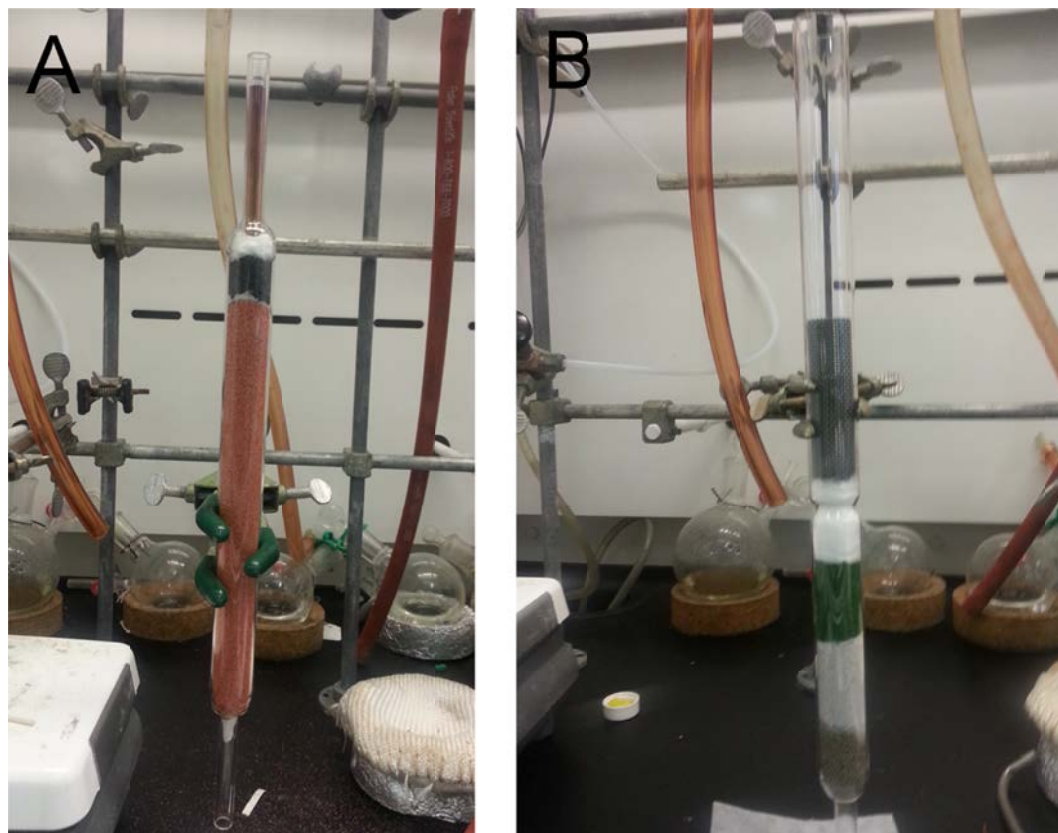


Figure A.3 – Photographs of (A) prepared reduction tube and (B) prepared combustion tube.

REFERENCES

1. Liebig, J. Uber einige stickstoff - verbindungen. *Annalen der Pharmacie* **1834**, 10 (1), 1-47.
2. Gmelin, L. Ueber einige verbindungen des melon's. *Annalen der Pharmacie* **1835**, 15 (3), 252-258.
3. Franklin, E. C. The ammono carbonic acids. *J. Am. Chem. Soc.* **1922**, 44, 486-509.
4. Pauling, L.; Sturdivant, J. H. The structure of cyameluric acid, hydromelonic acid and related substances. *Proceedings of the National Academy of Sciences of the United States of America* **1937**, 23 (12), 615-20.
5. Schroeder, H.; Kober, E. Some reactions of cyameluric chloride. *Journal of Organic Chemistry* **1962**, 27 (12), 4262-&.
6. Redemann, C. E.; Lucas, H. J. Ionization constants and hydrolytic degradations of cyameluric and hydromelonic acids. *J. Am. Chem. Soc.* **1939**, 61 (12), 3420-3425.
7. Redemann, C. E.; Lucas, H. J. Some derivatives of cyameluric acid and probable structures of melam, melem and melon. *J. Am. Chem. Soc.* **1940**, 62 (4), 842-846.
8. Hosmane, R. S.; Rossman, M. A.; Leonard, N. J. Synthesis and structure of tri-s-triazine. *J. Am. Chem. Soc.* **1982**, 104 (20), 5497-5499.
9. Kouvetakis, J.; Kaner, R. B.; Sattler, M. L.; Bartlett, N. A novel graphite-like material of composition bc₃, and nitrogen-carbon graphites. *Journal of the Chemical Society-Chemical Communications* **1986**, (24), 1758-1759.
10. Sekine, T.; Kanda, H.; Bando, Y.; Yokoyama, M.; Hojou, K. A graphitic carbon nitride. *Journal of Materials Science Letters* **1990**, 9 (12), 1376-1378.
11. Liu, A. Y.; Cohen, M. L. Prediction of new low compressibility solids. *Science* **1989**, 245 (4920), 841-2.
12. Han, H.-X.; Feldman, B. J. Structural and optical properties of amorphous carbon nitride. *Solid State Communications* **1988**, 65 (9), 921-923.
13. Maya, L.; Cole, D. R.; Hagaman, E. W. Carbon nitrogen pyrolyzates - attempted preparation of carbon nitride. *Journal of the American Ceramic Society* **1991**, 74 (7), 1686-1688.
14. Kouvetakis, J.; Bandari, A.; Todd, M.; Wilkens, B.; Cave, N. Novel synthetic routes to carbon-nitrogen thin-films. *Chem. Mater.* **1994**, 6 (6), 811-814.

15. Hughbanks, T.; Tian, Y. C. On the structure and composition of carbon nitride. *Solid State Communications* **1995**, *96* (5), 321-325.
16. Kawaguchi, M.; Nozaki, K. Synthesis, structure, and characteristics of the new host material [(c₃n₃)(₂)(nh)(₃)](n). *Chem. Mater.* **1995**, *7* (2), 257-264.
17. Montigaud, H.; Tanguy, B.; Demazeau, G.; Alves, I.; Birot, M.; Dunogues, J. Solvothermal synthesis of the graphitic form of C₃N₄ as macroscopic sample. *Diamond and Related Materials* **1999**, *8* (8-9), 1707-1710.
18. Gillan, E. G. Synthesis of nitrogen-rich carbon nitride networks from an energetic molecular azide precursor. *Chem. Mater.* **2000**, *12* (12), 3906-3912.
19. Khabashesku, V. N.; Zimmerman, J. L.; Margrave, J. L. Powder synthesis and characterization of amorphous carbon nitride. *Chem. Mater.* **2000**, *12* (11), 3264-3270.
20. Komatsu, T. Attempted chemical synthesis of graphite-like carbon nitride. *J. Mater. Chem.* **2001**, *11* (3), 799-801.
21. Miller, D. R.; Wang, J. J.; Gillan, E. G. Rapid, facile synthesis of nitrogen-rich carbon nitride powders. *J. Mater. Chem.* **2002**, *12* (8), 2463-2469.
22. Komatsu, T. The first synthesis and characterization of cyameluric high polymers. *Macromol. Chem. Phys.* **2001**, *202* (1), 19-25.
23. Komatsu, T. Prototype carbon nitrides similar to the symmetric triangular form of melon. *J. Mater. Chem.* **2001**, *11* (3), 802-805.
24. Plass, M. F.; Popov, C.; Ivanov, B.; Mandl, S.; Jelinek, H.; Zambov, L. M.; Kulisch, W. Correlation between photoluminescence, optical and structural properties of amorphous nitrogen-rich carbon nitride films. *Applied Physics a-Materials Science & Processing* **2001**, *72* (1), 21-27.
25. Kroke, E.; Schwarz, M.; Horath-Bordon, E.; Kroll, P.; Noll, B.; Norman, A. D. Tri-s-triazine derivatives. Part i. From trichloro-tri-s-triazine to graphitic C₃N₄ structures. *New Journal of Chemistry* **2002**, *26* (5), 508-512.
26. Jurgens, B.; Irran, E.; Senker, J.; Kroll, P.; Muller, H.; Schnick, W. Melem (2,5,8-triamino-tri-s-triazine), an important intermediate during condensation of melamine rings to graphitic carbon nitride: Synthesis, structure determination by X-ray powder diffractometry, solid-state NMR, and theoretical studies. *J. Am. Chem. Soc.* **2003**, *125* (34), 10288-300.
27. Lotsch, B. V.; Schnick, W. From triazines to heptazines: Novel nonmetal tricyanomelaminates as precursors for graphitic carbon nitride materials. *Chem. Mater.* **2006**, *18* (7), 1891-1900.

28. Wang, J.; Miller, D. R.; Gillan, E. G. Photoluminescent carbon nitride films grown by vapor transport of carbon nitride powders. *Chem Commun (Camb)* **2002**, (19), 2258-9.
29. Cameron, D. C. Optical and electronic properties of carbon nitride. *Surf Coat Tech* **2003**, *169*, 245-250.
30. Deifallah, M.; McMillan, P. F.; Corà, F. Electronic and structural properties of two-dimensional carbon nitride graphenes. *J. Phys. Chem. C* **2008**, *112* (14), 5447-5453.
31. Thomas, A.; Fischer, A.; Goettmann, F.; Antonietti, M.; Müller, J.-O.; Schlögl, R.; Carlsson, J. M. Graphitic carbon nitride materials: Variation of structure and morphology and their use as metal-free catalysts. *J. Mater. Chem.* **2008**, *18* (41), 4893.
32. Cao, S.; Low, J.; Yu, J.; Jaroniec, M. Polymeric photocatalysts based on graphitic carbon nitride. *Adv. Mater.* **2015**, *27* (13), 2150-76.
33. Ong, W. J.; Tan, L. L.; Ng, Y. H.; Yong, S. T.; Chai, S. P. Graphitic carbon nitride (g-C₃N₄)-based photocatalysts for artificial photosynthesis and environmental remediation: Are we a step closer to achieving sustainability? *Chemical reviews* **2016**, *116* (12), 7159-329.
34. Wang, X.; Maeda, K.; Thomas, A.; Takanabe, K.; Xin, G.; Carlsson, J. M.; Domen, K.; Antonietti, M. A metal-free polymeric photocatalyst for hydrogen production from water under visible light. *Nature materials* **2009**, *8* (1), 76-80.
35. Ge, L. Synthesis and photocatalytic performance of novel metal-free g-C₃N₄ photocatalysts. *Materials Letters* **2011**, *65* (17-18), 2652-2654.
36. Dong, F.; Wu, L.; Sun, Y.; Fu, M.; Wu, Z.; Lee, S. C. Efficient synthesis of polymeric g-C₃N₄ layered materials as novel efficient visible light driven photocatalysts. *J. Mater. Chem.* **2011**, *21* (39), 15171.
37. Nakata, K.; Fujishima, A. TiO₂ photocatalysis: Design and applications. *J. Photoch. Photobio. C* **2012**, *13* (3), 169-189.
38. Fujishima, A.; Rao, T. N.; Tryk, D. A. Titanium dioxide photocatalysis. *J. Photoch. Photobio. C* **2000**, *1* (1), 1-21.
39. Fujishima, A.; Honda, K. Electrochemical photolysis of water at a semiconductor electrode. *Nature* **1972**, *238* (5358), 37-38.
40. Ni, M.; Leung, M. K. H.; Leung, D. Y. C.; Sumathy, K. A review and recent developments in photocatalytic water-splitting using TiO₂ for hydrogen production. *Renew Sust Energ Rev* **2007**, *11* (3), 401-425.
41. Fang, W.; Xing, M.; Zhang, J. Modifications on reduced titanium dioxide photocatalysts: A review. *J. Photoch. Photobio. C* **2017**, *32*, 21-39.

42. Dahl, M.; Liu, Y.; Yin, Y. Composite titanium dioxide nanomaterials. *Chem. Rev.* **2014**, *114* (19), 9853-89.
43. Navarro, R. M.; del Valle, F.; Villoria de la Mano, J. A.; Álvarez-Galván, M. C.; Fierro, J. L. G. Photocatalytic water splitting under visible light. **2009**, *36*, 111-143.
44. Kitano, M.; Hara, M. Heterogeneous photocatalytic cleavage of water. *J. Mater. Chem.* **2010**, *20* (4), 627-641.
45. Fox, M. A.; Dulay, M. T. Heterogeneous photocatalysis. *Chem. Rev.* **1993**, *93* (1), 341-357.
46. Kraeutler, B.; Bard, A. J. Heterogeneous photocatalytic preparation of supported catalysts. Photodeposition of platinum on titanium dioxide powder and other substrates. *J. Am. Chem. Soc.* **1978**, *100* (13), 4317-4318.
47. Wenderich, K.; Mul, G. Methods, mechanism, and applications of photodeposition in photocatalysis: A review. *Chem. Rev.* **2016**, *116* (23), 14587-14619.
48. Kabra, K.; Chaudhary, R.; Sawhney, R. L. Solar photocatalytic removal of Cu(II), Ni(II), Zn(II) and Pb(II): Speciation modeling of metal-citric acid complexes. *J. Hazard. Mater.* **2008**, *155* (3), 424-32.
49. Kabra, K.; Chaudhary, R.; Sawhney, R. L. Solar photocatalytic removal of metal ions from industrial wastewater. *Environmental Progress* **2008**, *27* (4), 487-495.
50. Prairie, M. R.; Evans, L. R.; Stange, B. M.; Martinez, S. L. An investigation of titanium dioxide photocatalysis for the treatment of water contaminated with metals and organic chemicals. *Environ. Sci. Technol.* **1993**, *27* (9), 1776-1782.
51. Hoffmann, M. R.; Martin, S. T.; Choi, W.; Bahnemann, D. W. Environmental applications of semiconductor photocatalysis. *Chem. Rev.* **1995**, *95* (1), 69-96.
52. Scheck, C. Degradation of phenol and salicylic acid by ultraviolet radiation/hydrogen peroxide/oxygen. *Water Research* **1995**, *29* (10), 2346-2352.
53. Alfano, O. M.; Bahnemann, D.; Cassano, A. E.; Dillert, R.; Goslich, R. Photocatalysis in water environments using artificial and solar light. *Catalysis Today* **2000**, *58* (2-3), 199-230.
54. Vinodgopal, K.; Bedja, I.; Hotchandani, S.; Kamat, P. V. A photocatalytic approach for the reductive decolorization of textile azo dyes in colloidal semiconductor suspensions. *Langmuir* **1994**, *10* (6), 1767-1771.
55. Mamba, G.; Mishra, A. K. Graphitic carbon nitride (g-C₃N₄) nanocomposites: A new and exciting generation of visible light driven photocatalysts for environmental pollution remediation. *Appl. Catal. B-Environ.* **2016**, *198*, 347-377.

56. Wen, J.; Xie, J.; Chen, X.; Li, X. A review on g-C₃N₄ -based photocatalysts. *Appl. Surf. Sci.* **2017**, *391*, 72-123.
57. Zheng, Y.; Lin, L.; Wang, B.; Wang, X. Graphitic carbon nitride polymers toward sustainable photoredox catalysis. *Angew. Chem. Int. Ed.* **2015**, *54* (44), 12868-84.
58. Wang, X.; Blechert, S.; Antonietti, M. Polymeric graphitic carbon nitride for heterogeneous photocatalysis. *ACS Catal.* **2012**, *2* (8), 1596-1606.
59. Wang, Y.; Wang, X.; Antonietti, M. Polymeric graphitic carbon nitride as a heterogeneous organocatalyst: From photochemistry to multipurpose catalysis to sustainable chemistry. *Angew. Chem. Int. Ed.* **2012**, *51* (1), 68-89.
60. Zhu, J.; Xiao, P.; Li, H.; Carabineiro, S. A. Graphitic carbon nitride: Synthesis, properties, and applications in catalysis. *ACS Appl Mater Interfaces* **2014**, *6* (19), 16449-65.
61. Kessler, F. K.; Zheng, Y.; Schwarz, D.; Merschjann, C.; Schnick, W.; Wang, X.; Bojdys, M. J. Functional carbon nitride materials — design strategies for electrochemical devices. *Nature Reviews Materials* **2017**, *2* (6), 17030.
62. Kroke, E.; Schwarz, M. Novel group 14 nitrides. *Coordination Chemistry Reviews* **2004**, *248* (5-6), 493-532.
63. Kouvetakis, J.; Todd, M. Carbon nitride and its synthesis from chemical vapor deposition of 1,3,5-triazine derivatives. 5606056, 1997.
64. Kumar, S.; Kumar, B.; Surendar, T.; Shanker, V. g-C₃N₄/natao₃ organic–inorganic hybrid nanocomposite: High-performance and recyclable visible light driven photocatalyst. *Mater. Res. Bull.* **2014**, *49*, 310-318.
65. Zhang, Y.; Thomas, A.; Antonietti, M.; Wang, X. Activation of carbon nitride solids by protonation: Morphology changes, enhanced ionic conductivity, and photoconduction experiments. *J. Am. Chem. Soc.* **2009**, *131* (1), 50-1.
66. Lan, H.; Li, L.; An, X.; Liu, F.; Chen, C.; Liu, H.; Qu, J. Microstructure of carbon nitride affecting synergetic photocatalytic activity: Hydrogen bonds vs. Structural defects. *Appl. Catal. B-Environ.* **2017**, *204*, 49-57.
67. Dong, G.; Zhang, L. Porous structure dependent photoreactivity of graphitic carbon nitride under visible light. *J. Mater. Chem.* **2012**, *22* (3), 1160.
68. Fina, F.; Callear, S. K.; Carins, G. M.; Irvine, J. T. S. Structural investigation of graphitic carbon nitride via XRD and neutron diffraction. *Chem. Mater.* **2015**, *27* (7), 2612-2618.

69. Holst, J. R.; Gillan, E. G. From triazines to heptazines: Deciphering the local structure of amorphous nitrogen-rich carbon nitride materials. *J. Am. Chem. Soc.* **2008**, *130* (23), 7373-9.
70. Schwarzer, A.; Saplinova, T.; Kroke, E. Tri-s-triazines (s-heptazines)—from a “mystery molecule” to industrially relevant carbon nitride materials. *Coordination Chemistry Reviews* **2013**, *257* (13-14), 2032-2062.
71. Horvath-Bordon, E.; Kroke, E.; Svoboda, I.; Fuess, H.; Riedel, R.; Neeraj, S.; Cheetham, A. K. Alkalicynamelurates, $m_3[c_6n_7o_3].Xh_2o$, $m = li, na, k, rb, cs$: UV-luminescent and thermally very stable ionic tri-s-triazine derivatives. *Dalton transactions* **2004**, (22), 3900-8.
72. Cui, Y.; Ding, Z.; Liu, P.; Antonietti, M.; Fu, X.; Wang, X. Metal-free activation of H₂O₂ by g-C₃N₄ under visible light irradiation for the degradation of organic pollutants. *PCCP* **2012**, *14* (4), 1455-62.
73. Ishida, Y.; Chabanne, L.; Antonietti, M.; Shalom, M. Morphology control and photocatalysis enhancement by the one-pot synthesis of carbon nitride from preorganized hydrogen-bonded supramolecular precursors. *Langmuir* **2014**, *30* (2), 447-51.
74. Dong, F.; Zhao, Z.; Xiong, T.; Ni, Z.; Zhang, W.; Sun, Y.; Ho, W. K. In situ construction of g-C₃N₄/g-C₃N₄ metal-free heterojunction for enhanced visible-light photocatalysis. *ACS Appl Mater Interfaces* **2013**, *5* (21), 11392-401.
75. Kiskan, B.; Zhang, J.; Wang, X.; Antonietti, M.; Yagci, Y. Mesoporous graphitic carbon nitride as a heterogeneous visible light photoinitiator for radical polymerization. *ACS Macro Letters* **2012**, *1* (5), 546-549.
76. Su, F.; Mathew, S. C.; Lipner, G.; Fu, X.; Antonietti, M.; Blechert, S.; Wang, X. Mpg-c(3)n(4)-catalyzed selective oxidation of alcohols using o(2) and visible light. *J. Am. Chem. Soc.* **2010**, *132* (46), 16299-301.
77. Meyer, A. U.; Lau, V. W.-h.; König, B.; Lotsch, B. V. Photocatalytic oxidation of sulfinates to vinyl sulfones with cyanamide-functionalised carbon nitride. *Eur J Org Chem* **2017**, *2017* (15), 2179-2185.
78. Wang, X.; Maeda, K.; Chen, X.; Takanebe, K.; Domen, K.; Hou, Y.; Fu, X.; Antonietti, M. Polymer semiconductors for artificial photosynthesis: Hydrogen evolution by mesoporous graphitic carbon nitride with visible light. *J. Am. Chem. Soc.* **2009**, *131* (5), 1680-1.
79. Zhang, G.; Zhang, J.; Zhang, M.; Wang, X. Polycondensation of thiourea into carbon nitride semiconductors as visible light photocatalysts. *J. Mater. Chem.* **2012**, *22* (16), 8083.

80. Shalom, M.; Gimenez, S.; Schipper, F.; Herraiz-Cardona, I.; Bisquert, J.; Antonietti, M. Controlled carbon nitride growth on surfaces for hydrogen evolution electrodes. *Angewandte Chemie* **2014**, *53* (14), 3654-8.
81. Chen, X.; Jun, Y.-S.; Takanabe, K.; Maeda, K.; Domen, K.; Fu, X.; Antonietti, M.; Wang, X. Ordered mesoporous sba-15 type graphitic carbon nitride: A semiconductor host structure for photocatalytic hydrogen evolution with visible light. *Chem. Mater.* **2009**, *21* (18), 4093-4095.
82. Goettmann, F.; Fischer, A.; Antonietti, M.; Thomas, A. Chemical synthesis of mesoporous carbon nitrides using hard templates and their use as a metal-free catalyst for friedel-crafts reaction of benzene. *Angew. Chem. Int. Ed.* **2006**, *45* (27), 4467-71.
83. Niu, P.; Zhang, L.; Liu, G.; Cheng, H.-M. Graphene-like carbon nitride nanosheets for improved photocatalytic activities. *Adv. Funct. Mater.* **2012**, *22* (22), 4763-4770.
84. Cao, Y.; Zhang, Z.; Long, J.; Liang, J.; Lin, H.; Lin, H.; Wang, X. Vacuum heat-treatment of carbon nitride for enhancing photocatalytic hydrogen evolution. *J. Mater. Chem. A* **2014**, *2* (42), 17797-17807.
85. Botari, T.; Huhn, W. P.; Lau, V. W.-h.; Lotsch, B. V.; Blum, V. Thermodynamic equilibria in carbon nitride photocatalyst materials and conditions for the existence of graphitic carbon nitride g-C₃N₄. *Chem. Mater.* **2017**, *29* (10), 4445-4453.
86. Lau, V. W.-h.; Yu, V. W.-z.; Ehrat, F.; Botari, T.; Moudrakovski, I.; Simon, T.; Duppel, V.; Medina, E.; Stolarczyk, J. K.; Feldmann, J.; Blum, V.; Lotsch, B. V. Urea-modified carbon nitrides: Enhancing photocatalytic hydrogen evolution by rational defect engineering. *Advanced Energy Materials* **2017**, *7* (12), 1602251.
87. Lau, V. W.; Moudrakovski, I.; Botari, T.; Weinberger, S.; Mesch, M. B.; Duppel, V.; Senker, J.; Blum, V.; Lotsch, B. V. Rational design of carbon nitride photocatalysts by identification of cyanamide defects as catalytically relevant sites. *Nat Commun* **2016**, *7*, 12165.
88. Montoya, A. T.; Gillan, E. G. Enhanced photocatalytic hydrogen evolution from transition-metal surface-modified TiO₂. *ACS Omega* **2018**, *3* (3), 2947-2955.
89. Yan, S. C.; Li, Z. S.; Zou, Z. G. Photodegradation performance of g-C₃N₄ fabricated by directly heating melamine. *Langmuir* **2009**, *25* (17), 10397-401.
90. Bojdys, M. J.; Muller, J. O.; Antonietti, M.; Thomas, A. Ionothermal synthesis of crystalline, condensed, graphitic carbon nitride. *Chemistry* **2008**, *14* (27), 8177-82.
91. Lotsch, B. V.; Schnick, W. New light on an old story: Formation of melam during thermal condensation of melamine. *Chemistry* **2007**, *13* (17), 4956-68.

92. Jiang, L.; Yuan, X.; Zeng, G.; Chen, X.; Wu, Z.; Liang, J.; Zhang, J.; Wang, H.; Wang, H. Phosphorus- and sulfur-codoped g-C₃N₄: Facile preparation, mechanism insight, and application as efficient photocatalyst for tetracycline and methyl orange degradation under visible light irradiation. *ACS Sustainable Chem. Eng.* **2017**, *5* (7), 5831-5841.
93. Maeda, K.; Wang, X.; Nishihara, Y.; Lu, D.; Antonietti, M.; Domen, K. Photocatalytic activities of graphitic carbon nitride powder for water reduction and oxidation under visible light. *J. Phys. Chem. C* **2009**, *113* (12), 4940-4947.
94. Chang, F.; Li, C. L.; Luo, J. R.; Xie, Y. C.; Deng, B. Q.; Hu, X. F. Enhanced visible-light-driven photocatalytic performance of porous graphitic carbon nitride. *Appl. Surf. Sci.* **2015**, *358*, 270-277.
95. Xiao, T.; Tang, Z.; Yang, Y.; Tang, L.; Zhou, Y.; Zou, Z. In situ construction of hierarchical WO₃/g-C₃N₄ composite hollow microspheres as a z-scheme photocatalyst for the degradation of antibiotics. *Appl. Catal. B-Environ.* **2018**, *220*, 417-428.
96. Thomas, A.; Goettmann, F.; Antonietti, M. Hard templates for soft materials: Creating nanostructured organic materials. *Chem. Mater.* **2008**, *20* (3), 738-755.
97. Vinu, A.; Ariga, K.; Mori, T.; Nakanishi, T.; Hishita, S.; Golberg, D.; Bando, Y. Preparation and characterization of well-ordered hexagonal mesoporous carbon nitride. *Adv. Mater.* **2005**, *17* (13), 1648-1652.
98. Goettmann, F.; Fischer, A.; Antonietti, M.; Thomas, A. Metal-free catalysis of sustainable friedel-crafts reactions: Direct activation of benzene by carbon nitrides to avoid the use of metal chlorides and halogenated compounds. *Chem. Commun.* **2006**, (43), 4530-4532.
99. Goettmann, F.; Fischer, A.; Antonietti, M.; Thomas, A. Mesoporous graphitic carbon nitride as a versatile, metal-free catalyst for the cyclisation of functional nitriles and alkyne. *New Journal of Chemistry* **2007**, *31* (8), 1455-1460.
100. Standard thermodynamic properties of chemical substances. In *CRC handbook of chemistry and physics*, 98th Edition (Internet Version) ed.; Rumble, J. R., Ed. CRC Press/Taylor & Francis: Boca Raton, FL, 2018; pp 5-3-5-41.
101. Petterson, R. C.; Grzeskowiak, U.; Jules, L. H. N-halogen compounds. II.1,2the n—cl stretching band in some n-chloroamides. The structure of trichloroisocyanuric acid. *The Journal of Organic Chemistry* **1960**, *25* (9), 1595-1598.
102. Gao, H.; Yan, S.; Wang, J.; Huang, Y. A.; Wang, P.; Li, Z.; Zou, Z. Towards efficient solar hydrogen production by intercalated carbon nitride photocatalyst. *Physical chemistry chemical physics : PCCP* **2013**, *15* (41), 18077-84.

103. Sangster, J.; Pelton, A. D. Phase diagrams and thermodynamic properties of the 70 binary alkali halide systems having common ions. *J. Phys. Chem. Ref. Data* **1987**, *16* (3), 509-561.
104. Zhang, G.; Zhang, M.; Ye, X.; Qiu, X.; Lin, S.; Wang, X. Iodine modified carbon nitride semiconductors as visible light photocatalysts for hydrogen evolution. *Adv Mater* **2014**, *26* (5), 805-9.
105. Strmcnik, D.; Escudero-Escribano, M.; Kodama, K.; Stamenkovic, V. R.; Cuesta, A.; Markovic, N. M. Enhanced electrocatalysis of the oxygen reduction reaction based on patterning of platinum surfaces with cyanide. *Nat. Chem.* **2010**, *2* (10), 880-5.
106. Shaik, K.; Petersen, J. An investigation of the leaching of Pt and Pd from cooperite, sperrylite and column bioleached concentrates in thiocyanate-cyanide systems. *Hydrometallurgy* **2017**, *173*, 210-217.
107. Groenewolt, M.; Antonietti, M. Synthesis of g-C₃N₄ nanoparticles in mesoporous silica host matrices. *Adv. Mater.* **2005**, *17* (14), 1789-+.
108. Lin, B.; Xue, C.; Yan, X.; Yang, G.; Yang, G.; Yang, B. Facile fabrication of novel SiO₂/g-C₃N₄ core-shell nanosphere photocatalysts with enhanced visible light activity. *Appl. Surf. Sci.* **2015**, *357*, 346-355.
109. Dong, F.; Wang, Z.; Li, Y.; Ho, W. K.; Lee, S. C. Immobilization of polymeric g-C₃N₄ on structured ceramic foam for efficient visible light photocatalytic air purification with real indoor illumination. *Environ. Sci. Technol.* **2014**, *48* (17), 10345-53.
110. Fu, J. W.; Yu, J. G.; Jiang, C. J.; Cheng, B. g-C₃N₄-based heterostructured photocatalysts. *Advanced Energy Materials* **2018**, *8* (3), 1701503.
111. Lu, X.; Wang, Q.; Cui, D. Preparation and photocatalytic properties of g-C₃N₄/TiO₂ hybrid composite. *Journal of Materials Science & Technology* **2010**, *26* (10), 925-930.
112. Zhou, X.; Jin, B.; Li, L.; Peng, F.; Wang, H.; Yu, H.; Fang, Y. A carbon nitride/TiO₂ nanotube array heterojunction visible-light photocatalyst: Synthesis, characterization, and photoelectrochemical properties. *J. Mater. Chem.* **2012**, *22* (34), 17900.
113. Miranda, C.; Mansilla, H.; Yáñez, J.; Obregón, S.; Colón, G. Improved photocatalytic activity of g-C₃N₄/TiO₂ composites prepared by a simple impregnation method. *J. Photochem. Photobiol., A* **2013**, *253*, 16-21.
114. Villa, K.; Murcia-López, S.; Andreu, T.; Morante, J. R. On the role of WO₃ surface hydroxyl groups for the photocatalytic partial oxidation of methane to methanol. *Catalysis Communications* **2015**, *58*, 200-203.

115. Tomita, O.; Otsubo, T.; Higashi, M.; Ohtani, B.; Abe, R. Partial oxidation of alcohols on visible-light-responsive WO_3 photocatalysts loaded with palladium oxide cocatalyst. *ACS Catal.* **2016**, *6* (2), 1134-1144.
116. Huang, J.; Xiao, L.; Yang, X. WO_3 nanoplates, hierarchical flower-like assemblies and their photocatalytic properties. *Mater. Res. Bull.* **2013**, *48* (8), 2782-2785.
117. Zhao, G.; Huang, X.; Fina, F.; Zhang, G.; Irvine, J. T. S. Facile structure design based on C_3N_4 for mediator-free Z-scheme water splitting under visible light. *Catal. Sci. Technol.* **2015**, *5* (6), 3416-3422.
118. Aslam, I.; Cao, C.; Tanveer, M.; Khan, W. S.; Tahir, M.; Abid, M.; Idrees, F.; Butt, F. K.; Ali, Z.; Mahmood, N. The synergistic effect between WO_3 and $\text{g-C}_3\text{N}_4$ towards efficient visible-light-driven photocatalytic performance. *New J. Chem.* **2014**, *38* (11), 5462-5469.
119. Kailasam, K.; Fischer, A.; Zhang, G.; Zhang, J.; Schwarze, M.; Schroder, M.; Wang, X.; Schomacker, R.; Thomas, A. Mesoporous carbon nitride-tungsten oxide composites for enhanced photocatalytic hydrogen evolution. *ChemSusChem* **2015**, *8* (8), 1404-10.
120. Ding, J.; Wang, L.; Liu, Q. Q.; Chai, Y. Y.; Liu, X.; Dai, W. L. Remarkable enhancement in visible-light absorption and electron transfer of carbon nitride nanosheets with 1% tungstate dopant. *Appl. Catal. B-Environ.* **2015**, *176*, 91-98.
121. Gangwar, J.; Gupta, B. K.; Tripathi, S. K.; Srivastava, A. K. Phase dependent thermal and spectroscopic responses of Al_2O_3 nanostructures with different morphogenesis. *Nanoscale* **2015**, *7* (32), 13313-44.
122. Benson, J.; Kohn, H.; Boudart, M. On the reduction of tungsten trioxide accelerated by platinum and water. *J. Catal.* **1966**, *5* (2), 307-313.
123. Castro, F. J.; Tonus, F.; Bobet, J. L.; Urretavizcaya, G. Synthesis of hydrogen tungsten bronzes H_xWO_3 by reactive mechanical milling of hexagonal WO_3 . *Journal of Alloys and Compounds* **2010**, *495* (2), 537-540.
124. Wang, X. J.; Huang, Q. M.; Chen, X. F.; Wu, W.; Xiang, X. D.; Fu, Z.; Li, W. S. Electrodeposition fabrication of pore-arrayed hydrogen tungsten bronze as support of platinum nanoparticles for electrocatalytic oxidation of methanol oxidation. *Electrochim Acta* **2014**, *147*, 527-534.
125. Guayaquil-Sosa, J. F.; Serrano-Rosales, B.; Valadés-Pelayo, P. J.; de Lasa, H. Photocatalytic hydrogen production using mesoporous TiO_2 doped with Pt. *Appl. Catal. B-Environ.* **2017**, *211*, 337-348.
126. Galińska, A.; Walendziewski, J. Photocatalytic water splitting over Pt- TiO_2 in the presence of sacrificial reagents. *Energy & Fuels* **2005**, *19* (3), 1143-1147.

127. Chen, Z. D.; H. N. Miller, E., *Photoelectrochemical water splitting: Standards, experimental methods, and protocols*. Springer: New York, 2013.
128. Graetzel, M. Artificial photosynthesis: Water cleavage into hydrogen and oxygen by visible light. *Acc. Chem. Res.* **2002**, *14* (12), 376-384.
129. Valero, J. M.; Obregón, S.; Colón, G. Active site considerations on the photocatalytic H₂ evolution performance of Cu-doped TiO₂ obtained by different doping methods. *ACS Catal.* **2014**, *4* (10), 3320-3329.
130. Wu, N. L.; Lee, M. S. Enhanced TiO₂ photocatalysis by Cu in hydrogen production from aqueous methanol solution. *Int. J. Hydrogen Energy* **2004**, *29* (15), 1601-1605.
131. Chen, W.-T.; Chan, A.; Sun-Waterhouse, D.; Moriga, T.; Idriss, H.; Waterhouse, G. I. N. Ni/TiO₂: A promising low-cost photocatalytic system for solar H₂ production from ethanol–water mixtures. *J. Catal.* **2015**, *326*, 43-53.
132. Dhandole, L. K.; Mahadik, M. A.; Kim, S. G.; Chung, H. S.; Seo, Y. S.; Cho, M.; Ryu, J. H.; Jang, J. S. Boosting photocatalytic performance of inactive rutile TiO₂ nanorods under solar light irradiation: Synergistic effect of acid treatment and metal oxide co-catalysts. *ACS Appl. Mater. Interfaces* **2017**, *9* (28), 23602-23613.
133. Di Paola, A.; Marci, G.; Palmisano, L.; Schiavello, M.; Uosaki, K.; Ikeda, S.; Ohtani, B. Preparation of polycrystalline TiO₂ photocatalysts impregnated with various transition metal ions: Characterization and photocatalytic activity for the degradation of 4-nitrophenol. *J. Phys. Chem. B* **2002**, *106* (3), 637-645.
134. Asahi, R.; Morikawa, T.; Ohwaki, T.; Aoki, K.; Taga, Y. Visible-light photocatalysis in nitrogen-doped titanium oxides. *Science* **2001**, *293* (5528), 269-71.
135. Hattori, A.; Yamamoto, M.; Tada, H.; Ito, S. A promoting effect of NH₄F addition on the photocatalytic activity of sol-gel TiO₂ films. *Chem. Lett.* **1998**, *27* (8), 707-708.
136. Li, Z.; Xin, Y.; Wu, W.; Fu, B.; Zhang, Z. Phosphorus cation doping: A new strategy for boosting photoelectrochemical performance on TiO₂ nanotube photonic crystals. *ACS Appl. Mater. Interfaces* **2016**, *8* (45), 30972-30979.
137. Ohno, T.; Akiyoshi, M.; Umebayashi, T.; Asai, K.; Mitsui, T.; Matsumura, M. Preparation of S-doped TiO₂ photocatalysts and their photocatalytic activities under visible light. *Appl. Catal. A-Gen* **2004**, *265* (1), 115-121.
138. Coleman, N.; Perera, S.; Gillan, E. G. Rapid solid-state metathesis route to transition-metal doped titanias. *J. Solid State Chem.* **2015**, *232*, 241-248.

139. Lin, J.-D.; Yan, S.; Huang, Q.-D.; Fan, M.-T.; Yuan, Y.-Z.; Tan, T. T.-Y.; Liao, D.-W. TiO₂ promoted by two different non-noble metal cocatalysts for enhanced photocatalytic H₂ evolution. *Appl. Surf. Sci.* **2014**, *309*, 188-193.
140. Luo, Y.; Xu, Y.; Liu, X.; Xue, H.; Qian, Q.; Chen, Q. Design of Cu–Ce co-doped TiO₂ for improved photocatalysis. *J. Mater. Sci.* **2016**, *52* (3), 1265-1271.
141. Jung, M.; Hart, J. N.; Scott, J.; Ng, Y. H.; Jiang, Y.; Amal, R. Exploring Cu oxidation state on TiO₂ and its transformation during photocatalytic hydrogen evolution. *Appl. Catal. A-Gen* **2016**, *521*, 190-201.
142. Kubacka, A.; Muñoz-Batista, M. J.; Fernández-García, M.; Obregón, S.; Colón, G. Evolution of H₂ photoproduction with Cu content on CuO_x-TiO₂ composite catalysts prepared by a microemulsion method. *Appl. Catal. B-Environ.* **2015**, *163*, 214-222.
143. Wang, Y. Y.; Wan, C. C. Investigation of photoelectrochemical reduction of cupric ions over TiO₂ in the presence of methanol. *J. Photochem. Photobiol., A* **1994**, *84* (2), 195-202.
144. Jacobs, J. W. M. Copper photodeposition on TiO₂ studied with hrem and exafs. *J. Electrochem. Soc.* **1989**, *136* (10), 2914.
145. Reiche, H.; Dunn, W. W.; Bard, A. J. Heterogeneous photocatalytic and photosynthetic deposition of copper on titanium dioxide and tungsten(VI) oxide powders. *J. Phys. Chem.* **1979**, *83* (17), 2248-2251.
146. Lin, W.-Y. Photocatalytic removal of nickel from aqueous solutions using ultraviolet-irradiated TiO₂. *J. Electrochem. Soc.* **1997**, *144* (8), 2751.
147. Montini, T.; Gombac, V.; Sordelli, L.; Delgado, J. J.; Chen, X.; Adami, G.; Fornasiero, P. Nanostructured Cu/TiO₂ photocatalysts for H₂ production from ethanol and glycerol aqueous solutions. *ChemCatChem* **2011**, *3* (3), 574-577.
148. Clarizia, L.; Vitiello, G.; Luciani, G.; Somma, I. D.; Andreozzi, R.; Marotta, R. In situ photodeposited nano Cu on TiO₂ as a catalyst for hydrogen production under uv/visible radiation. *Appl. Catal. A-Gen* **2016**, *518*, 142-149.
149. Korzhak, A. V.; Ermokhina, N. I.; Stroyuk, A. L.; Bukhtiyarov, V. K.; Raevskaya, A. E.; Litvin, V. I.; Kuchmiy, S. Y.; Ilyin, V. G.; Manorik, P. A. Photocatalytic hydrogen evolution over mesoporous TiO₂/metal nanocomposites. *J. Photochem. Photobiol., A* **2008**, *198* (2-3), 126-134.
150. Vanysek, P., "Electrochemical series". In *CRC handbook of chemistry and physics*, 98th Edition (Internet Version) ed.; Rumble, J. R., Ed. CRC Press/Taylor & Francis: Boca Raton, FL, 2018; pp 5-77-5-83.
151. Nist X-ray photoelectron spectroscopy database, version 4.1 (national institute of standards and technology, gaithersburg, 2012). <http://srdata.nist.gov/xps/>.

152. Andersson, S. L. T.; Howe, R. F. An x-ray photoelectron study of metal-clusters in zeolites. *J. Phys. Chem.* **1989**, *93* (12), 4913-4920.
153. Tan, B. J.; Klabunde, K. J.; Sherwood, P. M. A. XPS studies of solvated metal atom dispersed (smad) catalysts. Evidence for layered cobalt-manganese particles on alumina and silica. *J. Am. Chem. Soc.* **1991**, *113* (3), 855-861.
154. Dube, C. E.; Workie, B.; Kounaves, S. P.; Robbat, A.; Aksu, M. L.; Davies, G. Electrodeposition of metal alloy and mixed-oxide films using a single-precursor tetranuclear copper-nickel complex. *J. Electrochem. Soc.* **1995**, *142* (10), 3357-3365.
155. Yu, J.; Hai, Y.; Cheng, B. Enhanced photocatalytic H₂-production activity of TiO₂ by Ni(OH)₂ cluster modification. *J. Phys. Chem. C* **2011**, *115* (11), 4953-4958.
156. Yu, J.; Ran, J. Facile preparation and enhanced photocatalytic H₂-production activity of Cu(OH)₂ cluster modified TiO₂. *Energy & Environmental Science* **2011**, *4* (4), 1364.
157. Chan, G. H.; Zhao, J.; Hicks, E. M.; Schatz, G. C.; Van Duyne, R. P. Plasmonic properties of copper nanoparticles fabricated by nanosphere lithography. *Nano Lett.* **2007**, *7* (7), 1947-1952.
158. Praveen Kumar, D.; Shankar, M. V.; Kumari, M. M.; Sadanandam, G.; Srinivas, B.; Durgakumari, V. Nano-size effects on CuO/TiO₂ catalysts for highly efficient H₂ production under solar light irradiation. *Chem. Commun.* **2013**, *49* (82), 9443-5.
159. Zuo, F.; Wang, L.; Wu, T.; Zhang, Z.; Borchardt, D.; Feng, P. Self-doped Ti³⁺-enhanced photocatalyst for hydrogen production under visible light. *J. Am. Chem. Soc.* **2010**, *132* (34), 11856-7.
160. Lian, Z.; Wang, W.; Li, G.; Tian, F.; Schanze, K. S.; Li, H. Pt-enhanced mesoporous Ti³⁺/TiO₂ with rapid bulk to surface electron transfer for photocatalytic hydrogen evolution. *ACS Appl. Mater. Interfaces* **2017**, *9* (20), 16959-16966.
161. Kawai, T.; Sakata, T. Photocatalytic hydrogen production from liquid methanol and water. *J. Chem. Soc., Chem. Commun.* **1980**, (15), 694.
162. Gage, S. H.; Trewyn, B. G.; Ciobanu, C. V.; Pylypenko, S.; Richards, R. M. Synthetic advancements and catalytic applications of nickel nitride. *Catalysis Science & Technology* **2016**, *6* (12), 4059-4076.
163. Clavel, G.; Molinari, V.; Kraupner, A.; Giordano, C. Easy access to Ni₃C- and Ni-carbon nanocomposite catalysts. *Chemistry* **2014**, *20* (29), 9018-23.
164. Han, L.; Feng, K.; Chen, Z. Self-supported cobalt nickel nitride nanowires electrode for overall electrochemical water splitting. *Energy Technology* **2017**, *5* (11), 1908-1911.

165. Kang, J. S.; Kim, J.-Y.; Yoon, J.; Kim, J.; Yang, J.; Chung, D. Y.; Kim, M.-c.; Jeong, H.; Son, Y. J.; Kim, B. G.; Jeong, J.; Hyeon, T.; Choi, M.; Ko, M. J.; Sung, Y.-E. Room-temperature vapor deposition of cobalt nitride nanofilms for mesoscopic and perovskite solar cells. *Advanced Energy Materials* **2018**, *8* (13), 1703114.
166. Wu, A.; Xie, Y.; Ma, H.; Tian, C.; Gu, Y.; Yan, H.; Zhang, X.; Yang, G.; Fu, H. Integrating the active oer and her components as the heterostructures for the efficient overall water splitting. *Nano Energy* **2018**, *44*, 353-363.
167. Baiker, A.; Maciejewski, M. Formation and thermal stability of copper and nickel nitrides. *Journal of the Chemical Society, Faraday Transactions 1: Physical Chemistry in Condensed Phases* **1984**, *80* (8), 2331.
168. Liu, T.; Li, M.; Dong, P.; Zhang, Y.; Zhou, M. Designing and synthesizing various nickel nitride (Ni₃N) nanosheets dispersed carbon nanomaterials with different structures and porosities as the high-efficiency non-enzymatic sensors. *Sensors and Actuators B: Chemical* **2018**, *260*, 962-975.
169. Fischer, A.; Muller, J. O.; Antonietti, M.; Thomas, A. Synthesis of ternary metal nitride nanoparticles using mesoporous carbon nitride as reactive template. *ACS Nano* **2008**, *2* (12), 2489-96.
170. Fukasawa, Y.; Takanabe, K.; Shimojima, A.; Antonietti, M.; Domen, K.; Okubo, T. Synthesis of ordered porous graphitic-C₃N₄ and regularly arranged ta₃n₅ nanoparticles by using self-assembled silica nanospheres as a primary template. *Chem Asian J* **2011**, *6* (1), 103-9.
171. Hwang, S.; Lee, S.; Yu, J. S. Template-directed synthesis of highly ordered nanoporous graphitic carbon nitride through polymerization of cyanamide. *Appl. Surf. Sci.* **2007**, *253* (13), 5656-5659.
172. Chen, X.; Zhang, J.; Fu, X.; Antonietti, M.; Wang, X. Fe-g-C₃N₄-catalyzed oxidation of benzene to phenol using hydrogen peroxide and visible light. *Journal of the American Chemical Society* **2009**, *131* (33), 11658-9.
173. Möhlmann, L.; Baar, M.; Rieß, J.; Antonietti, M.; Wang, X.; Blechert, S. Carbon nitride-catalyzed photoredox C-C bond formation with n-aryltetrahydroisoquinolines. *Advanced Synthesis & Catalysis* **2012**, *354* (10), 1909-1913.
174. Zhang, P.; Wang, Y.; Li, H.; Antonietti, M. Metal-free oxidation of sulfides by carbon nitride with visible light illumination at room temperature. *Green Chemistry* **2012**, *14* (7), 1904.
175. Li, X.-H.; Wang, X.; Antonietti, M. Solvent-free and metal-free oxidation of toluene using O₂ and g-C₃N₄ with nanopores: Nanostructure boosts the catalytic selectivity. *ACS Catal.* **2012**, *2* (10), 2082-2086.

176. Gage, S. H.; Ruddy, D. A.; Pylypenko, S.; Richards, R. M. Deep eutectic solvent approach towards nickel/nickel nitride nanocomposites. *Catalysis Today* **2018**, *306*, 9-15.